Helsinki University of Technology Publications in Laboratory of Theoretical and Applied Mechanics
Teknillisen korkeakoulun mekaniikan laboratorion julkaisuja
Espoo 1999 57

PROCEEDINGS OF THE TWELFTH NORDIC SEMINAR ON COMPUTATIONAL MECHANICS (NSCM-12)

Reijo Kouhia and Martti Mikkola (editors)

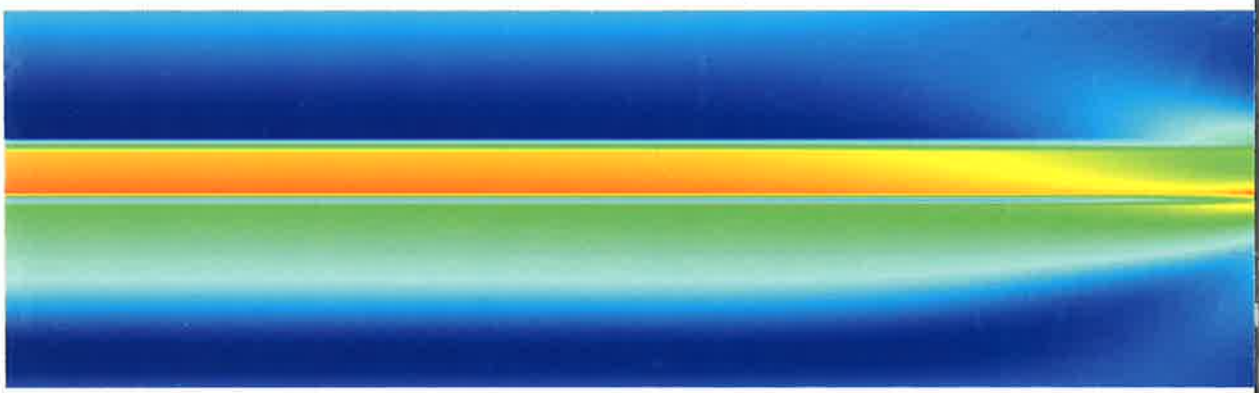

TEKNILLINEN KORKEAKOULU
TEKNISKA HÖGSKOLAN
HELSINKI UNIVERSITY OF TECHNOLOGY
TECHNISCHE UNIVERSITÄT HELSINKI
UNIVERSITE DE TECHNOLOGIE D'HELSINKI

Helsinki University of Technology Publications in Laboratory of
Theoretical and Applied Mechanics
Teknillisen korkeakoulun mekaniikan laboratorion julkaisuja
Espoo 1999 57

PROCEEDINGS OF THE TWELFTH NORDIC SEMINAR ON COMPUTATIONAL MECHANICS (NSCM-12)

Reijo Kouhia and Martti Mikkola (editors)

Helsinki University of Technology
Department of Engineering Physics and Mathematics
Laboratory of Theoretical and Applied Mechanics

Teknillinen korkeakoulu
Teknillisen fysiikan ja matematiikan osasto
Mekaniikan laboratorio

Distribution:
Helsinki University of Technology
Laboratory of Theoretical and Applied Mechanics
P.O. Box 1100
FIN-02150 HUT
Tel. +358-9-451 3068
Fax. +358-9-451 3070
E-mail: Tuula.Donskoi@hut.fi

ISBN 951-22-4731-3
ISSN 1456-6311

Oy Edita Ab
Helsinki 1999

PREFACE

The Nordic Association for Computational Mechanics (NoACM) was founded in October 1988. Its objective is to stimulate and promote research and applications within the area of computational mechanics. The main activity of NoACM is the annual two day seminar which provides a forum for personal contacts and for the exchange of ideas. These proceedings contain the presentations of the 12th Nordic Seminar on Computational Mechanics, held at Helsinki University of Technology, Finland, 22-23 October 1999.

This year's seminar contained five invited lectures and 44 contributed presentations divided into ten sessions. In the present volume, the contributed papers are placed first, in the order of appearance, and all the invited lectures in the later part.

The organizers of the seminar would like to thank all the invited lecturers and the contributors for their efforts in preparing the presentations and the texts for these proceedings. The editors are also very grateful to Mrs Tuula Donskoi for her indispensable help in organising the seminar. The financial support granted by the Academy of Finland and the hospitality provided by the City of Espoo are gratefully acknowledged.

Espoo, October, 1999

Reijo Kouhia and Martti Mikkola

CONTENTS

SESSION 9: Applications

SESSION 10: Non-linear Analysis

KEYNOTE SPEAKERS

SENSITIZING THE TRANSIENT TIMOSHENKO BEAM FINITE ELEMENT SOLUTION

Jouni Freund[(1)] and Eero-Matti Salonen[(2)]
[(1)]Department of Physiology, Finnish Institute of Occupational Health
[(2)] Laboratory of Theoretical Mechanics, Helsinki University of Technology

SUMMARY
Two extensions of the steady sensitized finite element formulation of the Timoshenko beam problem to the transient case are discussed. Accuracies of the semidiscrete Galerkin, and sensitized Galerkin formulations, obtained by calculating the relative error in the angular frequencies, are compared. The results indicate that the beneficial effect of sensitizing found in the steady case may improve the accuracy considerably also in the transient case.

INTRODUCTION
Least-squares type terms, based on the governing equation residuals, are used frequently to improve the properties of the standard Galerkin method. For example, these terms are necessary for stability reasons when one applies the finite element method to a convection dominated flow problem. The same approach can be used also in connection with solid mechanics problems. Then, however, the difficulties are often due to locking, and the additional terms are needed to destabilize the formulation. As the terms may then act to stabilize or destabilize a formulation we call them, following Courant, 'sensitizing terms' [1].

In this paper we discuss effect of sensitizing on the accuracy of the finite element solution in the transient case. Instead of trying to invent the optimal sensitizing, we extend the method for the steady case in a simple way. We consider the constant property Timoshenko beam equations

$$\left.\begin{aligned} R &\equiv kGA(w''-\theta')-m\ddot{w}=0 \\ S &\equiv kGA(w'-\theta)+EI\theta''-J\ddot{\theta}=0 \end{aligned}\right\} \quad (x,t)\in\Omega\subset\mathbb{R}^2, \tag{1}$$

(with obvious meaning of the notations) whose finite element solution by the standard Galerkin method is known to suffer from locking when the beam becomes thin. Equations (1) form a useful preparatory model for the more complicated Reissner-Mindlin equations for plates [2].

Remark. If the material is isotropic, shear correction factor $k=5/6$, Poisson ratio $\nu=1/3$ and the cross-section rectangular, the coefficients are given by $m=\rho tb$, $J=\rho t^3 b/12$, $kGA=5/16\cdot Ebt$ and $EI=Ebt^3/12$, where E is the Young's modulus, ρ is the density, t is the height and b the width of the beam cross-section.

EXACT SOLUTION
The exact solution to the model problem is taken to be of the series form

$$w=\sum_j A_j\cos(\omega_j t)\sin(j\pi x/L), \quad \theta=\sum_j B_j\cos(\omega_j t)\cos(j\pi x/L), \tag{2}$$

which corresponds to a simply supported beam or to a periodic solution in space (with period equal to the length of the domain L), if in the latter case the summation index is restricted to

take even values only. Substituting the typical mode j in (1) gives a homogeneous linear system of equations for A and B (we omit the subscripts of A_j, B_j and ω_j). A solution exists only if the determinant of the matrix of the system vanishes, which gives equation

$$(\lambda_L \bar{\omega}^2 - a^2)(\bar{\omega}^2 - \varepsilon_L a^2 - 1) - a^2 = 0 \tag{3}$$

for the angular frequency. The shorthand notations used are $\bar{\omega}^2 = \omega^2 J/(kGA)$, $a = j\pi$, $\varepsilon_L = EI/(kGAL^2)$ and $\lambda_L = mL^2/J$.

SENSITIZED FORMULATION

The sensitized weak formulation corresponding to (1) can be written as: find $(w,\theta) \in U \times V$ such that

$$EI(\delta\theta', \theta')_\Omega + kGA(\delta w' - \delta\theta, w' - \theta)_\Omega + J(\delta\theta, \ddot{\theta})_\Omega + m(\delta w, \ddot{w})_\Omega + (\tau\delta S, S)_\Omega = 0 \tag{4}$$

$\forall(\delta w, \delta\theta) \in U \times V$. Formulation (4), containing a least-squares term with sensitizing parameter τ, is a straightforward extension of the practical formulation discussed in [2] for the steady case. We do not specify function sets U and V of the continuous case, but proceed directly to the discrete formulation.

Formulation (4) can be used for simultaneous discretization with respect to temporal and spatial coordinates and also for the partial discretization with respect to the spatial coordinate only. In the latter case, the approximations are chosen to be of the form

$$\tilde{w} = \sum_{i=1}^{n} N_i(x) w_i(t), \quad \tilde{\theta} = \sum_{i=1}^{n} N_i(x) \theta_i(t) \tag{5}$$

in which $N_i(x)$ are the given shape functions, n is the number of nodes and $w_i(t)$, $\theta_i(t)$ are the nodal parameters depending on time. In what follows we assume that the mesh is uniform, use representations (see equation (2))

$$w_i = \sum_j \tilde{A}_j \cos(\tilde{\omega}_j t) \sin(j\pi \frac{i}{n}), \quad \theta_i = \sum_j \tilde{B}_j \cos(\tilde{\omega}_j t) \cos(j\pi \frac{i}{n}), \tag{6}$$

and consider only the typical j:th mode. When the approximation is linear, a stable and accurate formulation is obtained with $\tau = -h^2/(12EI + kGAh^2)$ (h is the element length) and by using one point quadrature with respect to the spatial coordinate in the second and last terms of (4).

The equation for $\tilde{\omega}$ of the numerical solution can be obtained in the same manner as in the case of the exact solution (one needs some formulas concerning sin and cos such as $\sin(aj + a) - \sin(aj - a) = 2\sin(a)\cos(aj)$ in the manipulations). The following coefficients, depending on the smoothness of a mode relative to the mesh $a_n = a/n = j\pi/n$, turn out to be important:

$$F_1 = \frac{12\sin^2(a_n/2)}{a_n^2(2 + \cos a_n)}, \quad F_2 = \frac{3\sin(a_n)}{a_n(2 + \cos a_n)}, \quad F_3 = \frac{3\cos^2(a_n/2)}{(2 + \cos a_n)}. \tag{7}$$

It is noteworthy that the coefficients approach the value one when the number of nodes n is large compared to j.

Standard Galerkin formulation

The standard Galerkin method can be obtained by selecting $\tau = 0$ and using exact quadratures in (4). The set of ordinary differential equations giving the nodal parameters as functions of time is

$$\begin{aligned} &\{r\}_G \equiv kGA[D^2]\{w\} - kGA[D^1]^T\{\theta\} + m[D^0]\{\ddot{w}\} = \{0\}, \\ &\{s\}_G \equiv EI[D^2]\{\theta\} - kGA[D^1]\{w\} + kGA[D^0]\{\theta\} + J[D^0]\{\ddot{\theta}\} = \{0\}, \end{aligned} \tag{8}$$

where $\{\theta\}, \{w\}$ denote the vectors of nodal parameters, and $[D^2],[D^1],[D^0]$ are matrices of the well-known difference stencils corresponding to the linear approximation and second, first and zero order spatial derivatives, respectively. The equation for the angular frequency is

$$[\lambda_L \bar{\omega}^2 - F_1 a^2][\bar{\omega}^2 - \varepsilon_L F_1 a^2 - 1] - (F_2 a)^2 = 0. \tag{9}$$

It is easy to see that in the limit, when $n \to \infty$ with $nh = L$, equations (9) and (3) coincide.

Sensitized Galerkin formulation

When discretizing the equations only with respect to the spatial coordinate, one may use *spatial* variations $\delta\tilde{w}$, $\delta\tilde{\theta}$ defined by condition that the variations of the derivatives with respect to time are zeros. Then $\delta\tilde{S} = kGA(\delta\tilde{w}' - \delta\tilde{\theta})$, $\tilde{S} = kGA(\tilde{w}' - \tilde{\theta}) - J\ddot{\tilde{\theta}}$ (linear approximation in space) and the set of ordinary differential equations reads

$$\begin{aligned} &\{r\}_{SG} \equiv \{r\}_G + \tau(kGA)^2[D^2]\{w\} - \tau(kGA)^2[D^1]^T\{\theta\} - \tau kGA\, J[D^1]^T\{\ddot{\theta}\} = \{0\}, \\ &\{s\}_{SG} \equiv \{s\}_G - \tau(kGA)^2[D^1]\{w\} + \tau(kGA)^2[D^0]\{\theta\} + \tau kGA\, J[D^0]\{\ddot{\theta}\} = \{0\} \end{aligned} \tag{10}$$

making the overall mass-matrix unsymmetric. The equation for the angular frequency of this formulation is given by

$$[\lambda_L \bar{\omega}^2 - F_1 a^2(1+\bar{\tau})][\bar{\omega}^2 - \varepsilon_L F_1 a^2 - F_3 + \bar{\tau}(\bar{\omega}^2 - 1)F_3] - (1+\bar{\tau})[1 - \bar{\tau}(\bar{\omega}^2 - 1)](F_2 a)^2 = 0, \tag{11}$$

where $\bar{\tau} = \tau kGA$. Also now, when $n \to \infty$ with $nh = L$, equations (11) and (3) coincide.

Symmetric sensitized Galerkin formulation

Non-symmetric mass matrix can be avoided by using a spatio-temporal variation as then $\delta\tilde{S} = kGA(\delta\tilde{w}' - \delta\tilde{\theta}) - J\delta\ddot{\tilde{\theta}}$, $\tilde{S} = kGA(\tilde{w}' - \tilde{\theta}) - J\ddot{\tilde{\theta}}$ and the least squares terms gives a symmetric contribution. The set of ordinary differential equations (8) is

$$\begin{aligned} &\{r\}_{SSG} \equiv \{r\}_{SG} = \{0\}, \\ &\{s\}_{SSG} \equiv \{s\}_{SG} - \tau J\, kGA[D^1]\{\ddot{w}\} + \tau J\, kGA[D^0]\{\ddot{\theta}\} + \tau J^2[D^0]\{\theta^{(4)}\} = \{0\}. \end{aligned} \tag{12}$$

It is noteworthy that the problem is of the fourth order now. The equation for the angular frequency of this formulation is

$$[\lambda_L\bar{\omega}^2 - F_1a^2(1+\bar{\tau})][\bar{\omega}^2 - \varepsilon_L F_1a^2 - F_3 - \bar{\tau}(\bar{\omega}^2-1)^2F_3] - [1-\bar{\tau}(\bar{\omega}^2-1)]^2(F_2a)^2 = 0. \qquad (13)$$

Again, when $n \to \infty$ with $nh = L$, equations (13) and (3) coincide.

ERROR IN $\tilde{\omega}$

The error $(\tilde{\omega}-\omega)/\omega$ in the largest angular frequency with a fixed j was taken as the measure of accuracy. To study the effect of sensitizing, the error was calculated as function of the element size h and relative thickness t/L of the beam. The other parameters were $L=1$, $b=1/10$, $\nu=1/3$ and $k=5/6$. It turned out that the error could be represented approximately by $(\tilde{\omega}-\omega)/\omega = Ch^2$ where C depends on the formulation and the relative thickness of the beam. Table 1 shows that the coefficient of the standard Galerkin method is roughly inversely proportional to t/L whereas the coefficients of the sensitized formulations are bounded in t/L.

Table 1. Coefficient C as function of the relative thickness t/L of the beam (C_G ~ standard Galerkin, C_{SG} ~ sensitized Galerkin, C_{SSG} ~ symmetric sensitized Galerkin).

t/L	C_G	C_{SG}	C_{SSG}
1/1000	6000000	328	328
1/100	149794	321	314
1/10	1779	193	58
1/1	180	164	1

CONCLUDING REMARKS

The effect of sensitizing was discussed in connection with a transient Timoshenko beam model problem and semi-discretized formulation. It turned out that sensitizing improves the accuracy of the angular frequency of a typical mode in particular when the beam is thin. The version leading to a symmetric mass-matrix was more accurate than the unsymmetric one. On the other hand, the appearance of the fourth time derivative may be somewhat inconvenient in practice.

REFERENCES

[1] J. Freund , E.-M. Salonen, *Sensitizing according to Courant the Timoshenko beam finite element solution*, accepted for publication in International Journal for Numerical Methods in Engineering.

[2] J. Freund, E.-M. Salonen, *Sensitizing the Timoshenko beam and the Reissner-Mindlin plate finite element solution*, Teknillisen Korkeakoulun mekaniikan laboratorion julkaisuja 50, 1998.

An analysis of finite element locking in a parameter dependent model problem

V. Havu J.Pitkäranta

September 30, 1999

Institute of Mathematics, Helsinki University of Technology,
+358-9-4513018, Ville.Havu@hut.fi

Locking, or parametric error amplification is a well-known phenomenon that may arise when solving parametric elliptic problems with the finite element method. Here we consider the bilinear finite element approximation of smooth solutions to a simple model problem, the problem of highly anisotropic heat conduction. The standard bilinear form associated with such a problem is

$$\mathcal{A}(u,v) = < \frac{\partial u}{\partial \xi}, \frac{\partial v}{\partial \xi} > + \epsilon^2 < \frac{\partial u}{\partial \eta}, \frac{\partial v}{\partial \eta} >,$$

where ξ and η are the principal directions of heat conduction and ϵ is a positive parameter, usually small compared to unity. This model problem displays the characteristics of a typical shell problem in that depending on the boundary and load conditions the asymptotic solution when $\epsilon \to 0$ can fall into two different states. These could be named as the *cool state* and the *hot state*, respectively. In the cool state, the main heat conduction occurs in the direction of high conductivity, whereas in the hot state, the conduction in the direction of low conductivity dominates.

Under favorable circumstances that depend on both the finite element mesh and on the type of boundary conditions, the effect of parametric

locking of the standard FEM can be reduced performing a simple variational crime. In this model problem we choose to commit the crime inserting the orthogonal L^2-projection onto elementwise constant functions in front of the term $\frac{\partial u}{\partial \xi}$ hoping to be able to reduce the locking constraint $\frac{\partial u}{\partial \xi} = 0$ thus obtaining a bilinear form

$$\mathcal{A}_h(u,v) = < R_h\frac{\partial u}{\partial \xi}, R_h\frac{\partial v}{\partial \xi} > + \epsilon^2 < \frac{\partial u}{\partial \eta}, \frac{\partial v}{\partial \eta} > + \epsilon^2 < (I - R_h)\frac{\partial u}{\partial \xi}, \frac{\partial v}{\partial \xi} >,$$

where R_h is the projection in question. The last term in this formulation is added to keep the formulation at least ϵ-stable. However, a word of caution is in place here since switching to this reduced bilinear form entails a consistency error component that must also be treated.

To show the relation of a mesh to the performance of the reduced scheme we consider four different types of meshes, each with the cool and the hot state separately:

1. General quadrilateral mesh.
2. Rectangular mesh.
3. Piecewise uniform rectangular mesh: Ω is divided into N subrectangles Ω_i, and each Ω_i is subdivided by a uniform rectangular mesh.
4. Uniform rectangular mesh: case 3 with $N = 1$.

The analysis of the reduced scheme is based on splitting the total relative error

$$e = \frac{|||u - u_h|||_h}{|||u|||}$$

in two components, the approximation error e_A and the consistency error e_C satisfying

$$e^2 = e_A^2 + e_C^2 ,$$

and treating these separately. Here u is the exact solution of the problem, u_h is the FE approximation, and $|||\cdot|||$, $|||\cdot|||_h$ denote the (semi) norms generated by $\mathcal{A}(\cdot,\cdot)$ and $\mathcal{A}_h(\cdot,\cdot)$ respectively. Then we can show that for the approximation error defined as

$$e_A = \frac{|||u - \tilde{u}_h|||_h}{|||u|||},$$

the bound

$$e_A \leq Ch$$

holds in the cool state and the bounds

$$e_A \leq \begin{cases} C\frac{h}{\epsilon} & \text{on a general mesh} \\ C\frac{h^2}{\epsilon} & \text{on a rectangular mesh} \\ C(N)h & \text{on a piecewise uniform mesh} \end{cases}$$

are valid in the hot state. Here C is a constant independent of ϵ. As for the consistency error component e_C defined as

$$e_C = \sup_{v \in \mathcal{V}_h^0, v \neq 0} \frac{(\mathcal{A} - \mathcal{A}_h)(u,v)}{|||u||| \, |||v|||_h}.$$

where $\mathcal{V}_h^0$ is the FE space, we have the bounds

$$e_C \leq \begin{cases} C\frac{h}{\epsilon} & \text{in the cool state} \\ Ch & \text{in the hot state} \end{cases}$$

on a general quadrilateral mesh and the bounds

$$e_C \leq \begin{cases} C\frac{h^2}{\epsilon} & \text{in the cool state} \\ Ch^2 & \text{in the hot state} \end{cases}$$

on a rectangular mesh and finally the bound

$$e_C \leq CQh^2 + C(N)Qh^{3/2} \text{ in the cool state}$$

on a piecewise uniform mesh with $C(1) = 0$.

In addition to theoretical calculations we show also some numerical results displaying the capabilities and limitations of the modified scheme.

On Latin Hypercube Sampling for Stochastic Finite Element Analysis

A. Olsson and G. Sandberg
Lund University, Division of Structural Mechanics
P.O. Box 118, SE-221 00 Lund, Sweden
e-mail: bmao@byggmek.lth.se

ABSTRACT

Summary An efficient sampling method for stochastic structural analysis is suggested. The Latin hypercube sampling plan, with correlation control, is brought into line with finite element applications. The procedure involves transformation of the correlated random input variables to a set of uncorrelated random variables. The number of random variables can in many cases be reduced which significantly improves the efficiency of the correlation controlled Latin hypercube sampling plan.

Introduction

Nowadays elaborated deterministic numerical methods and models, including sophisticated strategies for dealing with a variety of mechanical processes, have become widespread and are employed in everyday engineering design practice. However, in most design cases the engineer is left with uncertainties about how to actually model a structure. The uncertainties can be directed towards the stiffness values of structural members or connections, geometrical or material properties. Also production errors or damage, caused by accidents or inadequate management are in many civil engineering structures uncertain parameters that should be considered in the analysis.

Unavoidable uncertainties must be considered in a computational scheme to produce reliable computational and engineering results. Traditionally, designers have used safety factors to provide increased confidence of the structural performance, but this approach does not take into account the underlying, more sophisticated probability characteristics and does not provide the designer with adequate information about the reliability of the entire system. This has lead to rather extensive research aiming to combine efficient methods of structural analysis, with stochastic analysis where the influence of random variables are evaluated.

The only method that has become widespread in engineering design practice is the Monte Carlo simulation technique. Probabilistic design parameters are sampled and a number of deterministic computations are performed to provide information about the distribution, or some statistics of response parameters. This is an accurate and simple approach, but also very expensive in terms of computer resources. Several methods that could be employed at a lower computational cost have been proposed. These could be divided into three main categories. The methods of the first concern the sampling itself of the Monte Carlo technique in order to reduce the sample size required to provide reliable statistics of the response. To this category belong stratified sampling, and Latin hypercube sampling. Most work in this area is carried out by mathematical statisticians, and elaborated sampling techniques are rarely employed in the field of structural analysis using finite elements. A major advantage of these methods is that the consequent analysis, i.e. the runs determined by the sample, is identical to the deterministic analysis. Thus full advantage could be taken of existing commercial code developed for deterministic analysis, (Sandberg et al. 1997), and (Sandberg and Olsson 1999).

The methods of the second category also employs Monte Carlo simulations. However, the

strategy is to reduce the computational work by using efficient solutions techniques for the equation system of each run by making use of the similarity between the different realizations. The Neumann expansion method, and the preconditioned conjugate gradient method belong to this category.

Methods of the third category do not compute the response statistics through Monte Carlo simulations but through series expansions of the random variables. Naturally, this criteria result in a category containing many different methodologies. The most well know are probably; the Taylor series expansion method, in which a truncated Taylor series of the response variable is established, and the Neumann expansion method, in which a truncated Neumann series is employed for the equation system.

The present work makes a contribution to the first category of methods. The Latin hypercube sampling method, with correlation control, is further developed to overcome the restriction that the number of realizations must exceed the number of correlated random variables. The method could, without obstacles, be combined with methods from the second category.

Latin hypercube sampling

Latin hypercube sampling for computational planning was first proposed by (McKay et al. 1979). As for the standard Monte Carlo method the desired accuracy in the estimated distribution function determines the required number of realizations. Let n denote the required number of realizations and k the number of stochastic input variables, the sampling space is then k-dimensional. An $n \times k$ matrix $\mathbf{P}$ is established in which each of the k columns is a random permutation of (1,n). Then the sampling matrix $\mathbf{U}$ is determined as

$$\mathbf{U} = F^{-1}\left(\frac{\mathbf{P} - \mathbf{R}}{n}\right) \tag{1}$$

where $\mathbf{R}$ is an $n \times k$ matrix of independent random numbers from the uniform (0,1) distribution, and F^{-1} represents the inverse of the distribution function of each of the k stochastic variables. Each row in $\mathbf{U}$ now contains sample inputs for one deterministic computation. For two input variables and five realizations, a possible sampling plan is shown in Figure 1. Note that the sample is spread over the entire sampling space as the generation of the Latin hypercube sampling plan requires one image from each row and each column. If n realizations from the entire sampling space had been chosen completely at random, as in standard Monte Carlo sampling, there is a risk that they form a cluster and some parts of the sample space would not be investigated.

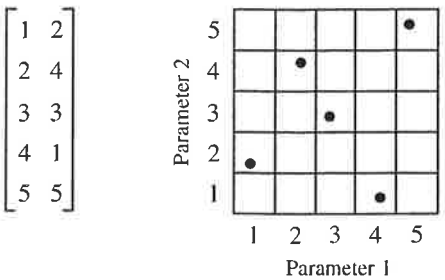

Figure 1: Latin cube, two variables and five realizations. The 5×2 matrix a) determines the plan illustrated in b).

Correlation control in Latin hypercube sampling

Even though the marginal distribution of each variable is efficiently represented there is a risk that some unwanted correlation appear, Figure 2 a). However, it has been shown (Iman and

Conover 1982) that such unwanted correlation can be reduced by modifications in the permutation matrix $\mathbf{P}$. The elements of $\mathbf{P}$ is divided by the number of realizations plus one, and mapped on the (0,1) Gaussian distribution,

$$\mathbf{Y} = \Phi^{-1}_{(0,1)}\left(\frac{\mathbf{P}}{n+1}\right) \tag{2}$$

Then the covariance matrix of $\mathbf{Y}$, $\mathbf{C}_y$, is estimated and Cholesky decomposed as

$$\mathbf{L}\mathbf{L}^T = \mathbf{C}_y \tag{3}$$

where $\mathbf{L}$ is lower triangular. A new matrix $\mathbf{Y}^*$ with sample covariance equal to the identity is computed as

$$\mathbf{Y}^* = \mathbf{Y}(\mathbf{L}^{-1})^T \tag{4}$$

and the ranks of the elements of the columns of $\mathbf{Y}^*$ become the elements in the columns of the matrix $\mathbf{P}^*$. If $\mathbf{P}$ in Eq. 1 is replaced by this matrix the sampling matrix $\mathbf{U}$ will contain a considerably lower amount of unwanted correlation. Figure 2 illustrates the effect of the correlation reduction procedure in a two variable sampling plan, a) represents the sampling plan before, and b) the sampling plan after the correlation reduction.

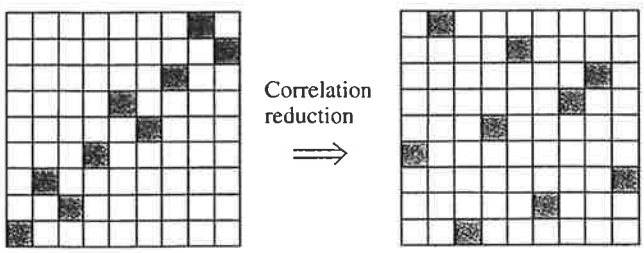

a) b)

Figure 2: Unwanted correlation of sampling plan a) is reduced in plan b).

If the target correlation matrix is different from unity the target correlation can easily be applied by multiplying, to the right, the right part of Eq. 4 by the upper triangular matrix from the Cholesky decomposition of the target correlation matrix.

It is important to note that the correlation reduction procedure described above requires the covariance matrix of $\mathbf{Y}$, $\mathbf{C}_y$, to be positive definite. This means that the inequality $n > k$ must be fulfilled. Unfortunately this is a severe restriction in many applications. If, for example, the random field is discretized to coincide with the finite element mesh the correlation control requires the number of realizations to be higher than the number of finite elements. However, if the random properties of adjacent elements are correlated the original set of random variables can be represented by a lower number of uncorrelated random variables. This is taken advantage of in the sampling procedure proposed below.

Correlation control in transformed variable space

The target correlation matrix $\mathbf{C}$ can be factorized as

$$\mathbf{D} = \mathbf{Z}^T\mathbf{C}\mathbf{Z} \tag{5}$$

where $\mathbf{D}$ is the eigenvalue matrix of $\mathbf{C}$, and $\mathbf{Z}$ is the corresponding, orthogonal eigenvector matrix. If the values at different locations of the discretized random field are significantly

correlated the sum of the r largest eigenvalues, where r is a small number compared to the total number of eigenvalues, is approximately equal to the trace of $\mathbf{D}$. This means that if the r largest eigenvalues are stored in the diagonal $r \times r$ matrix $\tilde{\mathbf{D}}$ and the corresponding eigenvectors are stored in the $k \times r$ matrix $\tilde{\mathbf{Z}}$ the target correlation matrix is approximately equal to $\tilde{\mathbf{C}}$ where

$$\tilde{\mathbf{C}} = \tilde{\mathbf{Z}}\tilde{\mathbf{D}}\tilde{\mathbf{Z}}^T \tag{6}$$

The original set of k correlated random variables, with target correlation matrix $\mathbf{C}$, can thus be replaced by a set of r uncorrelated random variables with target correlation matrix $\tilde{\mathbf{D}}$. This representation is commonly employed in conjunction with standard Monte Carlo sampling to decrease the computer effort of generating random numbers, and it is easy to transform the uncorrelated random numbers back to the correlated space.

When, the random variable representation is employed in conjunction with Latin hypercube sampling, with correlation reduction, it also contribute to relax the restriction; $n > k$. The new restriction read, $n > r$, and in many situations, as stated above, $r \ll k$. The Latin hypercube sampling on the uncorrelated variables starts by generating an $n \times r$ matrix $\tilde{\mathbf{P}}$ in which each of the r columns is a random permutation of (1,n). Then the procedure continues, equivalent to Eq. 2–4, as

$$\tilde{\mathbf{Y}} = \Phi^{-1}_{(0,1)}\left(\frac{\tilde{\mathbf{P}}}{n+1}\right) \tag{7}$$

$$\tilde{\mathbf{L}}\tilde{\mathbf{L}}^T = \mathbf{C}_{\tilde{y}} \tag{8}$$

$$\tilde{\mathbf{Y}}^* = \tilde{\mathbf{Y}}(\tilde{\mathbf{L}}^{-1})^T \tag{9}$$

where $\mathbf{C}_{\tilde{y}}$ is the estimated covariance matrix of $\tilde{\mathbf{Y}}$. Now the ranks of the elements of the columns of $\tilde{\mathbf{Y}}^*$ become the elements in the columns of the new matrix $\tilde{\mathbf{P}}^*$, and the final sampling matrix, in the original variable space, is established as

$$\tilde{\mathbf{U}} = F^{-1}\left(\Phi\left(\Phi^{-1}_{(0,1)}\left(\frac{\tilde{\mathbf{P}}^* - \tilde{\mathbf{R}}}{n}\right)\sqrt{\tilde{\mathbf{D}}}\tilde{\mathbf{Z}}^T\right)\right) \tag{10}$$

where $\tilde{\mathbf{R}}$ is an $n \times r$ matrix of independent random numbers from the uniform (0,1) distribution. The sampling matrix $\tilde{\mathbf{U}}$ represents the random field efficiently with respect to the marginal distributions, as well as to the correlation structure. This will be confirmed during the presentation by means of numerical examples. It will also be shown that the method, in conjunction with the Neumann series expansion method, is a very efficient, and generally applicable approach compared to alternative stochastic finite element approaches.

References

Iman, R. L., and Conover, W. J. (1982), "A distribution-free approach to inducing rank correlation among input variables," *Communications in Statistics, Part B - Simulation and Computation*, **11**, 311–334.

McKay, M. D., Conover, W. J., and Beckman R.J. (1979), "A comparison of three methods for selecting values of input variables in the analysis of output from a computer code," *Technometrics*, **21**, 239–245.

Sandberg, G., Kjell, G., and de Maré, J. (1997), "Computational planning using Latin hypercube sampling," *Report TVSM-7118*, Lund Inst. of Techn., Div. of Struct. Mech., Lund, Sweden.

Sandberg, G., and Olsson, A., (1999), "Failure sensitivity analysis of engineering structures," *Computers and Structures*, **72**, 525–534.

Level-Set Approach to the Finite Element Method

Peter Råback
Center for Scientific Computing
P.O.Box 405, FIN-02101 Espoo
E-mail: Peter.Raback@csc.fi

Introduction

There are many practical problems of interest where the physical shape changes with time. These include processes in growth, etching and molding. In order to solve such problems a tool which can track the free surface and solve the equations of change in the continuous domains is needed.

In this paper we propose a novel version of the finite element method for solving the free surface problems. The basic idea is to use a fixed mesh in which the elements are divided at the zero level-set so that the shape of the free surfaces is accurately described.

Computational Method

In the level-set method the free surface which may be difficult to track is presented by zero level-set of a time dependent function, $\phi(\vec{r}, t)$ [1, 2]. In the conventional level-set method the differential equation is written directly in terms of ϕ. In the presented method we use the standard finite element method to calculate the rate at which the free surfaces move [3, 4]. This data is then used to determine the level-set function at the free boundary. At other nodes the level-set function is obtained by

$$\phi(\vec{r}, t) = \min\left(\phi(\vec{r}', t) \pm |\vec{r} - \vec{r}'|\right)|_{\vec{r}' \in \Gamma}\ , \tag{1}$$

where the sign is selected so that the free boundary moves in the negative direction. The signed distance ensures that the level-set function is smooth and continuous. The free boundary on the next time-step is obtained by finding a new zero level-set using the original mesh.

The original elements are divided to smaller elements so that the boundary is accurately described. The initial mesh consists of bilinear elements that a line may divide in several ways, some of which are shown in Figure 1. If two lines are considered even more cases are introduced.

If the line crosses the element very close to an original node, a new node at that point would result to a poor aspect ratio for the new elements. Therefore a minimum

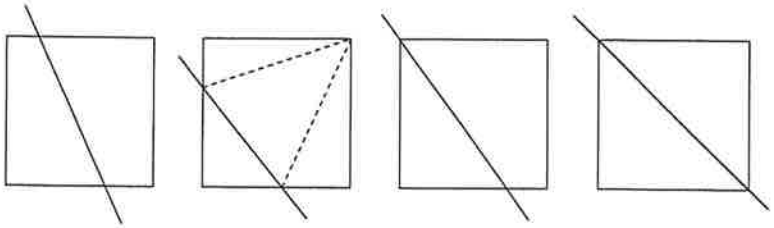

Figure 1: Different ways of dividing a rectangular element by a line

deviation, ε, in the value of the local coordinate is required before a new node is created. This creates consistency problems since if the change in the coordinate is small the free boundary may get stuck to the fixed nodes. Therefore we keep book of the introduced errors so that even multiple tiny steps will eventually free the boundary from the node.

Numerical Example

We apply the method for a simple problem that might represent isotropic etching driven by diffusion of a reactant. The stationary form of the diffusion equation yields

$$-\nabla^2 c = 0, \quad \vec{r} \in \Omega, \tag{2}$$

where c is the concentration. At the surfaces the reactant is consumed at a rate proportional to its amount,

$$\frac{\partial c}{\partial n} = -kc, \quad \vec{r} \in \Gamma_1, \tag{3}$$

where k is a constant. The solid material is eaten by the reactant and thus the etch rate is also proportional to the concentration. The change in the level-set function is thus

$$d\phi = k' c \, dt, \quad \vec{r} \in \Gamma_1, \tag{4}$$

where dt is the time-step and k' a constant. The time-step may be chosen so that the mean change in the level-set function $\langle d\phi \rangle$ is the desired one. The process is driven by an external fixed concentration,

$$c = c_0, \quad \vec{r} \in \Gamma_0. \tag{5}$$

The test geometry consists of a rectangular block (size 1×2) that is being etched from both sides, on the left $c = 1$ and on the right $c = 2$. Other parameters are $k = 100$ and $\langle d\phi \rangle = 0.005$. Figure 2 shows the computational boundaries at different steps. The boundaries move smoothly and the changes in topology are handled without any problems.

The computational mesh at step 104 is shown in Figure 3. The original mesh consists of 3060 elements and 3189 nodes. The diffusion equation is only solved outside the solid block which makes the number of unknowns vary with the step.

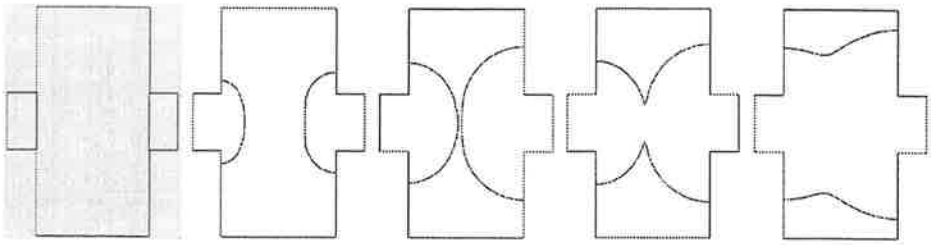

Figure 2: The computational boundaries at steps 1, 50, 100, 104 and 140.

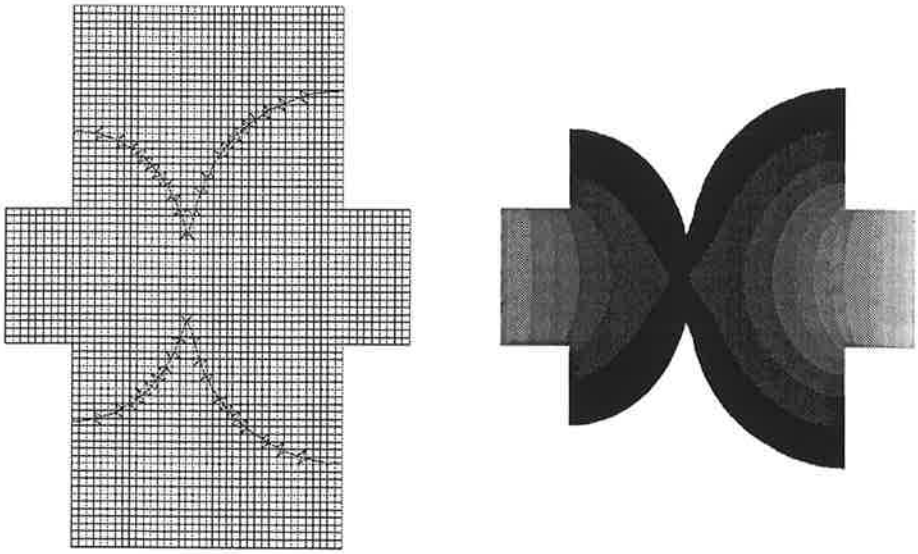

Figure 3: The computational mesh and the concentration at step 104.

The solution of 150 steps with Compaq AlphaServer running with 525 MHz took only 8.7 CPU-seconds. When the number of nodes was doubled the time increased to 32.1 seconds.

Conclusions

The method works as intended and can be used to resolve complicated free surface problems. The accuracy of the method is difficult to estimate. Small errors are introduced when the approximation for the free surface is set. Due to the problem of locking the grid convergence is not automatically obvious.

The simple example shows the power of the method. However, the physics is not realistic and further work is required for practical applications. The modification is

quite straight-forward since it only affects the equations of change. The method could be further developed for three dimensional problems as well. The number of ways that an element may be divided would be larger but the principle is yet the same.

References

[1] J. A. Sethian. *Level Set Methods and Fast Marching Methods.* Cambridge University Press, 1999.

[2] D. Adalsteinsson and J. A. Sethian. A level set approach to a unified model for etching, deposition, and lithography, I: Two-dimensional simulations. *Journal of Computational Physics*, 120(1):128–144, 1995.

[3] H. Kardestuncer and D. H. Norrie, editors. *Finite Element Handbook.* McGraw-Hill Book Company, 1987.

[4] G. A. Mohr. *Finite Elements for Solids, Fluids, and Optimization.* Oxford University Press, 1992.

OPTIMIZATION OF LAYERED STRUCTURES WITH RESPECT TO LAMINATION PARAMETERS AND LAY-UP PARAMETERS

By Maija Autio
Department of Mechanical Engineering, University of Oulu
PO Box 4200, FIN-90401Oulu, Finland
e-mail: Maija.Autio@me.oulu.fi

Abstract

The layered composites consist of thin orthotropic plies, in which stiff fibres are embedded in softer plastic matrix material. Thus, the properties of a lamina are highly directional and anisotropic, and the properties of structures made of these laminae can be tailored to fulfill specific needs by varying the orientations and thicknesses of the plies, for example.

As the composite material itself can be considered as a structure, see Fig. 1, the number of possible design variables in designing of structures made of composites is larger than in designing of structures made of isotropic materials. Lay-up parameters, i.e. the number of layers and orientation and thickness of the plies, are usually applied directly as design variables. Consequently, all kinds of thermomechanical properties can be considered in the same problem: layer properties, such as values of failure criteria, as well as global properties, such as stiffnesses of the laminate. The limitations of manufacturing can be taken into account in tailoring, and after design the manufacture of the structure is more or less straightforward. However, most thermomechanical properties depend on lay-up parameters in a nonlinear way, and optimization with respect to lay-up parameters often suffers on various local optima. Also, number of design variables may be rather high some of them being continuous but some discrete in character.

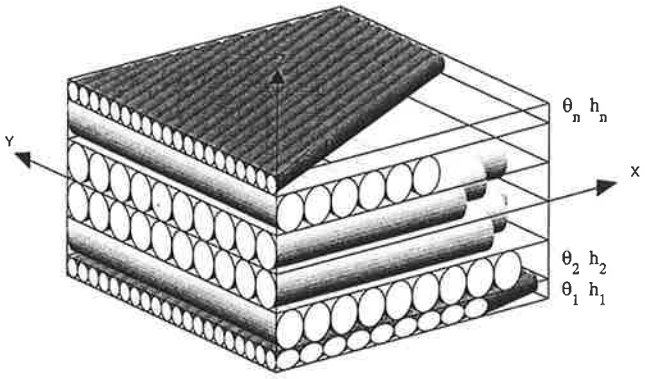

Fig. 1. Structure of a layered laminate.

The lamination parameters are moments of trigonometric functions through the thickness of the laminate, with which the terms of sines and cosines appearing in rotation formulas of an orthotropic material can be replaced (Tsai & Pagano, 1968). As the number of lamination parameters needed is sufficiently small, and as many thermomechanical properties are linear in the lamination parameters, they are useful as design variables in optimizing the global properties of laminates. Then the number of design variables is independent of the number of layers and all variables have continuous character. The most attractive benefit of using lamination parameters as design variables is that optimization problems often become convex (Grenestedt & Gudmundson, 1993), and thus the convergence to the local optima can be avoided. Drawbacks in using lamination parameters as design variables are that only the global properties of the laminate, such as the natural frequencies, can be presented as functions of lamination parameters. Also, after finding optimal lamination parameters, some procedure is needed to generate a real lay-up corresponding to these optimal parameters.

Here the optimization of laminated structures is divided into two phases: first an optimization task considering global properties with the lamination parameters as design variables is solved and then another optimization search is formulated for creating real lay-ups having lamination parameters as close as possible to the optimal ones. In the first phase global properties of the laminate, i.e. stiffnesses, natural frequencies etc. are minimized/maximized with respect to lamination parameters. Gradient-based algorithms can be employed in optimization, because these problems are often convex. If laminates considered are supposed to be symmetrically laminated, in-plane and bending behaviour of the laminate can be usually handled in separated problems. In the second phase lay-ups having lamination parameters as close as possible to the optimal ones are searched by minimizing the difference between the lamination parameters in the current design set and the target ones. As now the detailed lay-up of the current design point is known, also the

layer-wise properties can be taken into account. In-plane and bending behaviour can now be connected and laminates having both in-plane and bending lamination parameters as close as possible to the optimal ones can be generated. Stochastic optimization algorithms are beneficial in optimization with respect to lay-ups of laminates, because gradients with respect to design variables may be difficult to define analytically and some design variables, such as thicknesses, are often of a discrete character.

In this work genetic algorithms (GA) are applied for determining lay-ups having optimal or close to optimal lamination parameters. The GAs are well suited for that kind of problems, because the computation of the values of the lamination parameters is fast, and no time-consuming FEM solutions are needed during the iteration. Often the thicknesses and orientations of different layers can have only discrete values and the number of available uni/multiaxial plies may be limited. This can be handled easily in the GA searches, where all the design variables are discrete in character.

In examples coupled thermal-structural problems of laminated plates are considered. The strain energy, or certain displacements of laminated plates due to given boundary temperatures and displacement boundary conditions are optimized with respect to in-plane lamination parameters, and corresponding lay-ups are searched by using the GA. Also, buckling of the laminated plate due to given boundary temperatures is considered. The buckling factors for thermal loading can be expressed as a function of four in-plane and four bending lamination parameters, and the smallest buckling factor is maximized with respect to these parameters. Lay-ups having the lamination parameters as close as possible to these eight optimal ones are finally searched.

References

Grenestedt, J.L.; Gudmundson P. 1993: Layup optimization of composite material structures. In: Pedersen, P.(ed.) *Optimal Design with Advanced Materials.* Elsevier Science Publishers B.V. , 311 – 336.

Tsai, S. W.; Pagano, N. J. 1968: Invariant properties of composite materials. *Composite Materials Workshop* Technomic, 233 – 253

On structural optimization problems using the homogenization approach

A. Hillebrand * T. Kärkkäinen * and M. Miettinen †

1 Introduction

An abstract structural optimization problem of the material layout can be formulated as follows:

$$\inf_{a\in A_{ad}} / \sup_{a\in A_{ad}} J(a,u) \text{ such that } F(a,u)=0, \tag{1}$$

where a is the control variable (e.g., the conductivity or the elasticity tensor), u the state variable (e.g., the temperature or the displacement vector), J the cost function (e.g., the conductivity or the compliance of the structure), F the state equation (e.g., the heat or the elasticity equation), and A_{ad} is the set of the admissible controls (structures). Assume that we have k phases having different material properties represented by a_i, $i=1,...,k$. Then A_{ad} is defined by

$$A_{ad} = \{a : a=\sum_i \chi_i a_i + \text{possible constraints}\}$$

in which χ_i is the characteristic function of material i.

The studied problem can be interpreted as follows: Having several different materials at our disposal find the structure, i.e. the distribution of the available materials which minimizes/maximizes the given criteria. For example, the aim could be to find the stiffest or the most compliant structure in elasticity or the structure having the minimal or the maximal resistivity in conduction.

Usually such problems do not have a solution in a classical sense: one gets better and better structures by mixing the given materials on finer and finer scales. Therefore, we have to extend the basic class of structures A_{ad} into $\bar{A}_{ad}$, which includes also the generalized structures, (e.g., laminated or fiber reinforced) composites. The homogenization method allows us to determine the macroscopic properties of the composites from their microgeometry, which, for laminates, is determined by the

*University of Jyväskylä, Department of Mathematical Information Technology, PO Box 35 (MaE), 40351 Jyväskylä, Finland

†University of Jyväskylä, Department of Mathematics, PO Box 35 (MaD), 40351 Jyväskylä, Finland

width and orientation of the layers. Moreover, it can be shown that the relaxed problem arising from (1), where A_{ad} is replaced with $\bar{A}_{ad}$, has a solution.

The main difficulty in the homogenization approach is the determination of $\bar{A}_{ad}$, the set of all possible mixtures of the initial phases. In the homogenization theory this set is called the G-closure, and its explicit characterization in general cases is unknown. However, in practical structural optimization problems (e.g., due to the manufacturing constraints) one is usually allowed to use only a limited number of basic structures. In this case the cost function J can be optimized in $\tilde{A}_{ad}$ for which $A_{ad} \subsetneq \tilde{A}_{ad} \subsetneq \bar{A}_{ad}$. For example, $\tilde{A}_{ad}$ could contain the original phases i and all possible single laminates arising from them. In general this approach is referred as the partial relaxation of (1). Usually we can not guarantee the existence of the optimal structure, but even the "suboptimal" structures in $\tilde{A}_{ad}$ can improve substantially the value of the cost functional.

2 Model problems and their parametrization

Let us assume that we have two linearly conducting isotropic materials with the conductivity tensors αI and βI with $\alpha < \beta$. Then the set of admissible materials is defined by:

$$A_{ad} = \{a \mid a = \big((1-\chi(x))\alpha + \chi(x)\beta\big)I \ \text{ and } \ \int_\Omega \chi(x)\,dx = p\,|\Omega|\,\}, \tag{2}$$

where p is the volume fraction of the better conducting but presumably more expensive material β. As the state equation $F(a,u) = 0$ we choose the linear conductivity equation:

$$\begin{cases} -\mathrm{div}(a(x)\,\nabla u) = f & \text{in } \Omega, \\ \text{boundary conditions} & \text{on } \partial\Omega, \end{cases} \tag{3}$$

where $\Omega \subset \mathsf{R}^2$ and f is a given heat source or a sink term.

Example 1 *A problem of maximization/minimization of the torsion rigidity of an elastic bar made of two materials with different shear moduli μ_1 and μ_2. Assuming that the bar is cylindrical and infinitely long with the cross-section Ω, we can formulate this problem as*

$$\inf_{a\in A_{ad}} \Big/ \sup_{a\in A_{ad}} \int_\Omega u(x)\,dx, \tag{4}$$

where u solves (3) with $f = 1$ and $u|_{\partial\Omega} = 0$. Above the conductivity represents the inverse of the shear modulus: $\alpha = 1/\mu_1$ and $\beta = 1/\mu_2$. Hence, the minimization of the temperature means the maximization of the torsional rigidity and vice versa.

Example 2 *A problem of minimal temperature. For $\Omega = (0,l_1)\times(0,l_2)$ with $\partial\Omega = \cup_{i=1}^4 \Gamma_i$ and $\Gamma_1 = (0,l_1)\times\{0\}$, $\Gamma_2 = \{l_1\}\times(0,l_2)$, $\Gamma_3 = (0,l_1)\times\{l_2\}$, $\Gamma_4 = \{0\}\times(0,l_2)$,*

the body Ω is heated from the upper part Γ_3 and cooled from the lower part Γ_1 while the other boundaries are insulated. We want the average temperature in the subdomain $\Omega_0 \subset \Omega$ to be as low as possible, which yields the optimization problem

$$\inf_{a \in A_{ad}} \int_{\Omega_0} u(x)\, dx. \tag{5}$$

Again, u solves (3) with $f = 0$ and $u = 0$ on Γ_1, $u = 1$ on Γ_3, and $a\nabla u \cdot \vec{n} = 0$ on $\Gamma_2 \cup \Gamma_4$.

Consider next the homogenization based relaxation of the set A_{ad} in (2). We approximate the G-closure $\bar{A}_{ad}$ of A_{ad} (in this case we obtain the full relaxation) using a rotated 2-laminated structure. The actual construction is illustrated in Figure 1.

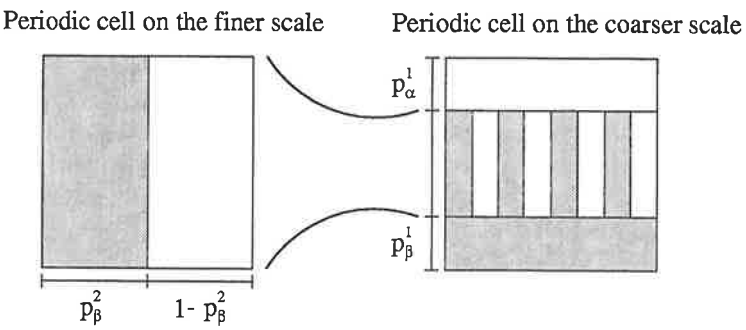

Figure 1: *2-laminated structure and its parametrization.*

The parametrization of the laminated structure can be described using the three volume fractions $p_\beta^2, p_\beta^1, p_\alpha^1$. The unknowns p_β^2, p_β^1 correspond to the amount of better material used on the two scales, and p_α^1 refers to the amount of the material α on the coarser scale. Finally, the relaxation is completed with an extra unknown θ to describe the rotation $R(\theta)$ of the laminate. This construction yields the full relaxation

$$\bar{A}_{ad} = \{\ a = R(\theta)^T a_0\, R(\theta) \ \mid \quad 0 \le p_\beta^2 \le 1,\ 0 \le p_\beta^1 \le 1,\ 0 \le p_\alpha^1,\ p_\alpha^1 + p_\beta^1 \le 1,$$
$$\int_\Omega p_\beta(p_\beta^2, p_\beta^1, p_\alpha^1) \le p\,|\Omega|\ \}, \tag{6}$$

where

$$p_\beta(p_\beta^2, p_\beta^1, p_\alpha^1) = p_\beta^1 + p_\beta^2(1 - p_\alpha^1 - p_\beta^1), \tag{7}$$

$$a_0 = a_0(p_\beta^2, p_\beta^1, p_\alpha^1) = \begin{pmatrix} a_0^1 & 0 \\ 0 & a_0^2 \end{pmatrix} \tag{8}$$

with

$$a_0^1 = \frac{-\beta^2 p_\beta^1(-1 + p_\beta^2) + \alpha^2 p_\alpha^1 p_\beta^2 + \alpha\beta(1 + p_\beta^1(-1 + p_\beta^2) - p_\alpha^1 p_\beta^2)}{\beta + \alpha p_\beta^2 - \beta p_\beta^2},$$

$$a_0^2 = \frac{\alpha\beta(\alpha(-1 + p_\beta^2) - \beta p_\beta^2)}{\alpha^2 p_\beta^1(-1 + p_\beta^2) - \beta^2 p_\alpha^1 p_\beta^2 + \alpha\beta(-1 + p_\beta^1(1 - p_\beta^2) + p_\alpha^1 p_\beta^2)}.$$

Here the symbol p_β denotes the volume fraction of the material β and a_0 the effective, homogenized conductivity tensor of the 2-laminated structure.

3 Numerical realization

The numerical realization of the structural optimization problems given in the previous chapter is based on the finite element method (FEM). The original domain Ω is divided into subdomains Ω_i, i.e. so-called material elements, where a piecewise constant approximation is applied for the set of unknowns $((p_\beta^2)_i, (p_\beta^1)_i, (p_\alpha^1)_i, \theta_i)$ arising from the periodic cells. The state variable u is approximated in the same mesh using quadratic polynomials as basis functions.

The actual optimization is performed using an SQP-method (Sequential Quadratic Programming) with a limited memory quasi-Newton based approximation for the Hessian. To have an efficient numerical realization, we have performed the sensitivity analysis of the discretized problem in order to find the gradient with respect to the unknows via solving the so-called adjoint state equation. The adjoint variable is discretized using the same basis as the state variable u, and a preconditioned Conjugate Gradient method is applied for solving the linear systems arising from the discretized state and adjoint equations.

To this end, Figure 2 contains a numerically computed optimal structure of the maximal torsional rigidity problem in Example 1 with $\alpha = 1$, $\beta = 2$, and $p = 0.5$. The white color represents more rigid material and the arrow the rotation of the laminated structure.

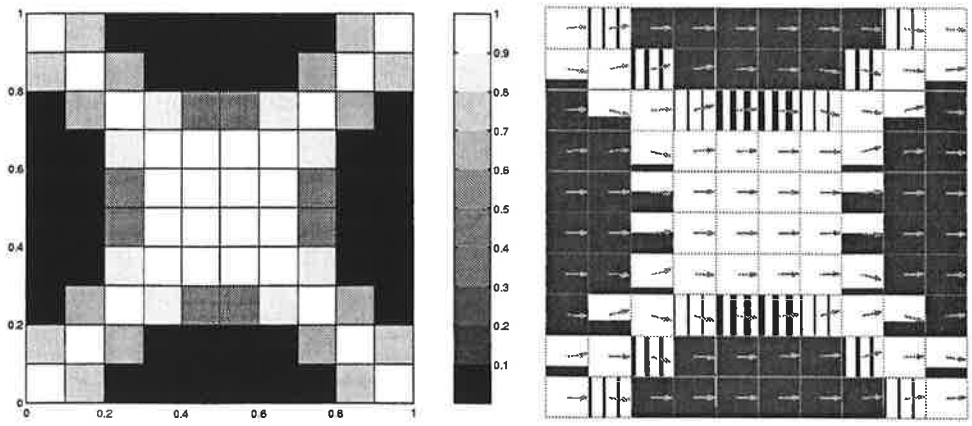

Figure 2: Computed optimal structure in Example 1.

OPTIMIZATION OF CLAMPED PLASTIC SPHERICAL SHELLS

J. Lellep and E. Tungel

Institute of Applied Mathematics,
Tartu University
Vanemuise 46, Tartu, ESTONIA

1. INTRODUCTION

Due to the simplicity of their manufacturing the special significance have the designs of piece wise constant thickness. Optimal designs for stepped plastic shallow shells have been established by J. Lellep and H. Hein (1993, 1994) and for deep spherical caps by J. Lellep and E. Tungel (1998).

In the present paper the stepped shells clamped at the edge and pierced with a central hole are considered. The exact solutions are established under the assumption that the material of the shells obeys the generalized square yield condition and the associated flow law.

2. FORMULATION OF THE PROBLEM

Consider a spherical shell of radius A subjected to the uniform external pressure of intensity P (Fig. 1). The external edge of the shell (the circle at $\varphi = \beta$) is clamped and the inner edge (at $\varphi = \alpha$) is absolutely free. Here the angles α and β are considered as given angles.

We are looking for the design of the shell confining our attention to the case of the stepped shell with one step in the thickness. Thus thickness of the shell is

$$h = \begin{cases} h_0, & \varphi \in (\alpha, \alpha_1) \\ h_1, & \varphi \in (\alpha_1, \beta) \end{cases} \tag{1}$$

where h_0, h_1, α_1 are to be considered as unknown constant parameters. These parameters have to be determined so that the load carrying capacity P of the cap attains the maximal value over the set of shells of the same weight (or mass, or material volume).

3. BASIC EQUATIONS

The equilibrium equations can be presented as

$$\begin{aligned} &(n_1 \sin\varphi)' - n_2 \cos\varphi = s \sin\varphi, \\ &(n_1 + n_2 + p)\sin\varphi = -(s \sin\varphi)', \\ &k\,[(m_1 \sin\varphi)' - m_2 \cos\varphi] = s \sin\varphi, \end{aligned} \tag{2}$$

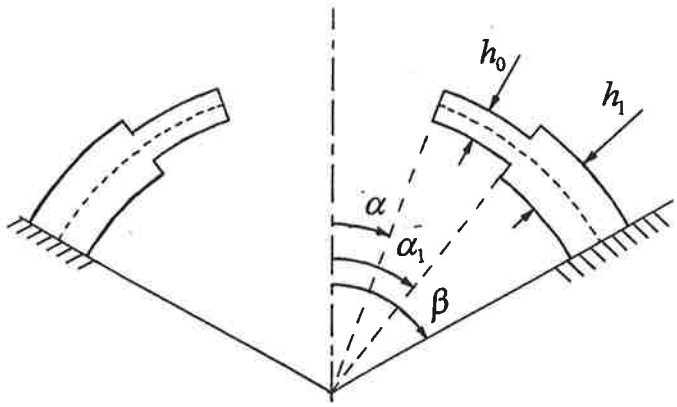

Figure 1: Spherical cap

where

$$n_{1,2} = \frac{N_{\varphi,\Phi}}{N_*}, \quad m_{1,2} = \frac{M_{\varphi,\Phi}}{M_*}, \quad s = \frac{S}{N_*}, \quad w = \frac{W}{A}, \quad u = \frac{U}{A},$$
$$\gamma_0 = \frac{h_0}{h_*}, \quad \gamma_1 = \frac{h_1}{h_*}, \quad k = \frac{h_*}{4A}, \quad p = \frac{PA}{N_*}. \tag{3}$$

Material of the shell is assumed to be an isotropic, homogeneous rigid-plastic one obeying the generalized square yield condition suggested by R. Sakaranarayanan (1964). This yield condition has its own application area but it can be handled as an approximation to the Tresca yield condition as well.

The exact yield surface in the space of generalized stresses is approximated as a generalized square yield condition.

It is resonable to assume that the stress state of the shell corresponds to the sides of the squares on the planes of moments and membrane forces, respectively where

$$M_\Phi = M_0, \quad N_\Phi = -N_0. \tag{4}$$

where M_0 and N_0 stand for the yield moment and yield force, respectively, e.g. $M_0 = \sigma_0 h^2/4$, $N_0 = \sigma_0 h$.

Evidently, at the section $\varphi = \alpha_1$ moment m_1 attains its maximal admissible value, e.g. the hinge circle appears at $\varphi = \alpha_1$. Assuming that $h_0 < h_1$ one has an intermediate condition

$$m_1(\alpha_1) = -\gamma_0^2. \tag{5}$$

The boundary conditions for the considered case of geometry of the shell are following

$$m_1(\alpha) = n_1(\alpha) = s(\alpha) = 0, \quad m_1(\beta) = -\gamma_1^2. \tag{6}$$

Making use of the non-dimensional quantities (5) one can present the weight of the shell as

$$v = (\cos\alpha - \cos\alpha_1)(3\gamma_0 + 4k^2\gamma_0^3) + (\cos\alpha_1 - \cos\beta)(3\gamma_1 + 4k^2\gamma_1^3). \tag{7}$$

4. SPHERICAL CAP OF PIECE WISE CONSTANT THICKNESS

Substituting (4) in (2) and integrating leads to the result

$$\begin{aligned} s &= \frac{1}{2}(2\gamma_0 - p)(\varphi - \alpha) + \frac{p}{2}\frac{\sin\alpha}{\sin\varphi}\sin(\varphi - \alpha); \\ n_1 &= \gamma_0 \cot\varphi(\alpha - \varphi) + \frac{p}{2}\cot\varphi(\varphi - \alpha + \sin\alpha\cos\alpha) - \frac{p}{2}\cos^2\alpha; \\ m_1 &= \gamma_0^2 + \frac{1}{k}\left[\frac{1}{2}(2\gamma_0 - p)(1 - \varphi\cot\varphi + \alpha\cot\varphi) + \frac{p}{2}\sin^2\alpha + \right. \\ &+ \left. \frac{p}{2}\sin\alpha\cos\alpha\cot\varphi\right] - \frac{\sin\alpha}{\sin\varphi}\left(\gamma_0^2 + \frac{\gamma_0}{k}\right) \end{aligned} \tag{8}$$

for $\varphi \in (\alpha, \alpha_1)$.

Similarily one obtains

$$\begin{aligned} s &= \frac{1}{2}(2\gamma_1 - p)\varphi - D_1 + (D_2 + \gamma_1)\cot\varphi; \\ n_1 &= \frac{1}{2}(2\gamma_1 - p)(1 - \varphi\cot\varphi) + D_1\cot\varphi + D_2; \\ m_1 &= \gamma_1^2 + \frac{1}{k}\left[\frac{1}{2}(2\gamma_1 - p)(1 - \varphi\cot\varphi) + D_1\cot\varphi + D_2 + \gamma_1\right] + \frac{D_3}{\sin\varphi}, \end{aligned} \tag{9}$$

for $\varphi \in (\alpha_1, \beta)$. In (9) D_1, D_2, D_3 stand for arbitrary constants of integration.

Satisfying the continuity requirements for m_1, n_1 and s at $\varphi = \alpha_1$ whereas $m_1(\alpha_1) = -\gamma_0^2$ by the use of (8), (9) one can get D_1, D_2, D_3 and p.

Numerical results are presented in Table 1,2 and Figure 2 for several values of angles α and β.

Calculations carried out show that the load carrying capacity of the cap can be considerably increased when using the design of the shell with one step in the thickness. For instance, in the case $k = 0,02$, $\alpha = 0,8$ and $\beta = 1,0$ the limit load for the stepped cap exceeds the carrying capacity of the reference shell of constant thickness more than 20% (Table 1).

In Fig. 2 upper lines correspond to the reference shell wheas lower ones correspond to the stepped shell. It can be seen from Fig. 2 that the solutions obtained above are statically admissible.

Table 1: Design of maximal load carrying capacity ($k = 0,02$)

α	β	α_1	γ_0	γ_*	e	p	p_0
0,4	0,6	0,5221	0,6471	0,80	17,54	2,308	1,964
0,4	0,8	0,7384	0,8640	0,89	3,00	1,555	1,510
0,4	1,0	0,9542	0,9445	0,95	0,65	1,488	1,479
0,6	1,0	0,9326	0,8510	0,88	3,18	1,387	1,344
0,8	1,0	0,9277	0,6614	0,79	20,20	1,959	1,630

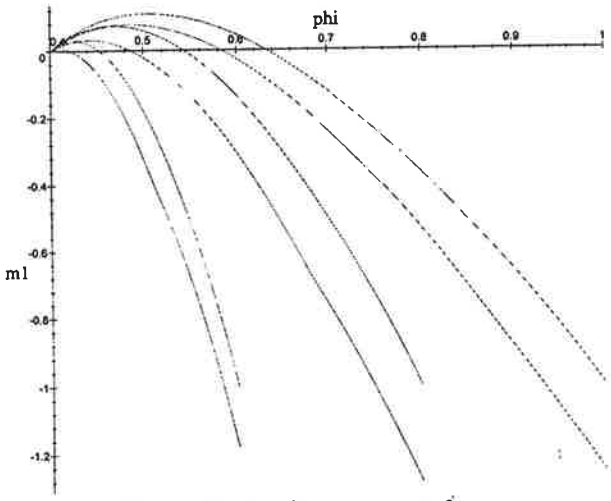

Figure 2: Bending moment for a cap

Table 2: The design of minimum weight $(k = 0,02)$

α	β	α_1	γ_1	γ_2	p	e
0,4	0,6	0,5209	0,7174	1,1208	2,785	10,55
0,4	0,8	0,7258	0,9319	1,1143	1,754	2,65
0,4	1,0	0,9458	0,9852	1,0571	1,570	0,63
0,6	1,0	0,9194	0,9245	1,1251	1,578	2,91
0,8	1,0	0,9161	0,6838	1,1221	2,330	12,41

ACKNOWLEDGEMENT

This research work was partly supported by Estonian Science Foundation through the grant No 2426.

REFERENCES

Lellep, J.; Hein, H. 1993: Optimization of rigid-plastic shallow spherical shells of piece-wise constant thickness. Struct. Optimiz. **6**, 2, 134-141.

Lellep, J.; Hein, H. 1994: Optimization of clamped rigid-plastic shallow shells of piece-wise constant thickness. Int. J. Non-Linear Mech. **29**, 4, 625-636.

Lellep, J.; Tungel, E. 1998: Optimization of plastic spherical shells of piecewise constant thickness. Proc. Estonian Acad. Sci. Phys. Math. **47**, 4, 260-269.

On sensitivities of optimal shapes

Pauli Pedersen

Department of Solid Mechanics
Technical University of Denmark, Building 404, 2800 Lyngby, Denmark

Introduction. In optimal design of structures and materials we base the optimization on an objective, on constraints and on a number of model parameters. Furthermore, our calculations are based on a numerical modelling. All these parameters have an influence on our resulting values for the response, like stresses and eigenvalues. They normally do also have an influence on the resulting optimal design and this last aspect is in focus for the present short note.

Problems of optimal design can be divided into three main categories: size, shape and topology. Like size problems, shape problems are described by continously varying parameters but the reference domain for the model is changing (for 1D−problem the length, for 2D−problem the boundary curve, and for 3D−problem the boundary surface). In the present note we discuss 2D−problems, as exemplified by the shape of a hole in a plate (disc).

We shall discuss the influence on the optimal shape of

- the chosen objective (minimum stress concentration, minimum compliance or constant energy density)
- finite size domain (interacting holes)
- boundary conditions (given displacements or given stresses)
- anisotropic material parameters
- Poisson's ratio for isotropic materials
- non−linear elastic material
- numerical modelling

A classical problem and its analytic solution. The 2D−hole problem is illustrated in fig. 1 and shown with a biaxial load case. Numerical results for this case are also contained in Kristensen and Madsen (1976) and these are compared to what is mentioned as the "analytical" results. Analytical studies of the problem are reported by Banichuk (1977) with reference to even earlier results by Cherepanov (1974). These analytical studies prove that a constant tangential stress $\sigma_t = \sigma_1 + \sigma_2$ is obtained with an elliptical shape design where the ratio of the two half axis a, b equals the ratio of the stresses, i.e. $a/b = \sigma_1/\sigma_2$, assuming equal signs for σ_1 and σ_2.

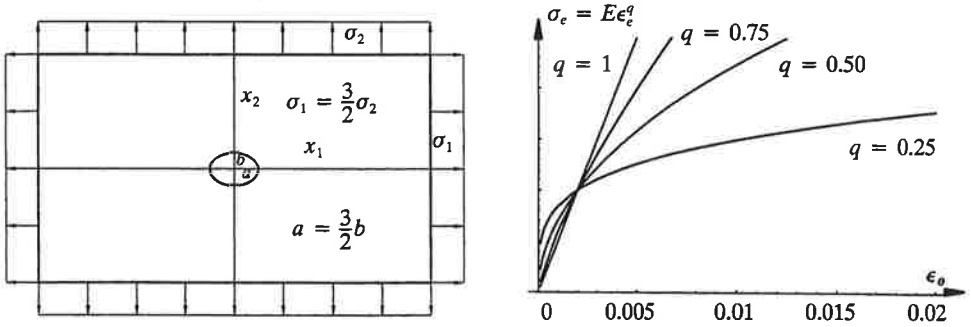

Fig. 1. Hole problem and applied materials for the discussions to follow.

A simple parametrization and an optimization method. This elliptical shape design will only be the solution for a hole in an infinite space (very small hole). Thus we need additional design parametrization and we choose the most simple one shown in fig. 2, with the three non−dimensional design parameters α, β and η. The specific optimization problem is then formulated by

$$\underset{(\alpha,\beta,\eta)}{\textit{Minimize}} \quad U = \sum U_e = \sum \overline{u}_e V_e \quad \textit{subject to} \quad V = \sum V_e = \overline{V} \tag{1}$$

where U is the strain energy, U_e the strain energy in element (domain) e, $\overline{u}_e$ the mean strain energy density, V_e the volume of element e, V the total volume (hatched in fig. 2) and $\overline{V}$ is a given volume.

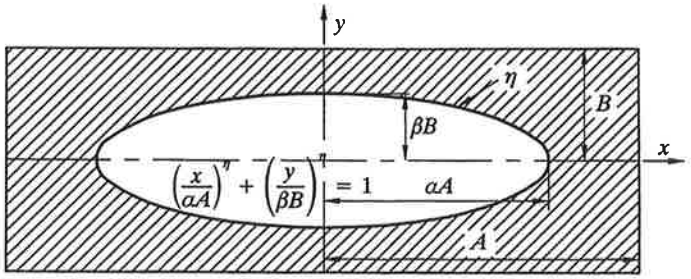

Fig. 2: The simplified shape parametrization used in Pedersen (1999) for material design.

As shown in Pedersen (1999) the resulting necessary optimality criterion for a solution to (1) is

$$\alpha \sum_s \overline{u}_s \frac{\partial V_s}{\partial \alpha} = \beta \sum_s \overline{u}_s \frac{\partial V_s}{\partial \beta} = \frac{\eta^2}{p(\eta)} \sum \overline{u}_s \frac{\partial V_s}{\partial \eta} = \lambda \tag{2}$$

restricted to summation over elements s at the shape boundary and with $p(\eta)$ defined by

$$p(\eta) = 2\Psi(2/\eta) - \Psi(1/\eta) - \Psi((\eta + 1)/\eta) \tag{3}$$

where Ψ is the Psi−function. The Lagrangian multiplier λ is chosen to satisfy $V = \overline{V}$. Optimal designs are located by an iterative method where the shape parameters α, β, η are redefined with the goal of satisfying the optimality criterion (2). The volume V depends monotonically on the parameters α, β and η and rapid convergence is experienced. The procedure is a traditional optimality criterion method and details will therefore not be given.

Influence of domain size. Only problems with symmetry relative to the x−axis as well as to the y−axis in fig. 2 will be dealt with and thus only results for the first quadrant of fig. 2 will be shown. With reference to fig. 2 we define the relative density ρ as the ratio of the area of the solid part (hatched) and the total area $(4AB)$. The asymptotic case of $\rho \to 1$ is a small hole for which classical analytical design results are available. The other asymptotic case of $\rho \to 0$ gives a frame structure and we shall concentrate on the intermediate cases of say $0.2 \le \rho \le 0.8$.

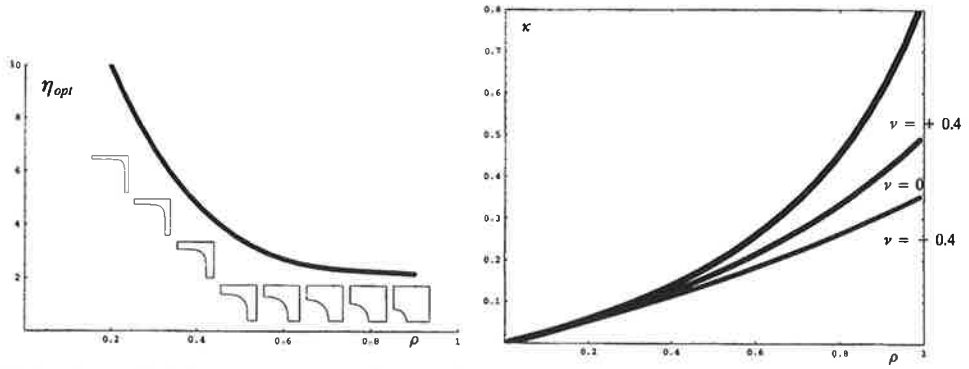

Fig. 3: Left the optimal shape parameter η as a function of relative volume density ρ and right the resulting "2D−bulk" modulus κ for three different values of Poisson's ratio ν.

The most simple case of design for maximum bulk modulus (here proportional to U) for a 2D−material is with the parametrization in fig. 2 described by a single parameter η, with $A = B$ and $\alpha = \beta$ uniquely determined by ρ and η. The resulting optimal designs are shown in fig. 3 left with the curves in fig. 3 right giving the resulting Hashin−Shtrikman bounds. For this case the obtained optimal designs are independent of Poisson's ratio, but the resulting bulk moduli are highly dependent. Note in fig. 3 right that for negative Poisson's ratio an almost linear dependence of κ as function of ρ, while for positive Poisson's ratio a higher order dependence is observed.

Influence of boundary conditions. The boundary conditions behind the solutions in fig. 3 was uniform forced displacements at $x = A$, $y = B$ corresponding to pure mean dilatation $\overline{\varepsilon}_y = \overline{\varepsilon}_x$. For $\rho \to 1$ (small holes)

this will also be the solution with forced uniform boundary stresses at $x = A$, $y = B$ corresponding to mean hydrostatic pressure $\bar{\sigma}_x = \bar{\sigma}_y$. For finite size domains the two solutions will be different as shown with the results in fig. 4.

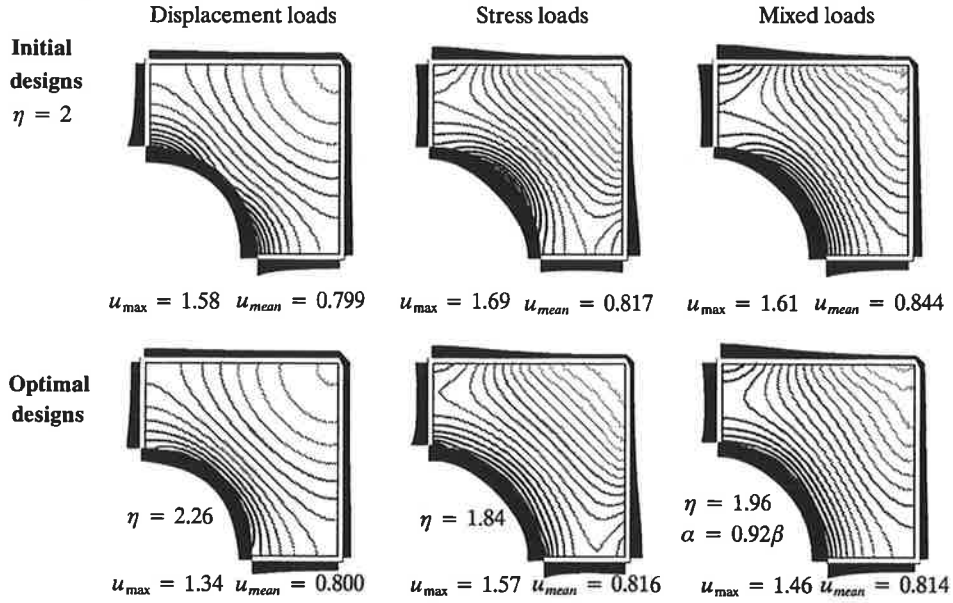

Fig. 4: Starting designs in upper row with $\eta = 2$ and optimal solutions in lower row with column left: forced displacements with $\eta = 2.26$, column middle: forced stresses with $\eta = 1.84$, column right: mixed loads with $\eta = 1.96$ and $\alpha = 0.92\beta$. Energy densities along the boundaries in black and isolines for the larger principal stresses.

Influence of Poisson's ratio. The results in fig. 4 was based on isotropic, zero Poisson's ratio linear elasticity. This was done to put the focus on the different boundary conditions. In earlier optimizations it was found that the optimal shape depended strongly on the anisotropy, see Pedersen, Tobiesen and Jensen (1992), but weak

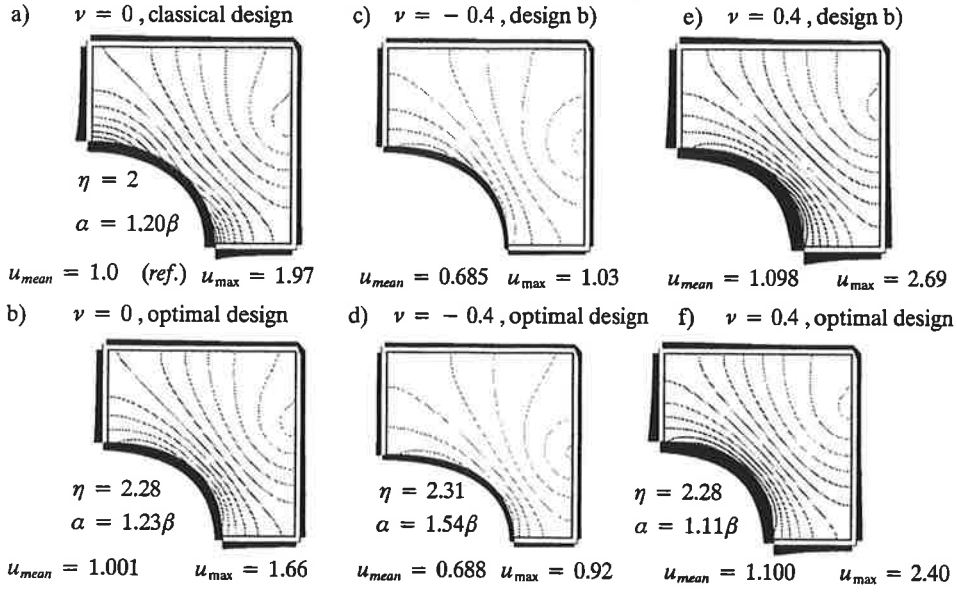

Isotropic material with $C_{1111} = 1$, square domain A = B, solid part $\rho = 0.75$, mean strains $\bar{\epsilon}_x = 1.2\bar{\epsilon}_y$

Fig. 5: Influence of Poisson's ratio for an isotropic material, non-symmetric displaced $\bar{\epsilon}_x = 1.2\bar{\epsilon}_y$. Strain energy densities at boundaries in black and isolines for the larger principal stresses.

dependence on Poisson's ratio and on the non−linearity was found. Also the design results in fig. 3 left are independent of ν. We will show the influence of Poisson's ratio and focus on the influence on the optimal shape design, rather than on the resulting stresses, strains and energies. It will be seen that for non−symmetric problems ($\bar{\epsilon}_x \neq \bar{\epsilon}_y$, $\bar{\sigma}_x \neq \bar{\sigma}_y$) the influence cannot be neglected. In this short note we will only in fig. 5, show the rather strong influence for an actual problem with only weak non−symmetry described by $\bar{\epsilon}_x = 1.2\bar{\epsilon}_y$.

Influence of non−linear elasticity. For power law non−linear elasticity ($1D: \sigma = E\epsilon^q$) we have in Pedersen and Taylor (1993) shown that in thickness design the optimal design does not depend on the non−linearity q. This is not the case for shape design. Let us assume a constant stress, strain, energy density element and that the strain state in element e is of magnitude ϵ_e that relates to the actual strain energy density u_e by

$$u_e = \frac{1}{q+1} E \epsilon_e^{q+1} \tag{4}$$

Then the element stiffness matrix $[S_e]$ and its derivative with respect to q can be written

$$[S_e] = \epsilon_e^{q-1}\left[\tilde{S}_e\right] \quad , \quad \frac{d[S_e]}{dq} = \ln(\epsilon_e)\epsilon_e^{q-1}\left[\tilde{S}_e\right] = \ln(\epsilon_e)[S_e] \tag{5}$$

where $\left[\tilde{S}_e\right]$ is not dependent on q. Thus for elements of equal energy density (equal effective strains ϵ_e) we get proportional change of the stiffness matrices and the optimal design is not changed. However, for shape design the effective strain ϵ_e is only constant along the boundary and thus a redistribution of displacements, strains and stresses will take place. As we see in the example in fig. 6, the optimal shape only changes slightly, probably due to the fact that the change in ϵ_e is only in the direction orthogonal to the shape.

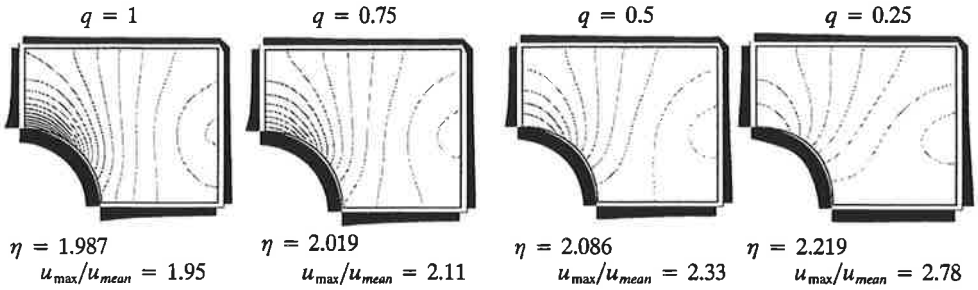

Fig. 6: Change in optimal design for increasing non−linearity $q = 0.75$, 0.50, 0.25. Energy densities at boundaries in black and isolines for the larger principal stresses. Power law $\sigma = E\epsilon^q$, orthotropic $C_{1111} = 1$, $C_{2222} = 0.1$, $C_{1122} = 0.3$, $C_{1212} = 0.3$, rectangular $A = 1.25B$, non−uniform mean strain $\nu_y = 2\nu_x$ at boundary, solid part $\rho = 0.85$.

References

Banichuk, N.V. (1977) Optimality Conditions in the Problem of Seeking the Hole Shapes in Elastic Bodies, PMM **41**(5), 946−951.

Cherepanov, G.P. (1974) Inverse Problems of a Plane Theory of Elasticity, PMM, **38** (6).

Kristensen, E.S. and Madsen, N.F. (1976) On the Optimum Shape of Fillets in Plates Subjected to Multiple In−Plane Loading Cases, Int. J. Numer. Meth. Engng. **10**, 1007−1019.

Pedersen, P. (1999) On Optimal Shapes in Materials and Structures. Structural Optimization, to appear.

Pedersen, P. and Taylor, J.E. (1993) Optimal Design Based on Power−Law Non−Linear Elasticity. In Optimal Design with Advanced Materials (ed. P. Pedersen), 51−66, Elsevier.

Pedersen, P., Tobiesen, L. and Jensen, S.H. (1992) Shapes of Orthotropic Plates for Minimum Energy Concentration. Mech. Struct. & Mach. **20**(4), 499−514.

Constitutive Models for Stress Analysis of Solder Joints

Reijo Kouhia[1], Pekka Marjamäki[2] and Jorma Kivilahti[2]
[1] *Laboratory of Structural Mechanics*
Helsinki University of Technology, P.O. Box 2100, 02015 HUT, Finland
[2] *Laboratory of Electronics Production Technology*
Helsinki University of Technology, P.O. Box 3000, 02015 HUT, Finland *

Introduction

Increased packaging density of electronic components on printed wiring boards (PWBs) has raised mechanical reliability concerns. The thermomechanical problems are mainly induced by the mismatch of the thermal expansion coefficients between the individual components and the boards. Most of the current methodologies for predicting the solder joint reliability are empirical. Since the empirical methods suffer from serious drawbacks computational modelling is increasingly used to assess the response and reliability of electronic devices.

Computational modelling of solder materials is, however, exceedingly difficult. In general, solder is a viscoplastic material in which the material parameters depend upon the microstructure. Processing influences the initial microstructure which then changes during the thermomechanical loading process induced by the electrical functioning of the product.

Constitutive Models

Quite a few viscoplastic material models have been developed for solder alloys. A rather popular constitutive model in solder joint reliability computations has been developed by Anand and Brown [1], [2]. This model can account for strain rate and temperature sensitivity and the dynamic recovery processes. It uses single internal parameter which represents the averaged isotropic resistance to macroscopic plastic flow offered by the underlying isotropic strengthtening mechanisms such as solid solution strenghtening and grain size effects.

To make the grain-coarsening more explicit an internal state model taking into account hardening, recovery and grain coarsening has been developed in refs. [3], [4]. In this model the inelastic strain rate, $\boldsymbol{d}^{\text{in}}$, is given by

$$\boldsymbol{d}^{\text{in}} = \tfrac{3}{2}\gamma \boldsymbol{n} = \tfrac{3}{2} f \exp\left(\frac{-Q}{R\theta}\right)\left(\frac{\lambda_0}{\lambda}\right)^p \sinh^m\left(\frac{\bar{\sigma}}{\sigma_y}\right)\boldsymbol{n} \tag{1}$$

where γ is the magnitude of the inelastic deformation rate, f, p, m and Q are material parameters, R is the gas constant, θ the absolute temperature, λ, λ_0 are the current and initial grain sizes (average diameters). The scalar $\bar{\sigma}$ is the equivalent stress

$$\bar{\sigma} = \sqrt{\tfrac{3}{2}\left(\boldsymbol{s} - \tfrac{2}{3}\boldsymbol{B}\right) : \left(\boldsymbol{s} - \tfrac{2}{3}\boldsymbol{B}\right)},$$

*E-mail addresses: Reijo.Kouhia@hut.fi, Pekka.Marjamaki@hut.fi, Jorma.Kivilahti@hut.fi

where $\boldsymbol{s}$ is the stress deviator and $\boldsymbol{B}$ is the back stress accounting for the kinematic hardening and the normal $\boldsymbol{n}$ is defined as: $\boldsymbol{n} = (\boldsymbol{s} - \frac{2}{3}\boldsymbol{B})/\bar{\sigma}$.

In refs. [3], [4] the Hall-Petch type dependency of the flow stress on the grain size is used

$$\sigma_y = Y + k(\lambda_0/\lambda)^\beta, \tag{2}$$

where the material parameters Y, k and β depend on temperature. The grain size growth rate $\dot{\lambda}$ depends on the current grain size and, according to Clark and Alden [5], is proportional to the excess vacancy concentration c_v^x. The evolution equations for the grain size and excess vacancy concentration are:

$$\dot{\lambda} = A\frac{c_v^x + c_v^0}{\lambda} \qquad \dot{c}_v^x = B\gamma - Cc_v^x,$$

where A, B and C are material parameters, and c_v^0 is the equilibrium vacancy concentrations.

Rather complex hardening rules, adapted from the constitutive model of Miller [6], are used in refs. [3], [4]:

$$\dot{Y} = H_1\gamma - (H_2\gamma + H_3)(Y - Y_0)^2, \qquad \dot{\boldsymbol{B}} = K_1\boldsymbol{d}^{\text{in}} - (K_2\gamma + K_3)\left(\sqrt{\tfrac{2}{3}\boldsymbol{B} : \boldsymbol{B}}\right)\boldsymbol{B},$$

where $H_1, ..., H_3, K_1, ..., K_3$ and Y_0 are material parameters.

Example

To show the grain coarsening effect in a cyclic loading test a simple computation has been carried out. The loading is imposed by prescribing the horizontal displacements at the upper boundary and it is varied by sinusoidal time amplitude relation $u(x,h) = (h/100)\sin(\pi t/t_0)$. The computed time interval has been $20t_0$ with $t_0 = 100$ s. An uniform quadrilateral mesh with 200 bilinear elements is used, see fig. 1, where the material parameters are also tabulated. The material data is taken from ref. [4], which represents mechanical properties of the binary near eutectic Sn40Pb solder. However, the grain diameter dependency from the flow stress has been neglected as well as the kinematic and isotropic hardening effects. Isothermal conditions are assumed.

Fig. 2 shows the grain size distribution after the cyclic loading. Increase in the grain size is distributed like the distribution of the accumulated equivalent inelastic strain.

Discussion

The model (1) can predict the grain coarsening effect. However, there is evidence that the solder alloys can behave in a very ductile manner, even exhibiting superplastic behaviour. Shear-band formation have been observed in experiments, see fig. 3. For superplastic behaviour to occur recrystallisation has necessarily to happen. However, the model (1) cannot simulate recrystallisation. In addition, the use of the Hall-Petch equation (2) is questionable; it is mainly developed for steels and it predicts larger flow stresses when the grain size is decreased, which is in contradiction to behaviour observed in superplastic materials.

The ongoing research will focus on the development of a microstructurally based constitutive model which should be able to predict the grain growth as well as the recrystallisation processes. In addition, damage evolutiong of solder materials should also be accounted for in order to obtain realistic life-time predictions of electronic products.

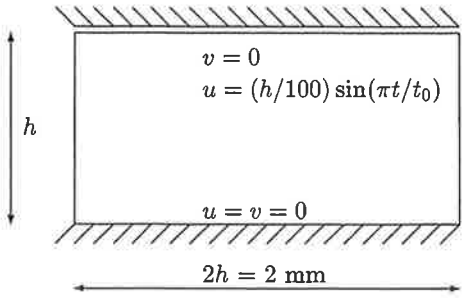

E	=	33 GPa		Q	=	12 kcal/mol
ν	=	0.3		R	=	$2{\cdot}10^{-3}$ kcal/mol·K
σ_0	=	20 MPa		f	=	10^5 s^{-1}
m	=	3.5		c_v^0	=	10^{-9}
p	=	2		A	=	$3.74{\cdot}10^4$ (μm)^{2}s^{-1}
λ_0	=	30 μm		B	=	$4.1{\cdot}10^{-3}$ s^{-1}
k	=	0		C	=	$1.67{\cdot}10^{-2}$ s^{-1}

Figure 1: Test example and material parameters.

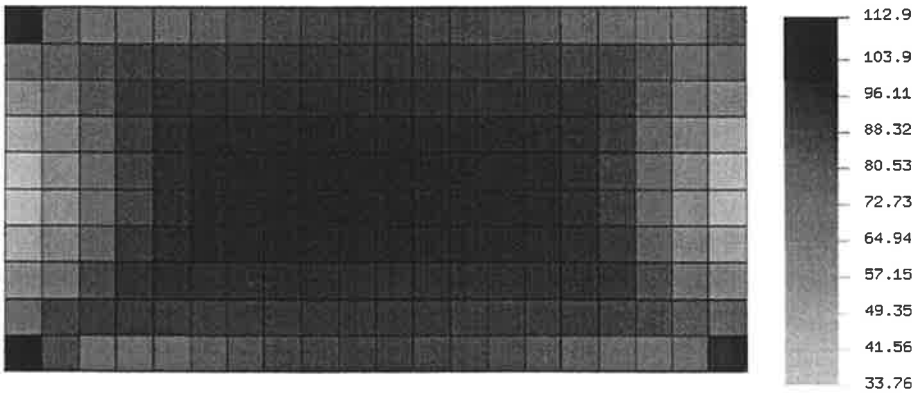

Figure 2: Computed grain size distribution after ten full cycles (in μm).

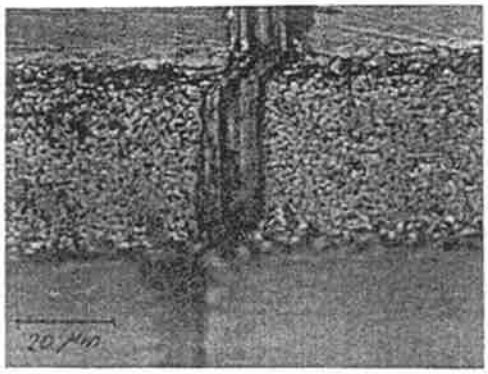

Figure 3: Deformation of 62Sn36Pb2Ag solder joint in shear test, from ref. [7] figure 5 page 215.

References

[1] L. Anand and S. Brown. Constitutive equations for large deformations of metals at high temperatures. In J. Chandra and R.P. Srivastav, editors, *Constitutive Models of Deformation*, pages 1–26, 1987.

[2] S.B. Brown, K.H. Kim, and L. Anand. An internal variable constitutive model for hot working of metals. *International Journal of Plasticity*, 5:91–130, 1989.

[3] D.R. Frear, S.N. Burchett, M.K. Neilsen, and J.J. Stephens. Microstructurally based finite element simulation of solder joint behaviour. *Soldering & Surface Mount Technology*, 1(25):39–42, 1997.

[4] S.N. Burchett, M.K. Neilsen, D.R. Frear, and J.J. Stephens. Computational continuum modelling of solder interconnects. In R.K. Mahidhara et al., editor, *Design and Reliability of Solders and Solder Interconnects*, pages 171–178, The Minerals, Metals & Materials Society, 1997.

[5] M.A. Clark and T.H. Alden. Deformation enhanged grain growth in a superplastic Sn-1% Bi alloy. *Acta Metallurgica*, 21:1195–1206, 1973.

[6] A. Miller. An inelastic constitutive model for monotonic, cyclic and creep deformations: Part I – equations development and analytical procedures. *Journal of Engineering Materials Technology*, 98:97–105, 1976.

[7] G. Grossmann and L. Weber. Metallurgical considerations for accelerated testing of soft solder joints. *IEEE Transactions on Components, Packaging, and Manufacturing Technology - Part C*, 20(3):213–218, 1997.

Coupled Model for Partially Saturated Swelling Clay

Antti J. Lempinen
Laboratory of Theoretical and Applied Mechanics

Helsinki University of Technology, Finland

e-mail: Antti.Lempinen@hut.fi

ABSTRACT

Summary In this paper, a thermodynamically consistent model for mechanical behaviour of expansive clays is presented. An implementation for numerical simulations of stress field in a high level nuclear waste repository is shown.

In Finland, as in several other countries, it is planned to be dispose of the high level nuclear waste in bedrock at a depth of several hundred meters. The composite copper and steel canisters containing the spent fuel will be placed in the in boreholes drilled in the floors of deposition tunnels. An engineered clay buffer is constructed between bedrock and the canister. The clay which forms the buffer is bentonite, which is expansive and considered practically impermeable when saturated with water. The purpose of the buffer is to isolate the canister from ground water.

Because of the swelling pressure of bentonite and of the huge mass of the canisters, mechanical stability of bentonite buffer systems is not trivial. It has to be ensured that the canisters remain surrounded by bentonite for very long times. The analyses of mechanical stability can be divided in two parts: elastic behaviour of the saturating phase and long-time viscous behaviour of fully saturated system.

In this paper, a thermodynamically consistent numerical model for simulating mechanical behaviour of unsaturated expansive clays is presented. It is based on solving the momentum balance equation with the finite element method. The constitutive equations are derived from Clausius-Duhem inequality for porous medium, which is constructed from conservation laws and laws of thermodynamics. This inequality is an multi-phase extension of the one for saturated porous media [1].

The model is essentially macroscopic. The microscopic phenomena are taken into account in the choice of state variables. The swelling is introduced by swelling pressure, and a modified concept of effective stress is adopted. Suction pressure and degree of saturation are considered inapplicable quantities for media with strong adsorption.

The material behaviour is non-linear [3], so the constitutive equations are given in incremental forms. Transport of water is introduced as moisture diffusion.

Since the model is intended to be used in systems with rigid boundaries, framework of small displacements is used.

An implementation of this model to computer simulations of saturation of a bentonite buffer system is presented. The numerical method uses segregation to deal with scale differences. Non-linearity of the model is solved by calculating the parameter values from previous time step. The non-linearity also requires subsequent solving of displacement field and deviatoric stress field at every time step. The canister is assumed to be rigid, so it is modelled with rigid connections of boundary nodes.

The stress fields after full saturation can be used as starting points for long-time analysis of the depository assessment performance.

REFERENCES

[1] Olivier Coussy. Mechanics of Porous Continua. John Wiley & Sons Ltd, Chichester, (1995)

[2] L. Jing, J. Rutqvist, O. Stephansson, C.-F- Tsang, F. Kautsky (ed.). DECOVALEX - Mathematical models of coupled T-H-M processes for nuclear waste repositories. Report of Phase III. Technical Report 95:80. Swedish Nuclear Power Inspectorate, (1995).

[3] Lennart Börgesson, Lars-Erik Johannesson, Torbjörn Sandén Jan Hernelind. Modelling of the physical behaviour of water saturated clay barriers. Technical report 95-19. Swedish Nuclear Fuel and Waste Management Co., (1995)

Searching material models for deep-drawing metal forming analysis using uniaxial tensile tests and numerical simulation

Mika Reivinen, Jouni Freund
Helsinki University of Technology
Laboratory of Theoretical and Applied Mechanics
P.O.Box 1100, FIN-02015 HUT
e-mail: Mika.Reivinen@hut.fi
web page: http://www.hut.fi/HUT/Dynamics/

Summary. In this study proper material models for deep-drawing metal forming processes of relatively thin metal sheet are searched using numerical simulation. Isotropic and orthotropic material models with various hardening rules are studied. The Eulerian finite element method based on the space-time approach is discussed. As a numerical example, necking of a ideal plastic strip in a tension is analyzed and the results are compared to available experimental data.

1 INTRODUCTION

Deep drawing is a metal forming process used to manufacture for example auto-body components, cans, cups, sinks, and other similar products by stamping rolled metal sheets into their final geometric form. If the process parameters are not properly arranged, there is the potential for various defects in the process. Possible defects are for example bottom tearing, flange wrinkling and earing of the flange, which may occur for example due to anisotropy. The sheets are anisotropic as a consequence of the rolling process.

Examples mentioned show that there is need for an accurate process simulation when designing a new deep-drawing product. Using computational simulation, more accurate knowledge of material flow, improved dimensional accuracy and optimization of metal forming processes can be attained. For the lack of experimental results, non-linear material models for multiaxial states of stress are often based on generalisations of uniaxial test results.

2 INCREMENTAL ELASTO-PLASTICITY

Due to the form of the stress-strain relation and large displacements, the use of an incremental approach is necessary at some stage of the solution procedure. In the present study, the problem is parameterised with the aid of pseudo-time $t \in [0,1]$ scaling, for example, the external forces or forced displacements, and the equations are written in an Eulerian coordinate system. The basic unknowns are the coordinates $x_i \in \Omega$ of the material points and plasticity parameter L, which are functions of coordinates $\bar{x}_i$ of the reference domain $\bar{\Omega}$ and loading parameter t. Given the triple $(\bar{\Omega}, \bar{\sigma}_{ik}, \bar{L})$ corresponding to $t = \bar{t}$, the goal is to find the new triple (Ω, σ_{ik}, L) corresponding to $t = \bar{t} + \Delta t$. Then the solution is searched in a step-by-step manner by increasing t gradually.

If the external body forces such as gravity are assumed negligible, the governing equations of the typical step are

$$\sigma_{ij,j} = 0 \text{ in } \bar{\Omega}. \tag{1}$$

In principle, equations (1) should be satisfied in Ω but one may use $\bar{\Omega}$ if the displacement is small. The boundary conditions are taken to be of the Dirichlet or Neuman type i.e. either displacement or traction is given.

Assuming that the increment Δt is small enough, the relative displacement is given by $\Delta u_i(\bar{x}_k) = x_i(\bar{x}_k) - \bar{x}_i$, and the small strain and rotation tensors are $\Delta\varepsilon_{ik} = (\Delta u_{i,k} + \Delta u_{k,i})/2$, $\Delta\omega_{ik} = (\Delta u_{i,k} - \Delta u_{k,i})/2 + \delta_{ik}$, respectively. The incremental form of the stress-strain relation of an isotropic material is here

$$\sigma_{ij} = \Delta\omega_{ik}\Delta\omega_{jl}\bar{\sigma}_{kl} + \lambda\delta_{ij}\Delta\varepsilon_{kk} + 2\mu(\Delta\varepsilon_{ij} - \Delta L\, b_{ij}), \tag{2}$$

where μ, λ are the material parameters, b_{ik} gives the correction 'direction' to the yield surface and ΔL is the increment of plasticity parameter. In the first term, the stress of the reference domain has been transformed to the new domain.

The yield criterion, defining the value of the plasticity parameter, is written in the form

$$\begin{cases} \Delta L = 0 & G < 0, \\ G = 0 & \text{otherwise}, \end{cases} \tag{3}$$

where $G = 0$ is the equation of the yield surface in the stress space. In the first case stress belongs to the elastic region and expression (2) reduces to the usual one for linearly elastic isotropic material.

3 MATERIAL MODELS FOR PLANE STRESS ELASTO-PLASTICITY

Steel or other metals conform nicely to the theory that initial yielding will occur when the distortional strain energy density at some point reaches a certain critical value. Generally, the combination of the isotropic and kinematic hardening laws can be represented as follows[1]

$$G = F[\sigma_{ij} - \alpha_{ij}(\varepsilon_{kl}^{pl})] - \kappa(\varepsilon_{ij}^{pl}) = 0 \tag{4}$$

where F is a homogeneous function and κ represents a hardening or softening parameter and is a function of the plastic strain ε_{ij}^{pl}. For most forming processes the term α_{ij} (back stress) can be dropped out. For isotopic and pressure-independent material, and if the Bauschinger effect need not to be taken into account (which is the case for most forming analysis), equation simplifies to the von Mises criterion

$$G = J_2 - \kappa(\varepsilon_{ij}^{pl}) = 0\,. \tag{5}$$

That means that the plastic flow occurs when the second invariant of the deviatoric stress tensor J_2 (or the effective stress) reaches some critical value, which corresponds to the uniaxial yield limit. In strain hardening the effective stress (or equivalent stress) is a scalar measure of the stress state. For the von Mises yield criterion, a multiaxial and uniaxial state of stress are considered equivalent when $J_2(multiaxial) = J_2(uniaxial)$ which gives for the effective stress[1] $\sigma_{eff} = \sqrt{3J_2}$.

Nonlinear models for uniaxial loading

Hollomon's equation states, that for many engineering alloys in the plastic regime $\sigma = k\varepsilon^n$ where constant k is the strength coefficient and n is work-hardening rate or work-hardening exponent. For the rate-dependent case, the material law can be written for example in multiplicative form $\sigma = k\varepsilon^n \dot{\varepsilon}^m$ where m is the strain-rate sensitivity index, see for example Ghosh[2]. As a simple rule, in the tensile test the work-hardening rate n affects the stress-strain curve primarily up to the uniform strain, and the strain-rate-sensitivity index m affects behavior primarily in the post-uniform or necking region[3]. Other uniaxial material models are for example ideal plastic material, linear material, Hollomon's material law, Swift's law, Ludwik's material law, and Voce's material law which has a saturation hardening term of the exponential type[4]. Maximum load can be determined for example using the Considere criterion which yields $n = \varepsilon$ at uniform elongation[3].

Some yield functions for anisotropic material

For the von Mises' material the yield surface is stationary and it can be considered as multiaxial generalization of the uniaxial ideal plastic material law and it is discussed earlier. Generally, the yield surface will evolve with straining. Anisotropy arises for example in the rolling process due the changes in microstructure.

Hill's quadratic yield function[5] is, for its conciseness, the most widely used anisotropic yield surface and it can be expressed as follows

$$G(\sigma) = A(\sigma_2 - \sigma_3)^2 + B(\sigma_1 - \sigma_3)^2 + C(\sigma_1 - \sigma_2)^2 - 1, \quad (6)$$

where A, B, and C are constants, σ_i are the three principal stresses. The subscript 1 corresponds to the rolling direction, 2 corresponds to the rectangular direction in the sheet plane, and 3 is the thickness direction. This yield function is pressure-independent and it does not allow for a Bauschinger effect. In the determination of the coefficients A, B, and C, the plastic anisotropy parameter R, which characterizes the true width strain and true thickness strain ratio, is used. However, many disadvantages of this conventional theory have been pointed out[6,7]. Other quadratic yield conditions are presented for example by Parmar and Mellor[8,9], Logan and Hosford[10], Bassani[11], and Gupta[12]. A fourth order yield function in plane stress state is presented by Gotoh[6,7].

4 NUMERICAL METHOD

The numerical method based on the Eulerian scheme is discussed in more detailed way by Freund and Reivinen[14,15]. The weak form of the problem, giving the domain, stress field and the plasticity parameter in a typical loading step, can be written as: find $(x_i, s_{ik}, L) \in U \times V \times W$ such as

$$(\delta\Delta u_{i,j}, \sigma_{ij})_{\bar{\Omega}} + (\delta s_{ij}, s_{ij} - \sigma_{ij})_{\bar{\Omega}} + (\delta L, (1-\alpha)G - \alpha\kappa\Delta L)_{\bar{\Omega}} = 0 \quad (7)$$

for all $(\delta x_i, \delta s_{ik}, \delta L) \in U \times V \times W$. Function α has the value one in the elastic part of the domain and is otherwise zero, and the stress expression is given in equation (2). In practice, the increment of the loading parameter Δt is sought by trial-and-error and only steps with small enough relative changes in all the unknowns are accepted.

The Dirichlet type of boundary conditions are satisfied in the weak sense to simplify treatment of moving boundaries. Then the first term of (7) is replaced by

$$(\delta\Delta u_{i,j}, \sigma_{ij})_{\bar{\Omega}} - \langle\delta\Delta u_i, t_i\rangle_{\bar{\Gamma}} + \langle\delta t_i, u_i - g_i\rangle_{\bar{\Gamma}} + \langle\tau\delta\Delta u_i, u_i - g_i\rangle_{\bar{\Gamma}}, \quad (8)$$

where the traction vector is defined as $t_i = \sigma_{ik} n_k$ (n_k is the unit outward normal vector to the boundary), and the stability parameter is given by $\tau = C\mu / h$.

5 NUMERICAL EXAMPLE

For the material to be drawn, there is available a lot of experimental data obtained in an uniaxial tension tests with isothermal conditions at different temperatures and at different loading rates[13]. A typical test arrangement is depicted for example by Wagoner[3] et. al. or by Partinen[13]. This data can be used in determining the parameters of the chosen model. Then, simulation yields results on a more complex geometry or loading conditions.

Figure 1 shows a tensile test simulation of metal specimen by using two-dimensional elasto-plastic model based on plane-stress assumption. The yield function was $G = F - \kappa$, where κ is constant and F is the von Mises stress measure. The problem was parameterized by multiplying the g_i of expression (8) by t.

6 CONCLUSIONS

For simplicity, the present models were constructed assuming isothermal conditions. However, temperature changes can significantly affect material behaviour. Experiments suggest that, for metals at least, the yield surfaces usually shrink in size for elevated temperatures and most material parameters will significantly be affected by the temperature increase. In computational terms, this means that the yield condition now needs to be extended to include dependence on temperature T, and the yield condition can be written as $G(\sigma_{ik}, \varepsilon_{ik}^{p_i}, \kappa, T) = 0$.

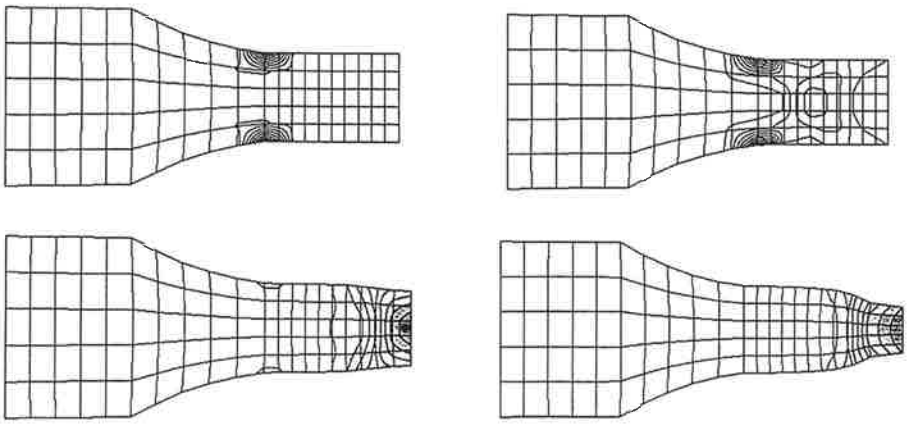

Figure 1. Simulated geometry of a test specimen subjected to forced displacement of the right end (only the left half is shown) and level sets of the plasticity parameter (white ~ minimum value, black ~largest value). Yielding starts from points where the boundary line is not smooth and moves then to the symmetry axis. The values of the material parameters of the example case were $E = 1\text{Pa}$, $\nu = 0.2$, $\kappa = E/10$, and the lenght of the specimen was 1.5m

REFERENCES

[1] E. Hinton (ed.), *NAFEMS Introduction to Nonlinear Finite Element Analysis*, (1992).
[2] A. K. Ghosh, *Acta Metallurgica*, Vol. 25, pp. 1413-1424, Pergamon Press, (1977).
[3] R.H. Wagoner, J-L. Chenot, *Fundamentals of metal forming*, Wiley, (1997).
[4] J.C. Simo, T.J.R Hughes, *Computational inelasticity*, Springer-Verlag, Berlin, (1998).
[5] R. Hill, *The Mathematical Theory of Plasticity*, Clarendon Press, (1950).
[6] M. Gotoh, *Int. J. Mech. Sci.*, Vol. 19, pp. 505-512, (1977).
[7] M. Gotoh, *Int. J. Mech. Sci.*, Vol. 19, pp. 513-520, (1977).
[8] A. Parmar, P.B. Mellor, *Int. J. Mech. Sci*, Vol. 20, pp. 385-391, (1978).
[9] A. Parmar and P.B. Mellor, *Int. J. Mech. Sci*, Vol. 20, pp. 707-720, (1978).
[10] R. W. Logan and W. F. Hosford, *Int. J. Mech. Sci.*, Vol. 22, pp. 419-430, (1980).
[11] J.L. Bassani, *Int. J. mech. Sci.*, Vol. 19, pp. 651-660, (1977).
[12] Y.M. Gupta, *Acta Metallurgica*, Vol. 25, pp. 1509-1513, Pergamon Press, (1977).
[13] S. Partinen, *KES'97-PROJEKTI* (in Finnish), (1996).
[14] J. Freund, *Acta Polytechnica Scandinavica, Ma 79*, (1996).
[15] M. Reivinen, J. Freund: *On the Finite Element Analysis of Large Deformation Metal Forming Processes*, Espoo 1999, (in print).

ON COMPUTATIONAL PREDICTION OF OPTIMAL ELASTIC-MODULUS TENSOR FIELDS

J.E. TAYLOR - janos@umich.edu
Aerospace Engineering
University of Michigan
Ann Arbor, Michigan 48109 - USA
Velux Guest-Professor, Mechanical Engineering
Aalborg University, Dk 9220 Aalborg East

Introduction A number of problem situations are treated as examples of the application of recently developed methods for the prediction of optimal structural design, including especially those formulated for the prediction of optimal material properties fields. The design of material properties alone is exemplified first with the treatment of several cases in 2D where a homogeneous strain field is imposed. Results in some of these cases, e.g simple dilatation, are counterintuitive, while in pure shear the uniquely shear - stiff material is optimal. A different aspect of material design, one showing change in the optimal material with evolving strain state, is demonstrated from a set of solutions where elements of the imposed strain are prescribed in varying proportion. Finally, example results of 'single purpose designs' and of 'evolving material fields' are presented for the more general case of inhomogeneous loading or imposed strain. The portrayal of optimal material properties being local in nature, results for inhomogeneous problems are sensitive to relative coarseness of the discretization mesh and this feature is discussed, as is the interpretation of material properties fields into the form of discrete topologies that may correspond to practical composites design. The mechanics of what is described in this paper corresponds in form to the usual modelling for linear elasticity of structures composed of general anisotropic materials.

Out of the broad collection of reported developments where reference is made to material property design in the context of structural optimization, most start with designation of a particular form for local material properties (e.g. isotropic) as an assumption [e.g. Cherkaev & Gibiansky (1992), Gibiansky & Cherkaev (1984), Milton (1990)]. In this sort of approach, material properties are interpreted eventually as 'effective properties' in the sense identified with an homogenization modelling interpretion of the

for presentation at the: 12th Nordic Seminar on Computational Mechanics,
Helsinki University of Technology
October 22-23, 1999

design problem [the subject is surveyed effectively in Bendsφe (1995); the forthcoming book by Cherkaev (1999) provides a virtual compendium of related elements in applied mathematics]. While results that derive from this conventional approach in structural optimization have supported a wide range of practical applications in engineering design [see Olhoff et al (1993) as an example], because of the intial restriction to 'assumed local material properties' and the related requirement for 'relaxation in the model'to achieve a mathematically viable form [see e.g. Lipton (1993)], these results are inherently limited. Following an alternative approach to the continuum structures design problem, one where the unrestricted modulus tensor itself has the role of 'design variable' [Bendsφe, et al (1994, 1995), Bendsφe (1995)], optimal local material property fields may be predicted directly out of the optimal design model. This provides for consideration of the role of material constitution in general in the structural optimization setting, an aspect of design that cannot be addressed using earlier interpretations for the design of continuum structures. Local-scale aspects of the structural system, i.e. the actual material properties themselves, comprise *the fundamental elements of design* and all other attributes such as material distribution, layout or topology, and so forth are at least implicit within them. Thus to support elastic continuum design in its broadest form, the latter alternative approach is followed here in place of the conventional homogenization-based model.

Formulation for Optimal Continuum Structures The formulation for structural optimization is stated in the form of an isoperimetric problem, where the objective measures efficiency relative to structural purpose and the isoperimetric constraint reflects a limit on 'structural resource'or cost. To be sensible for the present purpose, i.e to predict the best composition from among arbitrary elastic continua, the cost constraint must be expressed in a form appropriate to reflect the contribution of individual components of the material modulus tensor. An expression suitable for this purpose [Taylor & Washabaugh (1995)] is based on an interpretation of unit strain energy in terms of independent components, each component identified with independent material contributions of energy. If the mechanics part of the formulation is interpreted in terms of the same basis of strain energies, the entire structural optimization problem can be stated in a compact and convenient form [Taylor (1998)]. In the problem statement given below, the quantities symbolized by B_γ; B_γ^+; B_γ^- are unique to a given material and represent constitutive design. At the same time, they comprise the basis for expression of generalized cost, the argument of the isoperimetric constraint for the design (outer) part of the problem. Note that this form for the inner problem corresponds to 'minimum compliance'

optimal design. The number (N+C) of components in the basis is consistent with the number of independent elements of the modulus tensor. The η_{ij}^{β} represent a fixed set of reference strains - actual strain ε_{ij} is given in terms of them by $\varepsilon_{ij} = \sum_{1}^{N} c_\beta \eta_{ij}^{\beta}$ - and coefficients $e_\gamma(x)$ in the argument under the integral of 'min' (the unit strain energy) are quadratic in coefficients $c_\gamma(x)$. The complete design problem is stated in minmax form as:

$$\max_{B_\gamma, B_\gamma^+, B_\gamma^-} \quad \min_{c_\alpha(x); u_k(x)} \left\{ \int_\Omega \left[\sum_{1}^{N} e_\gamma B_\gamma + \sum_{N+1}^{N+C} e_\gamma \left(B_\gamma^+ - B_\gamma^- \right) \right] dV \right\}$$

subject to

$$\underline{B}_\gamma \le B_\gamma \le \overline{B}_\gamma \qquad \gamma = 1, \ldots N$$

$$0 \le B_\gamma^+ \le \overline{B}_\gamma^+ \qquad \gamma = (N+1), \ldots (N+C)$$

$$0 \le B_\gamma^- \le \overline{B}_\gamma^-$$

$$\int_\Omega \left(\sum_{1}^{N} b_\gamma B_\gamma + \sum_{N+1}^{N+C} \left(b_\gamma^+ B_\gamma^+ + b_\gamma^- B_\gamma^- \right) \right) dV - R \le 0$$

subject to

$$\underline{W} - \left\{ \int_\Omega f_i u_i \, dV + \int_{\Gamma_t} t_i u_i \, dS \right\} \le 0$$

$$\frac{1}{2}\left(u_{i,j} + u_{j,i}\right) - \sum_\alpha c_\alpha \eta_{ij}^{\alpha} = 0$$

Here b_γ stand for unit cost, u_i represents displacement field, and $f_i \& t_i$ symbolize respectively the body forces and boundary forces.

On Computational Procedure The inner part of the maxmin formulation, covering elastostatics for the continuum structure, is a quadratic program while the design part is linear in the design variables. Among the various approaches readily available for problems having this form, a method for iterative cycling between the max and min parts proves to be effective. A commercial routine was used to solve the QP, and a conventional form of optimality condition based redesign rule [see e.g. Prager(1974); Rozvany(1989)] is used for the redesign part of the cycle. The model is tested on several basic examples in 2D where the optimal design is predicted for a specified homogeneous strain state. In the case of loading in pure shear, out of all possibilities for the unrestricted modulus tensor the optimal material is composed of the single element E1212, as expected. For strain state comprised of equal strains in orthogonal directions, say x1 and x2, the optimal material is again composed of a single element of the tensor, this time E1122. A somewhat more complex material is predicted as the stiffest one to resist varying ratios of orthogonal normal strain. As the final example of this type, the optimal material is predicted for a square specimen pinned on diagonally opposite corners and loaded diagonally at the remaining corners. To demonstrate a different aspect of design, the topology for optimal

reinforcement is shown (see Figure below) for a cantilevered beam made of a two-material composite [Rodrigues, et al (1998); Guedes & Taylor (1997].

Acknowledgement Most of the example results reported here were generated through the efforts of Helder Rodrigues and Ciro Soto. The author is grateful for these contributions and for many useful discussions of the basic modelling as well.

References

Bendsøe, M.P. (1995), *Optimization of Structural Topology, Shape, and Material*, Springer - Verlag, Berlin, Heidelberg, London.

Cherkaev, Andrej (1999), *Variational Methods for Structural Optimization* to appear.

Cherkaev A.V., & L.V. Gibiansky (1992), "The exact coupled bounds foreffective tensors of electrical and magnetic propertiespf two-component two dimensional composites, Proc. Royal Soc. Edingurgh Sect., A 122, 93 - 125, (first published in Russian, 1988).

Gibiansky, L.V. & A.V. Cherkaev (1984), "Design of Composite plates of Extremal Rigidity", Report 914, Ioffe Physico-Technical Inst., Acad. of Sci., Leningrad, USSR.

Milton, G.W. (1990), "A Brief Review of the Translation Method for Bounding Effective Elastic Tensors of Composites", *Continuum mpdels and discrete systems*, Vol. 1, (Dijon, 1989, Longman Sci. Tech., Harlow, pp60 - 74.

Lipton, R. (1993), "On Implementation of Partial Relaxation for Optimal Structural Compliance Problems", in P. Pedersen (ed), *Optimal design with advanced materials*, Elsevier, Amsterdam, the Netherlands.

Olhoff, Niels, J. Thomsen & J. Rasmussen (1993), "Topology Optimization of Bi-material Structures", in Pedersen P. (ed), *Optimal Design with Advanced Materials*, Elsevier, Amsterdam.

Bendsøe, M.P.; Guedes, J.M.; Haber, R.B.; Pedersen, P.; Taylor, J.E. (1994) "An Analytical Model to Predict Optimal Material Properties in the Context of Optimal Structural Design." J. Applied Mech., Vol. 61, No.4, 930-937.

Bendsøe, M.P.; Diaz, A.; Lipton, R.; Taylor, J.E. (1995), "Optimal Design of Material Properties and Material Distribution for Multiple Loading Conditions", Int. J. Num. Methods in Engrg. Vol 38, pp 1149-1170.

Taylor, J.E. and P.D. Washabaugh (1995), "A Generalized Expression of Cost for Prediction of The Optimal Material Properties Tensor", *in* Trends in Application of Mathematics to Mechanics, D P Monteiro Marques & Jose Francisco Rodrigues, eds., Longman, Essex, England.

Taylor, J.E. (1998), "An Energy Model for the Optimal Design of Linear Continuum Structures", Structural Optimization, Vol.16, Nos 2/3, pp 116 - 127; see also 'Corrigendum', same title ... to appear

Prager, Wm. (1974), *Introduction to Structural Optimization*, (Course No. 212, CISM - Udine, October 1974), Springer - Verlag, Heidelberg.

Rozvany, G.I.N. (1989), *Structural Design via Optimality Criteria*, Kluwer Academic Publisher's Group, Dordrecht, the Netherlands.

Guedes, J. M. & J.E. Taylor (1997), "On the Prediction of Material Properties and Topology for Optimal Continuum Structures", Structural Optimization, Vol. 14, 193-199

Rodrigues, H., Ciro A. Soto & J.E. Taylor (1998), "A Method for the Optimal Design of Composite Continuum Structures", Structural Optimization, Vol. 17, pp 186 - 198.

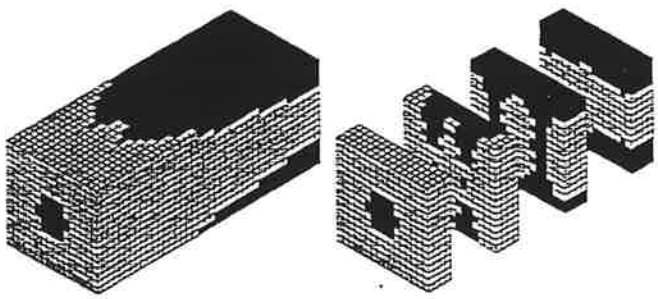

3D TOPOLOGY DESIGN FOR A COMPOSITE - MATERIAL CANTILEVERED BEAM

Stress updating using ODE-methods

Mathias Wallin and Matti Ristinmaa
Division of Solid Mechanics.
Lund University, Box 118, S-221 00 Lund, Sweden.

The most widely spread tool for solving problems in solid mechanics is the finite element method. When non-linear material behavior (elasto-plasticity, viscoplasticity) is considered the inelastic response of the material is governed by constitutive equations of rate form. Although it has been shown that assuming the strain rate to be constant within the increment results in a closed-form solution for some special choices of material model, it is in general necessary to adopt numerical methods in order to obtain the solution for the constitutive equations.

The standard method today is to utilize the fully implicit generalized midpoint rule, which for the von Mises yield surface is more known as the radial return method. The incitements for adopting the radial return method are stability properties and the simplicity of the method (for non-complex methods). However, since the material models has become more complex the simplicity has been lost and, more important, the accuracy of the method for some rather complex material models turns out to be unsatisfying.

An alternate method is to use some assumption of the strain rate and solve the constitutive relations using some ODE-method. Collecting the plastic strains and the internal variables in a column matrix $\boldsymbol{y}$ and making use of the chosen strain rate assumption allow the constitutive equations to be written as a system of ordinary differential equations $\dot{\boldsymbol{y}} = \boldsymbol{f}(\boldsymbol{y}, t)$, which are integrated to yield the updated state. Available methods within the ODE-methods are for example multi-step methods like Adams-Bashforth methods and single-step methods like the Runge-Kutta methods. For the embedded Runge-Kutta methods, which are considered here, an estimation of the error can be obtained, without any extra function evaluations, thus allowing the accuracy of the solution to be controlled.

In order to solve the global equilibrium equations and avoiding so-called drift, global equilibrium iterations are usually performed. The efficiency of a Newton-Raphson method is highly dependent on the consistent tangent stiffness tensor or algorithmic stiffness tensor (ATS). The algoritmic stiffness tensor, D^{ATS}_{ijkl}, is defined from the relation

$$d(\sigma^{n+1}_{ij}) = D^{ATS}_{ijkl} d(\epsilon^{n+1}_{kl})$$

The derivation of the algorithmic stiffness tensor for the Runge-Kutta family turns out to be extremly expensive. However, it turns out that an inexpensive approximation for the algoritmic stiffness tensor can be obtained if the ATS-tensor is calculated using the trapezodial rule, i.e.

$$\boldsymbol{y}^{n+1} - \boldsymbol{y}^{n} = \frac{1}{2}(\boldsymbol{f}|_{t=t_c} + \boldsymbol{f}|_{t=t_{n+1}})$$

Differentiation of $\boldsymbol{y}^{n+1}$ with respect to ϵ_{ij}^{n+1} yields the missing term in the ATS tensor. Moreover, a more accurate approximation for the algorithmic stiffness tensor is obtained if the integration is performed in two steps.

To analyze the integration scheme and the ATS-tensor two different material models are considered, an elasto-plastic mixed hardening/damage model based on the von Mises yield surface and an isotropic hardening viscoplastic Drucker-Prager model. For the elasto-plastic model the constant strain rate assumption is used whereas a linear strain rate assumption is utilized in the viscoplastic model.

The accuracy of the proposed algorithm turns out to be very satisfying. Moreover, the convergence properties of the approximate algorithmic stiffness tensor are almost as good as for the true algoritmic stiffness tensor. Some typical results are shown below.

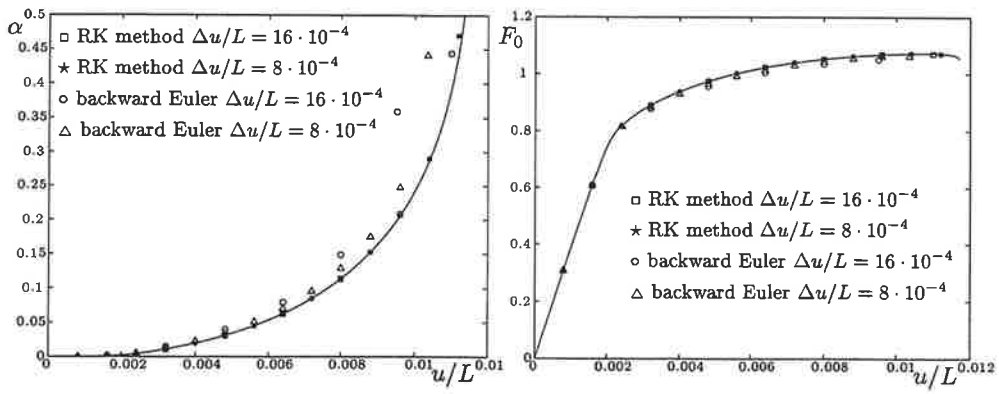

Figure 1: Mixed isotropic/kinematic hardening von Mises plasticity coupled with damage. a) Damage-displacement graph for the most damaged element. b) Load-displacement graph.

ROLLER-CHAIN DRIVES MECHANICS USING MULTIBODY DYNAMICS TOOLS

JORGE A. C. AMBRÓSIO
IDMEC Pólo I.S.T., Rua Rovisco Pais, 1, 1096 Lisboa, Portugal
JOHN M. HANSEN
Dept. of Solid Mechanics, Technical University of Denmark, DK-2800 Lyngby, Denmark

1. Introduction

In this study the dynamics of a system of one or more sprockets connected through a roller-chain is modeled using multibody dynamics. The dynamics of the roller chain drives is characterized by a complex behavior with impacts between the chain links and sprockets and by discontinuities in the system components velocities giving raise to transversal and longitudinal vibrations on the spans of the chain. Several investigators have looked at the problem using various approaches, for example [1-6]. In these studies it is pointed out that several phenomena occurs in the roller-chain drives. As the individual links of the chain engages and disengages at discrete times, between which the system exhibits continuos behavior, a so-called *polygonal effect* occur. This effect in itself causes transverse vibrations of the chain, and at the same time it creates instantaneous changes of lengths of the chain spans between sprockets, causing axial vibrations. The consequence of this is that there is a strong coupling between axial and transverse vibrations, and even though the driving sprocket may rotate with constant angular velocity, the driven sprockets will rotate with time variant angular speed.

Here, an integrated model describing the complex dynamics of the roller chain drive including tensioners and sprockets is proposed. The roller chain drive model, based on a multibody dynamics formulation, has one driving sprocket and one or more driven sprockets. The complete chain is modeled by lumped masses connected by spring-damper uniaxial elements. Special attention is paid to the capture and release of the rollers by the sprockets in order to have an accurate model of the moving boundary conditions and impact phenomenon.

2. The model

The system of chain and sprockets is modeled as indicated in Fig. 1. Each chain link is modeled as a mass particle, and the sprockets are modeled as polygons, in which each corner corresponds to the seating between two teeth.

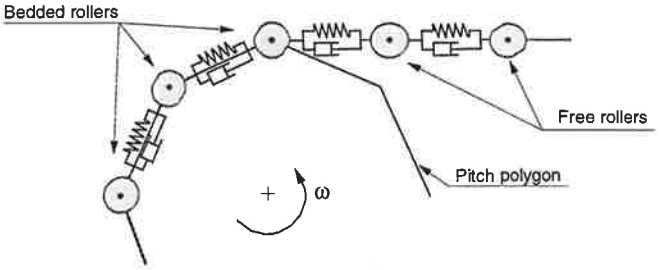

Fig. 1. Model of the roller-chain drive.

For all the rollers that are not engaged in a sprocket, the equations of motion are

$$\begin{bmatrix} m_r & & & & \\ & m_r & & & \\ & & \ddots & & \\ & & & m_r & \\ & & & & m_r \end{bmatrix} \begin{Bmatrix} \ddot{x}_1 \\ \ddot{y}_1 \\ \vdots \\ \ddot{x}_{n_l} \\ \ddot{y}_{n_l} \end{Bmatrix} = \begin{Bmatrix} f_{x_1} - f_{x_{n_l}} \\ f_{y_1} - f_{y_{n_l}} - m_r g \\ \vdots \\ f_{x_{n_l}} - f_{x_{n_l-1}} \\ f_{y_{n_l}} - f_{y_{n_l-1}} - m_r g \end{Bmatrix} \tag{1}$$

where n_l is the number of non-seated rollers, and the f-terms are the forces acting between the rollers. These terms are given by

$$\mathbf{f}_i = \begin{bmatrix} f_{x_i} \\ f_{y_i} \end{bmatrix} = k \begin{bmatrix} \delta_{x_i} \\ \delta_{y_i} \end{bmatrix} + c \begin{bmatrix} \dot{\delta}_{x_i} \\ \dot{\delta}_{y_i} \end{bmatrix} \tag{2}$$

where the δ-terms are the elongation of the individual chain links. These terms can be written in terms of the positions and velocities of the links. For example, as may be deduced from Fig. 2, the spring forces may be written as

$$\mathbf{f}_i = k \begin{Bmatrix} (x_{i+1} - x_i)\left(1 - \dfrac{L_0}{L_{i+1}}\right) - (x_i - x_{i-1})\left(1 - \dfrac{L_0}{L_i}\right) \\ (y_{i+1} - y_i)\left(1 - \dfrac{L_0}{L_{i+1}}\right) - (y_i - y_{i-1})\left(1 - \dfrac{L_0}{L_i}\right) \end{Bmatrix} \tag{3}$$

For a sprocket having a moment of inertia J_s and an external applied force, $\mathbf{f}_s$, and torque n_s, the equations of motions are given in Eq. (4), in which $\dot{\omega}_s$ is the angular acceleration. The external forces are made up from the forces with which the chain affect the sprocket and from optional directly applied forces.

$$\begin{bmatrix} m_s & & \\ & m_s & \\ & & J_s \end{bmatrix} \begin{Bmatrix} \ddot{x}_s \\ \ddot{x}_s \\ \dot{\omega}_s \end{Bmatrix} = \begin{Bmatrix} f_{x_s} \\ f_{y_s} \\ n_s \end{Bmatrix} \tag{4}$$

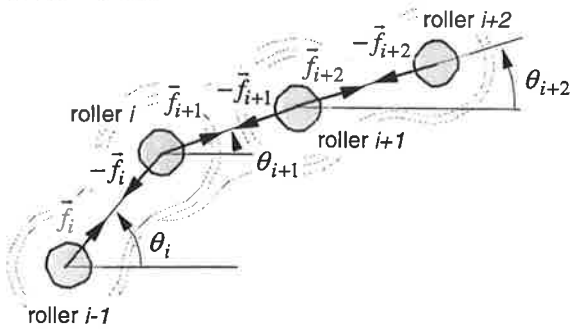

Fig. 2. Forces due to the link flexibility acting on roller i.

The rollers that are seated on the sprockets are treated here as constrained bodies. Let the sprocket s having n_{s_t} teeth, represented in Fig. 3, have a body fixed coordinate system $(\xi,\eta)_s$ attached to its center of mass. Then the location and angular orientation of the sprocket with respect to the inertial frame X,Y is described by vector $\mathbf{q}_s = \{x_s \;,\; y_s \;,\; \theta_s\}^T$.

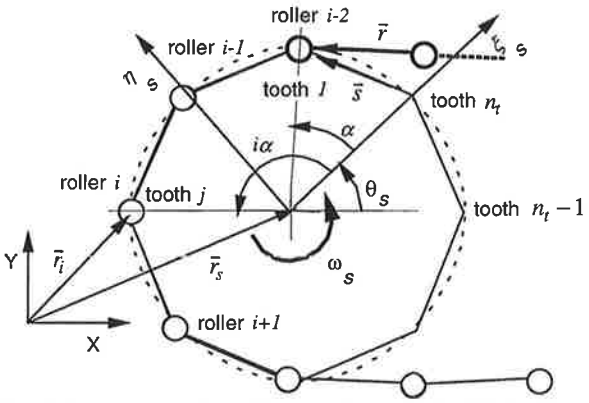

Fig. 3. Representation of a sprocket with bedded rollers.

For a bedded roller i fixed to the pitch circle of the sprocket, the constraint equations may be written as

$$\Phi^{(s,i)} = \begin{cases} x_i - x_s - R_s\cos(\theta_s + j\alpha) = 0 \\ y_i - y_s - R_s\sin(\theta_s + j\alpha) = 0 \end{cases} \tag{5}$$

Differentiating these equations twice with respect to time, and using the Lagrange multiplier technique [7], the total set of equations may be setup as

$$\begin{bmatrix} m_s & & & & & & & & & -1 & & \cdots & -1 & & \\ & m_s & & & & & & & & & -1 & \cdots & & -1 & \\ & & J_s & & & & & & & S_1 & C_1 & \cdots & S_{n_r} & C_{n_r} & \\ & & & m_r & & & & & & 1 & & & & & \\ & & & & m_r & & & & & & 1 & & & & \\ & & & & & \ddots & & & & & & \ddots & & & \\ & & & & & & m_r & & & & & & 1 & & \\ & & & & & & & m_r & & & & & & 1 & \\ -1 & & S_1 & 1 & & & & & & & & & & & \\ & -1 & C_1 & & 1 & & & & & & & & & & \\ \cdots & \cdots & \cdots & & & \ddots & & & & & & & & & \\ -1 & & S_{n_r} & & & & 1 & & & & & & & & \\ & -1 & C_{n_r} & & & & & 1 & & & & & & & \end{bmatrix} \begin{Bmatrix} \ddot{x}_s \\ \ddot{y}_s \\ \ddot{\theta}_s \\ \ddot{x}_1 \\ \ddot{y}_1 \\ \cdots \\ \ddot{x}_{n_r} \\ \ddot{y}_{n_r} \\ \lambda_{11} \\ \lambda_{21} \\ \cdots \\ \lambda_{1n_r} \\ \lambda_{2n_r} \end{Bmatrix} = \begin{Bmatrix} f_{xs} \\ f_{ys} \\ -n_s \\ f_{x1} \\ f_{y1} \\ \cdots \\ f_{xn_r} \\ f_{yn_r} \\ C_1^* \\ S_1^* \\ \cdots \\ C_{n_r}^* \\ S_{n_r}^* \end{Bmatrix} \tag{6}$$

in which

$$S_j = R_s\sin(\theta_s + j\alpha)$$
$$C_j = R_s\cos(\theta_s + j\alpha)$$
$$S_j^* = -C_j(\dot{\theta}_s)^2$$
$$C_j^* = S_j(\dot{\theta}_s)^2$$

The λ–terms are the reaction forces needed to constrain the bedded rollers to the sprockets.

3. Roller engagement and disengagement

We now assume a perfect chain, i.e. a chain that is not worn or elongated. In this case, as can be seen from Fig. 3, a roller that engages will get bedded exactly in the bottom of the teeth profile. Let roller k precede roller j, where roller j is the last bedded roller on sprocket s. Then roller k will leave the span and seat on the sprocket when the vector $\bar{r}$, the vector from roller k to roller j, is parallel with vector $\bar{s}$, the vector defined along the side of the pitch polygon of the sprocket. After some manipulation, this can be expressed as

$$(x_j - x_k)\cos\left[\theta_s + (j+½)\alpha\right] + (y_j - y_k)\sin\left[\theta_s + (j+½)\alpha\right] = 0 \tag{7}$$

For roller i to leave a sprocket s and become part of the "free" chain segment again, the reaction force between the sprocket and the roller must change from a pushing force to a pulling force. This may be expressed as

$$\lambda_{1i}\cos(\theta + i\alpha) + \lambda_{2i}\sin(\theta + i\alpha) \geq \sqrt{\lambda_{1i} + \lambda_{2i}}\cos\frac{\pi - \alpha}{2} \tag{8}$$

where the λ-terms are the reaction force components from Eq. (6) for roller i.

4. Discussion

With this model it is possible to perform a dynamic simulation of the roller-chain/sprocket system, which includes the effects that appear when the individual chain links engages and disengages with the sprockets, and the coupling between axial and transverse vibrations. The model does, however, not include for example clearance between pin and bushing, the rotational inertia of the link elements, tooth flexibility, and the actual shape of the teeth. A model based on contact-impact forces instead of kinematical constraints, that will handle some of these effects, is however also developed, but not implemented yet.

References:

[1] Wang, K.W., Liu, S.P., On the Noise and Vibration of Chain Drive Systems, *The Shock and Vibration Digest*, 23(4), 8-13, 1991.

[2] Veikos, N., Freudenstein, F., On the Dynamic Analysis of Roller Chain Drivers: Part I - Theory, *Mechanical Design and Synthesis DE-Vol.46*, ASME, 431-439, 1992.

[3] Veikos, N., Freudenstein, F., On the Dynamic Analysis of Roller Chain Drivers: Part II - Case Study, *Mechanical Design and Synthesis DE-Vol.46*, ASME, 441-450, 1992.

[4] Mahalingam, S., Polygonal Action on Chain Drives, *J. Franklin Inst.*, **265**(1), 23-28, 1958.

[5] Bouillon, G., Tordion, G.V., On Polygonal Action in Roller Chain Drives, *Journal of Engineering for Industry*, ASME Transactions, **87**, 243-250, 1965.

[6] Choi, W., Johnson, G., Vibration of Roller Chain Drives at Low, Medium and High Operating Speeds, *Vibrations of Mechanical Systems and the History of Mechanical Design*, DE-Vol. 63 ASME, 29-40, 1993.

[7] Nikravesh, P.E., *Computer-Aided Analysis of Mechanical Systems*, Prentice-Hall, Englewood-Cliffs, New Jersey, 1988.

WAVE PROPAGATION IN SOILS RELATED TO HIGH-SPEED TRAINS

Torbjörn Ekevid, Nils-Erik Wiberg
Department of Structural Mechanics
Chalmers University of Technology
S-412 96 Göteborg, Sweden
email: torek@sm.chalmers.se

Intoduction

The modern community has become very dependent on a well working infrastructure. People as well as goods need to be transported in a fast and reliable way. During the century the amount of transportation work has increased in an accelerating manner, and will with high reliability do so even in the future. Therefore, governments have made, and will make, large investments in new infrastructure as e.g. roads, railroads and airports. In Sweden as well as in many countries all over Europe the government have made investments in a well working railroad net for high-speed trains. Most of these commitments are working very well, but in a few places a new kind of problems, related to the high-speed train have occurred, after the railroads have opened for traffic.

Wave propagation in the surrounding media will always be present to some extension, when a train passes on the railroad embankment. The level of vibrations is highly dependent on the material properties of the ground the embankment is built on. In places where the conditions of the ground material are bad, as for example in soft clays, the deformations seems to increase in an extreme way when the speed of the train approaches shear wave velocity in the subground material. This phenomenon is similar to the supersonic boom, occurring when an aeroplane reaches the natural velocity in air. As a result of the large deformations, the trains have been forced to limit their operational speed, or very expensive reinforcements of the ground have been carried out.

An intensive research activity has been deducted to this problem in order to understand the mechanisms beyond the phenomenon, and to demonstrate what factors are the most critical. Different approaches have been made. In [1] and [2] V. Krylov presented an analytical solution based on some assumptions e.g. that the load was quasi-static, for a train passing on a Wrinkler beam lying on elastic media. A number of more or less advanced numerical calculations based on finite differences or finite elements have also been carried out, see e.g. [3] and [4].

Our approach is to use the time-discontinuous Galerkin finite element method when attacking the problem. This method has a rigorous theoretical base and convergence as well as error estimations have been derived. In [8], Hughes and Hulbert introduced the time-discontinuous Galerkin method for the second order hyperbolic wave equation. Additional least square terms were added in order to prove convergence for the method. Further Johnson in [5] proved for the case of linear interpolations, that there was no need for the additional least-square terms in the formulation to achieve convergence.

Generally, the dG method generates a system of coupled equations larger than a direct time integration scheme e.g. the Newmark scheme. An efficient and accurate solution algorithm [6], [7] is thus of great importance if the dG-method should be able to compete with the traditional semi-discrete methods used in dynamics.

Theory

Consider the second-order hyperbolic equation describing the dynamic response of a linear elastic continuum (1), with boundary and initial condition (2) (damping effects are omitted).

$$\begin{cases} \rho \dot{\boldsymbol{v}} - \tilde{\nabla}^T D \tilde{\nabla} \boldsymbol{u} = \boldsymbol{f}(\boldsymbol{x},t) \\ \dot{\boldsymbol{u}} - \boldsymbol{v} = 0 \end{cases} \qquad in\ \Omega \times I \tag{1}$$

$$\begin{cases} \boldsymbol{u} = \boldsymbol{g} & on\ \ \Gamma_g \times I \\ \boldsymbol{n} \cdot \boldsymbol{\sigma} = \boldsymbol{h} & on\ \ \Gamma_h \times I \end{cases} \qquad \begin{cases} \boldsymbol{u}(\boldsymbol{x},0) = \boldsymbol{u}_0 \\ \boldsymbol{v}(\boldsymbol{x},0) = \boldsymbol{v}_0 \end{cases} \tag{2}$$

where $\boldsymbol{u}$ and $\boldsymbol{v}$ denotes the displacement- and velocity field, respectively, Ω is the spatial domain and I is the actual time interval.
Our aim is to define a finite element method such that the displacement- and velocity fields are continuous in space and in time on each "time slab", see Figure 1, but where we allow the fields to be discontinuous at the time level where adjacent time slabs meet. These discontinuities, denoted $[u^h]$ and $[v^h]$, will later serve as error indicators and enable us to control the time step size.

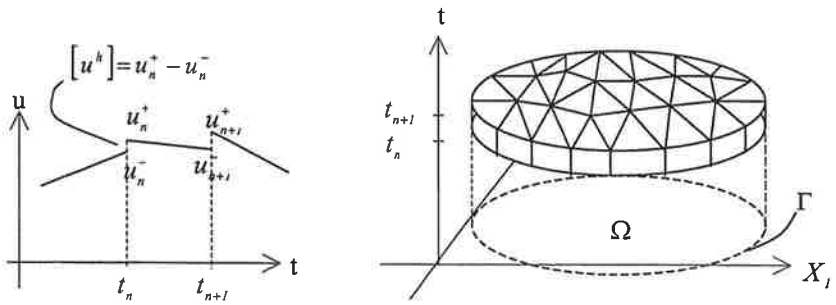

Figure 1. Schematic illustration of nodal notations and a space-time slab

In order to make a weak formulation of (1) we have to define appropriate spaces where to chose trial- and test functions from. The proposed finite element method can easily be derived from the weighting residual form (3) 33of the two-field partial differential equation on each time slab, since the test functions are nonzero just in this time interval.

$$\begin{aligned} \boldsymbol{R}_n = & \underbrace{\int_{\Omega \times I_n} \boldsymbol{w}_v^h \cdot \left(\rho \dot{\boldsymbol{v}}^h - \tilde{\nabla}^T \boldsymbol{D} \tilde{\nabla} \boldsymbol{u}^h - \boldsymbol{f}(x,t)\right) d\Omega\, dt}_{(dynamic\ equation)} + \underbrace{\int_{\Omega \times I_n} \boldsymbol{w}_u^h \cdot \left(\tilde{\nabla}^T \boldsymbol{D} \tilde{\nabla} \left(\dot{\boldsymbol{u}}^h - \boldsymbol{v}^h\right)\right) d\Omega\, dt}_{(definition\ of\ velocity)} \\ & + \underbrace{\int_{\Omega} \boldsymbol{w}_u^h(t_n^+) \cdot \tilde{\nabla}^T \boldsymbol{D} \tilde{\nabla} \left[\boldsymbol{u}^h(t_n)\right] d\Omega\, dt}_{(displacement\ continuity)} + \underbrace{\int_{\Omega} \boldsymbol{w}_v^h(t_n^+) \cdot \rho \left[\boldsymbol{v}^h(t_n)\right] d\Omega\, dt}_{(velocity\ continuity)} = 0 \end{aligned} \tag{3}$$

After performing integration by parts, integration in space will just result in the ordinary mass- and stiffness matrices **M, K**. If the integration in time is then done explicitly we end up with the matrix equation (4). The invoked displacements and velocities at time t_n^- have been moved to the right hand side.

$$\begin{bmatrix} \frac{1}{2}\boldsymbol{K} & \frac{1}{2}\boldsymbol{K} & -\frac{1}{3}\Delta t_n \boldsymbol{K} & -\frac{1}{6}\Delta t_n \boldsymbol{K} \\ -\frac{1}{2}\boldsymbol{K} & \frac{1}{2}\boldsymbol{K} & -\frac{1}{6}\Delta t_n \boldsymbol{K} & -\frac{1}{3}\Delta t_n \boldsymbol{K} \\ \frac{1}{3}\Delta t_n \boldsymbol{K} & \frac{1}{6}\Delta t_n \boldsymbol{K} & \frac{1}{2}\boldsymbol{M} & \frac{1}{2}\boldsymbol{M} \\ \frac{1}{6}\Delta t_n \boldsymbol{K} & \frac{1}{3}\Delta t_n \boldsymbol{K} & -\frac{1}{2}\boldsymbol{M} & \frac{1}{2}\boldsymbol{M} \end{bmatrix} \begin{bmatrix} \boldsymbol{u}_n^+ \\ \boldsymbol{u}_{n+1}^- \\ \boldsymbol{v}_n^+ \\ \boldsymbol{v}_{n+1}^- \end{bmatrix} = \begin{bmatrix} \boldsymbol{K}\,\boldsymbol{u}_n^- \\ 0 \\ \boldsymbol{F}_1 + \boldsymbol{M}\,\boldsymbol{v}_n^- \\ \boldsymbol{F}_2 \end{bmatrix} \tag{4}$$

where $\mathbf{u}_n^+, \mathbf{v}_n^+$ and $\mathbf{u}_{n+1}^-, \mathbf{v}_{n+1}^-$ denotes nodal displacement and velocities at time t_n^+ and t_{n+1}^-, respectively, see Figure 1, and

$$\begin{bmatrix} \boldsymbol{F}_1 \\ \boldsymbol{F}_2 \end{bmatrix} = \int_{\Omega \times I_n}\!\!\int w_v^h \; f(x,t)\, d\Omega dt + \int_{\Gamma_h \times I_n}\!\!\int w_v^h \; h\, d\Gamma dt \tag{5}$$

By elementary matrix manipulations of the system matrix, the two last equations can be decoupled from the two firsts and solved separately. The nodal deformations $\left(\boldsymbol{u}_n^+,\, \boldsymbol{u}_{n+1}^-\right)^T$, can after $\left(\mathbf{v}_n^+,\, \mathbf{v}_{n+1}^-\right)^T$ are known easily be obtained from the first two equations.

Numerical Experiment

In this section results from adaptive finite element computation are presented. The model is a simplified model of a ground section where a train bogie load is passing on the upper boundary. The shear wave velocity for the ground material in the example is around 15.5 m/s. Geometry of the section studied can be found in Figure 2. Some Rayleigh damping i.e. a linear combination of the mass- and the stiffness matrices, $\boldsymbol{C} = a\boldsymbol{M} + b\boldsymbol{K}$, where $a = b = 0.005$ has been added. The relative error for the solution $\eta_t^{TOL} = 0.1\%$, for time and $\eta_s^{TOL} = 12\%$ for space are specified and satisfied during the computation. The computation is performed over the time interval $[0, 9.0]$ s.

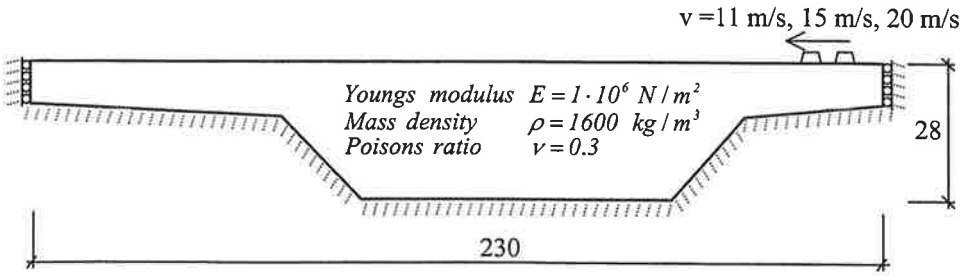

Figure 2. A railroad section charged by a moving train bogie load.

An obvious observation is that the deformations increase very rapidly when the speed of the bogie load approaches the shear velocity. The maximum stress level will increase in a very

similar manner. Notice also the effects when the boundary traction is moving with a "supersonic speed".

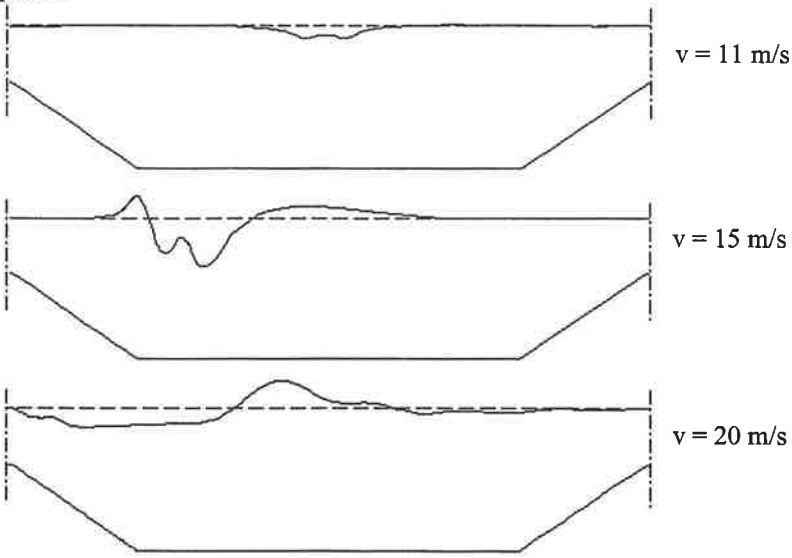

Figure 3. Deformations of the upper boundary with load velocity 11 m/s, 15 m/s and 20 m/s. Vertical displacements are scaled by a factor 20.

REFERENCES

[1] V.V. Krylov, Ground vibration boom from high-speed trains: Prediction and reality. *Acoustics Bulletin*. July/August 1998.

[2] V.V. Krylov. Effects of track properties on ground vibrations generated by high-speed trains. *Acta Acustica*, Vol. 84, pp 78-90, 1998.

[3] W. Gardien, H. Stuit and F. de Boer. Finite element wave propagation model. *Proc. Second European LS-DYNA Users Conference*, Gothenburg, Sweden. 1999

[4] B. Andréasson. High speed lines on soft ground. Evaluation and analyses of measurements from the West Coast line. Appendix 11. 1999

[5] C. Johnson, Discontinuous Galerkin finite element methods for second order hyperbolic problems, *Comput. Methods Appl. Mech. Engrg.*, Vol 107, pp117-129, 1993

[6] X. D. Li and N.-E. Wiberg, Structural dynamic analysis by a discontinuous Galerkin finite element method, *Int. J. numer. methods Eng*, Vol. 39, pp 2131-2152, 1996

[7] X. D. Li, Adaptive finite element procedures in structural dynamics. *Ph.D. Thesis, Chalmers University of Technology, Department of Structural Mechanics*, Göteborg, Sweden, 1996

[8] G. M. Hulbert and T. J. R. Hughes, Space-time finite element methods for second-order hyperbolic equations, *Comput. Methods Appl. Mech. Engrg.*, Vol. 84, pp 327-348, 1990

Advances in numerical analysis models for dynamic and aeroelastic actions of long-span bridges

R. Kiviluoma

Consultant, Finnish National Road Administration, Consulting
Graduate student, Helsinki University of Technology, Laboratory of Bridge Engineering
E-mail: risto.kiviluoma@tieh.fi

Abstract: In this paper a numerical analysis model and its implementation are represented for coupled-mode buffeting and flutter analysis of long-span bridges. The model combines both phenomenons to be analysed simultaneously by means of spectral analysis method of random vibration theory. To model has capability to analyse fully coupled equations of motions required for classical flutter and detailed 3-dimensional structural models. Furthermore, the implementation of the model, the "BWIND" code, is made flexible to allow usage of full sets of wind-tunnel data, variety turbulence models including those measured on-site and modal-analysis results imported from virtually any Finite Element (FE) codes.

Introduction

In wind-resistant design of long-span bridges, the wind tunnel testing of two-dimensional scale-models of deck section has been proven useful for choosing between aerodynamically stable and unstable cross-section shapes. To this aim, dimensionless coefficients named as flutter derivatives are typically extracted from amplitude records of damped free vibrations of spring supported model. For small initiating amplitudes of potentially divergent oscillations of the scale-model, the flutter derivatives are shown to be independent of the amplitude of the motion, but depended on reduced frequency $K = Bn/U$, in which B = the deck width, n = the frequency of vibration, and U = the flow velocity. What is typically encountered for unstable cross-section is, that in a certain critical value of K the torsional motion of the model become divergent indicating tendency to torsional flutter. Wether or not the cross-section shape candidate is acceptable for design is depending on the mechanical characteristics, especially torsional stiffness, of the bridge's girder and the extreme wind velocities expected into the bridge site.

For buffeting analysis the steady aerodynamic coefficients of the deck section need to be extracted. While the drag coefficient can be conservatively approximated from tabulated data found in literature, the same is not true for the lift coefficient and its derivative respect to angle of attack. Wind tunnel tests are in most cases required. They could be conducted by well-established methods of fixing the scale model in rigid balance and by measuring the resultant reactions. Due to fluid wake behind the non-streamlined body, the resulting steady aerodynamic coefficients should be understood to describe the time-averaged values of the drag, lift and moment. The formation of buffeting loads (which are time depended in nature) by means of steady aerodynamic coefficients, calls for correction factors for eddies that are small in comparison to dimensions of the cross-section. As far as frequency-domain methods are applied the correction factors, termed as aerodynamic admittances, can be given as a function of K. The response reduction effect of aerodynamic admittance is significant for most bridges. Overlooking this fact in analysis can lead to overestimation of the response of some 2...3 times.

The characteristics on natural wind turbulence are generally described by statistical quantities

among which spectral densities, coherence functions and turbulence intensities are most often applied for engineering purposes. The spectral density and the coherence function are due to definitions truly frequency-depended quantities. By summarising the phenomenons described above, it is easy to emphasize the advantages the frequency domain methods, in comparison to time-domain methods, imply to rigorous analysis of bridges for wind load.

Considering the most challenging modern long-span bridge projects the final designs are tested applying the full-bridge models in wind tunnels. In such tests the response is measurable directly, and very simple or nonc post calculations are required. While these kinds of tests can be preformed in some wind tunnels owning a very wide working-section (4...30 m, say), it is clear that for most projects these are omitted and semi-empirical analysis models invoking section-models are chosen instead. This is the case in which the numerical model represented in this paper find its moment: Calculate, as accurately as possible, the response by means of aerodynamic data extracted through section model tests.

Fundamental equations of the model

The model combines the buffeting and flutter analysis via the Fourier-transformed equations of motion. For linearized vibration system subjected to buffeting loads they are expressed by formula

$$(-\omega^2\mathbf{M} + i\omega\mathbf{C} + \mathbf{K})\hat{\mathbf{X}}(\omega) = [i\omega\mathbf{C}_{Ae}(\omega) + \mathbf{K}_{Ae}(\omega)]\hat{\mathbf{X}}(\omega) + \hat{\mathbf{F}}_b(\omega) \ , \qquad (1)$$

in which ω = the circular frequency ($= 2\pi n$) , $\mathbf{F}_b$ = the vector of nodal buffeting loads, $\mathbf{X}$ = the vector of unrestrained nodal degrees of freedom, the symbol (^) denotes the Fourier-transform and i = the imaginary unit. Here $\mathbf{M}$, $\mathbf{C}$ and $\mathbf{K}$ are the mass, the damping and the stiffness matrices, respectively, due to the mechanical properties of the vibration systems. $\mathbf{C}_{Ae}(\omega)$ is the aerodynamic damping matrix and $\mathbf{K}_{Ae}(\omega)$ is the aeroelastic stiffness matrix to be defined in terms of flutter derivatives. The stability condition Eq. (1) implies, is independent of the buffeting loads. On the other hand, the buffeting response is dependent on aeroelastic forces, especially on aerodynamic damping.

Considering the buffeting loads as a stationary ergodic random process the cross co-covariance matrix can be constructed as

$$\mathbf{R}_b(\tau) = \lim_{T\to\infty}\frac{1}{T}\int_{-T/2}^{T/2}\mathbf{F}_b(t)\mathbf{F}_b^T(t+\tau)dt \ , \qquad (2)$$

where T = the time period, τ = the time lag and the superscript (T) means the transpose. The relation between the cross-spectral density matrices of the response $\mathbf{S}_x(\omega)$ and the buffeting loads $\mathbf{S}_b(\omega)$ can be expressed as

$$\mathbf{S}_x(\omega) = \mathbf{H}(\omega)\mathbf{S}_b(\omega)\mathbf{H}(\omega)^{T*}$$
$$\mathbf{H}(\omega) = \left[-\omega^2\mathbf{M} + i\omega[\mathbf{C} - \mathbf{C}_{Ae}(\omega)] + \mathbf{K} - \mathbf{K}_{Ae}(\omega)\right]^{-1} \ , \qquad (3)$$

in which the superscript (*) denotes complex conjugate, $\mathbf{H}(\omega)$ = the frequency-response matrix of the vibration system and the spectral densities are defined as the Fourier transform of the covariance functions. Although the solution is obtainable directly through equations above the

mode superposition approximation for $\mathbf{H}(\omega)$ is favourable for two reasons. Namely, for larger models the calculation of matrix $\mathbf{H}(\omega)$ through inversion of a large complex-valued matrix become extensive, but what is more important for the present model, it allows seamless integration to FE-codes via modal analysis result files. Here, because of the mass and the stiffness matrices are not explicitly accessible in most FE-codes. After some matrix operations the modal approximation to Eq. (3) can be shown to take the form

$$\begin{aligned} \mathbf{S}_{\lambda}(\omega) &= \tilde{\mathbf{\Phi}}\tilde{\mathbf{H}}(\omega)\mathbf{S}_{Q}(\omega)\tilde{\mathbf{H}}(\omega)^{T*}\tilde{\mathbf{\Phi}}^{T} \\ \tilde{\mathbf{H}}(\omega) &= \left\{ -\omega^2\tilde{\mathbf{I}} + i\omega\tilde{\mathbf{\Phi}}^{T}\mathbf{C}\tilde{\mathbf{\Phi}} + \tilde{\mathbf{\Omega}} - \tilde{\mathbf{\Phi}}^{T}\left[i\omega\mathbf{C}_{Ae}(\omega) + \mathbf{K}_{Ae}(\omega)\right]\tilde{\mathbf{\Phi}} \right\}^{-1} \qquad (4) \\ \mathbf{S}_{Q}(\omega) &= \tilde{\mathbf{\Phi}}^{T}\mathbf{S}_{b}(\omega)\tilde{\mathbf{\Phi}} \ , \end{aligned}$$

in which $\tilde{\mathbf{\Phi}}$ = the reduced modal matrix including prescribed number of the first eigenvectors and $\tilde{\mathbf{\Omega}}$ = the diagonal matrix of associated eigenvalues ω_i^2. For simplicity, the mode shapes are assumed here to be normalized respect to modal masses. It can be notified that if $\tilde{\mathbf{\Phi}}$ is an invertible square matrix (all mode shapes are included), then Eq. (4) is not more than a linear transformation of the basic equations and the characteristics of the original equations remain invariant.

The formulation of the problem at hand is straightforward and fruit-full to computer implementation. The phase in which turbulence statistics enters the model is the formation of matrix $\mathbf{S}_b(\omega)$. The details of this, as well as the procedure of formation of matrices $\mathbf{C}_{Ae}(\omega)$ and $\mathbf{K}_{Ae}(\omega)$, is omitted here but described in reference [1]. In general $\mathbf{S}_b(\omega)$ depends on steady aerodynamic coefficients, aerodynamic admittance functions and spectral densities of along-wind and vertical components of wind velocity vector.

Returning to the original problem of calculating the buffeting response and critical K and associated flutter velocity, the variance of the response in fixed wind speed is obtained by integrating the diagonal terms of response cross-spectral density matrix over the frequency range. Close the flutter velocity the variance increases rapidly being theoretically infinite above it. If the analysis algorithm is repeated for sequential wind speeds, the flutter velocity and frequency are directly detectable from response spectral densities. The peak response occurring in a given time interval, on the other hand, can be estimated by mathematical means provided that the turbulence is modelled as a Gaussian-process.

Implementation of the model and discussion

The model is implemented to the computer code "BWIND" programmed by standard Fortran-77 language. The body of the code consist on five separate program-units, Fig. (1), that are executed in sequential order for a given wind velocity. Disk-space and memory requirements are kept in a low level by considering only non-zero terms in matrix operations. While size of the analysis model (the basic FE-model) is unlimited the memory limitations guides the maximum number of mode-shapes and loaded nodes. A simple graphical postprocessing program is prepared, that can display 3-dimensional frequency-velocity-spectral density charts of the output.

Up today the BWIND-code is applied in academic research on the *Raippaluoto* and the *Kärkinen* bridges owning the longest cable-stayed spans in Finland. These bridges, despite that they are relatively stiff (lowest natural frequencies are of order 0.4 - 0.5 Hz), have interest in aerodynamical point-of-view, because they contain double-web stiffening girder, that was in early investigations [2] of 60's found problematic. The application of the model to these two bridges highlights several aspects on aerodynamics of bridges belonging to their class. Some of them are described below:

- Below the flutter velocity, the effect of aeroelastic forces is small, except for aerodynamic damping of vertical bending mode. Provided that the flutter velocity is high enough, the buffeting analysis of these bridges applying steady aerodynamic coefficients only, could yield acceptable results too.
- The aerodynamic admittance functions and coherence model assumed have considerable effect to the response. In general, these parameters require improved models and further research.
- The buffeting response of the bridges was relatively small suggesting that the vortex-shedding action, not considered in the study, could be a governing aerodynamic phenomenon.
- The modal analysis of the bridges applying detailed 3-dimensional models reveals the fact that the lowest eigenfrequencies and mode shaped are not well separated as, in experienced way, assumed in most analysis models found in literature. This follows from the fact that the masses of the pylons are comparable to mass of the girder and they interact with the pure mode shapes of the girder.

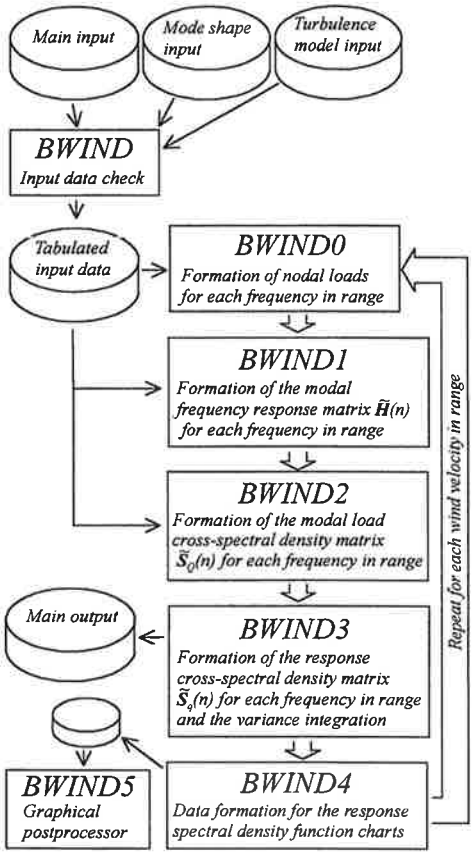

Fig 1. Flow-chart of the BWIND-2 - code.

Waiting for more numerical studies on very-long span bridges to come, the coupled-mode flutter analysis capabilities of the BWIND-code could also be demonstrated. It's shown after the wind tunnel experiments of current world-record suspended-span bridge, the Akashi-Kaikyo Bridge, that the coupled mode flutter (classical flutter) becomes dominant to very-long span suspension-bridges of its kind [3]. There is no doubt wether bridge-engineers'll plan new record span-lengths keeping the coupled-mode flutter analysis models, like the present model, under special interest in the future.

The author expresses his gratitude to Professor, Dr Tech. Aarne Jutila for supervising the work in Laboratory of Bridge Engineering. The author wishes to thank Dr Tech. Reijo Kouhia from Laboratory of Structural Mechanics for promoting the preparation of this paper.

References

[1] KIVILUOMA, R., Coupled-mode buffeting and flutter analysis of bridges. *Computers & Structures*, **70**(1998)2, pp. 219-228.

[2] SABZEVARI, A. & SCANLAN, R. H. Aerodynamic investigation of box girder bridges. *Journal of the Structural Division, ASCE*, **95**(1969)ST7, pp. 1517..1532.

[3] KATSUCHI, H., JONES, N. P. & SCANLAN, R. H. Multimode coupled flutter and buffeting analysis of the Akashi-Kaikyo Bridge. *Journal of Structural Engineering, ASCE*, **125**(1999)1, pp. 60...70.

DROP ANALYSIS FOR TRANSPORT CASK OF SPENT FUEL RODS

Pentti Varpasuo, Fortum Engineering Ltd, Vantaa

1. INTRODUCTION

This task is part of the design of Lianyungang nuclear power plant in Peoples Rebublic of China. The spent fuel cask is transported in and out of the reactor building through the equipment air lock that is located at the height of 26 meters from the elevation of grade. The aim of the analysis work is to show that the cask can withstand the accidental drop from that height oh the sand cushion without losing its integrity and leaktightness. The cask has been designed for the drop from 9 meters height to hard ground. In the following the preliminary numerical analysis is carried out for the perpendicular drop of the cask from the height of 26 m on the soil cushion consisting of 10 cm of asphalt, 40 cm of gravel and 4.5 m of soft sand.The results of drop to soil cushion are the compared with results of cask drop from 9m height on hard concrete.

2. GEOMETRY OF THE CASK

The cask is steel cylinder with base diameter of 2060 mm and height of 5500 mm and wall thickness of 350 mm. The total weight of the cask is 120 tons. The actual dropping angle of the cask is about 30 degrees from the vertical. The scheme for the cask drop to soft soil cushion has been depicted in the following Figure 1:

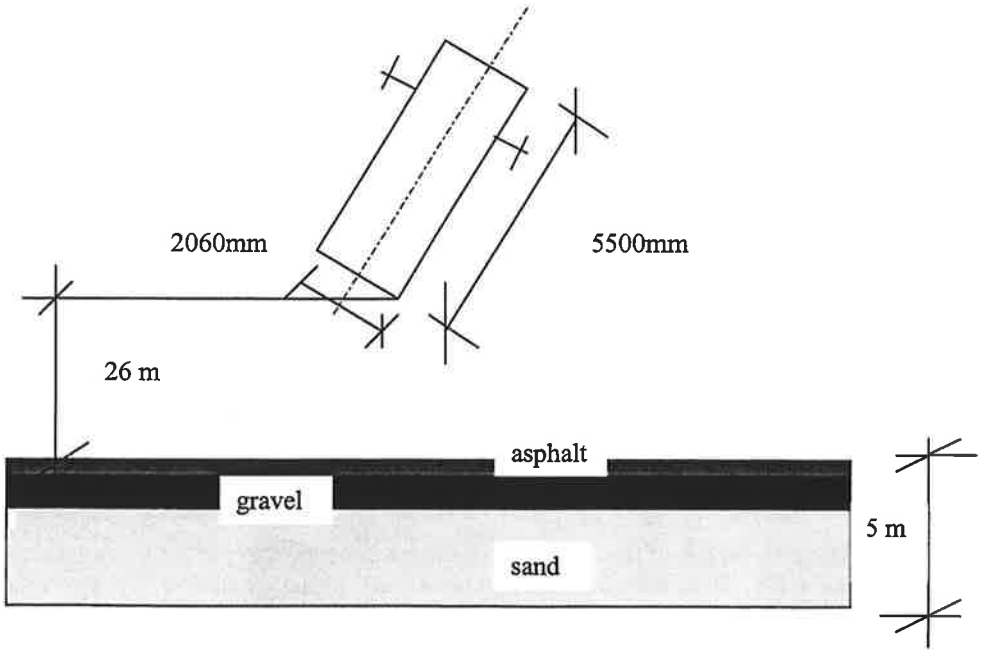

Figure 1 Drop of the transport cask on soft soil cushion

3. FINITE ELEMENT ANALYSIS OF THE DROP

The straight cask drop on soft soil cushion from the height of 26 m was modeled by finite element method. The model was developed using the twenty node solid elements available in MSC/NASTRAN [1]. The model consisted of the cask, gravel layer and sand layer. The dimensions of the cask are already given in Figure 1. The diameter of the soil cushion in the model was 7.2 m and the thickness of gravel layer was 0.4 meters and the thickness of sand layer was 5 meters. The boundary conditions, and model geometry and element mesh are shown in the following figure:

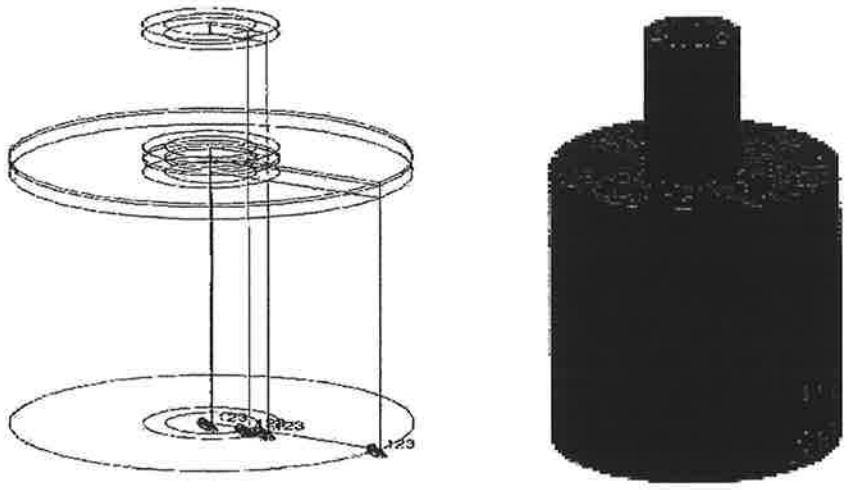

Figure 2 Geometry and boundary conditions of the finite element model and element mesh of the calculation model

4. COMPLETED ANALYSES

4.1. Linear Analysis of drop on soft soil cushion

In order to gain insight to the problem linear transient analysis was carried out first. The material properties in the linear analysis were taken as follows:

- Steel
  - E = 200 000 MN/m^2
  - ν = 0.3
- Gravel
  - E=10 000 MN/m^2
  - ν = 0.3
- Sand
  - E =2500 MN/m^2
  - ν = 0.3

The drop height of the cask was 26 meters corresponding to 22.6 m/s initial velocity of the cask. This velocity was given as the initial condition for all steel elements representing the cask. The lowest natural frequency and the corresponding natural period for the cask-soil system was estimated and the the value 0.05 seconds was obtained for the natural period. The time step used in the transient response analysis was

0.005 seconds and the length of the analyzed time window was 0.05 seconds representing one whole period of the vibrating system. The following two figures depict the vertical displacement time history for node 258 located in the lower edge of the cask and the von Mises stress time history for element 27 also in the lower edge of cask:

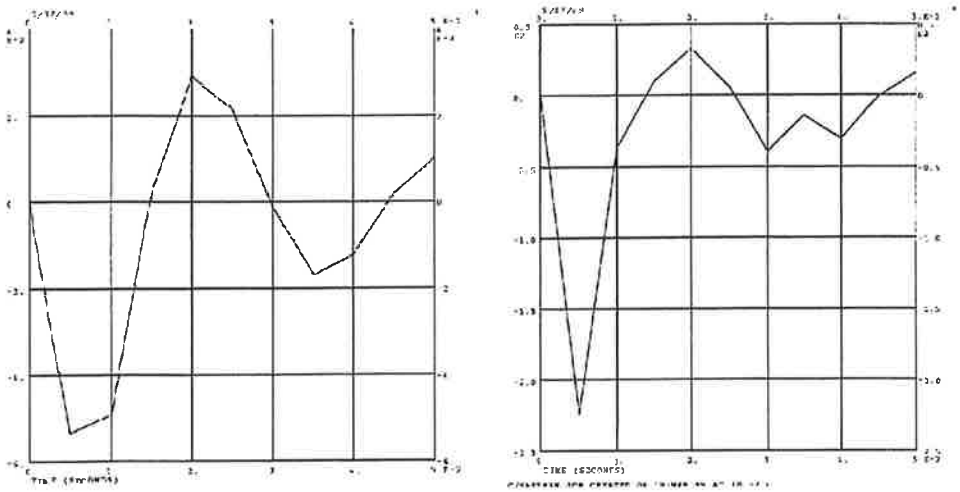

Figure 3 The vertical displacement history of node 258 of drop on soft soil cushion and Von Mises stress history of element 27of drop on soft soil cushion

As can be seen from Figures 3 the maximum displacement in the lower edge of the cask is about 6 centimeters and the maximum stress in the center of element 27 is about 200 MPa. These results are based on the linear analysis and in case of von Mises stresses the location of the monitoring point is in center of the element and do not represent the maximum that is in the edge of the element.

5. NONLINEAR ANALYSIS OF DROP ON SOFT SOIL CUSHION

The material properties in the nonlinear analysis were taken as follows:

- Steel: von Mises elastoplastic material model
  - E = 200 000 MN/m^2
  - ν = 0.3
  - Strain hardening slope 0.001
  - Yield stress σ_Y = 220 MN/m^2
  - Damping ratio 2% from critical
- Gravel: Mohr-Coulomb elastoplastic material model
  - E=10 000 MN/m^2
  - ν = 0.3
  - Strain hardening slope 0.001
  - Yield stress 10 MN/m^2
  - Friction angle 38 degrees
  - Damping ratio 10% from critical
- Sand: Mohr-Coulomb elastoplastic material model

- E =2500 MN/m^2
- $\nu = 0.3$
- Strain hardening slope 0.001
- Yield stress 2.5 MN/m^2
- Friction angle 30 degrees

The drop height of the cask was 26 meters corresponding to 22.6 m/s initial velocity of the cask. This velocity was given as the initial condition for all steel elements representing the cask. The lowest natural frequency and the corresponding natural period for the cask-soil system were estimated and the the value 0.05 seconds was obtained for the natural period. The time step used in the large displacement nonlinear transient response analysis was 0.001 seconds and the length of the analyzed time window was 0.1 seconds representing 100 time steps and approximately two and three quarters of the period of the vibrating system. The following two figures depict the vertical displacement time history for node 258 located in the lower edge of the cask and the von Mises stress time history for element 27 also in the lower edge of cask:

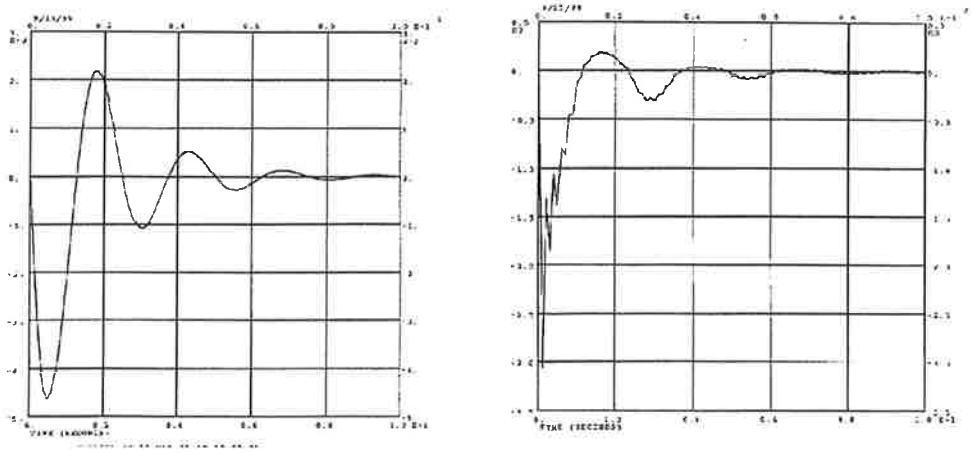

Figure 4 Displacement time history of node 258 calculated from nonlinear transient response analysis of drop on soft soil cushion and Von Mises stress time history of the edge node point of element 7 at lower edge of the cask calculated from the nonlinear transient response method of drop on soft soil cushion

6. NONLINEAR ANALYSIS OF DROP ON HARD GROUND

The material properties in the nonlinear analysis of cask drop on hard groundwere taken as follows:

- Steel: von Mises elastoplastic material model
  - E = 200 000 MN/m^2
  - $\nu = 0.3$
  - Strain hardening slope 0.001
  - Yield stress σ_Y = 220 MN/m^2
  - Damping ratio 2% from critical
- Concrete: Mohr-Coulomb elastoplastic material model

- E=30 000 MN/m^2
- $\nu = 0.3$
- Strain hardening slope 0.001
- Yield stress 30 MN/m^2
- Friction angle 38 degrees
- Damping ratio 5 % from critical

The drop height of the cask was 9 meters corresponding to 13.3 m/s initial velocity of the cask. This velocity was given as the initial condition for all steel elements representing the cask. The lowest natural frequency and the corresponding natural period for the cask-soil system were estimated and the the value 0.01 seconds was obtained for the natural period. The time step used in the large displacement nonlinear transient response analysis was 0.001 seconds and the length of the analyzed time window was 0.1 seconds representing 100 time steps and approximately two and three quarters of the period of the vibrating system. The following two figures depict the vertical displacement time history for node 258 located in the lower edge of the cask and the von Mises stress time history for element 27 also in the lower edge of cask:

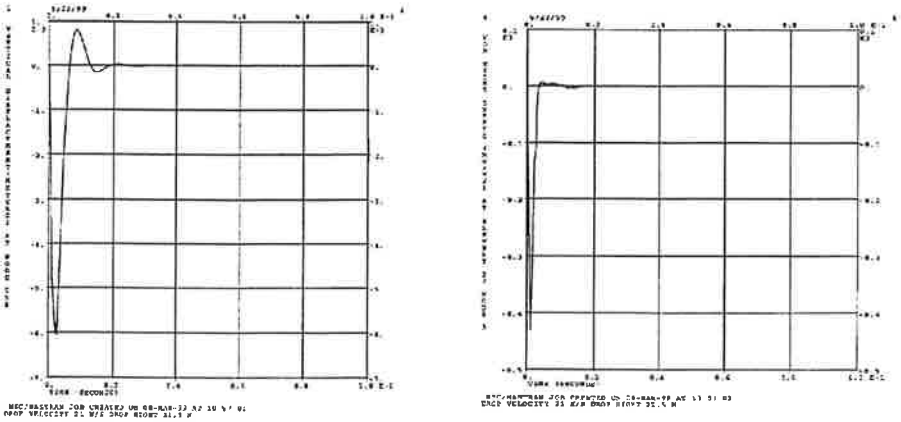

Figure 5 Displacement time history of node 258 calculated from nonlinear transient response of 9m drop on hard ground and von Mises stress time history of the edge node point of element 7 at lower wdge of the cask calculated by nonlinear transient response method from 9m drop on hard ground.

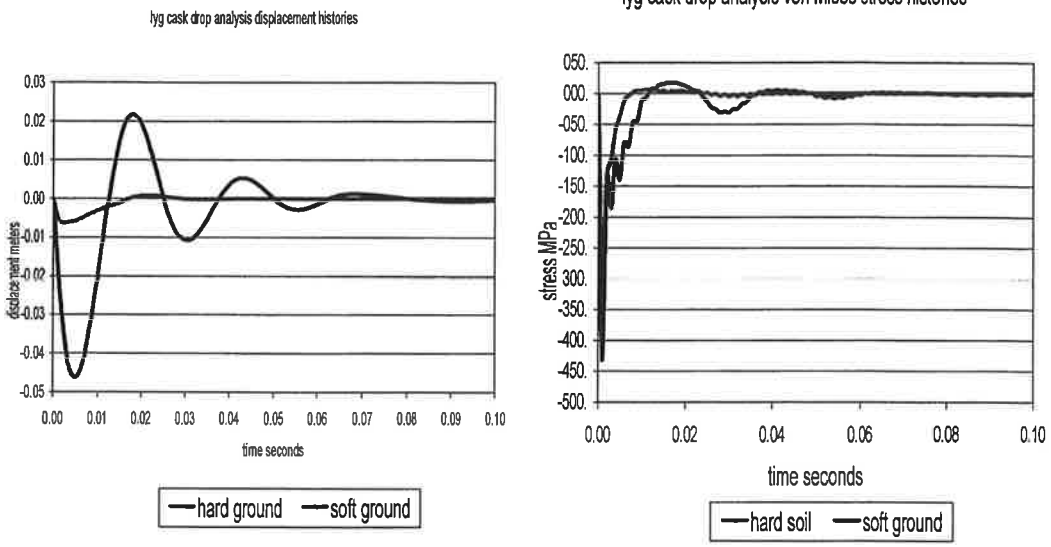

Figure 6 Comparison of vertical displacement histories of node 258 in soft and hard ground drops and comparison of von Mises stress time histories of the edge node point of element 7 at lower edge of the cask drop on soft and hard grounds calculated by the nonlinear transient response method

7. CONCLUSION

Based on the analyses performed above and on the results depicted in Figures 3, 4, 5 and 6 the following concluding remarks can be made. Displacements obtained for vertical drop on soft soil cushion were the same order of magnitude for both linear and nonlinear analysis. It can be expected that for skew drop on soft soil for instance in 30 degrees axis angle with the vertical produces displacements that are twice as large as for straight drop and could be about 10 cm. As for the equivalent von Mises stress it can be seen for from the Figure 4 that the stress at the edge point for vertical drop on soft soil exceeds the yield stress for extremely short time less than one millisecond. In case of skew drop on soft soil it could be expected that the yielding will last longer, say, the length of the compression phase of the first period or about 10 milliseconds. Even in this case the yield will be localised to the impacting edge zone and could be expected to occur within a radius of few centimeters from the impacting tangent point. The highly local nature of the yield will ensure that tightness of the cask is preserved for the case under consideration. The above discussion is confirmed by the comparison on displacement and von Mises stress time histories for drops from 26 m on soft soil cushion and from 9 m on hard ground. The displacement in hard ground case in Figure 6 are only a fraction of displacements in soft soil case and the peak von Mises stress is about 1.5 times as large as in soft soil case. So it can be concluded that the 9 m validation drop on hard soil ensures also the integrity of the for 26 m drop on soft soil cushion.

8. RFERENCES

[1] MSC/NASTRAN User's manual, McNeal-Schwendler Corp., Los Angeles,1998.

Structural Topology Optimization with Design Dependent Loads

Velaja B. Hammer and Niels Olhoff
Institute of Mechanical Engineering
Aalborg University, DK-9220 Aalborg Øst, Denmark

Abstract

This paper presents a generalization of topology optimization of linearly elastic continuum structures to problems involving loadings that depend on the design. Minimum compliance is chosen as the design objective, assuming the boundary conditions and the total volume within the admissible design domain to be given, and the topology optimization is based on the usage of a SIMP material model.

The type of loading considered in this paper occurs if free structural surface domains are subjected to e.g., static pressure or fluid flow loading, in which cases both the direction and location of the loading change with the structural design.

The presentation of the material is mainly given in a 2D context, but extension to 3D is straight-forward. An illustrative example is provided in the end of the paper.

1. Introduction

The field of structural topology optimization has developed extensively in the last two decades and has succesfully addressed a variety of problems within a wide range of applications, see e.g. Bendsøe (1995), Olhoff and Rozvany (1995), or Gutkowski and Mróz (1997). However, although being very common, the class of problems where applied surface loads on a continuum structure depend on the design of the structure itself, has yet to be solved.

The structural topology will be optimized with respect to minimum compliance subject to a constraint on the total structural volume using a SIMP material model, whose volume density parameter in each finite element play the role of design variable. The analysis model for the optimization problem is based on a fixed mesh, and the problem is solved by a numerical procedure of successive iterations.

For the problem under study, the principal extensions relative to the usual topology design methodology comprise a much more involved design sensitivity analysis based on an enhanced design model that encounters one or more parameterized, smooth surface domains associated with a prescribed iso-volumetric density of material. These surface domains serve to define the action of the design dependent loading on the structure, and are determined by the design variables, i.e., the distribution of the volumetric densities of material in the finite elements of the analysis model.

A more detailed account of the present problem is available in Hammer and Olhoff, (1999).

2. Formulation of the optimization problem

The optimization problem consists in minimizing the compliance of the structure subject to a constraint on the volume V

$$\min_{\rho(x),x\in\Omega} W(u^\star)$$
$$\text{s.t.} \quad V(\rho(x)) = \int_\Omega \rho d\Omega \leq V^\star \tag{1}$$

Here, x denotes the coordinates of any point belonging to the admissible design domain Ω in 2D or 3D, and $W(u^\star)$ is the compliance given by the displacement field $u^\star$ at equilibrium. W is then the work done by the external forces, which equals twice the total elastic energy at equilibrium. The design variables are the volume densities of material, $0 < \rho(x) \leq 1$, which we consider to be constant within each finite element, and to enhance black and white (1-0) solutions, a SIMP material model (Simple Isotropic Material with Penalization), Bendsøe (1989) is used

$$[E(x)] = \rho(x)^n [E^\star] \tag{2}$$

Here $[E]$ is the elasticity matrix of the SIMP material and n is a penalization power, $1 \leq n \leq 4$, which is increased gradually during the optimization process. $[E^\star]$ denotes the elasticity matrix of the solid, isotropic material for the structure.

3. The design model with the surface representation

As is common, the finite element mesh of the analysis model of the structure is kept unchanged throughout the optimization process. This however leads to jagged and edged designs and thus a need for a design model describing where and how the pressure acts in the current iteration. Such a smooth surface representation is primarily needed in the domains where the surface loading acts. This is extracted from the density distribution in a way following to a large extent the work of Maute & Ramm, (1994), (1995).
First the volume density of material is calculated in every corner-node as the average of the densities of all the elements that share the corner node. Next a set of points of volume densities equal to a preselected value for a surface of iso-volumetric density is found by interpolation from the corner node values. A set of Bezier cubic splines are used to fit these points by solving the least square problem of minimizing the distance between the data points and the corresponding points on the splines. The number of Bezier curves used is gradually increased from one until a predefined measure of the fit to the data points is obtained. Figure 1 illustrates for a 2D problem the procedure described above to find a curve (surface in 3D) of a given iso-volumetric density.

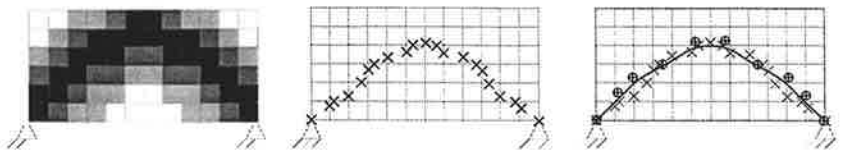

A B C

Figure 1: A: A 2D design with non-uniform density distribution. B: Points of equal density. C: Fit with set of Bezier curves and their control points.

The loading is applied to sub-domains of the surface of the structure. In order to keep track of these domains during the optimization process, their end points (in 2D) or end curves (in 3D) are defined *á priori*. In 2D either as fixed points (for instance associated with a nodal boundary condition), or as points allowed to vary according to the density distribution but only along some predefined curves. The pressure loading is then distributed to the surface or contour curve located between these end points or curves.
The load is then related to the finite element analysis model as sketched in figure 2. All the

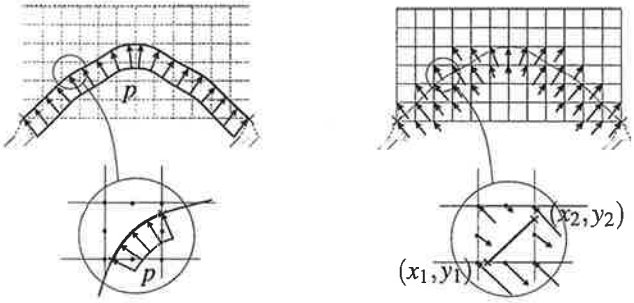

Figure 2: To the left the design model for the pressure loading. The consistent nodal loads on the finite element analysis model are shown to the right.

finite elements cut through by the curve for load application carry a part of the loading. The curve is approximated by a straight line in each finite element determined by its two points on the element boundary. In the analysis model, the load on an element is distributed to all the nodes of the element in the vector of consistent nodal forces. This way of distributing the load is advantageous in that the pressure is sort of spread over several nodes. Hereby the problem that loads may jump past nodes is less severe than if the loads were applied to, e.g., a single row of nodes.

4. The successive optimization scheme

The optimization process is performed by successive iterations making use of the finite element analysis model with fixed mesh on the one hand, and the design model with the parameterized iso-volumetric density surface (3D) or curve (2D) for the pressure loading on the other. The optimization performance can be tuned by optimizing the structure for fixed loading a couple of iterations before moving the pressure. As explained above the load curves in the design model are controlled by the density distribution in the finite element model and in turn fully determine the global load vector on the finite element model. Thus the sensitivity analysis is based on both the analysis and the design model. In the sensitivity analysis also the sensitivities of the load vector with respect to a design change must be evaluated. This is done by partial differentiation determining in turn the effect of a density variation on the points of fixed density, on the control points of the Bezier curves, and finally how this affects the nodal loads on the finite element model. All parts of the sensitivity analysis are determined analytically under the provision that the density variation is considered so small that the contour curve will stay within the same set of finite elements.

5. Numerical example

The method developed in this paper is illustrated by the optimization of the short cover-like structure shown in figure 3. The finite element analysis model consists of 2440 elements with one design variable per element. The structure is clamped in both lower endpoints and is subjected to a constant pressure loading from below. The curve for load application is kept fixed during the first few iterations whereupon the pressure is restricted to act on the curve of isovolumetric density, $\rho = 0.6$. As this curve varies from one iteration to another, so does the loading. A simple fixed-point type of optimality criteria algorithm, Cheng and Olhoff (1982), is used to determine the density distribution that yields minimum compliance, resulting in the quite distinct black ($\rho = 1$) and white ($\rho = 0$) design shown in figure 3.

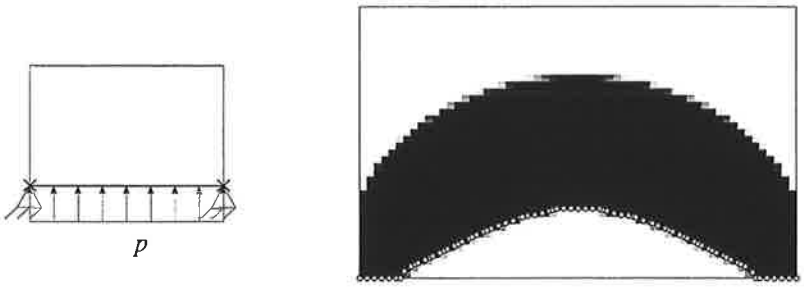

Figure 3: The design model with the initial pressure distribution from below and the optimized topology. The black domain corresponds to $\rho = 1$. The white dots mark the curve for load application.

References

Bendsøe, M. P.: 1989, Optimal shape design as a material distribution problem, *Structural Optimization* **1**, 193–202.

Bendsøe, M. P.: 1995, *Optimization of Structural Topology, Shape, and Material*, Springer-Verlag, Berlin, Germany.

Cheng, K.-T. and Olhoff, N.: 1982, Regularized formulation for optimal design of axisymmetric plates, *Int. J. Solids Structures* **18**(2), 153–169.

Gutkowski, W. and Mróz, Z. (eds): 1997, *Structural and Multidisciplinary Optimization*, WCSMO-2, Institute of Fundamental Technological Research, Warsaw, Poland, Zakopane, Poland.

Hammer, V. B. and Olhoff, N.: 1999, Topology optimization of continuum structures subjected to pressure loading, *Structural Optimization, (submitted)* .

Maute, K. and Ramm, E.: 1994, Adaptive techniques in topology optimization, *Proceedings of the 5th AIAA/USAF/NASA/ISSMO Symposium on Multidisciplinary Analysis and Optimization*, Panama City, Florida, pp. 121–131.

Maute, K. and Ramm, E.: 1995, Adaptive topology optimization, *Structural Optimization* **10**, 100–112.

Olhoff, N. and Rozvany, G. (eds): 1995, *Structural and Multidisciplinary Optimization*, WCSMO-1, Pergamon, Oxford, UK, Goslar, Germany.

Topology Optimization of Backplates with prestress: Application for Microphones

Niels L. Pedersen
Department of Solid Mechanics,
Technical University of Denmark, building 404, DK–2800 Lyngby, Denmark.

1. Introduction

Topology optimization is used to optimize the performance of a backplate used in a hearing aid. For reference on topology optimization see Bendsøe (1995) and references herein. The hearing aid is a rather big MicroElectroMechanical Systems (MEMS); with size of $2\ mm \times 2\ mm$ as indicated in figure 1. The principle of the hearing aid is that a pressure wave will deflect the diaphragm, see figure 1, leading to a capacitive change between the backplate and the diaphragm. To maximize this change in capacitance it is vital that there are holes in the backplate to let the pressure through, on the other hand the backplate should be as stiff as possible. In order to increase the stiffness of the backplate it is chosen to use prestressing.

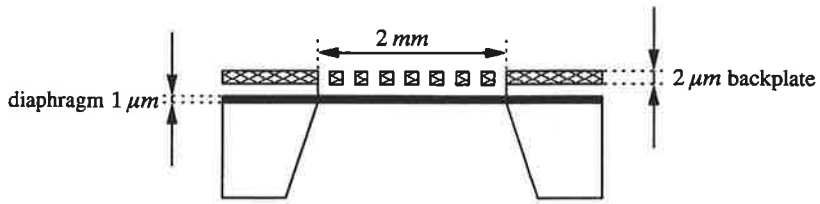

Figure 1. Schematic side view of hearing aid. The black part is the diaphragm while the crosshatch part is the backplate. There is air between the two parts.

The design of a presently used backplate can be seen in figure 2(a) and the design domain can be seen in figure 2(b). The center part of the backplate is dense with small holes but we may calculate a set of material data using e.g. the Hashin–Shtrikman bounds and then treat the center part as being solid with the new material data. The idea is now that we may use the same material to connect the center to the bounderies. This leads to a standard topology optimization formulation where material can be distributed in the white area of figure 2(b) while the center part is fixed.

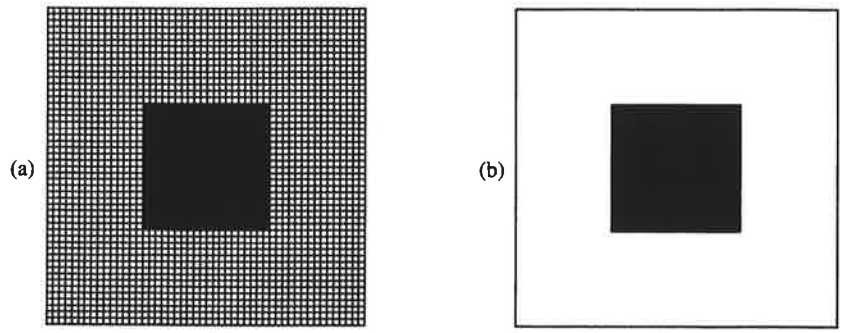

Figure 2. (a) Conventional design of backplate, the black center part is dense with very small holes (no visible), while the rest of the structure have bigger holes. (b) Design task: fill the white area with material in an optimal way.

2. Sensitivities

In the present paper it will be shown how the backplate can be optimized with respect to two objectives; minimization of compliance (minimum elastic energy) or maximization of the first eigenfrequency. Optimization of eigenfrequencies using topology optimization implies a number of difficulties which will not be discussed here, see Pedersen (1999). In order to perform the optimization we need the sensitivities. Because of the prestressing of the plate the derivation of the sensitivities of the objectives will be given. The prestressing of the plates results in an initial stress stiffness matrix $[K_\sigma]$ that can be found in e.g. Cook (1989). Including this matrix, the force displacement relation of the structure is given by

$$\{F\} = ([K] + [K_\sigma])\{D\} \tag{1}$$

where $\{F\}$ is the force, $[K]$ is the stiffness matrix and $\{D\}$ is the displacement. The compliance U is here defined as two times the elastic energy

$$U = \{D\}^T([K] + [K_\sigma])\{D\} \tag{2}$$

Taking the derivative of (1) and (2) with respect to the design parameter h yields

$$\frac{dU}{dh} = 2\{D\}^T([K] + [K_\sigma])\frac{d\{D\}}{dh} + \{D\}^T(\frac{d[K]}{dh} + \frac{d[K_\sigma]}{dh})\{D\} \tag{3}$$

$$\frac{d\{F\}}{dh} = (\frac{d[K]}{dh} + \frac{d[K_\sigma]}{dh})\{D\} + ([K] + [K_\sigma])\frac{d\{D\}}{dh} \tag{4}$$

Expression (3) includes the derivative of the displacement. These are removed by substituting (4) into (3)

$$\frac{dU}{dh} = -\{D\}^T\frac{d[K]}{dh}\{D\} - \{D\}^T\frac{d[K_\sigma]}{dh}\{D\} + 2\{D\}^T\frac{d\{F\}}{dh} \tag{5}$$

The first term in (5) is the standard expression for the derivative of the compliance. In topology optimization the design parameters are defined on element level and the first term may therefore be described on element level. The last term in (5) can be simplified by using that the force is given by

$$\{F\} = \{F_{ex}\} + \{F_\sigma\} \tag{6}$$

The derivative of the external force $\{F_{ex}\}$ with respect to the design parameters is zero, and the derivative of the force coming from the prestress, $\{F_\sigma\}$, can be given on element level. The second term in (5) gives rise to greater computational cost because the derivative of the initial stress stiffness matrix cannot be handled on element level. However in the examples in section 3 the prestress level is so high that the sensitivity of the compliance is totally controlled by the last term in (5). It is therefore chosen for the problem of compliance minimization to neglected the second term and this lowers the computational cost.

In order to find the sensitivity of the eigenfrequency we first define the double of the specific kinetic energy

$$T = \{D\}^T[M]\{D\} \tag{7}$$

With this definition the eigenvalue problem is given by

$$U - \omega^2 T = 0 \tag{8}$$

Taking the derivative with respect to a design parameter yields

$$\frac{d\omega^2}{dh} = 2\{D\}^T([K] + [K_\sigma] - \omega^2[M])\frac{d\{D\}}{dh} + \{D\}^T(\frac{d[K]}{dh} + \frac{d[K_\sigma]}{dh} - \omega^2\frac{d[M]}{dh})\{D\} \tag{9}$$

Using (8), the first term is zero leading to the final expression for the sensitivity

$$\frac{d\omega^2}{dh} = \{D\}^T\frac{d[K]}{dh}\{D\} - \omega^2\{D\}^T\frac{d[M]}{dh}\{D\} + \{D\}^T\frac{d[K_\sigma]}{dh}\{D\} \tag{10}$$

The first two terms constitute the standard expression for the sensitivity of the eigenfrequency and they may be evaluated on element level. The last term is the same term as was encountered in (5) but in this case this term can not be neglected. The initial stress stiffness matrix is given by

$$[K_\sigma] = \sum_{e=1}^{elements} [k_\sigma]_e \qquad [k_\sigma]_e = \int [G]^T [S][G] dV \tag{11}$$

The matrix $[G]$ is made from derivatives of the shape functions which are independent of h while the matrix $[S]$ contains the initial stress of the element, see Cook (1989). Taking the derivative with respect to design parameter h gives

$$\frac{d[k_\sigma]_e}{dh} = \int [G]^T \frac{d[S]}{dh} [G] dV \tag{12}$$

To find the derivative of matrix $[S]$ we need the derivative of the initial stress in the element. The stress is defined by

$$\{\sigma\} = [E](\{\epsilon\} - \{\epsilon_0\}) \tag{13}$$

here $[E]$ is the constitutive matrix, $\{\epsilon\}$ the strain and $\{\epsilon_0\}$ the initial strain. Taking the derivative of (13) gives

$$\frac{d\{\sigma\}}{dh} = \frac{d[E]}{dh}(\{\epsilon\} - \{\epsilon_0\}) + [E]\frac{d\{\epsilon\}}{dh} \tag{14}$$

The first term may be evaluated directly from the definition of the constitutive matrix used in topology optimization. To find the second term we need the finite element definition of the strain.

$$\{\epsilon\} = [B]\{D_\sigma\} \qquad \frac{d\{\epsilon\}}{dh} = [B]\frac{d\{D_\sigma\}}{dh} \tag{15}$$

where $[B]$ is the standard matrix in finite element that relates the displacement of the element to the strain of the element, $\{D_\sigma\}$ is the displacement coming only from the prestress. Using the force displacement equilibrium for the prestress

$$\{F_\sigma\} = [K]\{D_\sigma\} \tag{16}$$

we may find the derivative of the displacement.

$$[K]\frac{d\{D_\sigma\}}{dh} = \frac{d\{F_\sigma\}}{dh} - \frac{d[K]}{dh}\{D_\sigma\} \tag{17}$$

Although the stiffness matrix has already been inverted we need to solve (17) for each design parameter.

3. Examples

The power law approach with filtering technics is used in the topology optimization. For further details the reader is referred to the vast number of papers on topology optimization. Because of symmetry only one quarter of the structure is used in the optimization and it is discretizised into 40×40 elements. The dimensions of the backplate is given in figure 1 and the design domain is given in figure 2(b). The total allowed material is 25%. The material data and the prestress level is

$$E = 180{\cdot}10^9\ N/m^2 \qquad \nu = 0.06 \qquad \hat{\rho} = 2300\ kg/m^3$$

$$\sigma_{11} = 3.0\ 10^8\ N/m^2 \qquad \sigma_{22} = 3.0\ 10^8\ N/m^2$$

The first example is compliance optimization, the external force used is a force in the center. The result of the optimization is shown in figure 3. With no prestress we get the design shown in figure 3(a) and with prestress we get the design shown in figure 3(b). The second example is the maximization of the first eigenfrequency of the backplate, the result is given in figure 4. In the opti-

mized result shown in figure 4(b) only 20 × 20 elements were used.

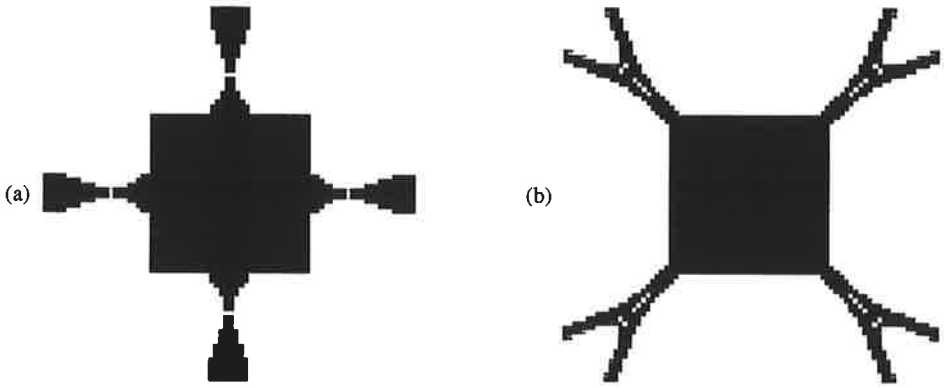

Figure 3. Optimized designs when optimized for compliance, (a) without prestress, (b) with prestress.

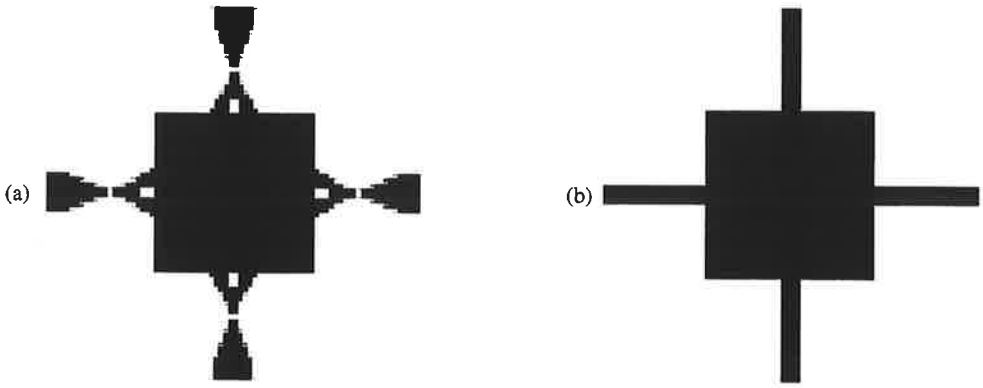

Figure 4. Optimized designs when optimized for maximum first eigenfrequency, (a) without prestress, (b) with prestress.

4. Conclusion

The examples shows that the prestressing of the plate has a big impact on the results of the optimization, and it is therefore important to include this in the formulation.

Acknowledgments

This work was supported by the Danish Technical Research Council through the THOR–programme (Technology for Highly Oriented Research): "Systematic design of MEMS". The support is highly appreciated.

References

Bendsøe, M. P. (1995) "Optimization of Structural Topology, Shape and Material". Springer

Cook, R. D., Malkus, D. S., Plesha, M. E. (1989) "Concepts and Applications of Finite Element Analysis". John Wiley & Sons, Inc.

Pedersen, N. L. (1999) "Maximization of Eigenvalues using Topology Optimization" (submitted)

TOPOLOGY OPTIMIZATION OF RESONATING ACTUATORS

Dmitri Tcherniak

Department of Solid Mechanics, Technical University of Denmark, DK-2800 Lyngby, Denmark

INTRODUCTION

Dynamic MicroElectroMechanical Systems (MEMS) are relatively new breed of mechanical devices in which forces induced by electricity are intended to be a source of vibrations. These excitation forces (or displacements) usually have electro-static or electro-thermal nature, and hence they are relatively small even in the micro-world scales. To provoke large-magnitude stable periodic displacements of MEMS parts, it is reasonable to utilize the resonance phenomenon.

The paper concerns the application of the topology optimization method to design of dynamic MEMS. Since the introduction of the method [1], it has gained widespread popularity in academia and is now being applied to many complex structural design problems. For example, topology optimization is a powerful tool for designing of micro-structures, e.g. designing of compliant mechanisms [2], non-linear mechanisms [3], thermo-electro actuators [4]. There have been attempts to apply the method to dynamical problems, eg. [5,6], where so-called multi-objective optimization method has been used. In the presented paper, another approach is considered.

PROBLEM FORMULATION AND ASSUMPTIONS

The problem of design of real resonant actuators is very complicated. Indeed, to design electro-thermo actuator, one has to solve the problems of distribution of potentials, temperature and mechanical deformations [4], which all vary in time. That is why in the initial stages of the investigation, the problem was significantly simplified: the excitation was considered to be a given point-force which varies harmonically in time.

The problem formulation is shown in Figure 1a. The design domain D is supported in the area Γ and subjected to the force $\mathbf{P}(t) = \mathbf{P}_0 \sin \Omega t$ with frequency Ω. Our goal is to maximize the magnitude of the dynamic response of the given point R in the specified direction $\mathbf{A}$.

Considering a linear dynamic problem, the dynamic response $\mathbf{X}(t)$ is defined by the solution to a differential equation of motion, which can be written in matrix notation as:

$$\mathbf{M}\ddot{\mathbf{X}} + \mathbf{C}\dot{\mathbf{X}} + \mathbf{K}\mathbf{X} = \mathbf{P}(t), \tag{1}$$

where $\mathbf{M}$, $\mathbf{C}$, $\mathbf{K}$ are mass, damping and stiffness matrices of the considered system, respectivly. Another assumption, that the stiffness matrix does not depend on stresses ($\mathbf{K}_\sigma = \mathbf{0}$), is already employed in (1). Since the formulation is linear, let us consider the excitation by a unit force: $|\mathbf{P}_0| = 1$.

The displacement of the input port, where the force is applied, is $\Delta_{in}(t) = k\,\mathbf{P}_0^{\mathrm{T}}\,\mathbf{X}(t)$, k is dimension coefficient. Similarly, the displacement of the output port is $\Delta_{out}(t) = k\,\mathbf{A}^{\mathrm{T}}\,\mathbf{X}(t)$, $|\mathbf{A}| = 1$. The ratio

$$GA_{dyn} = \Delta^A_{out} / \Delta^A_{in} \tag{2}$$

a) b)

Figure 1. a) Problem formulation. b) The second load case

can be called the *dynamic geometrical advantage* of the resonator and can serve as a convenient characteristic of its quality. The superscript A in Equation (2) denotes amplitude values of the corresponding time-periodic functions.

In the presented paper, the objective is formulated as maximizing GA_{dyn}. To prevent Δ_{in}^{A} from vanishing, one has to impose the constraint $\Delta_{in}^{A} \geq \Delta_{in}^{*}$, which has a simple physical meaning – the value of the real force must be finite to cause the displacement Δ_{in}^{*}. The estimation of the Δ_{in}^{*} value can be based on the actual design of the force generator.

Obviously, very compliant structures will demonstrate large dynamic deflections even for small excitations. Thus one has to prevent the stiffness of the structure to vanish. The obvious way is to impose the constraint $\lambda_1 = \Omega^2$ on the first natural frequency of the system. Another way, used in this paper, is to bound static deflection of the structure: the second load case which is shown on Figure 1b is considered. The structure is subjected to the unit *static* force $\mathbf{A}$ applied at the output port, the corresponding deflection of the output port is: $\Delta_{out2} = k\,\mathbf{A}^{\mathrm{T}}\mathbf{U}_2$, where $\mathbf{U}_2$ is defined by the solution of the equilibrium equation $\mathbf{K}_2\mathbf{U}_2 = \mathbf{A}$. Then the constraint $\Delta_{out2} \leq \Delta_{out2}^{*}$ controls the static stiffness (and, hence static behaviour) of the structure.

Summarizing the above-mentioned considerations, the optimization problem is written as

Maximize	:	Dynamic geometrical advantage GA_{dyn}
Subject to	:	Solution equation of motion (1)
and	:	volume constraint $V \leq V^*$
and	:	input displacement $\Delta_{in}^{A} \geq \Delta_{in}^{*}$
and	:	static stiffness: $\Delta_{out2} \leq \Delta_{out2}^{*}$,

where V^* is the allowed volume of the structure. Various other constraints may be imposed to adjust the design to specific requirements.

SOLUTION FOR THE EQUATION OF MOTION (1)

The approximated solution to Equation (1) is sought by means of the *mode acceleration method* (eg. Cook, 1989), where the exact solution is expressed as a quasistatic response $\mathbf{U}$, $\mathbf{KU} = \mathbf{P}_0$, plus some dynamic correction which accounts for inertia and viscous effects. The correction is an expansion on eigenmodes, and only the first m ($m << N$) eigenmodes are usually retained to get an approximate solution. Assuming that the *first mode resonance* occurred, one has to set the excitation frequency $\Omega = \sqrt{\lambda_1}$, and only the first term of the expansion can be kept. Then the approximation of the response

can be expressed in the following way:

$$\mathbf{X}(t) \approx \left(\mathbf{U} - \frac{\phi_1^T \mathbf{P}_0}{\Omega^2} \phi_1 \right) \sin(\Omega t) - \frac{\phi_1^T \mathbf{P}_0}{\Omega \phi_1^T \mathbf{C} \phi_1} \phi_1 \cos(\Omega t), \tag{3}$$

where ϕ_1, λ_1 are the first **M**-normalized eigenvector and eigenvalue for the generalized eigenproblem $(\mathbf{K} - \lambda_i \mathbf{M})\, \phi_i = \mathbf{0}$, $i = 1..N$, and damping is assumed to be small and proportional.

TOPOLOGY OPTIMIZATION PROCEDURES

Following the standard topology optimization scheme, the design domain is discretized by N bilinear finite elements. For modelling material properties, the power-law approach method is used: the Young's modulus in the element e is $E^e = (\rho^e)^\eta E^0$, where ρ^e is the density of the element e, and η is a penalization factor. Based on experience and theoretical predictions [7], η was chosen equal to 3.

A variety of standard and non-standard numerical methods were used in the procedure: The eigenvectors and eigenvalues for lowest modes were computed by subspace iterations. To prevent the appearance of local modes, the scheme suggested in [8], was used. The sensitivities of the eigenvector and eigenvalue were calculated by Nelson's method; the sensitivity of static responses, which appears in Equation (3) and in one of the constraints, was computed by the adjoint method. To prevent checkerboard generation, a filtering technique [9] was used. Finally, the Method of Moving Asymptotes served as the optimization algorithm.

EXAMPLES

The two examples shown on Figure 2, present resonant actuators optimized to maximize vertical (a) and horizontal response (b) due to excitation in the vertical direction. Two additional constraints were imposed: the first restricted the motion in the direction perpendicular to the desirable. The second constraint, imposed as $GA_{dyn}/GA_{stat} > Q^*$, controls the resonance magnification factor.

Both designs contain a lot of elements with intermediate density ("grey" elements). The author can not list the obvious reasons explaining this. Apparently, the rough resolution (26×14 finite elements in the presented example) could be the reason. However, finer resolution does not always converge to pure black-and-white design. Another possible reason is that stiffness penalization is not an efficient mechanism for "grey" elements elimination in the considered case.

CONCLUSION AND FURTHER RESEARCH

The paper is addressed to the application of the topology optimization method to the design problem of resonating actuators. A formulation for an optimization problem is proposed, the ways of solution are suggested.

Obviously, the problem is far from the final solution. Other problem formulations will probably lead to better results. It seems that alternative modelling of material properties, especially modelling of internal damping, can be very effective in the case of dynamic structures.

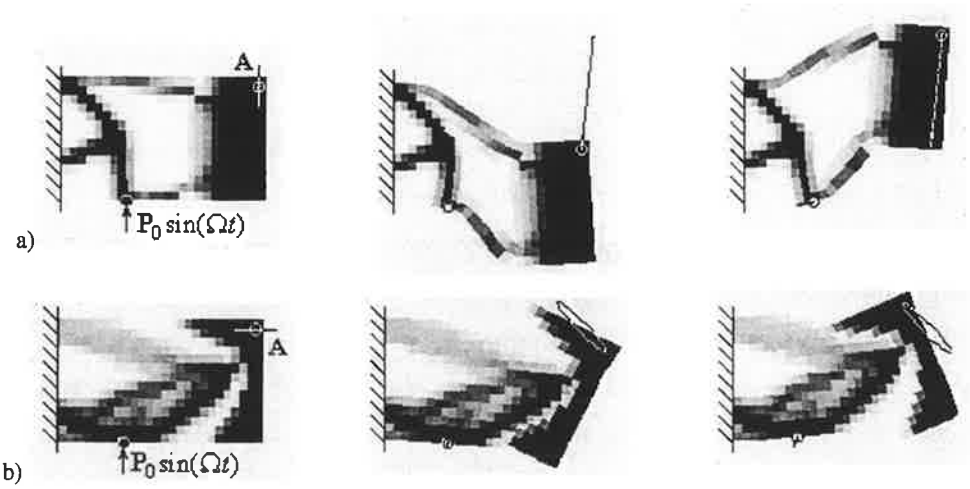

Figure 2. Optimal resonator topologies (left column) and extreme positions of their resonant motion (middle and right columns). a) Optimized for vertical response; b) for horizontal response.

Referring to the efficiency of the algorithm, it is important to notice that its bottleneck lies in the computing of eigenvector sensitivities. Hence, using alternative ways of the response representation, which is not based on eigenvectors (for example, Ritz vector superposition), the efficiency may be significantly improved.

REFERENCES

1. Bendsøe, M. P. and Kikuchi, N. (1988), Generating optimal topologies in optimal design using a homogenization method, *Computational Methods in Applied Mechanics and Engineering*, 71, pp. 197–224.

2. Larsen, U. D., Sigmund, O., Bouwstra, S. (1997), Design and fabrication of compliant mechanisms and material structures with negative Poisson's ratio, *Journal of Microelectromechanical Systems*, 6(2), pp. 99–106.

3. Buhl, T. , Pedersen , C. B. W., Sigmund O. (1999), Topology synthesis of large-displacement compliant mechanisms, 1999, Submitted.

4. Sigmund, O. (1998), Systematic design of electrothermomechanical microactuators using topology optimization. *In Modelling and Simulation of Microsystems, Semiconductors, Sensors and Actuators*, pp. 350-355, Santa Clara, California, MSM98.

5. Min, S., Kikuchi, N., Park, Y.C., Kim, S., Chang, S. (1999), Optimal topology design of structures under dynamic loads. *Structural Optimization*, 17, pp. 208-218.

6. Nishiwaki, S., Silva, E.C.N., Saitou, K., Kikuchi, N. (1999), Topology optimization of actuators using structural flexibility.

7. Bendsøe, M. P. and Sigmund, O. (1999), Material interpolation schemes in topology optimization», *Archieve of Applied Mechanics*, 69, (to appear).

8. Pedersen, N.L. (1999), Maximization of eigenvalues using topology optimization, *Structural Optimization*, (to appear).

9. Sigmund, O. (1994), *Design of Material Structures using Topology Optimization*. Ph.D. Thesis, Dept. Solid Mechanics, DTU, DCAMM special report S 69, Danish Center for Applied Mathematics and Mechanics.

ON PATCH RECOVERY METHODS AND UNBOUNDED DOMAINS

Jukka M. Aalto
Laboratory of Structural Mechanics
Helsinki University of Technology, P.O.Box 2100, 02015 HUT, FINLAND
e-mail: jukka.aalto@hut.fi

Introduction

The paper introduces a special technique of dealing patch recovery methods in connection with unbounded domains. This technique is based on (a) infinite strips of mapped elements called *"infinite element strips"* [1,2], which are used to connect the standard finite element grid to infinite boundaries of the domain in standard finite element analysis, (b) special polar coordinates for representing local polynomials, which are used in the mapped area of the grid in the patch recovery process, and (c) special way of representing the final, C^0-continuous, smoothed derivatives in the mapped finite elements. The paper presents in detail, how this technique is applied to the so called superconvergent patch recovery (SPR) method [3] and to a patch recovery method [4,5], which uses local polynomials containing information from the field equations *"built-in"*, (BUI). An infinite plate with a hole under unidirectional tension is studied as a numerical example. Experimental convergence studies and a comparison of the SPR- and BUI-methods is given.

Infinite element strips

Geometrical mapping of an infinte element strip [1] is defined by

$$\mathbf{r}(\rho,\sigma) = \frac{1}{1-\rho}[-\rho\check{\mathbf{r}}(\sigma) + \bar{\mathbf{r}}(\sigma)], \tag{1}$$

where ρ and σ are *"strip coordinates"*, $\check{\mathbf{r}}(\sigma)$ and $\bar{\mathbf{r}}(\sigma)$ are position vectors of *"pole line"* and *"interface line"* (between mapped and standard finite elements), respectively, which are defined using parametric line elements by

$$\check{\mathbf{r}}(\sigma) = \sum N_i(\sigma)\check{\mathbf{r}}_i, \quad \bar{\mathbf{r}}(\sigma) = \sum N_i(\sigma)\bar{\mathbf{r}}_i. \tag{2}$$

Natural coordinates ξ and η of an element in an infinite element strip and the strip coordinates are assumed to be linearly related so [1], that for a quadrilateral element we have

$$\rho = \frac{1}{2}(\rho_1^e + \rho_2^e) + \frac{1}{2}(\rho_2^e - \rho_1^e)\xi, \quad \sigma = \eta, \tag{3a}$$

where strip coordinates ρ_i^e $(i = 1,2)$ correspond to two opposite sides of the quadrilateral, and for a triangular element we have

$$\rho = \rho_3^e + (\rho_1^e - \rho_3^e)\xi + (\rho_2^e - \rho_3^e)\eta, \quad \sigma = \sigma_3^e + (\sigma_1^e - \sigma_3^e)\xi + (\sigma_2^e - \sigma_3^e)\eta, \tag{3b}$$

where strip coordinates ρ_i^e and σ_i^e $(i = 1,3)$ correspond to corners of the triangle. Successive equations (1) to (3) define the geometrical mapping of an element in an infinite element strip.

Special polar coordinates for patch polynomials

Special polar coordinates ϱ and ϑ are defined in terms of standard polar coordinates r and θ (pole at point P) by

$$\varrho = 1 - \frac{R}{r} \quad \vartheta = \theta, \tag{4}$$

where R is characteristic radius. In the original BUI-method (see Refs. [4,5]) patchwise representation of the basic unknown $\mathbf{u}$, which contains information from the field equations, is expressed

as a polynomial of x and y, ie. $\tilde{\mathbf{u}}(x,y)$. Here in patches, whose patch assembly point is connected to mapped elements, it is expressed as a polynomial of ϱ and ϑ ie. $\tilde{\mathbf{u}}(\varrho,\vartheta)$. In the original SPR- and BUI-methods local representation of the derivative quantities $\boldsymbol{\gamma}$ is expressed as a polynomial of x and y, ie. $\tilde{\boldsymbol{\gamma}}(x,y)$. Here in patches, whose patch assembly point is connected to mapped elements, it is expressed as

$$\tilde{\boldsymbol{\gamma}}(\varrho,\vartheta) = (1-\varrho)\tilde{\boldsymbol{\Gamma}}(\varrho,\vartheta), \tag{5}$$

where $\tilde{\boldsymbol{\Gamma}}(\varrho,\vartheta)$ is polynomial of ϱ and ϑ.

Representing final, smoothed derivatives

In the original SPR- and BUI-methods the final smoothed approximation of the derivative quantities $\boldsymbol{\gamma}$ is expressed as C^0-continuous finite element approximation ie. $\boldsymbol{\gamma}^*(\xi,\eta)$. Here in mapped elements it is expressed as

$$\boldsymbol{\gamma}^*(\xi,\eta) = [1-\rho(\xi,\eta)]\boldsymbol{\Gamma}^*(\xi,\eta), \tag{6}$$

where $\boldsymbol{\Gamma}^*(\xi,\eta)$ is C^0-continuous finite element approximation.

On the interface line, where $\rho = 0$ (see equation (1)), equation (6) gives $\boldsymbol{\gamma}^* = \boldsymbol{\Gamma}^*$. Thus the elsewhere continuous finite element representation of the smoothed derivatives is also continuous across the interface line.

Numerical example

Consider an infinite plate with a circular hole of radius a. The state of stress far ($r \to \infty$) from the hole is assumed to be $\sigma_x = \sigma_\infty$, $\sigma_y = 0$ and $\tau_{xy} = 0$. The displacements u and v will be infinite on the infinite boundaries of the domain and the corresponding nodal values should be infinite too. Thus u and v cannot be used as unknowns in the numerical analysis. We will take the displacement differences $u' = u - u_0$ and $v' = v - v_0$, where $u_0 = \sigma_\infty x/E$ and $v_0 = -\nu\sigma_\infty y/E$ are the displacements corresponding to uniform state of stress ($\sigma_x = \sigma_\infty$, $\sigma_y = 0$ and $\tau_{xy} = 0$), as new unknowns of the problem. They are finite and have the values $u' = 0$ and $v' = 0$ on the infinite boundaries.

Fig. 1 presents a typical grid ($h/a = 0.25$) of quadratic Serendip elements used in the analysis. Here all the nodal points of the pole line and the pole of special polar coordinates (4) are located at the center P of the hole. The interface line is broken line ABC. In order to show the whole (infinite) grid in this figure modified geometrical mapping

$$\mathbf{r}(\rho,\sigma) = \frac{1}{1-0.8\rho}[-0.8\rho\check{\mathbf{r}}(\sigma) + \bar{\mathbf{r}}(\sigma)], \tag{7}$$

which reduces the lenghts of the strips from infinite to finite, has been used instead of original mapping (1) in the plotting program. Four uniformly refined grids with $h/a = 0.5$, 0.25, 0.125 and 0.0625 were constructed for experimental convergence study.

Table 1 shows percent error in energy of the original finite element solution (FE) and the recovered solutions obtained using SPR- and BUI-methods. Approximate rates of convergence based on two densest grids ($h/a = 0.125$ and 0.0625) are 1.95, 2.72 and 2.85 for FE, SPR and BUI, respectively. Table 2 shows global effectivity index θ and standard deviation σ of local effectivity indices θ^e [6] of the Zienkiewicz-Zhu *a posteriori* error estimate [7] obtained using SPR- and BUI-methods, respectively.

Figs. 2 and 3 show distribution of local effectivity indices θ^e obtained using SPR- and BUI-methods, respectively. Grid size is $h/a = 0.25$.

Only numerical results with quadratic Serendip quadrilaterals have been presented here. Similar results with linear triangles, bilinear quadrilaterals, quadratic triangles and quadratic Lagrange quadrilaterals have also been obtained. These numerical results show, that the presented technique works both in connection with SPR- and BUI-methods. They also indicate, that BUI-method is slightly more accurate than SPR-method.

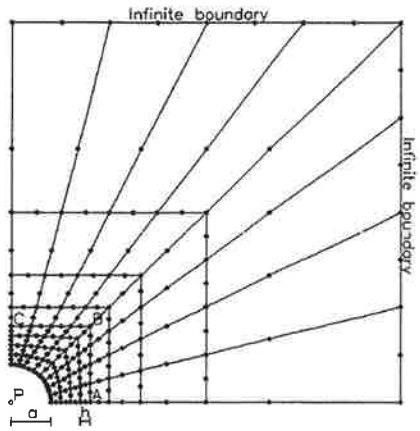

Figure 1: Typical grid of quadratic Serendip elements, $h/a = 0.25$

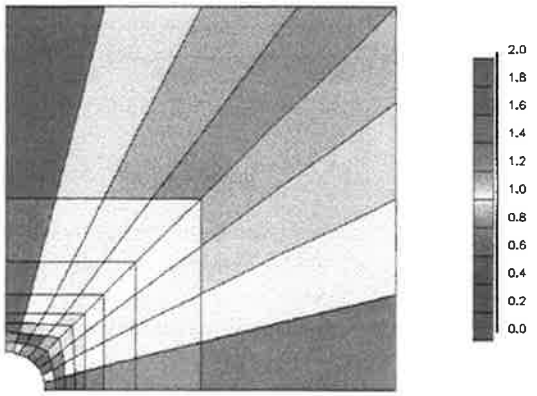

Figure 2: Effectivity index θ^e, SPR-method, $h/a = 0.25$

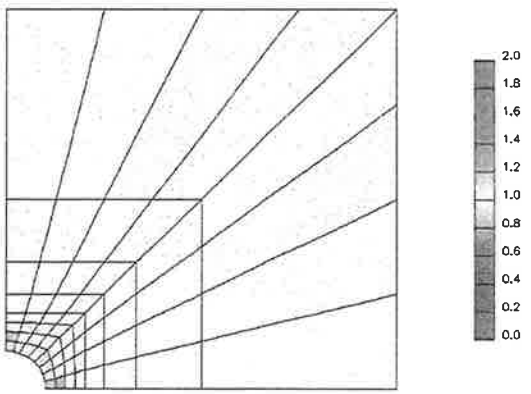

Figure 3: Effectivity index θ^e, BUI-method, $h/a = 0.25$

Table 1: Percent error in energy η_E

h/a	FE	SPR	BUI
0.5	11.71	15.62	11.35
0.25	3.520	2.564	1.497
0.125	0.959	0.370	0.195
0.0625	0.249	0.056	0.027

Table 2: Effectivity index θ and standard deviation σ

	θ		σ	
h/a	SPR	BUI	SPR	BUI
0.5	1.213	1.113	0.386	0.766
0.25	0.921	0.973	0.457	0.122
0.125	0.966	0.991	0.121	0.022
0.0625	1.006	0.999	0.066	0.012

Conclusions

Experimental convergence studies show, that the technique works. Thus it seems to be one possibility to enlarge the range of applicability of patch recovery methods to problems with unbounded domains.

References

1. J. Aalto and K. Kuula: *Infinite strips of mapped elements for unbounded domains.* In: J. Metsaveer (ed.), Proceedings of the Tenth Nordic Seminar on Computational Mechanics (NSCM X), NoACM, Tallinn, (1997)
2. J. Aalto and K. Kuula: *Mapped strips of elements for singularities and unbounded domains.* In: S.R. Idelsohn, E. Oñate and E.N. Dvorkin (eds.), Proceedings of the Fourth World Congress on Computational Mechanics (IV WCCM), CIMNE, Barcelona, (1998)
3. O.C. Zienkiewicz and J.Z. Zhu: *The superconvergent patch recovery and a posteriori error estimates. Part 1: The recovery technique.* Int. J. Num. Meth. Engng., **33**, (1992), 1331–1364
4. J. Aalto: *Built-in field equations for recovery procedures.* Computers & Structures, **64**, (1997), 157–176
5. J. Aalto and M. Åman: *Polynomial representations with built-in field equations for patch recovery procedures.* In: B.H.V. Topping (ed.), Proceedings of the Third International Conference on Computational Structural Technology (CST 96): Advances in finite element technology, Civil-Comp Press, Edinburgh, (1996), 109–125
6. J.T. Oden, L. Demkowicz, W. Rachowicz and T.A. Westermann: *Toward a universal h-p adaptive finite element strategy, Part 2. a posteriori error estimation.* Computer methods in applied mechanics and engineering, **77**, (1989), 113–180
7. O.C. Zienkiewicz and J.Z. Zhu: *A simple error estimator and adaptive procedure for practical engineering analysis.* Int. J. Num. Meth. Engng., **24**, (1987), 337–357

Quality Controlled Eigenvalues by Integrated Model Improvement and Rational Krylov Algorithms

Patrik Hager and Nils-Erik Wiberg
Department of Structural Mechanics,
Chalmers University of Technology, Göteborg, SE-41296 Sweden.
Email: patrikh@sm.chalmers.se

1. Introduction

Many problems in engineering, e.g. free undamped vibration and linear buckling problems, can be formulated as differential eigenproblems. These problems are often solved numerically using the finite element method, which requires the solution of an algebraic eigenproblem

$(K - \lambda^h M)U^h = 0$,

for eigenvalues λ_k^h and eigenvectors U_k^h. The finite element method usually only approximates the exact solution to the differential equation and an error analysis is therefore required. If the error is too large a reanalysis must be made on a modified finite element model.

This paper deals with efficient reanalysis by means of adaptive finite element technique of the *h*-version combined with efficient solution of the algebraic eigenproblem using Rational Krylov algorithms. The paper is intended as an outline of ideas for future research and does not present any new results.

The matrices, *K, M*, are real, symmetric, positive definite and sparse but can be very large. We require a small number of eigenpairs at the low end of the spectrum.

2. Quality Controlled Eigenvalues

The basic idea is to improve the FE-model successively in an outer iteration loop, to reach a required tolerance $TOL\lambda$ of the error of the eigenvalues. The error is estimated by the Superconvergent Patch Recovery technique (SPRD), see Figure 1. In an inner loop we will try to reduce the number of iterations to come below a required error tolerance $TOLRK$, by improving the starting values for the current FE-model by information from the previous cruder model.

3. Adaptive Model Improvement

Very important ingredients of the adaptive model improvement are the error estimation and the error indicator, and the calculation of the improved eigenpair (λ^*, U^*). Details and derivation of the technique can be found in [1] and [2]. We use SPRD technique on the prime variables to solve these tasks. SPRD is a variant of the Superconvergent Patch Recovery originally proposed by Zienkiewicz and Zhu, [3]. The main steps are found in Figure 2.

Caution is advised with $TOL\lambda$ as the error is underestimated, $TOL\lambda$ can be adjusted by $TOL\lambda = \theta TOL\lambda$ where θ is an estimation of the effectivity index. We estimate the effectivity index by $\theta = 1 - ch^{2\sigma}$ where c is a constant and σ is the order of superconvergence. However, it requires information from two discretisations to compute the estimate of θ, i.e. the start mesh and the first predicted mesh, so we cannot adjust $TOL\lambda$ before $j = 2$ in Figure 2.

The bilinear form $a(v,w)$ is a strain-energy-type scalar product, and $a(v,v)/2$ is the potential energy of v. In particular, we use $a_e(v,w)$ if we consider the strain energy in an element of the mesh.

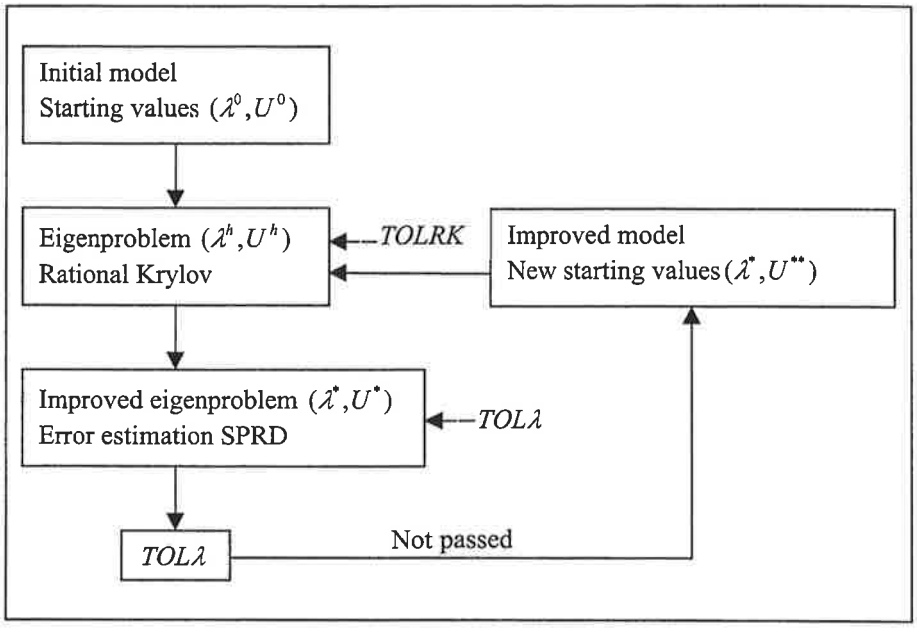

Figure 1. Quality controlled eigenvalues – Adaptive model improvement integrated with Rational Krylov iterations.

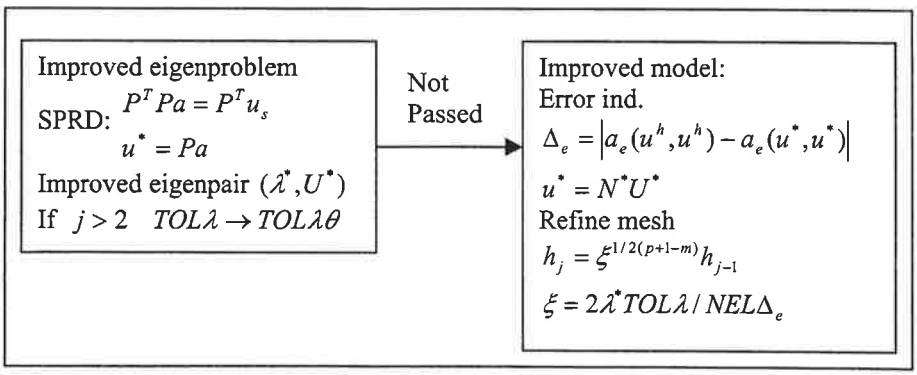

Figure 2. Improved eigenproblem and improved model based on SPRD.

4. Numerical Eigenproblem

We intend to study how the numerical eigenproblem can be solved effectively by the RKS algorithm below. Speed up of the RKS is anticipated by using λ^* as a shift, and project u^{j-1} to the new mesh by SPRD and use the projection as a start vector. Another aspect is how the discretisation error should be related to the error from the eigensolver. It is of no use to have sharp error bounds on the error of the

eigensolver in the beginning of the process whereby less demand in the beginning could speed up the overall process.

We also plan to investigate if it is effective to get higher order FE solutions for error estimation instead of (U^*, λ^*) by using (U^*, λ^*) as start vector and shift in the RKS algorithm. Clearly, it will increase the time spent in one adaptive iteration but it may pay off, as a smaller number of adaptive iterations may be required due to sharper error estimation. Moreover, since the order of superconvergence is known then the effectivity index can be estimated already at $j = 1$, and hence, *TOL* can be adjusted one adaptive iteration earlier.

5. Rational Krylov

In order to find eigenvalues at the low end of the spectrum the eigenproblem is inverted, and a shift can also be applied to speed up convergence. Hence, we consider the shifted and inverted problem

$$(C - \kappa I)U^h = 0, \quad C = (K - \mu M)^{-1} M$$

The Rational Krylov is similar to Lanczo and Arnoldi, in that a shifted and inverted problem is solved and in that an orthonormal basis V_j is built up one column at a time in an iteration scheme until convergence is achieved at the required error *TOLRK*. The iterations start with a random vector v_1^0. In each step a shifted and inverted matrix operator C_j is applied and the resulting vector is orthogonalised to the already computed part of the basis by means of Gram Schmidt. Rational Krylov differs from shifted and inverted Arnoldi in that it may use different shifts μ_j in different steps j. The reason for selecting the Rational Krylov rather than Lanczo is that in the future we expect to deal with nonsymmetric eigenvalue problems. The Rational Krylov is described in the RKS algorithm [4], [5], and shown in Figure 3.

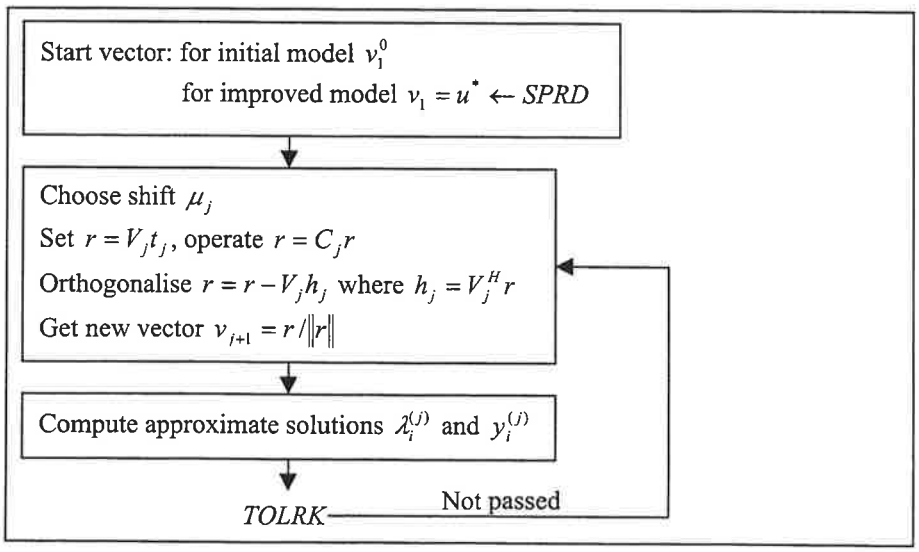

Figure 3. Modified Rational Krylov algorithm.

6. Numerical Example

We intend to study the natural eigenfrequencies of a Reissner Mindlin plate. We plan to use six node triangular elements with the vertical displacement and the rotations in the plane as degrees of freedom at each node. We prefer to use triangular element in adaptive analysis because we use automatic mesh generation that gives unstructured meshes, and the quality of quadrilateral elements can be very low. The quality of the elements does not only affect the accuracy of the FE solution it also affects the effectivity index, loosing the asymptotic exactness of the error estimator. An interesting detail to study here, beside the efficiency of the RKS algorithm, is the importance of capturing boundary layers for accurate eigenfrequencies. The Zienkiewicz-Zhu (SPR) updating is known to detect the boundary layers for static problems, and the author have by numerical experiments verified that also the SPRD updating detects the boundary layers for static problems.

Another aspect, complicating the error analys using elements of this type, is shear locking. Shear locking introduces large errors distributed over the domain, and the error estimator poorly captures these errors. Due to the large errors over the entire domain small elements are predicted everywhere, and due to that the error is not very well estimated rather many adaptive iterations are necessary. However, we believe that the choice of quadratic basis functions (or higher order basis functions) on the triangles and by using selective reduced integration that the shear locking can be avoided to such extent that the elements can be an efficient tool for adaptive analysis.

References

[1] P. Hager, 'Quality Controlled Finite Element Analysis of Vibration Problems in Structural Engineering', Licentiate Thesis Publ. 98:4, Dept of Structural Mechanics, Chalmers University of Technology, Göteborg, Sweden, 1998.

[2] P. Hager, N.-E. Wiberg, 'Adaptive Eigenfrequency Analysis by Superconvergent Patch Recovery', Comput. Methods Appl. Mech. Engrg, 176 (1999), pp 441-462.

[3] O. C. Zienkiewicz, J. Z. Zhu, 'The Superconvergent Patch Recovery and a Posteriori Error Estimators. Part 1 and 2 The Recovery Technique', Int. J. Numer. Meth. Engng, Vol. 33, pp. 1331-1382, 1992.

[4] A. Ruhe, 'Rational Krylov: a Practical Algorithm for Large Sparse Nonsymmetric Matrix Pencils', SIAM J. Sci. Comput., Vol. 19, No. 5, pp. 1535-1551.

[5] A. Ruhe, D. Skoogh, 'Rational Krylov Algorithms for Eigenvalue Computation and Model reduction', Dept of Mathematics , Chalmers Institute of Technology and the University of Göteborg.

Accuracy assessment of maximum displacement and stress

Per Kettil and Nils-Erik Wiberg
Department of Structural Mechanics, Chalmers University of Technology
S-41296 Göteborg, Sweden

1. How accurate is the maximum stress?

Numerical results from computations are always approximate. Accuracy/quality assessment, or in opposite words, error estimation, is fundamental in any reliable use of computation. The Finite Element Method (FEM), today used in a wide variety of engineering applications to analyze the behavior of physical systems, is by itself an approximate method. The finite elements approximate a continuum model by a finite number of unknowns that are efficiently calculated by a computer. Unfortunately, the finite elements introduce a discretization error.

As a result of the research effort during the last decades ("error estimation and adaptive FEM", see for example [1]-[4]) many commercial FE-packages today include routines to automatically ensure that the discretization error is kept within tolerable limits. Unfortunately, the error is usually measured globally in an "energy norm of the error percentage", that for most engineers has no real meaning. For example in structural engineering, the engineers are mainly concerned with point-wise, typically the maximum, values of displacement and stress. This short paper presents how to perform accuracy assessment in terms of stress and displacement, and a few numerical examples.

2. Influence functions gives the error at any point

The influence of the error over the domain to the result at any point may be determined by influence functions [1], [2]. The method is exactly the same as when the bridge engineer uses influence lines to determine the effect of various load positions.

Solving an appropriate dual problem generates the influence function: For example, if we need the error in displacement at a certain point the dual problem is a unit point load. To determine the error in stress we apply a unit strain, etc. The solution of the dual problem, i.e. the influence function, may be considered as a filter, or weight, that filters out the error over the domain to the local error in the original problem. We deduce the underlying mathematics below:

Let us assume we have computed an approximation u^h to the differential equation

$$Lu + f = 0$$

for some boundary conditions, for example using the finite element method. Inserting the approximate solution into the equation yields a residual load R (including the jumps between elements and boundaries)

$$Lu^h + f = R$$

Hence, the error $e = u - u^h$ is the solution of the equation

$$Le + R = 0$$

or in weak form

$$B(e,v) = (R,v)$$

We now introduce the dual problem. The dual problem has to be defined according to the local quantity of interest. For the error in displacement at a certain location $\hat{x}$ the dual problem is a unit point load, i.e. Dirac's delta $\delta(\hat{x})$,with Green's function G (the "influence function") as solution

$$LG = \delta(\hat{x})$$

Betti's principle

$$(f^*,u) = (f,u^*)$$

where u and f are the displacement and load of one problem, and u* and f* from another problem, makes it possible to filter out the local error $e(\hat{x})$

$$(\delta(\hat{x}),e) = (R,G)$$

$$e(\hat{x}) = (R,G) = B(e,G) = (Galerkin\ orthogonality) = B(e,e_D) = \sum_{k=1}^{numel} B(e,e_D)_{\Omega_k}$$

$$e_D = G - G^h$$

$$e(\hat{x}) \le (Cauchy - Schwarz) \le \sum_{k=1}^{numel} B(e,e)^{\frac{1}{2}}_{\Omega_k} B(e_D,e_D)^{\frac{1}{2}}_{\Omega_k}$$

$$\boxed{e(\hat{x}) \le \sum_{k=1}^{numel} \|e\|_k \|e_D\|_k}$$

by finite element computation at the modest additional cost of solving and performing error estimation for the one extra load vector of the dual problem. Note that in the case of 2D or 3D elasticity a point load is not well defined. This can be circumvented by regularization, i.e. to consider a patch load over a small region (e.g. a finite element) and interpret the estimated error divided by the area of the region as the average error over the region [2].

3. The numerical results are not always precise but useful in engineering terms

Figures 2 and 3 present two numerical examples showing the accuracy of the error estimate in practice. The error estimation is performed using stress smoothing by REP [3]. In these examples the ratio of estimated to true error (the "effectivity index") is in the range 1.0-3.0, which is not very precise but definutely useful in engineering applications. The error in stress is always larger then the error in displacement, since stresses are derivatives of the displacement.

Simply supported beam, 2D elasticity

Data:

Length 1.0 m	Height 0.1 m
Plane stress:	$E = 1.0 \times 10^6$ Pa
	$v = 0.3$
	Pressure 1.0 Pa

Results:

	Displacement u_y	Stress σ_x
Maximum, exact solution	0.160 mm	75.0 Pa
Maximum, FE* solution	0.142 mm	69.8 Pa
Estimated error	0.018 mm	12.5 Pa
Exact error	0.018 mm	5.2 Pa
Effectivity index	**1.0**	**2.4**

(*Using 2x20 bilinear finite elements and 3x21 nodes)

1. FE mesh, bc's, displacement u_y and stress σ_x

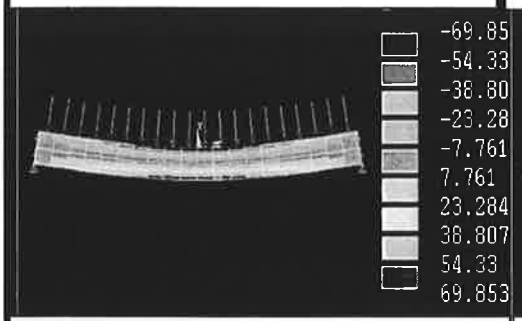

2. Energy norm of the error distribution

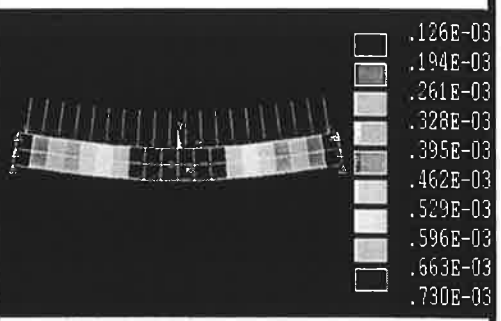

3. "Influence function"

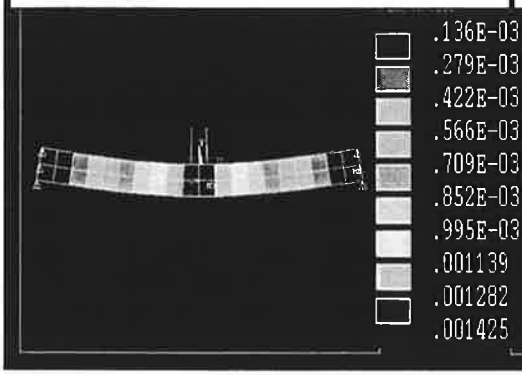

4. Error summing up to the error in max u_y

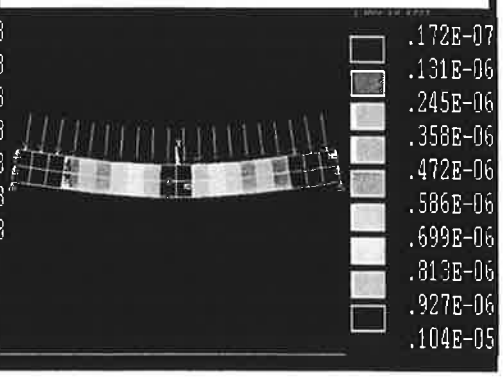

Figure 1. Simply supported beam – accuracy assessment of maximum displacement u_y and stress σ_x. A uniform load in the y-direction over the four middle elements defines the dual problem for the displacement. A unit strain in the x-direction over the two lower middle elements defines the dual problem for the stress.

The natural next step in the development is to adapt the mesh according to error distribution for the quantities of interest to reach a required degree of accuracy in the most efficient manner. Reference [2] presents examples of this.

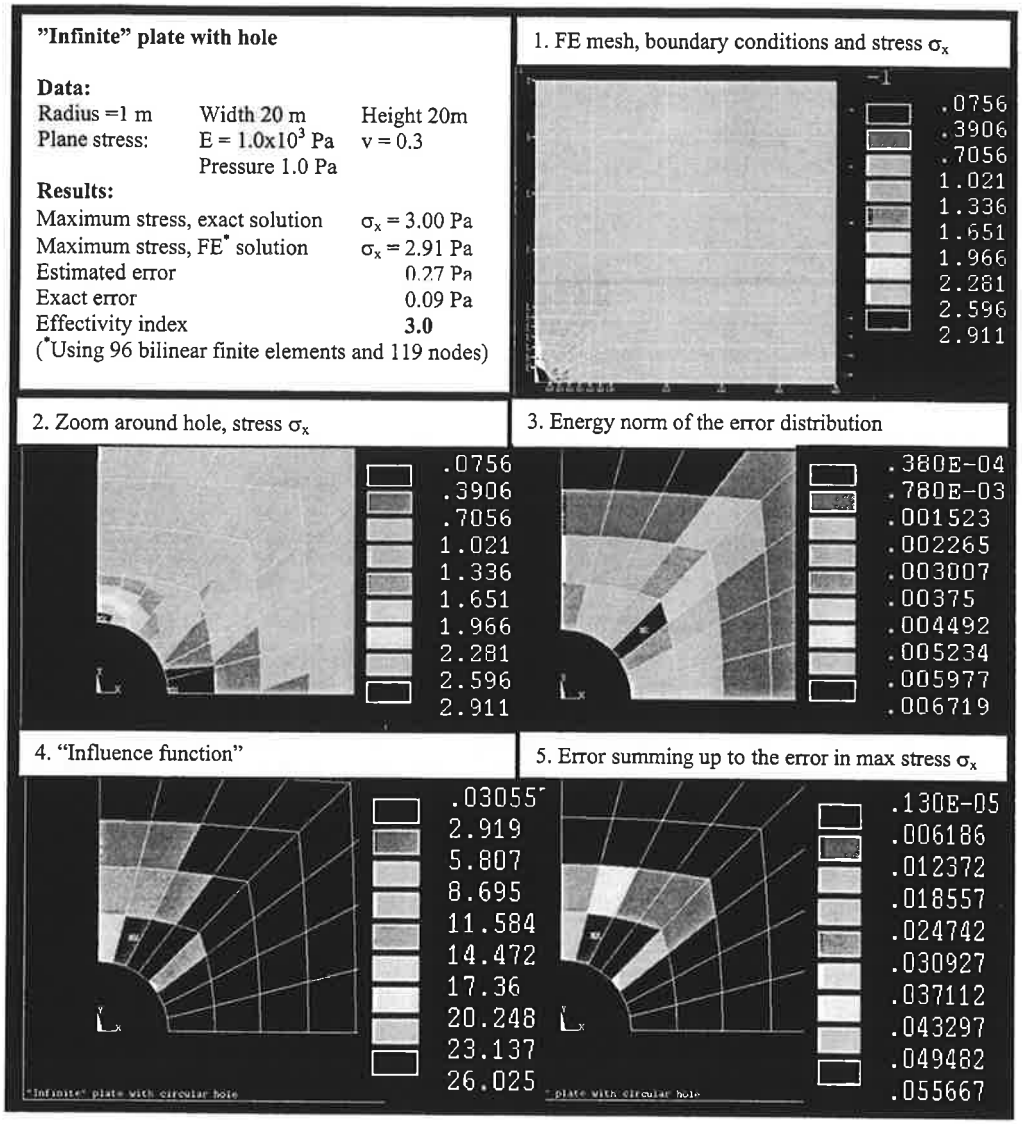

Figure 2. Infinite plate with hole – accuracy assessment of maximum stress σ_x
A unit strain in the x-direction over the element just above the hole defines the dual problem for the stress.

References

[1] K. Eriksson, D. Estep, P. Hansbo, C. Johnson, Computational Differential Equations, Studentlitteratur, Lund, Sweden, 1996.

[2] F. Cirac, A. Schleupen, E. Ramm, "Error estimates for local and global variables using duality principles", in proceedings of Computational Mechanics, New Trends and Applications, S. Idelsohn, E. Onate, E. Dvorkin (eds.), CIMNE, Buenos Aires, 1998.

[3] B. Borooomand, O.C. Zienkiewicz, "An improved REP recovery and the effectivity robustness test", Computers and Structures, Vol. 40, pp. 3247-3277, 1997.

[4] N.-E. Wiberg, F. Abdulwahab, X. D. Li, "Error estimation and adaptive procedures based on superconvergent patch recovery (SPR) techniques", Archives of Computational Methods in Engineering, Vol. 4, pp. 203-242, 1997.

Symbolic software application for modelling of wave interaction process

Andres Braunbrück and Arvi Ravasoo

Institute of Cybernetics at Tallinn Technical University,
Akadeemia tee 21, 12618 Tallinn, Estonia

Abstract. The nonlinear interaction of longitudinal waves in a homogeneous elastic material with nonlinear physical properties is investigated theoretically. The analytical solution of the one-dimensional problem of nonlinear interaction of a sine-waves, excited simultaneously on two opposite surfaces of the material is derived, making use of the symbolic software (Maple V). The detailed scheme of symbolic computation is presented.

1 Introduction

In this paper we study the possibility to use a relatively simple method to determine the physical properties of a nonlinear homogeneous elastic material on the basis of longitudinal waves nonlinear interaction data. Under consideration is the one-dimensional equation of motion [1]

$$\left[1 + k_1 \frac{\partial U}{\partial X}\right] \frac{\partial^2 U}{\partial X^2} = c^{-2} \frac{\partial^2 U}{\partial t^2}\,, \tag{1}$$

where t denotes the time, X is Lagrangian coordinate and U is displacement. The constants k_1 and c depend on material properties. The Eq. (1) is solved on the basis of the perturbation method [2,3] exploiting the software Maple V. The analytical solution is obtained and the algorithm of solution derivation is illustrated by the scheme of symbolic computation (Fig. 1).

2 The perturbation method

We make use of the perturbation method and seek an analytical solution of Eq. (1) in series of a small parameter ε [2,3]:

$$U(X,t) = \sum_{n=1}^{\infty} \varepsilon^n U^{(n)}(X,t), \tag{2}$$

Following the perturbation procedure, the series (2) is substituted into the Eq. (1). Equating to zero terms with equal power of ε, one arrives at a system of differential equations:

$O(\varepsilon)$:

$$U^{(1)}_{,XX}(X,t) - c^{-2}\, U^{(1)}_{,tt}(X,t) = 0, \tag{3}$$

$O(\varepsilon^2)$:

$$U^{(2)}_{,XX}(X,t) - c^{-2}\, U^{(2)}_{,tt}(X_1,t) = -k_1\, U^{(1)}_{,X}(X,t)\, U^{(1)}_{,XX}(X,t), \tag{4}$$

$O(\varepsilon^3)$:

$$U^{(3)}_{,XX}(X,t) - c^{-2}\, U^{(3)}_{,tt}(X,t) = \\ -k_1\, [\, U^{(1)}_{,X}(X,t)\, U^{(2)}_{,XX}(X,t) + U^{(1)}_{,XX}(X,t)\, U^{(2)}_{,X}(X,t)]. \tag{5}$$

This system of hyperbolic nonhomogeneous differential equations is solved under the following initial and boundary conditions:

$$U(X,0) = U_{,t}(X,0) = 0, \quad U_{,t}(0,t) = \varepsilon\, a_0\, \varphi(t)\, H(t), \quad U_{,t}(L,t) = \varepsilon\, a_L\, \psi(t)\, H(t). \tag{6}$$

Here $H(t)$ denotes Heaviside function, a_0 and a_L are constants. The functions $\varphi(t)$ and $\psi(t)$ determine the arbitrary and smooth initial wave profiles. They satisfy conditions $max \mid \varphi(t) \mid = 1$, $max \mid \psi(t) \mid = 1$ and ensure that $\lim_{t\to 0} U_{,t}(0,t) = \lim_{t\to 0} U_{,t}(L,t) = 0$ in consonance with the initial conditions. The scheme of symbolic computation is presented in Fig. 1. The Eq. (3) has a well-known D'Alambert solution and it can be solved using Laplace integral transform. After applying the Laplace integral transform to the hyperbolic nonhomogeneous differential equations (4) and (5), they transform to the second order nonhomogeneous differential equations, which can be solved directly. By applying the inverse Laplace integral transform to these solutions we get the solution to the n-th term in series (2).

To analyse the wave-material interaction, we define the initial wave profiles in (6) as sine functions with radial frequency ω:

$$\varphi(t) = \sin \omega t\,, \; \psi(t) = \sin \omega t. \tag{7}$$

Substituting (7) into (6) and following the symbolic computational scheme presented in Fig. 1., we arrive at the analytical solution. The symbolic computations to derive the sine-wave solution were carried out with mathematical software Maple V version 5.1.

The analytical solution is too cumbersome to include, but it can be studied graphically. It is convenient to study the solution in the form of deformation gradient since it characterizes the tension distribution in the material. The second order nonlinear effects are plotted in Fig. 2. The numerical data are taken for duralumin [2]. In the interval $t/\tau \geq 1$ the reflection amplitude at the boundaries $X/L = 0$ and $X/L = 1$ is essentially greater than in the interval $t/\tau < 1$.

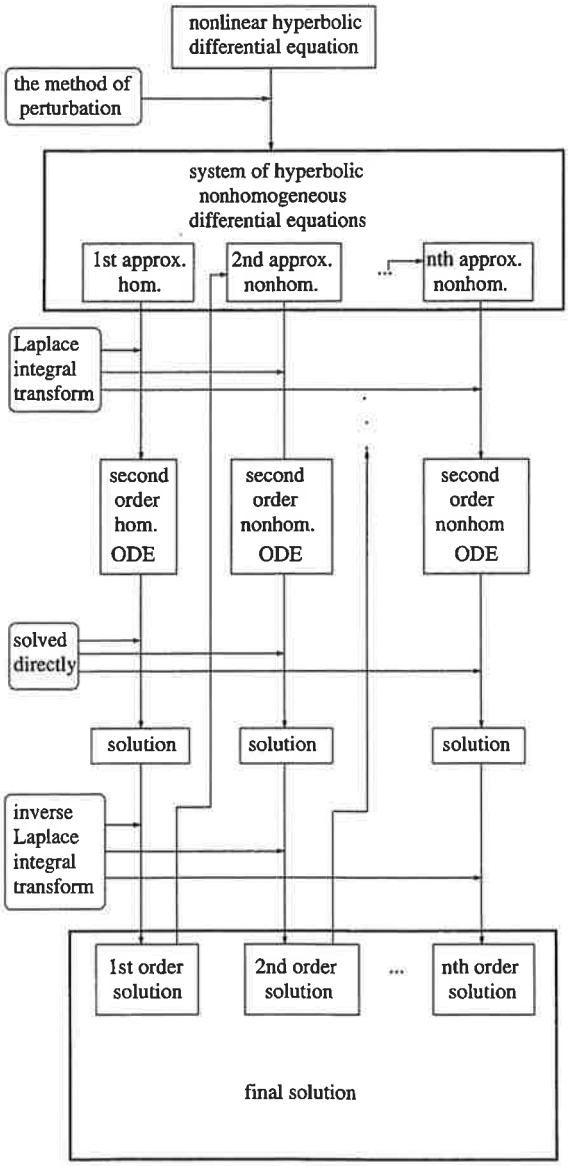

Fig. 1. Scheme of symbolic computation.

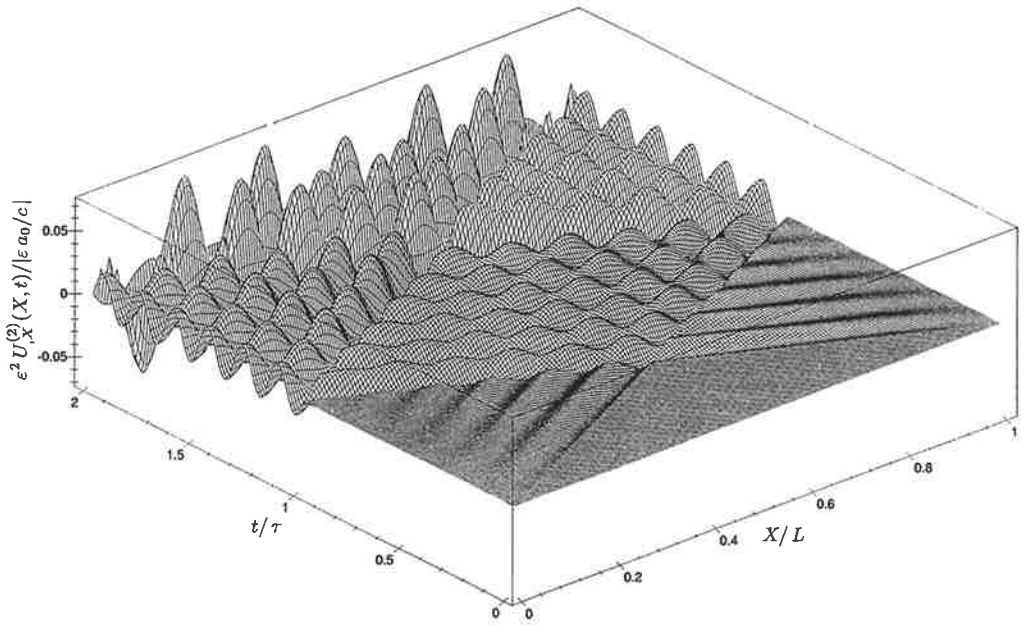

Fig. 2. Second order nonlinear effects that accompany the propagation of deformation gradient in duralumin ($L = 0.1$ m , $a_0 = -a_L = -c$ m/s, $\varepsilon = 1 * 10^{-4}$, $\tau = L/c$, $\omega = 1.15539 * 10^6$ rad / s).

3 Conclusions

The propagation, reflection and nonlinear interaction of two sine-waves is studied. The basic peculiarities of the considered problem are clarified on the basis of numerical experiment data. The utilization of symbolic software (Maple V) in solving complicated analytical problems turned out to be very effective.

References

1. Eringen, A. C. (1962), *Nonlinear Theory of Continuous Media,* McGraw-Hill, NewYork.

2. Ravasoo, A., and Braunbrück, A. (1999), Nonlinear interaction of longitudinal waves in elastic material, *Proc. Est. Acad. Sci. Phys. Math., 1999,* **48**, *3/4, 22-32*

3. Kevorkian, J., and Cole, J. D. (1981) *Perturbation Methods in Applied Mathematics,* Springer-Verlag, New York.

STRAIN MEASUREMENT OF THE COMPOSITE STRUCTURE WITH FIBER OPTIC SENSORS

Mika Jurvakainen
Engineering Mechanics Laboratory, University of Oulu
PL 4200, 90401 Oulu, Finland
Tel: +358 8 5532177, Telex: 358 8 5532026
E-mail: **Mika.Jurvakainen@me.oulu.fi**

Abstract

Fiber optic sensors embedded inside materials are used to determine the strain and temperature fields inside the composite structure. In this work, we consider the use of Fabry-Perot sensors and method based on time-of-light (TOF) of laser pulse travelling inside long optical fiber. The increasing interest in the optical fiber sensors includes their use in development of fiber optic smart structures[2].

In order to measure the strains and temperature in composite materials with embedded fiber optic sensors the relationships between the strains and temperature in composite and the strain and temperature in the sensor must be known.

The goal of our research is to measure the strain and temperature either on the surface or inside fiber reinforced composite material by using the fiber optic sensors. A sensor embedded inside the material disturbs the strain and temperature field. Our goal is to measure those strains and temperature which would exist at the location of the sensor in the absence of the sensor.

The relation between farfield and sensor strain fields depends on the following aspects: properties of the sensors and the coating (if the fiber is coated), the material surrounding the sensor, the orientation of the sensors inside the material. The values of these parameters are not often known exactly. These effects of uncertainties considerably take effects to the accuracy of the results. This work focus on these uncertainties and estimates their influences to the results by using of error analysis.

For Fabry-Perot sensors two semi-transparent mirrors are spliced into the optical fiber. In extrinsic Fabry-Perot sensors the substance between mirrors is air. When strain and temperature field in surrounding material change, the reflected light intensity of the Fabry-Perot sensor changes. The values of these changes are then deduced from these measured signal outputs. Procedures for calculating the sensor strains in terms of material strains and measured signal outputs have been taken from the book of Van Steenkiste and Springer[1].

The analysis is based on the following considerations. The temperature of the sensor and the material are assumed to be the same so that changes in farfield temperature is equal with the temperature changes inside the sensor. The deformations are assumed to be small and materials to be linear elastics. The bonding between sensor and surrounding material is assumed to be perfect.

In conclusion, the fiber optic sensors have shown their capabilities in the use of strain and temperature measurements in composite structures. Reliability of the measurement needs to be more carefully studied.

REFERENCES

1. Van Steenkiste, R.J. and Springer, G.S. Strain and Temperature Measurement with Fiber optic Sensors, Technomic publishing Company, Inc. 1997.
2. Udd, E. "Fiber sensors for smart structures"", in Optical Fiber Sensors, Proc. 6th Int. Conf. OFS'89, Paris, Springer-Verlag, pp392-399, 1989.
3. Kollar, L.P. and Van Steenkiste, R.J. "Calculation of the Stresses and Strains in Embedded Fiber Optic Sensors", Journal of Composite Materials, Vol 32, pp. 1647-1679. 1998.

SIMULATION OF AN ACTIVE A SUSPENSION SYSTEM FOR THE SEAT OF AN OFF-ROAD VEHICLES

Matti Kangaspuoskari

Department of Mechanical Engineering, University of Oulu,
PL 4200, 90401 Oulu, Finland
Tel: +358 8 553 2178, Telefax: +358 8 553 2026
E-mail: Matti Kangaspuoskari@Me.Oulu.fi

ABSTRACT

Off-road vehicles are subjected to strong vertical and horizontal vibrations. The driver is liable to high vibration loads which can lead to reduced performance and even damage to health. The most dangerous are high acceleration in directions unusual to natural human body. The main vibration in the off-road vehicle is the driver's seat. The common method to eliminate vibrations is to use passive elements in vertical direction.

This paper covers modelling and control of a fully active suspension system for the driver's seat. The fully active system involves the suspension mechanism with a hydraulic actuator which is controlled by a high frequency closed loop proportional valve [1]. The vehicle seat mechanism is modelled as a two degree of freedom two-dimensional structure [2] and so system has capability to minimize driver discomfort by controlling the seat dynamic state in horizontal as well as in vertical directions. The road inputs include horizontal, vertical and the pitch degree of freedom.

The driver's seat system is modelled by using the MATLAB/SIMULINK program. There are two different possibility to use defined model. In the first case the inputs are based on measurements by joint sensors in the real system and the model is used for computer control of the system. The second possibility is to use the defined model in simulation. For this purpose the equations of motion in Lagrange's formulation have been written. By solving the differential equation model numerically, the behaviour of the system can be determined. The performance of classical controller [3] is analyzed and compared with the performance of neural network controller [4]. Numerical examples are given in the paper to show the validity of the model [5].

References

1. Claar, II P.W. & Vogel, J.M., A Review of Active Suspension Control for On and Off-Highway Vehicles. SAE Transactions, Vol. **98** (1989), No.2, s. 557-568.
2. Burton, P., Kinematics and dynamics of planar machinery. Prentice-Hall, Inc., Englewood Cliffs, N.J. 1979.
3. Koivo, A. J., Fundamentals for control of robotic manipulators. John Wiley & Sons, Inc. New York 1989.
4. Moran, A. & Nagai, M., Optimal active control of nonlinear vehicle suspensions using neural networks. *JSME Int. Journal,* Series C. Vol. **37**. No.3 (1994). pp. 707-718.
5. Kangaspuoskari M., Ajoneuvon aktiivisen istuinripustuksen simulointi. Lisensiaattityö, 1999, Oulun yliopisto, konetekniikan osasto, 81 s.

Real-time visualisation of large fibre networks

J.Lindemann*, G. Sandberg and O. Dahlblom

Division of Structural Mechanics
Lund Institute of Technology, Lund University
P.O.Box 118, S-221 00 LUND, Sweden
e-mail: strucmech@byggmek.lth.se, web page: http://www.byggmek.lth.se/

ABSTRACT

This paper describes methods of visualising fracture and deformation of large fibre structures using VRML97 and OpenGL. Using a VRML visualisation tool for postprocessing creates a file that can be used to share information on the internet. A test implementation of a real-time visualisation tool in C++ has been developed.

BACKGROUND

A fibre network is a material that has a structure consisting of fibres, such as fluff and fibre insulation material. A computer program that simulates deformation and fracture in fibre networks is being developed by Heyden [1]. When three-dimensional fibre networks are simulated the numerical results are often difficult to interpret. To be able to analyse the time-dependent results different methods have been used to visualise the data. A special post processing tool has been developed by Olsson [2]. The tool is developed in MATLAB [4] and uses a special VRML toolbox [10]. Output from this tool is a VRML file that can be viewed in Netscape and Microsoft Internet Explorer with a special VRML plugin.

VRML97 IMPLEMENTATION

VRML97 [3] is a language specification. The basic datatype in the VRML97 specification is the node. There is a number of different node types in the VRML97 specification that can be used to describe a VRML model. Objects that are rendered is defined by the *Shape* node. This node contains a *Geometry* node and an *Appearance* node. In the *Geometry* node special geometry primtives are used, for example *Box, Sphere* and *IndexedFaceSet*. In the *Appearance* node the visual appearance of the object is given by using a *Material* and *Texture* node. *Shape* nodes do not contain any position and rotation information. To place a *Shape* in a VRML model it is placed in a *Transform* node. This node contains properties for describing position, rotation and scale for its child shape nodes. The following VRML sample code displays a red sphere.

```
#VRML V2.0 utf8
Transform {
  translation 3 0 1
  children [
    Shape {
      geometry Sphere { radius 2.3 }
      appearance Appearance {
        material Material {
          diffuseColor 1 0 0
        }
      }
    }
  ]
}
```

Animation of objects in VRML is done using *CoordinateInterpolator* and *ColorInterpolator*. These nodes are then connected to *Shape* nodes using a special *route* instruction in the code. A route can be described as an electrical wire that can convey information between objects in VRML. To initiate an animation the interpolation nodes must be connected to a sensor node. A sensor node generates events

depending on special conditions in the model. A *TimeSensor* node generates events as time passes. This can be used to drive an interpolator node to visualise time dependant data.

The creation of a VRML file can be time consuming. To be able to easily create VRML files a special MATLAB toolbox [10] is used. The toolbox defines a number of commands that makes it easy to create VRML code from MATLAB data. The previous VRML example can be created by using the following matlab commands:

```
fid = vrmlcreate('sample1.wrl');
vrmlsphere(fid,[3 0 1],[2.3],[1 0 0]);
vrmlclose(fid);
```

Most of the commands in this toolbox also take matrices as input, which makes it possible to create a large number of objects with only one call. By using this toolbox it was possible to create a platform independent visualisation tool for realtime visualisation of fibre networks, see Figure 1.

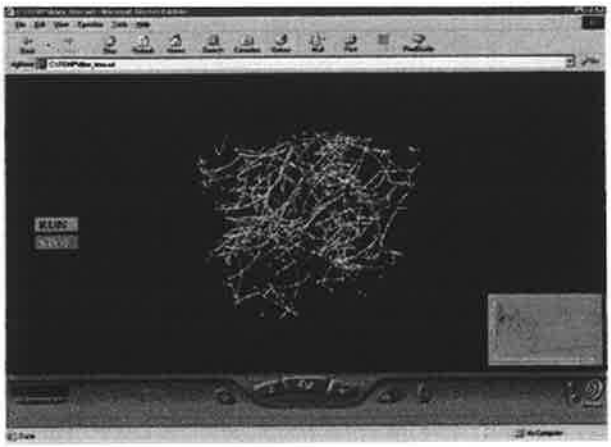

Figure 1 - VRML visualisation tool

The developed tool has been succesfully used with up to approximately 900 fibres (5 to 8 frames per second on an SGI Onyx2). The created file can be viewed with a VRML plugin in real-time if three-dimensional graphics hardware is installed. If the number of fibres increases the performance drops considerable even if viewed on an SGI Onyx2 system. This is probably due to poor hardware optimisation of the VRML plugin and browser overhead. Another way to visualise the VRML file is to import it into the IRIS Performer [5] real-time visualisation system. DRaW Computing Associates [6] provides a VRML reader for IRIS Performer which supports allmost all VRML97 nodes. By using IRIS Performer multiple processors and SGI Onyx2 hardware can be used to achieve higher performance. The disadvantage of using the IRIS Performer system is that it can only be used on high performance SGI machines.

IVF++ IMPLEMENTATION

To be able to create platform independent visualisations a special class library Interactive Visualisation Framework Ivf++ [11] has been developed. The class library is based on GLUT (OpenGL Utility Toolkit) by Kilgard [7], which is a library for creating system independent OpenGL applications. GLUT supports multiple windows, basic event processing and other routines needed to create OpenGL applications. Because of this system independence a program written using GLUT can be compiled on all platforms supporting OpenGL [8] or Mesa [9]. The Ivf++ class library is divided into two parts, general OpenGL classes for visualisation and a GLUT part supporting windows and callbacks. Using this library a simple test program was created to test how large fibre networks could be visualised. The test program is able to generate randomly generated networks with a given number

of fibres. Level of detail options can also be applied to reduce the complexity of the geometry rendered, see Figure 2.

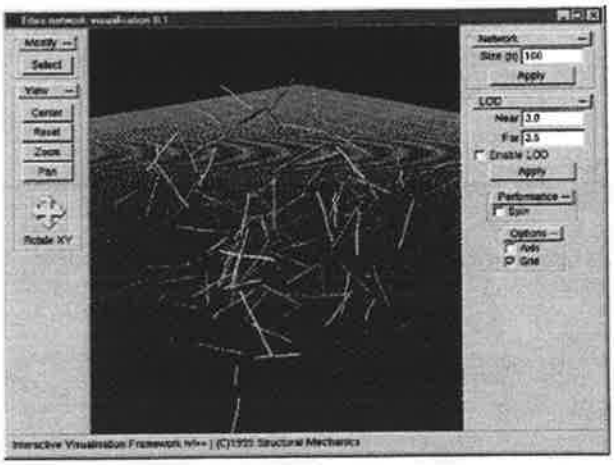

Figure 2 – Fibre visualisation test program

A study was done rendering six different structure sizes namely 80, 160, 320, 640, 1280 and 2560 fibres. Color depth was set to 16-bit and the rendering window had the same size on all platforms. Frame rate is measured by spinning the network in the idle loop of the test program and calculating a mean frame rate for 50 frames. The test was done on three PC:s and an SGI Onyx2 system. The PC:s were a Pentium Pro 200 MHz, Pentium II Celeron 400 MHz and an SGI 320 Pentium III 500 MHz. The tests showed that to visualise networks sizes larger than 500 fibres in real-time (~15 frames per second) advanced hardware was needed. Using level of detail (LOD), which is a technique to reduce the geometry complexity depending on the distance to the viewer and a modern PC with 3D graphics adapters (SGI 320 and Pentium II) fibre networks up to 640 fibres can be handled in the user interface without any significant delays on PC hardware (5 frames per second). If larger fibre networks is going to visualised with a highter frame rate a SGI Onyx2 or equivalent hardware is needed. Test results are given in the following diagram.

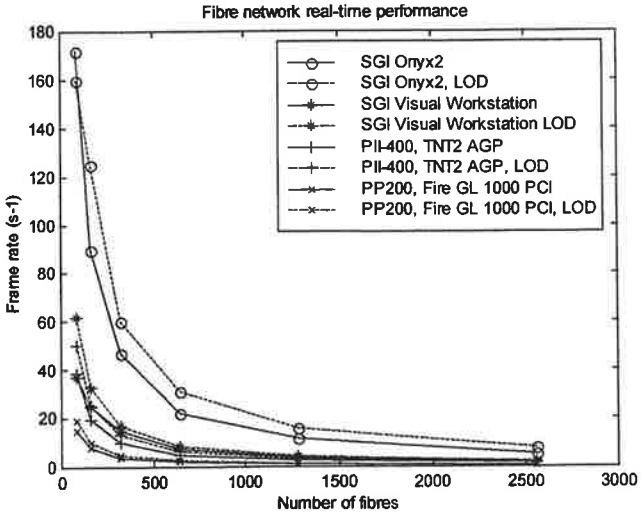

Figure 3 - Fibre network real-time performance

TEXTURE BASED METHODS

To handle very large networks containing more than 2500 fibres new techniques must be developed. A technique that is considered is the use of textures to emulate the curvature of the fibres. This will reduce the number of triangles needed to represent the fibre in the visualisation and makes it possible to visualise more fibres in an accurate way. The following figure shows a fibre consisting of two segments. In the left picture the fibre is implemented using a 8 sided section that is swept along a spine. The right picture shows a fibre implemented using a gradient texture map and transparency, this approach requires only 4 triangles per segment compared to 16.

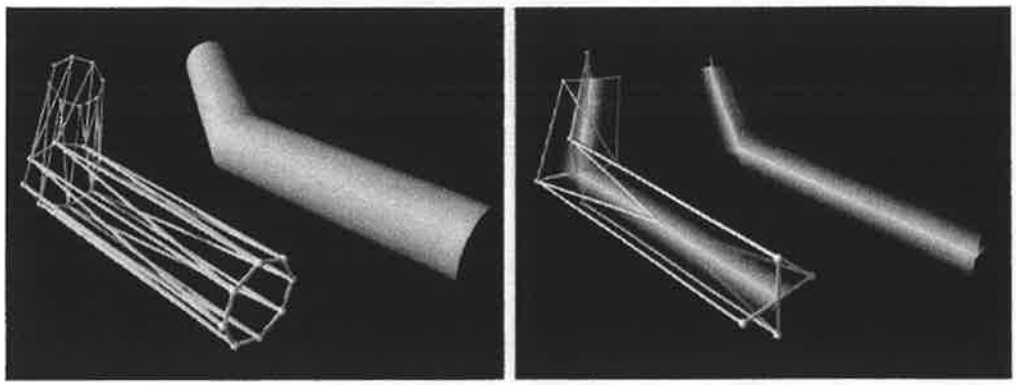

Figure 4 - Using texture maps and transparency to reduce triangles

REFERENCES

[1] Heyden, S. A 3D Network model for Evaluation of Mechanical Properties of Cellulose Fibre Fluff. Report TVSM-1011, Lund University, Division of Structural Mechanics, Lund, Sweden, To be published.

[2] Olsson, P. Visualisation of Deformation and Fracture in Fibre Materials. Report TVSM-5086, Lund University, Division of Structural Mechanics, Lund, Sweden

[3] VRML97, http://www.web3d.org/technicalinfo/specifications/vrml97, 1998-99

[4] MATLAB, The Mathworks Inc., http://www.mathworks.com, 1999

[5] IRIS Performer, Silicon Graphics, Inc., http://www.sgi.com/software/performer

[6] DRaW Computing Associates, Inc., http://www.drawcomp.com, 1999

[7] Kilgard, M. The OpenGL Utility Toolkit (GLUT) Programming Interface API Version 3, http://reality.sgi.com/opengl/spec3/spec3.html, 1999

[8] OpenGL, http://www.opengl.org, 1999

[9] The Mesa 3-D graphics library, http://www.mesa3d.org, 1999

[10] A VRML visualisation toolkit for MATLAB, Lund University, Division of Structural Mechanics, Lund, Sweden, Under development.

[11] Interactive Visualisation Framework Ivf++, Lund University, Division of Structural Mechanics, Lund, Sweden, Under development.

An attempt to standardize finite element derivation with *Maple*

Yunhua Luo, Anders Eriksson and Costin Pacoste

Structural Mechanics group, Dept. Structural Engineering,
Royal Institute of Technology, S-100 44 Stockholm, Sweden

Abstract Described in this short paper is an attempt to standardize the process for deriving finite elements based on commonly used formulations with *Maple*, mainly to obtain the expressions of element stiffness matrix and internal forces. The process is put in a tentative 'standard' way, with as many as possible factors considered. A preliminary version of new *Maple* package was developed based on this idea.

1 Introduction

In the field of finite element methods, efforts in finding new efficient elements has never been stopped and seems will last for a long time. As well known, symbolic operations involved in deriving finite elements, mainly the expressions of element stiffness matrix and internal forces, is a tedious and error-prone process, especially for higher order or nonlinear finite elements. After obtaining these expressions, the coding work also needs a lot of carefulness. With computer algebra applied, the situation can be largely improved [1], but very much work is still unnecessarily repeated in developing a new finite element. An element is a composite product with many ingredients involved: variational principle, strain definition, material definition, interpolation functions, integration rule and so on. In a new element, maybe only one ingredient is altered or replaced, while the rest remains unchanged, but the whole process has to be repeated by each finite element researcher or engineer. The main reason for this is that the process of developing finite elements is not standardized. Although the process is complex, it is possible to put it in a standard way, at least for the commonly used formulations and techniques. The work reported in this paper is an attempt on this way.

2 Main line in deriving finite elements

To standardize the process of developing finite elements, first thing, also the most important one, is to make clear the key steps in developing finite elements. In structural mechanics, the main steps in developing finite elements could be described with the flow chart in Fig. 1. The process begins with strain energy density $\phi(\boldsymbol{u}(\boldsymbol{x}), \boldsymbol{\sigma}(\boldsymbol{x})|\boldsymbol{\varepsilon}(\boldsymbol{x}))$ in an element, where $\boldsymbol{\sigma}$ and $\boldsymbol{\varepsilon}$ are stress and strain vectors, which are functions of position vector $\boldsymbol{x}$. Symbol '|' means that either stress or strain parameters are introduced. The energy density might have different expressions, depending on the adopted variational principle, strain and material definition. This will be addressed in a following section. After fixing the expression of strain energy density, nodal displacements and/or stress (or strain) parameters are introduced with the aid of interpolation functions. Meanwhile physical coordinates $\boldsymbol{x}$ can be converted to natural coordinates $\boldsymbol{\xi}$ if it is necessary. Then an integration is carried out to obtain the strain energy $\Phi(\bar{\boldsymbol{u}}, \bar{\boldsymbol{\sigma}}|\bar{\boldsymbol{\varepsilon}})$ in the element. The element stiffness matrix and internal forces are obtained by differentiating the strain energy with respect to element degrees of freedom. The introduced stress or strain parameters can be eliminated by a procedure similar to static condensation.

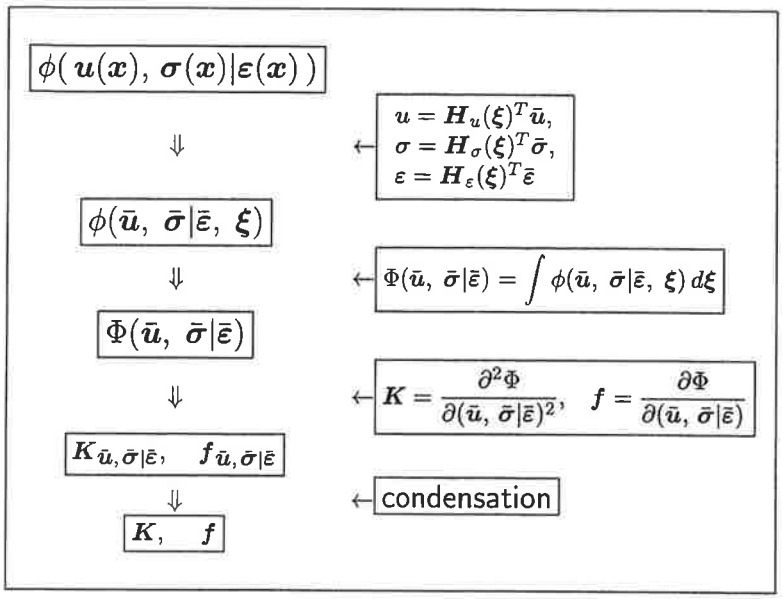

Figure 1: Main line in deriving finite elements

3 Variations in finite element formulas

In the above process, there are several points at which variations can be introduced. Different finite element formulations can thus be implemented. In the developed *Maple* package, user interfaces are built at these points so that users can creatively develop new finite elements.

3.1 Strain energy density

The first point, also the place which allows a lot of variations, is the expression of strain energy density in an element. The expression of strain energy density is mainly decided by three factors: the adopted variational principle, the strain and material definitions.

3.1.1 Variation principle

The adopted variational principle determines that the function of strain energy density could have different expression and different kind of variable(s). If the principle of minimum potential energy is used, the strain energy density is a function of displacements $\boldsymbol{u}$

$$\phi(\boldsymbol{u}) = \frac{1}{2}(\boldsymbol{L}\boldsymbol{u})^T\boldsymbol{D}\,(\boldsymbol{L}\boldsymbol{u}) \tag{1}$$

where $\boldsymbol{L}$ is a differentiation operator determined by strain definition. $\boldsymbol{D}$ is the material property matrix.

If an element is based on the Hellinger-Reissner principle, the strain energy density has the form

$$\phi(\boldsymbol{u}, \boldsymbol{\sigma}) = -\frac{1}{2}\boldsymbol{\sigma}^T\boldsymbol{d}\,\boldsymbol{\sigma} + \boldsymbol{\sigma}^T(\boldsymbol{L}\boldsymbol{u}) \tag{2}$$

which is a function of displacements $\boldsymbol{u}$ and stresses $\boldsymbol{\sigma}$. $\boldsymbol{d}$ is the inverse of matrix $\boldsymbol{D}$.

A more general case is the Hu-Washizu principle. In this case, the strain energy density is a function of displacements $\boldsymbol{u}$, stresses $\boldsymbol{\sigma}$ and strains $\boldsymbol{\varepsilon}$.

$$\phi(\boldsymbol{u}, \boldsymbol{\varepsilon}, \boldsymbol{\sigma}) = \frac{1}{2}\boldsymbol{\varepsilon}^T \boldsymbol{D}\, \boldsymbol{\varepsilon} + \boldsymbol{\sigma}^T(\boldsymbol{\varepsilon} - \boldsymbol{L}\boldsymbol{u}) \tag{3}$$

To improve computational efficiency, the stresses are eliminated by the orthogonal condition [2] or stress-strain relations [3]. Other variational principles can be introduced by a user interface.

3.1.2 Strain definition

In equations (1), (2) and (3), the differentiation operator $\boldsymbol{L}$ is determined by strain definition. A strain definition basically includes two aspects, describing how strains and displacements are related. One aspect is whether the element is expected to deal with geometrical nonlinearities, such as large rotation, large strain or both, without resorting other techniques such as a co-rotational formulation. If so desired, Green-Lagrangian strain definition or its degenerated forms, e. g. shallow arch or shallow shell, can be adopted. The other aspect is the so-called kinematic assumptions, which describe how a section deforms and what strain components are non-trivial. Kinematic assumptions are different from beams to plates, to shells, from Euler or Kirchhoff type to Timoshenko or Reissner type, and so on. Users can specify a strain definition or they can input their own strain definition.

3.1.3 Material definition

The matrix $\boldsymbol{D}$ or $\boldsymbol{d}$ contains material parameters. A library which stores commonly used material models can be established and thus allows a user specify a material from it. Also a user interface allows users to introduce their own material model. In the *Maple* package, isotropic and some composite materials are included.

3.2 Interpolation function

This is another place which allows users to use their creativity. There are quite several things to decide here: how many nodes the element has, how the nodes are distributed — how many on element edges and how many inside. The selection of interpolation functions has significant effects on element performance, especially for low-order ones [4] and thus needs more careful consideration. Incompatible modes are easy to introduce at this step. It is also possible to include other special finite element techniques such as MITC approach. For mixed field elements, the selection of assumed stress or assumed strain modes are also very important to element performance.

3.3 Integration rule

Users can specify an integration scheme from exact integration to various reduced integrations and can implement their own integration rule by a user interface.

4 A new *Maple* package

In previous versions of *Maple*, it was difficult for a nested procedure to access the variables of an outer procedure. Procedures could only share variables if the variables were global. New version of Maple allows to create nested procedure definitions. Procedures can be defined within other procedures, or return procedures as expected output. Lexical scoping allows a nested procedure to access the variables which are located in surrounding procedures. With this new feature, one can now program in *Maple* with better encapsulation. Lexical scoping actually provides a mechanism to do object oriented programming. Basic operations could be defined as functions

or procedures. A preliminary version of a new *Maple* package named '`fem.m`' was developed, which can automatically convert the obtained element stiffness matrix and internal forces into desired codes.

5 Concluding remarks

It must be pointed out that the work reported in this paper is only an initial exploration in the mentioned direction. The configuration described in Fig. 1 is not necessarily the optimal one, which needs more improvement and refinement to allow more special methods such as natural modes [5] to be implemented in the package. The package also needs update with new methods emerging.

References

[1] A. Eriksson and C. Pacoste, Symbolic software tools in the development of efficient finite elements, *Computers & Structures*, in press.

[2] J. C. Simo and M. S. Rifai, A class of mixed assumed strain methods and the methods of incompatible modes, *Int. J. Numer. Meth. Engng.*, **29**, 1595-1638, 1990.

[3] Y. H. Luo and A. Eriksson, An alternative assumed strain method, *Comput. Methods Appl. Mech. Engrg.*, **178**, 23-37, 1999.

[4] Y. H. Luo, Explanation and elimination of shear locking and membrane locking with field consistence approach, *Comput. Methods Appl. Mech. Engrg.*, **162**, 249-269, 1998.

[5] J. Argyris, L. Tenek and L. Olofsson, TRIC: a simple but sophisticated 3-node triangular element based on 6 rigid-body and 12 straining modes for fast computational simulations of arbitrary isotropic and laminated composite shells, *Comput. Methods Appl. Mech. Engrg.*, **145**, 11-85, 1997.

Disproving accepted hypotheses by means of CFD

Helge I. Andersson
Division of Applied Mechanics
Department of Applied Mechanics, Thermodynamics and Fluid Dynamics
Norwegian University of Science and Technology
N-7491 Trondheim, Norway
E-mail: Helge.I.Andersson@mtf.ntnu.no

Computerized flow analysis can be used to verify or disprove already accepted hypotheses pertaining to the physical behaviour of liquids and gases. In order to draw firm conclusions from CFD results, it is a prerequisite that the mathematical model to be solved is based on first principles and well-defined initial and boundary conditions. The governing equations should also be solved on a sufficiently fine mesh so that any grid-dependencies can be ruled out. Three examples are given in the presentation.

It is a generally accepted fact that the motion of a Newtonian fluid, i.e. liquid or gas, is governed by the Navier-Stokes equations, irrespective of whether the flow is laminar, transitional or turbulent. Thus, if the Navier-Stokes equations are integrated numerically on a sufficiently fine computational mesh, the resulting solution represents a true numerical realization of real fluid motion, thereby enabling firm conclusions to be drawn and hypotheses to be confirmed or rejected.

As a first example, we consider the shear-driven turbulent motion of an incompressible fluid between to parallel plates in relative motion; i.e. the plane Couette flow. The remarkable low level of turbulence energy measured in the core region of the flow led Schneider (1989) to postulate a significant diffusion of energy away from the core, i.e. in the direction of higher energy. We performed a direct numerical simulation (DNS) of a statistically steady plane Couette flow by means of a second-order accurate finite-difference technique for the time-dependent three-dimensional Navier-Stokes equations. The first- and second-order statistics compared well with available experimental data. However, data for the triple-velocity correlations were for the first time made available from the DNSs. These new data convincingly disproved the hypothesized counter-gradient diffusion of turbulence energy.

The next example is concerned with turbulent shear flows subjected to system rotation. It is well known that a shear flow is unstable with respect to the formation of counter-rotating streamwise-oriented vortices or roll cells if the background vorticity associated with the angular velocity of the rotating frame-of-reference is anti-parallel to the mean flow vorticity. It has so far been the prevailing assumption that the destabilizing Coriolis force also destabilizes the turbulence field; i.e. that the turbulent agitation is enhanced. To address this yet unproved hypothesis, a series of DNSs of rotating plane Couette flow were performed, simply by implementing Coriolis-force terms in the governing Navier-Stokes equations. The same finite-difference scheme as mentioned above was used to integrate the governing PDEs in time and space on a 256x70x256 mesh. A major observation was that the level of turbulence energy was reduced as compared to the non-rotating case when counter-rotating roll cells developed in the numerically generated flow field at moderate rotation rates.

Equally interesting was the observed increase in the turbulence level at higher rotation rates, at which the roll cells disappeared. We were thus able to conclude that the turbulence field is damped when roll cells are formed due to the destabilizing action of the Coriolis force field, i.e. contrary to the prevailing belief.

A final example is the laminar flow in a stenosed artery. In a computational study Johnston & Kilpatrick (1991) found that the flow resistance was reduced in the presence of surface irregularities as compared to the flow in a smooth stenosis. We recently reconsidered the same case adopting the irregular stenosis geometry obtained from an atherosclerotic main coronary artery casting of a man. The laminar flow was governed by the axisymmetric Navier-Stokes equations, which were solved numerically by a Galerkin finite-element method using the commercially available Polyflow package using up to 17945 grid elements. The results showed that the excess pressure drop predicted by Johnston & Kilpatrick (1991) across the smooth stenosis is not caused by its smoothness but is rather an effect of its higher degree of symmetry. We were moreover able to conclude that the flow resistance across the stenosed artery is practically unaffected by surface irregularities at low Reynolds numbers, whereas an excess pressure drop up to 10 per cent above that for a smooth stenosis is found for higher Reynolds numbers. The refined FEM analysis thus disproved the conclusion arrived at in the earlier investigation.

The computations were performed by Dr K.H. Bech (turbulent flows) and Ms R. Halden (laminar flows).

References

W. Schneider (1989) *Z. Flugwiss. Weltraumforsch.* **13**, 315-319.

P.R. Johnston & D. Kilpatrick (1991) *J. Biomech.* **24**, 1069-1077.

FREE SURFACE MODELLING BY THE LAGRANGIAN AND ARBITRARY LAGRANGE-EULERIAN APPROACHES

A. Kačeniauskas and **R. Kačianauskas**
Department Strength of Materials, Vilnius Gediminas Technical University
Saulėtekio 11, LT-2040 Vilnius, Lithuania

1. Introduction

Free surface flow governed by the Navier-Stokes equations is modelled by the finite element method. The Lagrangian (LA) and the Arbitrary Lagrange-Eulerian (ALE) approaches are used for problem formulation. The unsteady laminar newtonian and isothermal flow of viscous incompressible liquid is considered. The velocity correction method [1] is applied for the velocity pressure segregation in the Navier-Stokes equations. The numerical experiments simulate free oscillations in a tank. The influence of discretisation parameters on the accuracy of a numerical solution is investigated as well as the influence of an initial amplitude of oscillations and kinematics viscosity coefficient on the wave pattern. The detailed comparison of the numerical results obtained by the surface height method [2] based on ALE approach and prediction-correction method [3] based on LA approach is performed.

2. Physical model of the flow

The unsteady, laminar, newtonian and isothermal flow of viscous, incompressible liquid is investigated. The flow is described by the Navier-Stokes equations in LA or ALE reference frame

$$\rho\frac{Du_i}{Dt}=\rho F_i-\frac{\partial p}{\partial x_i}+\mu\Delta u_i, \tag{1}$$

$$\rho\left(\frac{\partial u_i}{\partial t}+(u_j-w_j)\frac{\partial u_i}{\partial x_j}\right)=\rho F_i-\frac{\partial p}{\partial x_i}+\mu\Delta u_i, \tag{2}$$

$$\frac{\partial u_i}{\partial x_i}=0, \tag{3}$$

where (p, u) is the vector of unknown primitive variables. It contains pressure p and velocity u, which consists of two components u_i, i=1, 2. ρ is the density, μ is dynamic viscosity coefficient, F=(0, -g) is gravity force, where g is the acceleration of gravity. The equation (1) of momentum conservation is written using purely LA approach, while equations (2) of momentum conservation is written considering ALE approach. The continuity equation (3) reefers to mass conservation.

In some investigated problems viscous stresses at the free surface are negligible compared to the inertial forces and can be neglected. This gives rise to a Dirichlet boundary condition for pressure and Newmann boundary condition for velocity on the free surface. Thus, the simplified boundary conditions on the free surface are

$$n_j\frac{\partial u_i}{\partial x_j}=0,\ p=p_{at}, \tag{4}$$

where $\boldsymbol{n}$ is the unit normal vector, p_{at} is the atmospheric pressure. Free surface height h could be computed from the free surface kinematic equation, which represents the fact that the interface is a material surface

$$\frac{\partial h}{\partial t}+u_1\frac{\partial h}{\partial x_1}=u_2, \tag{5}$$

Slip boundary conditions are prescribed on rigid walls. Zero initial conditions for both the velocity and pressure are used.

3. Segregated approach for the Navier-Stokes equations

In the present work we apply the velocity correction method, where velocity pressure segregation is done at the differential equation stage. The main advantages of this method are symmetric matrixes of finite element coefficients and equal order interpolation of velocity and pressure. Using ALE approach the velocity prediction

stage is stabilised by two steps Taylor-Galerkin procedure. The Lagrangian description of the flow does not include convective terms and velocity prediction is performed by the single step. It could be obtained from the second step dropping convective terms. Therefore, we only present segregated procedure for Navier-Stokes equations in ALE reference frame. The solution u^{n+1} at a given time step $t+dt$ is obtained in four steps described below.

The first step is a part of the Taylor-Galerkin stabilisation procedure. Intermediate velocities $\hat{u}$ are found using only the convective terms:

$$\hat{u}_i = u_i^n - \frac{dt}{2}(u_j^n - w_j^n)\frac{\partial u_i^n}{\partial x_j}. \tag{6}$$

The second step is the end of velocity prediction stage. Improved values of the predicted velocity u^* is obtained by substituting $\hat{u}$ in the convective terms of the first order Taylor-Galerkin equation:

$$\rho u_i^* = \rho u_i^n - dt\rho(u_j^n - w_j^n)\frac{\partial \hat{u}_i}{\partial x_j} + dt\ \rho F_i + dt\mu\Delta u_i. \tag{7}$$

It does not include the pressure term.

In the pressure calculation step the continuity equation for the velocity is replaced by a Poison equation for the pressure by using the predicted velocity u^* in the source term

$$\Delta p^{n+1} = \frac{\rho}{dt}\frac{\partial u_j^*}{\partial x_j}. \tag{8}$$

Gresho and Sani [4] have shown that the new pressure contributions make the velocity field divergence-free. The normal gradient of the pressure should satisfy consistent boundary conditions [4].

In the final step values of corrected velocity u^{n+1} are calculated by updating predicted velocities u^* with the contribution from the new pressure field

$$\rho u_i^{n+1} = \rho u_i^* - dt\frac{\partial p^{n+1}}{\partial x_i}. \tag{9}$$

4. Finite element formulation

The solution domain S is discretised by quadrilateral finite elements. Equal order bilinear shape functions are used for both the pressure and velocity components. These shape functions are used as weighting functions for all steps of the velocity correction method. The weak formulation of equations (6-9) could be found in the reference [5]. The Green-Gauss theorem is applied to both sides of equation (8) of pressure calculation step. In this particular case the pressure satisfies the consistent boundary conditions and solution should be more exact near the boundaries of a solution domain. The weak point of the applied segregated approach is strict limitations to the time step. This is due to semi-explicit formulation of the velocity prediction step.

Using LA approach the material time derivative can be approximately determined by the functions known at both deformed and undeformed positions during a short time increment. The function at the deformed position can not be obtained before computation. Thus, iterative computation is necessary. The procedure introduced by Ramaswamy *et al.* [3] is employed in this investigation. At the initial step of iterations and at the m-th step of iterations the location of a nodal point $x_i^{n+1(m)}$ at the time $t+dt$ is computed as

$$x_i^{n+1(0)} = x_i^n + dtu_i^n,\ x_i^{n+1(m)} = x_i^n + (dt/2)(u_i^n + u_i^{n+1(m-1)}), \tag{10}$$

where dt is a time increment, x_i^n is the location of a nodal point at the time t, u_i^n is the velocity of a nodal point at the time t. The superscripts in brackets mean the number of iteration. The three steps of the velocity correction method are performed at each iteration and velocity $u_i^{n+1(m-1)}$ is updated in (10) formula.

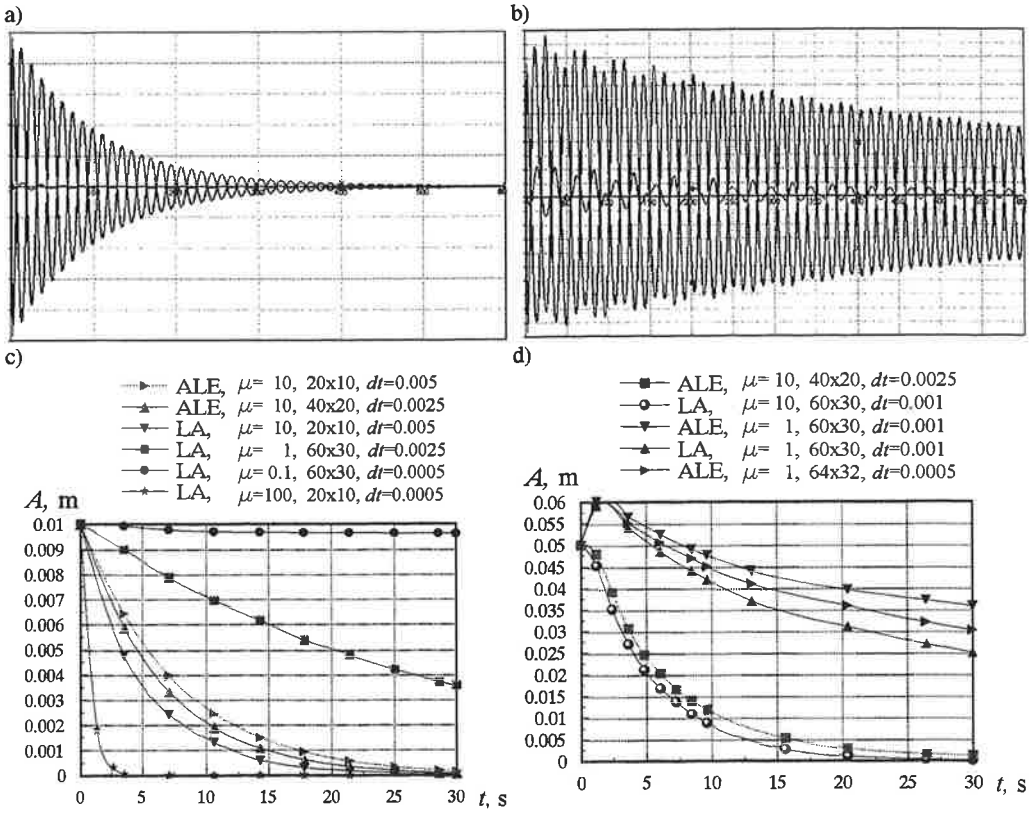

Figure 2. Free oscillations in the tank. The time histories of the amplitude. The displacements of two free surface boundary points and the center point are plotted in (a) and (b). The curves of maximal amplitude for different methods, viscosity coefficients and time steps are plotted in (c) and (d):
a) Lagrangian approach, A=0.01 m, μ=10 m^2/s, finite element mesh 20x10, time step dt=0.005 s,
b) Lagrangian approach, A=0.05 m, μ=1 m^2/s, finite element mesh 60x30, time step dt=0.001 s,
c) A=0.01 m, d) A=0.05 m

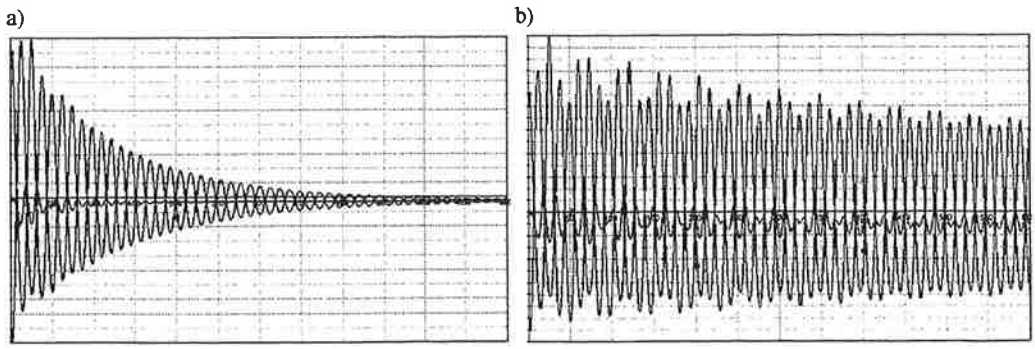

Figure 3. The time histories of the amplitude of oscillations, A=0.1 m, Arbitrary Lagrange-Eulerian approach:
a) μ=10 m^2/s, finite element mesh 40x20, time step dt=0.0025 s,
b) μ=1 m^2/s, finite element mesh 60x30, time step dt=0.001 s

Using ALE approach two steps Taylor-Galerkin procedure is applied for the stabilisation of the convective terms in the velocity prediction stage. The position of the free surface is obtained solving equation (5) at each time step. The linear shape functions N are used for surface height interpolation in equation (5). The convective terms are stabilised by Petrov-Galerkin method. The stream line diffusion terms are added to finite element formulation using particular weighting functions W. The equation (5) is discretised in time using Cranc-Nicolson scheme (θ=0.5). The ALE approach needs the algorithm of mesh movement. The surface height method and structured finite element meshes allow using very simple algorithm. Mesh does not move in x_1 direction. The locations of nodal points that are equally distributed in x_2 direction could be computed as

$$x_2^{n+1} = x_2^n + (h^{n+1} - h^n)\frac{x_2^n}{h^n}, \tag{11}$$

5. Numerical results and discussions

Numerical experiments simulate free oscillations in a rectangular tank. All numerical tests are performed using C++ library DIFFPACK [6]. The initial free surface is described by the sinusoidal curve $h(x_1, t=0) = 0.5 + A \cdot sin(\pi x_1)$. The density of a liquid ρ=1000 kg/m^3. The influence of the different initial amplitudes (A=0.01, 0.05, 0.1 m) to the flow pattern is investigated as well as the influence of different kinematic viscosity (μ=100, 10, 1, 0.1 m^2/s). The wave pattern (fig. 1) is regular for small initial amplitudes and large viscosity (small Reynolds numbers). Both investigated methods produce results that are in good qualitative agreement with the numerical results obtained in [3]. Fig. 2 shows displacements of nodal points allocated on the centre line of the tank. The solution becomes highly non-linear and non-regular for waves with large amplitudes (A=0.05, 0.1 m) and small viscosity. The predictor-corrector method based on LA approach is not applicable to flows with large displacements. Therefore, investigated flows with A=0.1 m are simulated using only surface height method based on ALE approach. Fig. 3 shows the maximal displacements of selected nodal points. The efficiency and accuracy of the predictor-corrector and surface height methods are compared for different initial amplitudes, viscosity coefficients and numerical parameters. It is very difficult to solve free surface kinematic equation (5) accurately for large surface deformations. An accurate solution requires very dens finite element mesh and small time steps.

5. Conclusions

Free surface flow governed by the Navier-Stokes equations is investigated. Free oscillations in a tank are modelled by finite element method. The predictor-corrector method based on Lagrangian approach and the surface height method based on Arbitrary Lagrange-Eulerian approach are investigated. The comparison of accuracy, efficiency and applicability of the methods is presented. The predictor-corrector method is more accurate and allows using coarser finite element meshes and larger time steps. The range of applicability of this method is very limited by large deformations of the mesh. The surface height method is more universal. The accurate solution of the oscillations with large amplitudes requires a big amount of computational resources.

Acknowledgements

We wish to thank Det Norske Veritas and Research Council of Norway for financial support.

References

1. M. Kawahara and K. Ohmiya. *Finite Element Analysis Of Density Flow Using The Velocity Correction Method.* Int. J. Numerical Methods in Fluids, 1986, 6, pp. 659-672.
2. R.E. Nickell, R.I. Tanner and B. Coswell. *The Solution Of Viscous Incompressible Jet And Free-Surface Flows Using Finite Element Method.* J. Fluid Mechanics, 1974, 65, pp. 189-206.
3. B. Ramaswamy, M. Kawahara and T. Nakayama. *Lagrangian Finite Element Method For The Analysis Of Two- Dimensional Sloshing Problems.* Int. J. Numerical Methods In Fluids, 1986, 6, pp. 659-670.
4. P.M. Gresho and R.L. Sani. On Pressure Boundary Conditions For The Incompressible Navier-Stokes Equations. Int. J. Numerical Methods in Fluids, 1987, 7, pp. 1111-1145.
5. A. Kačeniauskas, G. Skeie. *Modelling of Viscous Incompressible Flow with Free Surface by Level Set Method and Finite Elements.* Proc. from the International Symposium on Computational Methods for Fluid – Structure Interaction (eds. T. Kvamsdal *et al.*). Tapir Publishers, Trondheim, 1999, pp. 305-314.
6. H.P. Langtangen. *Computational Partial Differential Equations, Numerical Methods and Diffpack Programming.* Lecture Notes in Computational Science and Engineering, 2, Springer-Verlag, 1999.

Flow noise in a centrifugal pump *

Mikael A. Langthjem and Niels Olhoff
Institute of Mechanical Engineering, Aalborg University
Pontoppidanstræde 101, DK-9220 Aalborg East, Denmark

Keywords: flow with rotating mechanical components, discrete vortex method, acoustic analogy, fluid-structure interaction, boundary elements, finite elements

1 Introduction

Lighthill (1952) introduced the *acoustic analogy* to obtain *estimates* of jet noise. This type of noise originates in hydro/aero-dynamic forces and flow motions, rather than by externally applied forces such as in structural acoustics. Lighthill's basic idea was to reorder Navier-Stokes equations into a wave-equation with an acoustic source term on the right-hand side,

$$\left(\partial^2/c_0^2\partial t^2 - \nabla^2\right)\rho = \partial^2 T_{ij}/\partial x_i \partial x_j. \tag{1}$$

Here ρ is the density of the fluid, t is the time, c_0 is the speed of sound, x_j $(j = 1, 2, 3)$ are the spatial coordinates and T_{ij} is the stress tensor,

$$T_{ij} = \rho v_i v_j + (p - c_0^2\rho)\delta_{ij}, \tag{2}$$

where v_j is the velocity field, p is the pressure and δ_{ij} is the Kronecker delta. The double suffix summation convention is applied. Practical calculations are obtained by using for T_{ij} an estimate based on the equations of motion for an incompressible fluid. Acoustic back-reaction is thus ignored. It can be mentioned that T_{ij} corresponds to an acoustic *quadropole*.

In two recent papers, estimates of the acoustic pressure due to rotating elements were obtained by making use of the *discrete vortex method* to obtain estimates of the velocity field (as input to the acoustic analogy). Jeon and Lee (1999) calculated the acoustic pressure from a centrifugal pump impeller rotating nearby a wedge (but otherwise in free space). Yin, Ahmed and Dobrzynski (1999) studied the aeroacoustics of a non-uniformly rotating propeller. In the present work, the same basic idea is used to calculate the noise generation in a volute-type centrifugal pump. The differences between our analysis and that of Jeon and Lee are mainly the following: (*i*) in our problem the impeller rotates inside a spiral casing and the reflection and scattering of sound from it is included in the analysis (Jeon and Lee ignored the acoustic influence of the wedge), and (*ii*) the casing is compliant and full fluid-structure interaction is included.

The present extended abstract describes the mathematical formulation of the problem.

2 The discrete vortex method

A series of excellent experiments on the flow structure within the volute of a centrifugal pump has been conducted by Chu, Dong and Katz. In their paper from 1995 the pressure inside the

*Extended abstract, NSCM-12, October 22-23, 1999

volute is calculated from measured velocities[1] by using the Reynolds equation

$$\frac{\partial p}{\partial x_i} = -\rho \left[\frac{\partial v_i}{\partial t} + v_j \frac{\partial v_i}{\partial x_j} + \frac{\partial}{\partial x_j} (\overline{v_i' v_j'}) \right]. \tag{3}$$

Viscous stresses are ignored due to a high value of Reynolds number. The velocities v_j are phase-averaged. Turbulence is represented by the velocoties v_j' which are deviations of the instantaneous velocities, at a certain impeller orientation, from the phase-averaged values. The experiments are carried out using a pump with a 'two-dimensional' volute and two-dimensional calculations ($i, j = 1, 2$) compare well with measured data. It is found that turbulence (represented by the third term on the right-hand side of (3)) can be ignored but the vorticity

$$\partial v_2 / \partial x_1 - \partial v_1 / \partial x_2$$

gives a major contribution to the total pressure variation. The main conclusion is thus that *a potential flow model cannot provide an acceptable description of the flow.*

The discrete vortex method (DVM) was introduced by Rosenhead in 1931. It is an instationary, Lagrangian, grid-free method which is very useful to simulate flows with strong vortical structure. It was originally formulated for inviscid flows but has recently been formulated for viscous flows also. In the original, inviscid formulation the flow is modelled by a collection of discrete singularities, such as sinks, sources and vortices derived from potential flow theory. Each singularity induces a flow around it. In the centrifugal pump the blades of the impeller are covered with vortex elements with discrete, bound vortices. The inlet is modelled by a point source and the casing is covered with source panels. In an inviscid fluid, vorticity can only be generated at boundaries. In the DVM this is introduced by wake vortices shed from the trailing edges of the impeller blades and convected downstream with the local induced velocity. The local velocities determine the strength of a shed particle. Kelvin's theorem states that the total vortex strength must remain constant for any closed curve enclosing the same fluid particles. For the case of a centrifugal impeller this can be accounted for by demanding that the sum of all bound vortices on, and all shed vortices from, each individual blade must be zero at any time. Another condition to determine the strengths of the singularities is that the normal components of the induced velocities must match the normal velocities of the bounding solid surfaces and of the rotating impeller blades. This sums up, then, to an equation system of the form

$$\mathbf{J\Gamma} = \mathbf{v} \tag{4}$$

where $\mathbf{J}$ is a matrix which represents the singularity type and the geometry, $\mathbf{\Gamma}$ is the sought vector of vortex/source strengths and $\mathbf{v}$ is a vector of normal velocities (and zeroes for the Kelvin conditions).

3 Computation of acoustic pressure fluctuations

The apprach taken here to estimate the acoustic effects of the rotating impeller is to idealize it as a collection of discrete, time-dependent forces $\mathbf{f}_n(t)$, $n = 1, 2, ..., NF$, acting on the surrounding fluid inside the volute. These forces are calculated by obtaining the velocity field from the DVM and then evaluating the pressures at the control points on the impeller blades by using the instationary Bernoulli equation.

Isolated forces are acoustically equivalent to dipoles. Instead of (1) the starting point is thus taken in the equation

$$\left(\partial^2 / c_0^2 \partial t^2 - \nabla^2 \right) \rho' = -Q(\mathbf{x}, t), \tag{5}$$

[1]Obtained by Particle Displacement Velocimetry.

with

$$Q(\mathbf{x},t) = \sum_{n=1}^{NF} \left(\frac{\partial f_i}{\partial y_i}\right)_n \delta(\mathbf{x}-\mathbf{y}_n) = \sum_{n=1}^{NF} \nabla_{\mathbf{y}} \cdot \mathbf{f}_n \delta(\mathbf{x}-\mathbf{y}_n) \tag{6}$$

as the acoustic source term. Here $\rho' = \rho - \rho_0$ is the density perturbation of the fluid (ρ_0 is the density of the undisturbed fluid), $\mathbf{y}_n = \mathbf{y}_n(t)$ are the time-dependent coordinates for the NF moving forces and δ is the Dirac delta function.

With a compliant casing, the pressure boundary condition is

$$\mathbf{n} \cdot \nabla p = -\rho_0 \mathbf{n} \cdot \frac{\partial^2 \mathbf{d}_S}{\partial t^2} \tag{7}$$

where $\mathbf{n}$ is the normal vector and $\mathbf{d}_S$ is the surface displacement. If the casing is stiff, the left-hand side is set equal to zero.

In order to solve (5) we must solve the corresponding equation

$$\left(\partial^2/c_0^2\partial t^2 - \nabla^2\right) G = -\delta(\mathbf{x}-\mathbf{y})\delta(t-\tau), \tag{8}$$

for the Green's function $G(\mathbf{x},\mathbf{y},t,\tau)$. The solution in unbounded space is given by

$$G(\mathbf{x},\mathbf{y},t,\tau) = \frac{\delta(t-\tau-|\mathbf{x}-\mathbf{y}|/c_0)}{4\pi c_0^2 |\mathbf{x}-\mathbf{y}|}. \tag{9}$$

Now we multiply (5)by G and (8) by ρ', and after that subtract these two equations. This gives

$$\rho'\delta(\mathbf{x}-\mathbf{y})\delta(t-\tau) = GQ - \left[\rho'\frac{\partial^2 G}{\partial t^2} - G\frac{\partial^2 \rho'}{\partial t^2}\right] + c_0^2\left(\rho'\nabla^2 G - G\nabla^2\rho'\right). \tag{10}$$

It can be shown that the square-bracket is equal to zero. Integrations over the whole space $\mathbf{y}$ and over all times τ, and use of Green's theorem, then gives the perturbation pressure as

$$p'(\mathbf{x},t) = \sum_{n=1}^{NF} \frac{\nabla_{\mathbf{y}} \cdot \mathbf{f}_n(\mathbf{y}_n, t-|\mathbf{x}-\mathbf{y}_n|/c_0)}{4\pi|\mathbf{x}-\mathbf{y}_n|} + c_0^2 \int_S \left[p'\mathbf{n}\cdot\nabla G + \rho_0 G\mathbf{n}\cdot\frac{\partial^2 \mathbf{d}_S}{\partial t^2}\right] d^2\mathbf{y} \tag{11}$$

after the pressure boundary condition (7) has been inserted and it has been used that $p' = c_0^2\rho'$. S represents the casing surface. It should be noticed that the square bracket also must be evaluated to the retarded time $t_r = t - |\mathbf{x}-\mathbf{y}|/c_0$.

Numerical evaluation of the acoustic pressure

The surface integral in (11) is evaluated numerically by making use of boundary elements. The casing surface is divided into NE elements. Within each element (symbolized by a subscript e), casing displacements are divided into normal and tangential components and expanded as

$$d_n(\mathbf{x}_e) = \mathbf{n}\cdot\mathbf{d}_S(\mathbf{x}_e) = \mathbf{w}_n^T\mathbf{a}_{ne}, \quad d_\tau(\mathbf{x}_e) = \mathbf{t}\cdot\mathbf{d}_S(\mathbf{x}_e) = \mathbf{w}_\tau^T\mathbf{a}_{\tau e}, \tag{12}$$

and perturbation pressure as

$$p'(\mathbf{x}_e) = \mathbf{w}_n^T\mathbf{b}_e. \tag{13}$$

Here $\mathbf{w}_n$ and $\mathbf{w}_\tau$ are shape functions for the normal and the tangential components, respectively, and $\mathbf{t}$ is the tangential vector. From a variational formulation we obtain, by using (11, 12, 13), the linear equation system

$$(\mathbf{D}-\mathbf{F})\mathbf{b} = \mathbf{q} + \mathbf{G}\ddot{\mathbf{a}}_n, \tag{14}$$

where an 'overdot' denotes differentiation w.r.t. time t. The matrices are given by

$$\mathbf{D} = \sum_{e=1}^{NE} \int_{S_e} \mathbf{w}_n \mathbf{w}_n^T dS_e, \quad \mathbf{F} = c_0^2 \sum_{e=1}^{NE} \int_{S_e} \mathbf{w}_n \left\{ \int_{S_e} \mathbf{w}_n^T (\mathbf{n} \cdot \nabla G) dS_e \right\} S_e,$$
$$\mathbf{q} = \sum_{e=1}^{NE} \sum_{k=1}^{NF} \int_{S_e} \mathbf{w}_n \frac{\nabla_{\mathbf{y}} \cdot \mathbf{f}_k}{4\pi |\mathbf{x} - \mathbf{y}_k|} dS_e, \quad \mathbf{G} = \rho_0 c_0^2 \sum_{e=1}^{NE} \int_{S_e} \mathbf{w}_n \left\{ \int_{S_e} G \mathbf{w}_n^T dS_e \right\} S_e. \tag{15}$$

Fluid-structure interaction
The dynamics of the casing is, in finite element formulation, described by

$$\begin{bmatrix} \mathbf{M}_{11} & \mathbf{0} \\ \mathbf{0} & \mathbf{M}_{22} \end{bmatrix} \begin{Bmatrix} \ddot{\mathbf{a}}_n \\ \ddot{\mathbf{a}}_\tau \end{Bmatrix} + \begin{bmatrix} \mathbf{C}_{11} & \mathbf{0} \\ \mathbf{0} & \mathbf{C}_{22} \end{bmatrix} \begin{Bmatrix} \dot{\mathbf{a}}_n \\ \dot{\mathbf{a}}_\tau \end{Bmatrix} + \begin{bmatrix} \mathbf{K}_{11} & \mathbf{K}_{12} \\ \mathbf{K}_{21} & \mathbf{K}_{22} \end{bmatrix} \begin{Bmatrix} \mathbf{a}_n \\ \mathbf{a}_\tau \end{Bmatrix}$$
$$= \begin{Bmatrix} \mathbf{f}_n \\ \mathbf{f}_\tau \end{Bmatrix} - \begin{bmatrix} \mathbf{H}_{11} & \mathbf{0} \\ \mathbf{0} & \mathbf{0} \end{bmatrix} \begin{Bmatrix} \mathbf{b} \\ \mathbf{0} \end{Bmatrix} \tag{16}$$

where $\mathbf{M}_{ii}$ are mass matrices, $\mathbf{C}_{ii}$ are damping matrices, $\mathbf{K}_{ij}$ are stiffness matrices, $\{\mathbf{f}_n, \mathbf{f}_\tau\}^T$ is an external forcing vector, and $\mathbf{H}_{11}$ is the fluid-structure coupling matrix. The pressure vector $\mathbf{b}$ can be isolated from (14) and inserted in (16) to give an equation system in $\mathbf{a} = \{\mathbf{a}_n, \mathbf{a}_\tau\}^T$ and its time derivatives. Once $\ddot{\mathbf{a}}_n$ is known the pressure fluctuations can be determined from (13) and (14). The DMV equation (4) must be solved together with (14) and (16) at every time step. As (4) depends non-linearly on the casing geometry, the system of (4), (14) and (16) must be updated iteratively.

4 Concluding remarks

Our aim is to use the present method as a tool in Multidisciplinary Design Optimization. Future work on the present problem will include shape optimization of the tongue geometry, to minimize the flow noise level. It is clear that the noise level can be easily decreased if the hydrodynamic efficiency also is allowed to decrease. The optimization problem must then necessarily include a constraint on the efficiency.

Acknowledgements
Financial support from Aalborg University, Grundfos A/S, the Alexander von Humbolt Foundation, and the Danish Ministry of Research is gratefully acknowledged.

References

[1] Chu, S., Dong, R. & Katz, J. 1995 Relationship between unsteady flow, pressure fluctuations, and noise in a centrifugal pump - Part A: Use of PVD data to compute the pressure field. *Journal of Fluids Engineering* **117**, 24-29.

[2] Jeon, W.-H. & Lee, D.-J. 1999 An analysis of the flow and aerodynamic acoustic sources of a centrifugal impeller. *Journal of Sound and Vibration* **222**(3), 505-511.

[3] Lighthill, M.J. 1952 On sound generated aerodynamically. I. General theory. *Proceedings of the Royal Society (London)* **211** (A), 564-587.

[4] Yin, J.P., Ahmed, S.R. & Dobrzynski, W. 1999 New acoustic and aerodynamic phenomena due to non-uniform rotation of propellers. *Journal of Sound and Vibration* **225**(1), 171-187.

On the Equilibrium of Self-Aligning Hybrid Bearings

Mikko Lyly

VTT Manufacturing Technology
Maritime and Mechanical Engineering
P.O.Box 1705, FIN-02044 VTT, Finland

1. Introduction. In hybrid antifriction bearings, the distribution of the oil pressure is usually modelled by the Reynolds equation [1,2]. From the pressure one can then derive velocities, net-flows and other related functions, which describe the mechanical behaviour of the system. In self-aligning hybrid bearings, the Reynolds equation has to be coupled with appropriate equilibrium equations. In this paper we will discuss the modelling of such bearings. We first derive the equilibrium equations for a simple model bearing, and then solve them numerically by the finite element method. The modelling principles can be extended to cover also other self-aligning bearing configurations.

2. Preliminaries. Let us consider the hybrid bearing described in Figure 1. The lower surface of the bearing is assumed to consist of the lubrication surface Ω and relatively deep oil pockets Ω_i, $i = 1, 2, \ldots, N$. The position of the self-aligning pedestal is described by the transverse displacement Δ and rotation $\alpha << 1$ about the support pin. The thickness of the lubrication film is then given by $h = \bar{h} + \Delta + \alpha x$, where $\bar{h} = \bar{h}(x, y)$ is the film thickness in the reference configuration with $\Delta = \alpha = 0$.

The distribution of the oil pressure $p = p(x, y)$ on the lubrication surface Ω is modelled by the Reynolds equation

$$-\nabla^T(k\nabla p) = f, \tag{1}$$

where $\nabla = (\frac{\partial}{\partial x}, \frac{\partial}{\partial y})^T$. The equation is subjected to the following boundary conditions:

$$p = 0 \text{ on } \partial\Omega \quad \text{and} \quad p = P_i \text{ on } \partial\Omega_i, \; i = 1, 2, \ldots, N, \tag{2}$$

where P_i is the oil pressure in the pocket Ω_i. Here $k = h^3/\mu$ is the "stiffness" of the lubrication film and $f = -6U\frac{\partial h}{\partial x}$, where U is the speed of the upper surface in the x-direction. $\mu = \mu(x, y)$ is the dynamic viscosity of the oil.

The velocity $\mathbf{u} = \mathbf{u}(x, y, z) = (u_x(x, y, z), u_y(x, y, z))^T$ of the oil is obtained from

$$\mathbf{u} = \frac{z(z-h)}{2\mu}\nabla p + \frac{z}{h}\mathbf{U}, \tag{3}$$

where $\mathbf{U} = (U_x, U_y)^T$ is the constant velocity of the upper surface with $U_x = U$ and $U_y = 0$. In the transverse direction there is no flow, i.e., $u_z = 0$.

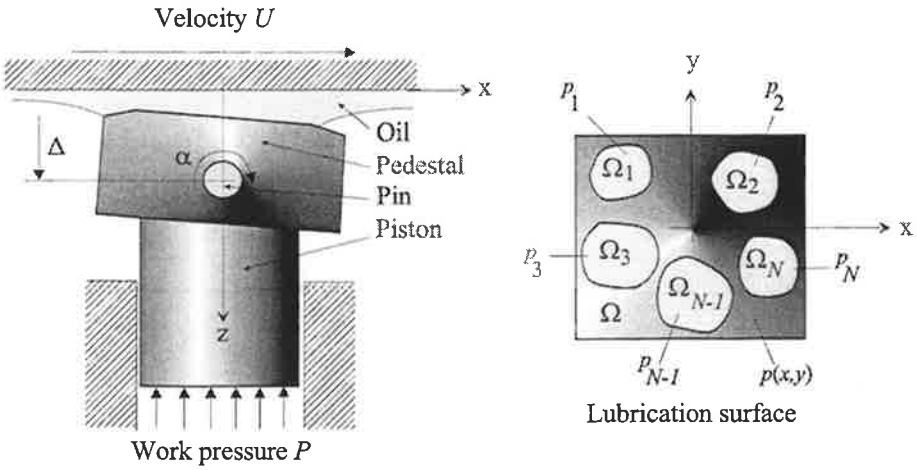

Figure 1. The self-aligning hybrid bearing. The oil pockets Ω_i are connected to the pressure source by thin capillary tubes, with capillary coefficients k_i.

3. Equilibrium. Let us consider the equilibrium of the system. Since the work pressure of the bearing is P, the support pin of the pedestal is subject to the reaction force

$$F^{int} = PA, \tag{4}$$

where A is the area of the cross section of the piston. The moment about the pin vanishes:

$$M^{int} = 0. \tag{5}$$

The oil pockets Ω_i are connected to the pressure source by thin capillary tubes, with capillary coefficients k_i. Hence, the net-flows into the pockets are obtained from

$$q_i^{int} = \frac{P - P_i}{k_i \mu}, \quad i = 1, 2, \ldots, N. \tag{6}$$

The problem is now to determine the displacement Δ, the rotation α, and the oil pressures P_i, $i = 1, 2, \ldots, N$, such that the pedestal is in equilibrium. In order to do this, we first note that the pin is subject to the resultant $F^{ext} = F^{ext}(\Delta, \alpha, P_1, P_2, \ldots, P_N)$ of the pressure on the lower surface of the bearing:

$$F^{ext} = \sum_{i=1}^{N} \text{Area}(\Omega_i) P_i + \int_\Omega p \, dxdy. \tag{7}$$

The moment $M^{ext} = M^{ext}(\Delta, \alpha, P_1, P_2, \ldots, P_N)$ about the pin is calculated from

$$M^{ext} = \sum_{i=1}^{N} \text{Area}(\Omega_i) P_i x_i + \int_\Omega px \, dxdy + HS, \tag{8}$$

where x_i is the x-co-ordinate of the midpoint of Ω_i, H is the average distance in the z-direction from the lubrication surface to the pin, and $S = S(\Delta, \alpha, P_1, P_2, \ldots, P_N)$ is the total shear force on the lubrication surface and pockets:

$$S = \sum_{i=1}^{N} \text{Area}(\Omega_i) \tau_i + \int_\Omega \tau \, dxdy. \tag{9}$$

Here $\tau_i \approx 0$ and $\tau = \mu \frac{\partial u_x}{\partial z}|_{z=h}$ are the shear stresses on Ω_i and Ω, respectively.

The net flow $q_i^{ext} = q_i^{ext}(\Delta, \alpha, P_1, P_2, \ldots, P_N)$ out of the pocket Ω_i is obtained from

$$q_i^{ext} = \int_{\partial\Omega_i}\int_0^h \mathbf{n}^T\mathbf{u}\, dz\, ds = -\frac{1}{12}\int_{\partial\Omega_i} k(\mathbf{n}^T\nabla p)\, ds + \frac{1}{2}\int_{\partial\Omega_i} h(\mathbf{n}^T\mathbf{U})\, ds, \tag{10}$$

where $\mathbf{n} - (n_x, n_y)^T$ is the unit outward normal to the boundary.

Setting $F^{int} = F^{ext}$, $M^{int} = M^{ext}$, and $q_i^{int} = q_i^{ext}$, $i = 1, 2, \ldots, N$, we get $N + 2$ equilibrium equations from which the $N + 2$ parameters Δ, α, and $P_1, P_2, \ldots, P_N$ may be determined. The equations can be written more concisely as

$$\mathbf{f}(\mathbf{x}) = \mathbf{0}, \tag{11}$$

where $\mathbf{x} = (\Delta, \alpha, P_1, P_2, \ldots, P_N)^T$ is the vector of unknowns, and $\mathbf{f}$ is a vector valued function of "equilibrium errors." The equation is non-linear.

4. Numerical solution. The Reynolds equation (1) may be solved efficiently by the finite element method. Writing

$$p \approx \sum_{i=1}^{n} \phi_i p_i, \tag{12}$$

where $\phi_i = \phi_i(x, y)$, $i = 1, 2, \ldots, n$, are the shape functions for the pressure, the finite element discretization of (1) leads to the following matrix equation:

$$\mathbf{KP} = \mathbf{F}, \tag{13}$$

where $\mathbf{K} = [k_{ij}]$ is the stiffness matrix, $\mathbf{P} = (p_1, p_2, \ldots, p_n)^T$ is the unknown dof-vector and $\mathbf{F} = (f_1, f_2, \ldots, f_n)^T$ is the force vector:

$$k_{ij} = \int_\Omega k\nabla\phi_i^T\nabla\phi_j\, dxdy \quad \text{and} \quad f_i = \int_\Omega f\phi_i\, dxdy, \quad i, j = 1, 2, \ldots, n. \tag{14}$$

The non-homogenous boundary conditions along the edges may be taken into account by standard means.

The equilibrium equation (11) may be solved e.g. by standard pattern search methods.

5. Numerical results. In this section we will give numerical results for the self-aligning hybrid bearing of Figure 2. In the same figure is shown the adaptive finite element mesh of linear triangular elements used in the calculations. The velocity and pressure are allowed to vary in the ranges $0 \le U \le 30\ \frac{m}{s}$ and $10\ bar \le P \le 100\ bar$, respectively. The dynamic viscosity of the oil is $\mu = 0.05\frac{kg}{ms}$. The capillary coefficients of the oil pockets are $k_i = 10^{12}\frac{1}{m^3}$, $i = 1, 2, 3, 4$. The main dimensions of the lubrication surface are $20\ cm \times 20\ cm$.

Figure 3 shows the pressure on the lubrication surface and in the oil pockets when $U = 20\ \frac{m}{s}$ and $P = 60\ bar$. Figures 4 and 5 give the average film thickness and rotation about the pin with respect to the velocity of the upper surface and work pressure. The solution time was a couple of hours on a standard personal computer.

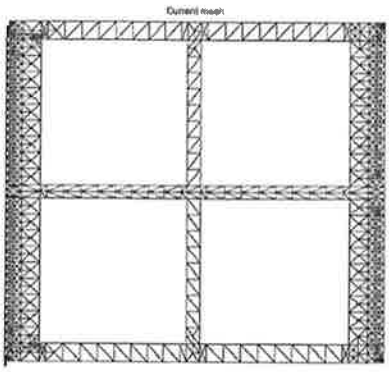

Figure 2. Geometry and finite element mesh of the lubrication surface.

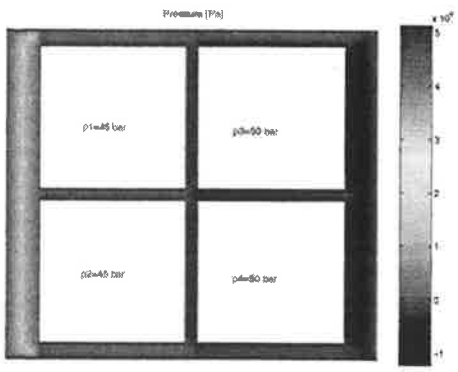

Figure 3. Pressure on the lubrication surface and oil pockets.

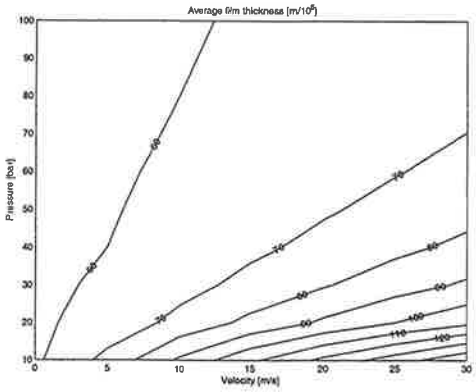

Figure 4. Average film thickness.

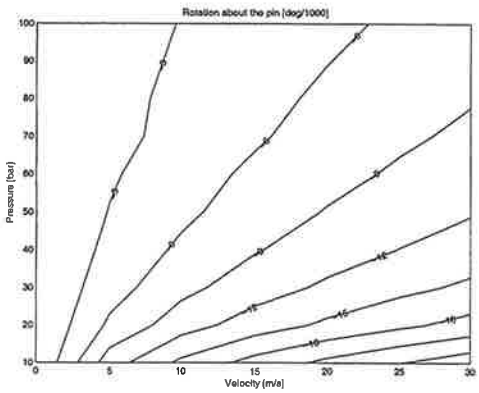

Figure 5. Rotation about the pin.

REFERENCES

[1] W.B. Rowe. Hydrostatic and hybrid bearing design. Butterworths, London, 1983. 240 pp. ISBN 0-408-01324-9.

[2] R. Bassani and B. Piccigallo. Hydrostatic lubrication. Elsevier, Amsterdam, 1992. 452 pp. ISBN 0-444-88498-x.

Two-dimensional CFD Modelling of the filling and emptying of the left Ventricle during a Cardiac Cycle using CFX4.2

Lotte T. Sørensen[1], Jens I. Madsen[2], Thomas J. Condra[1], Egon Toft[3]

[1]Institute of Energy Technology, Aalborg University
Pontoppidanstræde 101, DK-9220 Aalborg, Denmark
[2]Institute of Mechanical Engineering, Aalborg University
[3]Department of Cardiology, Aalborg University Hospital

Abstract: The overall behaviour of the human heart is reasonably well understood, while the hemodynamics involved in filling and emptying the heart chambers remain to be described satisfactorily. In this paper, the commercial CFD-code CFX4.2 has been used to model the blood flow in the left ventricle of the heart over an entire cardiac cycle. The elasticity of the heart wall is considered using a spring model to mimic the muscles of the myocardium (heart wall), which during the active state deform due to the contraction of the muscles, and during the passive state deform due to the pressure inside the ventricle. Due to lack of information on the elastic properties of the myocardium, these are identified so that the numerical model complies with the measured variation in ventricular volume in a least-squares sense.

Keywords: CFD, blood flow, heart mechanics, system identification

Introduction

Circulatory disorders account for about three out of four human deaths (Liepsch and Moravec, 1984), which underlines the importance of understanding the behaviour of the human heart. Moreover, in order to set the correct diagnostic treatment, it is important to understand the mechanisms involved in different disorders. For example, the initiation and immediate consequences of coronary thrombosis and occlusion must be understood, if the result of treatment is to be predicted. However, due to the complex physiology of the heart, involving metabolical, electrophysiological, and mechanical processes, cardiologists base their diagnosis on a comparison of clinical examinations with a large body of accumulated experience.

A reliable mathematical model of the physical behaviour of the heart would be of invaluable assistance in the understanding of pathophysiologic changes. The mathematical model should include the possibility of simulating pathological conditions, e.g. changing the local elastic properties of the heart wall to simulate suspected changes after e.g. myocardial infarction. Moreover, a numerical model may replace some of the clinical testing with new medical or surgical treatments, which may be both time consuming and ethically questionable. A further advantage is that one can simulate different treatments under identical conditions, which is not clinically feasible, because of the unpredictability of the results, as no two hearts have identical properties.

Related work on modelling cardiac mechanics, both fluid and solid, has been carried out by Peskin (1996). Extensive studies on heart wall deformations, under normal and pathological conditions, have been attempted by amongst others Nash (1998) and Rijcken (1998).

The heart is a muscular organ that pumps blood through the cardiovascular system, see Figure 1. It consists of two parts; a right part that maintains the pulmonary circulation required for oxidation of the blood, and a left part that maintains the systemic circulation, i.e. the remaining circulatory system. Each part consists of two chambers: an atrium (RA, LA) collecting blood returning from circulation and a ventricle (RV, LV) delivering the actual pumping action by cyclic muscle contractions activated by electric impulses.

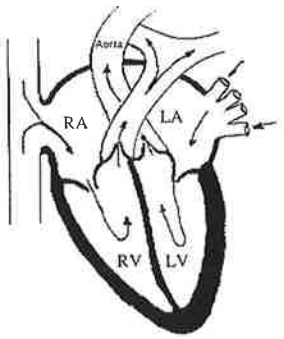

Figure 1: The heart, RA, LA, RV, and LV are the right and left atrium, and the right and left ventricle respectively (Folkow, 1971).

The left atrium (LA) is connected to the left ventricle (LV) by the mitral valve. The blood leaves the left ventricle and flows into the aortic artery via the aortic valve. Correspondingly, for the right side of the heart, the blood enters the ventricle through the tricuspid valve and exits through the pulmonary valve.

The present work aims at modelling the fluid mechanics of a cardiac cycle, taking into consideration the elastic behaviour of the heart wall. The study is limited to the left ventricle, since this is the more critical part, in the sense that it raises pressure by about four times as much as its right counterpart does.

Consider the left part of the heart (right hand of Figure 1). At the beginning the cardiac cycle, the ventricular volume is at its maximum, and both the mitral and aortic valves are closed. The ventricular muscle fibres then contract, leading to a pressure rise in the ventricle (iso-volumetric contraction). At some point, the ventricular pressure exceeds the aortic pressure, which causes the aortic valve to open. Under continued contraction of the muscles, the blood is ejected from the ventricle (ventricular ejection). When the pressure in the aorta exceeds the ventricular pressure again, the aortic valve closes. The ventricular muscles relax, enlarging the ventricular volume so that the pressure drops below that of the atrium, thereby opening the mitral valve (isovolumetric relaxation). Blood enters the left ventricle due to the pressure difference over the valve, and the so-called early ventricular filling starts. To obtain a larger volume of blood in the left ventricle, the atria muscles finally contract, which squeezes an extra portion into the ventricle (atrial systole).

In this paper, it is the relaxed part (diastole) of the cardiac cycle, which is of main interest, as this part of the heartbeat is not as well understood as the active part (systole). With reference to the above description, diastole is made up of the periods of isovolumetric relaxation, early ventricular filling, and atrial systole.

Mathematical Model

Boundary Conditions

The left ventricle is modelled as a two-dimensional ellipsoid, as this is a simple geometry but still in reasonable agreement with the actual geometry (Streeter, 1979). For instance, it corresponds well with the assumptions made in the clinical practice of cardiology when measuring ventricular volumes. During the active period of the cardiac cycle, the heart wall is moved to give the prescribed left ventricle volume. During the passive part of the cycle, the ventricular wall is moved due to the pressure inside the ventricle and the material properties of the myocardium. The flow into the left ventricle from the left atrium through the mitral valve is defined to vary in time as the real flow through the mitral valve. The flow out of the ventricle is defined and in addition, the pressure is defined to model the resistance the enlargement of the aorta creates. The remaining surfaces of the left ventricle are modelled as rigid walls all having the no-slip condition (Figure 2).

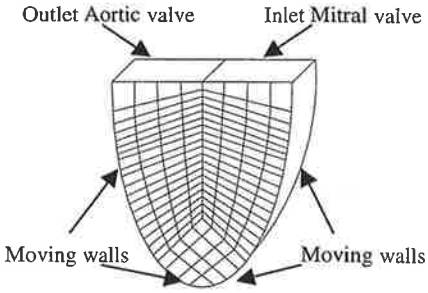

Figure 2: The position of the left ventricle (LV) boundaries.

Constitutive Relations for Blood

Blood is an incompressible, inhomogeneous, and non-Newtonian fluid, whose behaviour depends on both its history and composition. In this paper, blood is treated as homogeneous, as the size of the blood cells is very small compared to the ventricular volume. To model the non-Newtonian behaviour of blood, the constitutive relation is described by the weak Casson formulation, as it has been verified against experimental measurements on blood (Fung, 1993).

The Heart Wall

The heart wall is built up of layers of muscle fibres, where the direction of the fibres are distributed differently throughout the heart wall, as illustrated in Figure 3. The fibres are helically wound in layers parallel to the heart wall. Furthermore, anatomical dissections indicate that the fibre directions change from the inner to the outer wall surface (Rijcken, 1998).

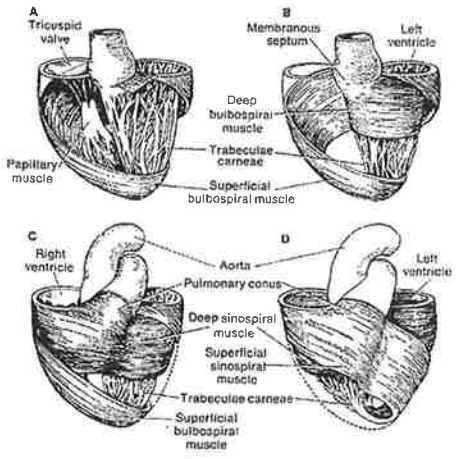

Figure 3: The orientation of the muscle fibres in the heart wall (Folkow, 1971)

To model the behaviour of the muscle fibres during diastole, a simplified assembly of two-dimensional springs is used. Each spring element has stiffness in both longitudinal and normal direction. The springs are positioned along the periphery of the left ventricle, as illustrated in Figure 4. In addition, to compensate for the three-dimensional effects in the plane model, a number of diagonal spring elements are added to simulate the influence of the real helix-like fibre distribution, see Figure 3.

Figure 4: Heart wall modelled by spring elements.

A "finite element"-like method is used to determine the displacement of the node-points. Each spring is a simple element only connecting two node-points. By choice of a wall discretization coinciding with the surface meshing of the CFD-model, the endpoint of springs correpond to cell vertices, and the calculated displacement of the heart wall can be transferred directly to the displacement of the CFD-mesh.

The local stiffness matrix for each spring is transformed to the global coordinate system, so that displacements in this frame are computed. Similarily, the pressure loads are decomposed into its corresponding Cartesian components. Summing up the contribution from each spring, yields a global stiffness matrix, which is used to set up the set of linear equations for the displacement of the node-points. As boundary conditions for the system of springs, the two end-points are fixed, i.e. they have zero displacements.

The elastic properties of the heart wall are of course important, when attempting to simulate the behaviour of the real heart. However, due to a lack of measured data pertaining to these properties, it is chosen to determine them by system identification in order to match a measured volume curve, using response surface regression techniques (Madsen, 1998). System identification by means of response surface regression seeks to adjust parameters of a numerical model, such that this yields results that correspond well with measured values. In this case, the object is to be able to compute the correct (measured) volume of the left ventricle at each time step.

Supplied with sufficiently many calculated volume curves, both longitudinal and normal stiffnesses for each individual spring could be decided. However, this has not been attempted, because it would be rather costly. Moreover, the variation in wall elasticity is only small for a healthy heart, so that it seems reasonable to divide the springs into only two groups, the peripheral and the diagonal ones, with all stiffnesses within each group being equal. It is assumed that the elastic properties of a heart vary less with position in the same subject than between different individuals. The ratio between the tangential and the normal stiffness is set equal for all of the springs.

The volume variation is not a sufficient measure, as there is obviously no unique set of spring stiffnesses associated with a volume variation curve. Thus, it is necessary to incorporate further criteria, such as a measure of the shape of the distended ventricle. For example, the ratio between the long and the short axis in the half ellipsoid representing the ventricular volume. At the end of diastole, the ratio should be approximately 0.5.

Considering the shape of the left ventricle, the replacement of blood inside the left ventricle is to be taken into account, as blood is not allowed to reside in the ventricle for several cardiac cycles, as this would cause clotting. A way of visualising the replacement of blood cells, would be to trace particles having the same density as these throughout a few heart cycles to make sure that all of the particles leave the ventricle.

After identifying the material properties of the heart wall, the properties of the heart wall can locally be changed in order to predict the effect of for instance a coronary thrombonesis

References

Folkow, B. and Neil, E.: "*Circulation*", Oxford University Press, 1971

Fung, Yuan-cheng: *"Biomechanics: Mechanical Properties of Living Tissues"* 2nd ed. Springer Verlag, New York, 1993 ISBN: 0-540-97947-6

Liepsch, D., Moravec, S.: *"Pulsatile Flow of Non-Newtonian Fluid in Distensible Human Arteries"*, Biorheology vol.21, no.4, pp.571-586, 1984

Madsen, J. I.: "*Design Optimization of Internal Flow Devices*" Ph.D. thesis Aalborg University, 1998, ISBN: 87-89179-24-2

Nash, M.: "*Mechanics and Material Properties of the Heart using an Anatomically Accurate Mathematical Model*", Ph.D. thesis, University of Auckland, New Zealand, 1998

Peskin, C. S., McQueen, D. M. *"Fluid Dynamics of the Heart and its Valves"* In Case Studies in Mathematical Modelling – Ecology,

Physiology, and Cell Biology, Prentice-Hall, Inc. Englewood Cliffs, New Jersey, 1996

Rijcken, J: *"Optimization of Left Ventricular Muscle Fiber Orientation"* Ph.D. Thesis University of Maastricht, Netherlands, 1998, ISBN: 90-9010880-7

Streeter Jr., D.D. *"Gross Morphology and Fiber Geometry of the Heart"* In R.M. Berne (ed.) Handbook of Physiology – The cardiovascular system I, pp.611-112, Am.Physiol.Soc., Bethesda, MD, 1979

Sørensen, L.T., Condra, T.J., Rosendahl, L.A., Madsen, J.I., Toft, E., and Korup, E., "Numerical Modelling of the Heart's Pumping Action", *Proceedings 5th Int. CFX User Conference*, Friedrichshafen, Germany, June 21-24, 1999.

LOCAL COLLAPSE ANALYSIS OF DEEP-WATER TITANIUM RISERS

ARVE BJØRSET[1],
BERNT J. LEIRA and *SVEIN REMSETH,*
Norwegian University of Science and Technology
N-7491 Trondheim, Norway.

ABSTRACT

Titanium is being considered as an alternative to steel for risers and flowlines, particularly for deep-water applications. However, capacity formulas for local buckling and collapse of titanium pipes subjected to bending and high external pressure are inadequate. If formulas developed for steel are applied directly, the model uncertainty is unknown. Ideally, extensive large- or small-scale model testing of titanium pipes is required. This paper discusses utilisation of a supplementary numerical approach based on Finite Element Analysis. The relationship between material model parameters being input to the analysis and the collapse/buckling capacity is investigated by performing a series of nonlinear FEM analyses.

Statistical models for the input material model parameters are established based on tests on small specimens cut from titanium pipes. These models are subsequently combined with results from the FEM analyses by application of response surface methods. As output from the analysis, the probability distribution of collapse capacity is obtained.

FROM GLOBAL TO LOCAL MODEL

A deep-water catenary (J-shape) titanium riser connected to a Tension leg Platform (TLP) at a water depth equal to 1000 m is employed as an example, see Figure 1a. The sag-bend area is of major concern when it comes to collapse of the riser cross-section (the sag-bend area is close to the seabed, also called the touch-down region, see circle in Figure 1a). The riser is in this particular area exposed to excessive bending and high external pressure.

Static and dynamic global response analyses are initially performed with the finite element program RIFLEX (1995). The internal diameter and the wall thickness are 20 in (508 mm) and 20.3 mm, respectively. The riser is modelled by constant axial, bending and torsion stiffness throughout the length. A ball joint connector is located at the top of the riser at the surface vessel (TLP). A load-duration of five wave periods is employed in a regular wave analysis to achieve stationary response. Analyses are performed in the time domain. The internal pressure is set equal to zero since that is the most severe condition. No internal pressure may occur in the installation phase and during production shut-down for maintenance or other purposes.

The present global riser analysis program is based on beam elements and is not suitable for ultimate capacity calculations of the riser pipe itself. The computer program does not account for any non-linear behaviour of the material nor local phenomena such as e.g. initial imperfections, local wall thickness variations, or increasing cross-sectional ovalisation. A local model in ABAQUS consisting of shell elements by use of the finite element method is employed as a numerical model to predict ovalisation, possible local buckling and collapse of the riser cross-section.

A local shell model replaces the global model where the greatest bending moments in the sag-bend area of the riser occur. Figure 1b shows the bending moment diagram for the whole riser. Figure 2 shows a 'close up' of the bending moment diagram for cross-sections in the

[1] Currently employed at MARINTEK, N-7450 Trondheim. E-mail: arve.bjorset@marintek.sintef.no

sag-bend at which the bending moment are greatest, also indicating the length for which the local model shall represent the global model.

Figure 3 gives an illustration of the local model. The maximum bending moment is symmetric for the actual length of the local model (see Figure 2). Hence, the point at which the maximum bending moment occurs is taken as a symmetric cross-section. Accordingly, only half of the length of the relevant pipe segment needs to be modelled. It is then possible to simplify the local analysis by establishing a local model as indicated in Figure 3 ('Symm.' is the symmetric cross-section). Furthermore, the loads and the response are symmetric in the bending plane in Figure 3. Half of the cross-section is then modelled in ABAQUS.

In the present study the load sequence is determined as follows: Maximum bending moment capacity is reached when the static vessel offset is increased. Hence, the external pressure remains constant, while the bending moment, the true axial force and the shear force will change. The sequence of these events implies that the so-called p→κ-path has to be used for the present shell analyses, i.e. reaching the maximum bending moment capacity by increasing the curvature, not the pressure.

MATERIAL MODEL

The stress-strain relationship for the relevant titanium alloy is established from uniaxial tension tests. The test specimens are taken from various locations and in various directions relative to the pipe axis in order to reveal possible anisotropic properties. The parameters of the material model are subsequently estimated for each of the experimental curves. Fitting of material constitutive equations is performed according to the equation, Voce (1948):

$$\sigma = \sigma_{EI} + R_1(1 - \exp(-C_1 \varepsilon_p)) + R_2(1 - \exp(-C_2 \varepsilon_p)) \quad (1)$$

where σ_{EI} is the elastic limit stress, ε_p is the true plastic stress, and R_1, R_2 , C_1 , C_2 are the parameters which are adjusted to fit each particular material curve. The strain hardening is modelled as isotropic. The value of the strain hardening parameter is furthermore set equal to a deterministic value. This is due to the negligible scatter in the values obtained from the tests. The von-Mises yield criterion is applied due to the isotropic properties observed from the tests.

RESPONSE SURFACE BASED ON COLLAPSE FEM-ANALYSES

The objective of employing response surface techniques is to establish an analytical approximation to the functional relationship between the structural response and the input variables. The response surface function will replace discrete estimates from the nonlinear finite element model by a smooth analytical function, representing an approximation to the true underlaying surface through all possible discrete values from the analysis.

The present study focuses on the maximum bending moment capacity, M_{max} as the primary 'response quantity' . As the interaction effects between the material parameters are found to be negligible, the response function for M_{max} may be established as a product of functions of each parameter. The variation in the strain hardening is as explained very small (a C.o.V. below 0.01), and is accordingly given a fixed value.

The response functions are established for the variation of the relevant random variables separately by keeping the other parameter at their base case (reference value). Designating variable number i by X_i, the corresponding interpolation polynomial of order k can be expressed as:

$$M_{\max}^{X_i} = A_{k,i}X_i^k + A_{k-1,i}X_i^{k-1} + \ldots A_{0,i} \quad (2)$$

where the constants A_{ik}, $A_{ik-1\,i}$ to A_{0i} are calculated from the response functions obtained from variation of each separate variable. The following parameters are varied in the probabilistic analysis, and are identified as the main input parameters to estimating the maximum bending moment capacity: (*i*) Yield stress (σ_Y), (*ii*) Young' s modulus (E), (*iii*) Uniform wall thickness (t), (*iv*) Initial ovality (f_0), (*v*) Cross-sectional orientation (o), (*vi*) Piercer eccentricity.

It is observed that the response function is quite linear for the pipe initial ovality. For the modulus of elasticity, a second order polynomial is employed. For the wall thickness and the orientation factor third order curves are required. For the yield stress, a linear relation is observed. The response surface is subsequently given as the normalised product of the function fitted along each of the variable axes:

$$M(X_1, X_2, .., X_6) = \left(M_{ref}\right) \cdot \prod_{i=1}^{4} \left(\frac{M_{\max}^{X_i}}{M_{ref}^{X_i}} \right) \cdot \frac{h\left(M_{\max}^{X_5}, M_{\max}^{X_6}\right)}{M_{ref}^{X_5} \cdot M_{ref}^{X_6}} \tag{3}$$

where M_{ref} is a base case reference value for the bending moment.

PROBABILISTIC CAPACITY ANALYSIS

A summary of the statistical models which are employed for the basic random variables are reported in Table 1.

Table 1. *A summary of statistical models for material parameters.*

Variable	Distribution	Mean value	C.o.V.
Yield strength	Normal	831.3 MPa	0.04
Young' s modulus	Normal	116 937 MPa	0.055
Initial ovality	Lognormal	1,5%	0.50
Wall thickness	Truncated normal	1,0 **	0.04
Orientation	Uniform	90 Deg.	0.58
Piercer eccentricity	Lognormal	0.5	0.10

** Normalized by nominal wall thickness (20.3 mm)

Figure 4 gives the probability density for the estimated maximum bending moment capacity based on the statistical parameters given in Table 1. By plotting the data in a probability paper, the distribution appears to be lognormal. The lognormal distribution can be given a certain plausibility in accordance to the Central Limit Theorem, which says that the product of a large number of independent variables becomes lognormally distributed, see e.g. Dougherty (1990).

CONCLUSIONS

The purpose of the present paper has been to illustrate how numerical simulations based on finite element modelling can be applied to gain insight into local collapse mechanisms for titanium pipes subjected to high external pressure in combination with bending moments. Combined with a probabilistic modelling of key input parameters, the resulting uncertainty and statistical properties of the bending moment capacity variation can be investigated. The relative importance of the various input statistical quantities can also be assessed.

The results from such a procedure can readily be utilised in combination with a more comprehensive reliability assessment, where also statistical models for load effects are introduced. Additional sources of uncertainty could be included. Calibration of both FE-

models and probabilistic models based on more extensive testing (large scale as well as small-scale) will contribute to obtain the best possible design basis for the maximum bending moment capacity.

It is believed that the results obtained by the present procedure provide useful insight in relation to full scale testing and for development of design formulas. The numerical scheme can also be employed to develop "deterministic" capacity formulas for titanium pipes to replace those adapted directly from steel pipes.

ACKNOWLEDGEMENTS

This current work relates to the CMC-project (Computational Mechanics in civil Engineering, see http://www.sintef.no/units/civil/bygg/sement/st-an.htm), which is currently being executed by SINTEF, MARINTEK and NTNU.

REFERENCES

Dougherty, E. R. (1990): "Probability and Statistics for Engineering, Computing and Physical Sciences", Prentice-Hall International Inc., ISBN 0-13-715913-7.
RIFLEX (1995): "Flexible Riser System Analysis Program", MARINTEK and NTNU, Trondheim, Norway.
Voce, E. (1948): Journal of Inst. Metals, 37, 537.

FIGURES

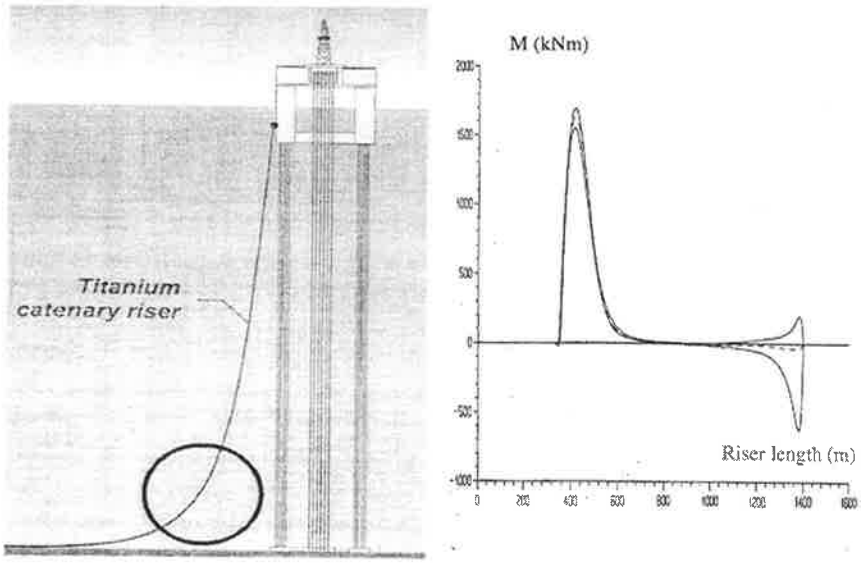

Figure 1a and 1b: (1a): The riser suspended from a TLP. (1b): Bending moment diagram for the whole riser.

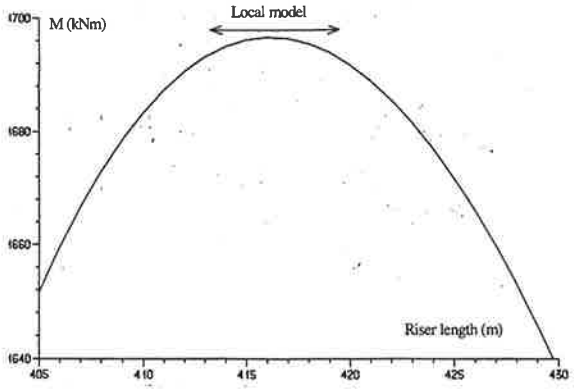

Figure 2: Zoomed maximum bending moment diagram from the global analysis indicating the local model representation.

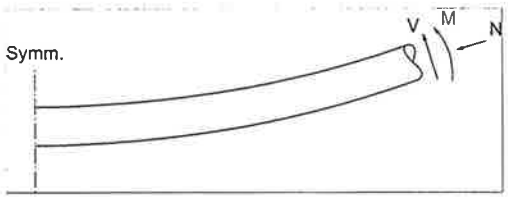

Figure 3: A schematic overview of the forces applied to the local model (external pressure neglected in the figure).

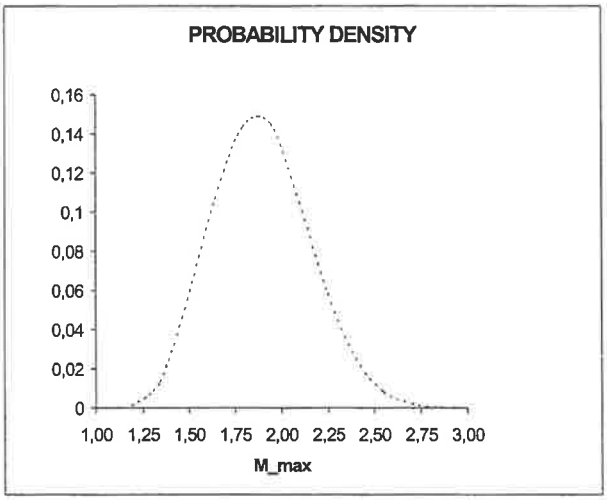

Figure 4: Probability density of the estimated maximum bending moment capacity.

Computational Mechanics in Civil Engineering (CMC)
Fire - Heat transfer – Stress analysis

M. Hendriks
TNO Building and Construction Research, The Netherlands

K. Høiseth
MARINTEK, Department of Structural Engineering, Norway

T. Hynne and J.A. Øverli
SINTEF Civil and Environmental Engineering, Norway

Introduction

CMC is a long –term research programme on computational mechanics issues in civil engineering, especially related to *integrated analysis* [1]. That is, analysis where two or more interacting effects or phenomena are analysed either staggered or simultaneously. CMC contains five main projects where frequently encountered problems in civil engineering will be treated by an integrated approach. One of the projects focuses on the analysis of solid concrete structures exposed to fires. In such an analysis there are two interacting effects. First, there is a coupling between a fire analysis and a heat transfer analysis of the solid structure. Secondly, there is a coupling between the heat transfer analysis and a stress analysis of the structure.

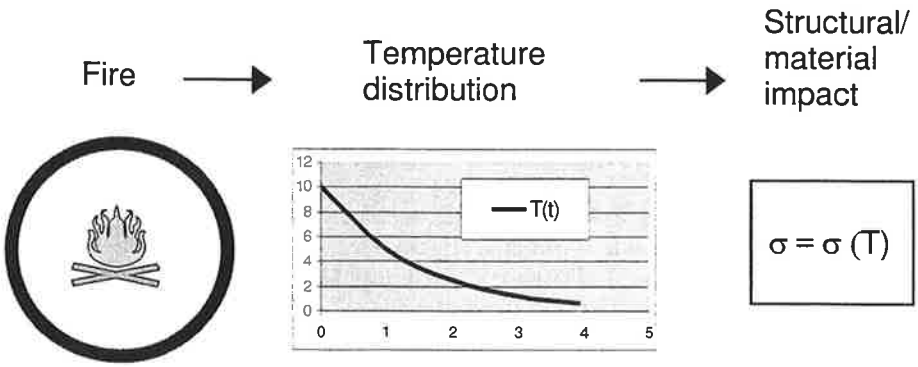

In the CMC-programme one of the main objectives is to apply state-of–the-art software to solve interdisciplinary and integrated civil engineering problems. In this project the simulations of the fire on solid structures are performed with the Computational Fluid Dynamics (CFD) code Kameleon FireEx [2]. The heat transfer and stress analyses are performed with the Finite Element (FE) code Diana [3]. By employing different software packages an interface program is necessary between the two programs.

Fire analysis

Kameleon FireEx is a general-purpose computer code for simulation of fluid flow, heat – and mass transfer in connection with combustion processes. The coupled set of partial differential equations related to continuity, conservation of momentum and energy is solved by means of the Finite Volume Technique. The code accounts for fire effects such as the interaction between turbulence and chemistry in flames, as well as soot formation and soot combustion. Kameleon FireEx is capable of simulating open and enclosed pool fires and jet fires. The most important results of a fire simulation, with respect to structural response, are the temperatures and radiant fluxes to obstacles, or structural components in the model grid.

Interface between fire analysis and heat analysis

FiHTSS-Fire and Heat Transfer Simulations of Solids is an interface between the Computational Fluid Dynamics (CFD) code Kameleon FireEx and the Finite Element (FE) code Diana.

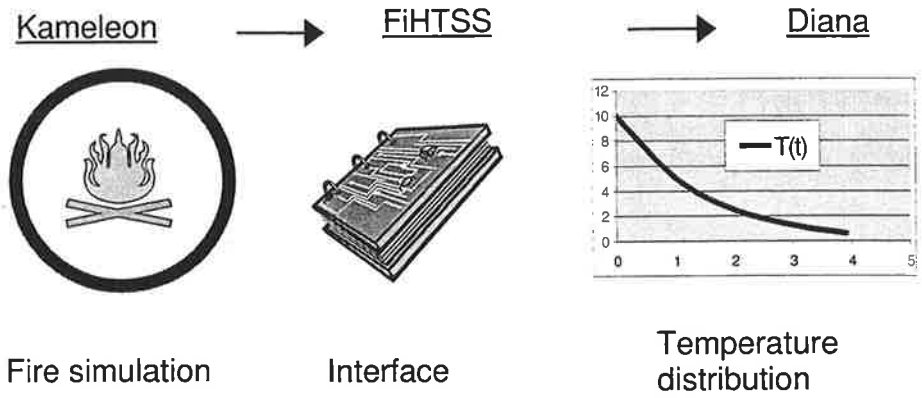

FiHTSS is implemented as a module in Diana. Based on results from Kameleon, the heat fluxes from both radiation and convection are calculated and put on surfaces exposed to the fire. Hence, it is a staggered analysis where the fire simulation is not influenced by the response in the finite element model.

Each finite element in the heat transfer model is treated individually by the Kameleon-Diana interface. Based on the element mid co-ordinates, the surface normal, the current surface temperature and the thermal properties of the surface, the interface module calculates the resulting heat flux. The finite element has to be located inside the calculation domain of the fire simulation. The computational domain grid, gas velocities, temperatures and the gas absorption coefficients are read from files written by the fire simulation program. These files form a transient development of the fire.

The incoming radiation is based on "The Discrete Transfer Method for Radiation" by Shah and Lockwood [4]. A number of rays are sent from the surface of the element and are followed until they hit the opposite boundary of the calculation domain. It is given

the radiation intensity defined by the temperature and the absorption coefficient of the wall point and followed back to the element surface. The radiation intensity is increased or decreased based on the conditions in the control volumes the ray passes through on its way back to the element.

Heat transfer and stress analysis

Diana is a general purpose Finite Element code, based on the displacement formulation, for simulation of structural response. In particular, the code contains state-of-the-art models for reinforced concrete structures, which is necessary regarding the objectives of the current work The code also offers a potential flow module applicable for simulation of transient heat flow through solid materials. Both simultaneous analysis, where there is a mutual interaction between heat flow and mechanical response, and staggered analysis, where merely the heat flow influence the response and not vice versa, can be performed.

In solid concrete structures exposed to a fire, cracking and spalling dominate the structural response. Cracking due to temperature gradients can be described using existing constitutive models. However, the structural deterioration due to spalling is difficult to formulate in a consistent manner [5]. To assess the risk of spalling in a particular concrete structure, the analysis has to include transport of fluids and vapours. Also the thermal and mechanical properties of concrete under exposure of high temperatures have to be determined. In this project a more direct model based on experimental results will be implemented to take into account spalling.

References

[1] Høiseth,H., Lu,M. and Svanø,G., 1998, Computational Mechanics in Civil Engineering (CMC). In Eriksson.A. and Pacoste,C., editors, Proceedings of the NSCM-11.

[2] Kameleon FireEx-98, 1998, SINTEF Energy Research, Norway.

[3] Diana 7 User's Manual, 1998, TNO Building and Construction Research, The Netherlands.

[4] Lockwood,F.C. and Shah,N.G. A new radiation solution method for incorporation in general combustion prediction procedures. In Eighteenth Symposium (International) on Combustion, The Combustion Institute, Pittsburgh, 1981, pp. 1405-1414.

[5] Hynne,T., 1999. SINTEF Report STF22 A99732. Mechanical Material Models for Concrete Subjected to Fire –A Literature Survey.

DEFORMATION OF COMPOSITE ROLLS DUE TO GRINDING

Ari Kinnunen

Engineering Mechanics Laboratory, University of Oulu,
PL 4200, 90401 Oulu, Finland
Tel: +358 8 5532179, Telefax: +358 8 5532026
E-mail: Ari.Kinnunen@me.oulu.fi

Abstract

In the process of manufacturing papermachine rolls made from carbonfiber and epoxi one of the problems that occurred during the grinding process was deformation of the casing.

The aim of this study was to find out reasons for deformations of the casing due to the grinding process, to develop a FEM model for simulating the structure and to give suggestions how to solve these problems. The effect of ring stiffeness (placed inside the casing) on deformations was also considered.

The FEM modeling was made by using I-DEAS and ABAQUS programs. I-DEAS was used in preprocessing and also for postprocessing of results obtained by ABAQUS.

The deformation was revealed to depend on how unevenly material was removed during the grinding process. Part of the residual stresses relaxed in top layers causing the deformation. Things that cause the roll to be deformed before

grinding are e.g. deflection caused by the gravity forces, moment caused by fastening to the grinding machine and variation of the shell thickness caused by the filament winding. In figure 1 is shown an example of the grinding pattern used to simulate deflection caused by the gravity. Different colours simulate the amount of material being removed.

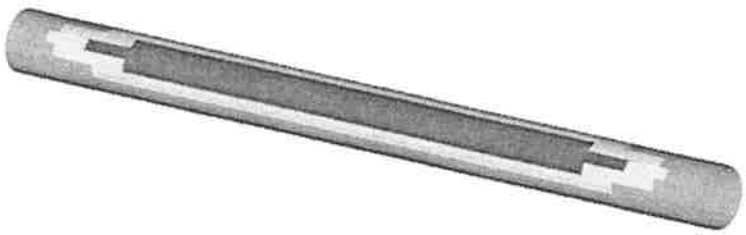

Fig. 1. The grinding pattern caused by the gravity forces.

The calculations were carried out in several steps. First the residual stresses in the casing was obtained by changing the temperature from the curing temperature to the room temperature. Then the elements of stiffness rings were activated (when taking rings into account) and finally the grinding pattern was simulated by changing material stiffness properties of the remuved plies close to zero.

The deformations were noticed to be above the limits even though only a small amount of material was removed. In figure 2 is shown the maximum deformation of the casing due to grinding in two different cases of grinding pattern using the same laminate. Case one is the same as in the example above.

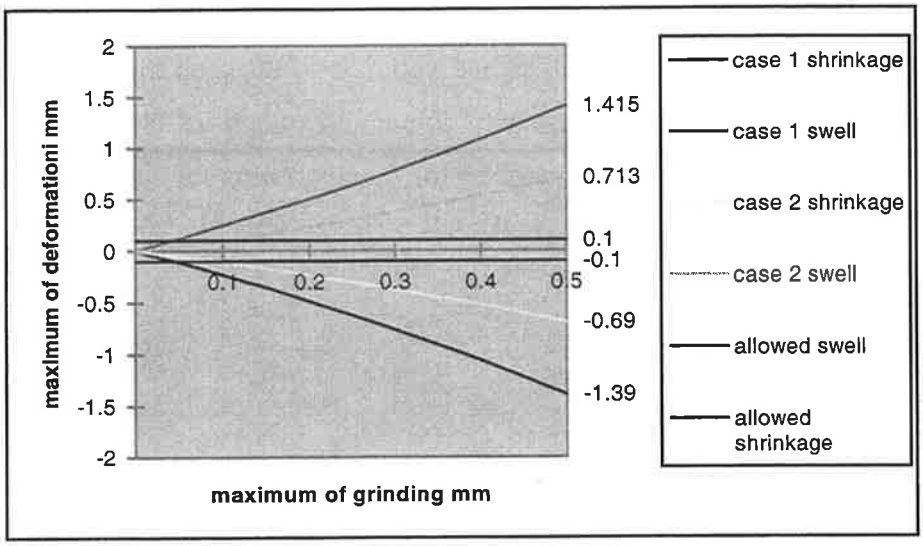

Fig. 2. The maximum deformation of the casing due to grinding in two different cases of grinding pattern using the same laminate

Making the shell thicker, changing unsymmetric laminate to a symmetric one and placing a special grinding layer on top of the shell was found to decrease the deformation to given limits. Stiffness rings were also found necessary because of their stiffening effect and as balancing mass fastening aids.

Reference

1. Kinnunen, A. Deformation of the Composite Roll due to Grinding. Master's Thesis. Oulu 1998, University of Oulu, Department of Mechanical Engineering. 51 p.

Numerical Simulation of Road Deterioration

J. Olsson* and N.-E. Wiberg*
*Department of Structural Mechanics
Chalmers University of Technology
S–412 96 Gothenburg, Sweden
e-mail: johol@sm.chalmers.se , new@sm.chalmers.se

1. Introduction

The expense for the maintenance is a considerable part of the total cost of keeping the road network an acceptable state. With the increasing number of roads and the following increase in expenses, a wish have sprung for a tool by which the road administrator and/or a contractor could predict deterioration and a more optimal road structure can be built and by which the need for maintenance can be planned ahead. The development of such an instrument includes solving the coupled and complex MHT-problem (Mechanical, Hydrological and Thermal-problem) to predict the overall physical behavior of the road. One component in such a tool could consist of a FE-module which in its ultimately form should be able to calculate the mechanical impact of environment and loads on the pavement structure.

2. The deterioration of roads

The most common road type is the so-called flexible pavement, which is a multilayer construction with materials that exhibits vastly different behavior [1,2,4]. The surface layer is often made of asphalt concrete and the layers beneath consist of gravel and finally the natural foundation. Deterioration of the pavement can be divided into two major components; wear caused by mechanical impact from e.g. studded tyres and the second component is the irrecoverable inelastic deformations of the materials in each layer. There actually exists some relatively good methods/models that describes the wear mode of the deterioration these are often based on statistic databases and empiricism. The methods/models for predicting the second part of the deterioration i.e. the material deformation process is not as refined as the one for wear. They are often based on the assumption that the materials behaves linear elastic which in combination with some multi-layer model e.g. Burmister [6] gives the strains in certain pre-designated part of the pavement construction. These are then compared to some maximum vales of strain, which often are based on empirical knowledge. This approach is common in the design codes that are used in several countries among these is the Swedish code Road 94 [2]. The strength of a method like that are the rather simple and fast calculations. The elastic theory also limits the need for input data to modules of elasticity (E) and Poisson's ration (v). This is however an indirect method that due to the choice of constitutive representation can not be used to directly predict the permanent deformation that occurs, such a tool have include material models which includes both elastic and plastic behavior.

3. Problem description

The materials in a flexible pavement can be divided in to two main groups bounded materials such as asphalt-concrete and unbounded i.e. the gravel layers, *Figure 1*.

Asphalt-concrete consists of crushed rock gravel, bitumen and some additives. This mixture is very sensitive to temperature and aging. The physical behavior changes from a nearly viscous fluid at high temperature to a brittle material at low temperature. In Sweden the surface temperature can be in the interval -30 — + 60°C. Brittle behavior results in cracks in the surface, while if the asphalt is ductile either densification (compaction) and/or lateral material movements can occur. Rutting that occurs in the asphalt-concrete as a result of ductile response has characteristic humps at the sides. There are also a few studies performed that indicates that the response to the applied load may depend on the rate of the application of fast loads that occurs at high velocities which means that the load bearing part of the top layer actually is the bitumen. At low loading rate the gravel acts like a skeleton structure which distributes the load.

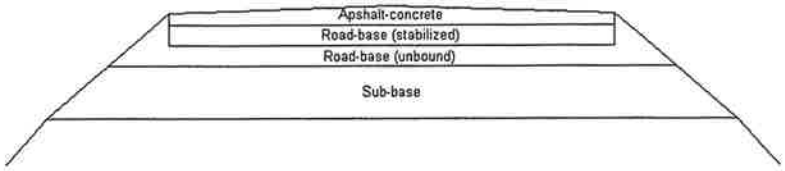

Figure 1 A cut through a flexible pavement

The **Granular layers** in the road exhibits rather varying response to loads due to the fact that there often is a variation of the quality and size distribution of the material through the pavement construction. The top layers often consists of material of higher quality and coarser size (up to 50 mm in diameter) of the particles and this in combination with the circumstance that these layers are relatively thin compared with the largest particles creates difficulties in the constitutive modelling [2]. The lower layers have a size distribution that also includes fine grade materials. The parameter that determines the behavior that these materials are foremost size distribution, temperature, moisture/water. Another important factor especially for the top layers is the enforced compaction during construction of these layers. The compaction introduces extra stresses so that the in-situ stress not only depends on the self-weight. This implies that the strain/stress history of the material is of great importance for the quality of the results.

The **loads** that are used in standard design codes are very often static surface load that is supposed to simulate the impact from a standard axis from a standard truck, [1]. The real load is a dynamic load that actually moves on the surface inducing another form of load characteristic. The Road administrators have allowed an increase in maximum allowed truckloads causing the axis loads in the reality to be larger then the standard axis in the design codes. There is also an ongoing development of the tyres in the direction of using so-called super single tyres, which means that there are only two tyres at an axis instead of four.

4. The FE-modelling

Creating the simulation tool is to create a tool that in its final form solves a complex MHT-problem. The first and important step will be to identify the parameters that have the grates impact on the quality of the solution. This means that in the long term development the overall model have to be parallel and in symbiosis, *figure 2*,with the development of the other tools e.g. the program that simulates the temperature distribution through the pavement body so that the output is given in such a form that it can be used directly as input to the overall deterioration model. The first step in the development of a possible FE-based simulation tool for simulation of the rutting which takes place in the surface layer have been to seek a representative material model which can be altered if necessary. This first attempt only considers the elastic-plastic mode of the deformations in the asphalt concrete layer. The initial assumption have been to use a material model based on a flow law according to suggestion by Perzyna. The inelastic deformation is triggered by a yield surface of Drucker-Prager type, described by e.g. O. C. Zienkiewicz in [5], *see equation (1)*. Both the flow/creep law and shape of the yield surface have to be dependent of the temperature due to that this parameters has great influence response of the asphalt-concrete, *see* [3].

$$f(I_1, J_2) = aI_1 + \sqrt{J_2} - k \qquad (1)$$

However this combination only covers the ductile behavior and must be combined by some constitutive model for the brittle behavior in the future.

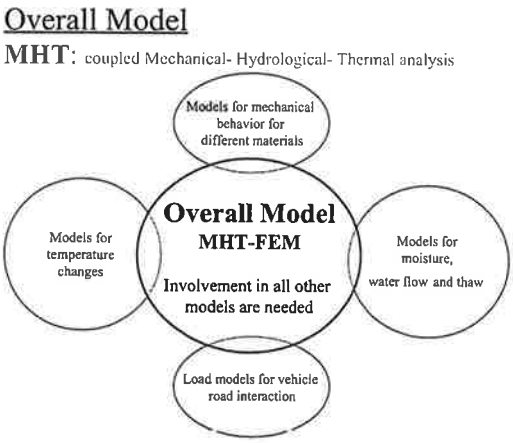

Figure 2 The MHT-FEM model and its involvement in other models.

Most finite element simulations have up to now been reduced to 2D-cases. Because of the complex behavior due to boundary condition and the moving load a complete 3D-analysis has to be performed to be able to understand the mechanics of the road in a wider sense.

5. Numerical example

As an initial attempt to simulate the impact from a standard load (equivalent to an axis of a lorry) a full 3D-model, *see figure 3*, has been made with the commercial FE-program ABAQUS. The dimensions of the simulated road section were LxWxH=15x17x3 m and it consisted of over 10000 nodes. The input data was based on material parameters given in the Swedish design code for pavement design [2]. These are however based on the assumption that all the materials in the road construction are linear elastic. The aim with this simulation was mainly to compare the results from FE-calculations with other commercial or semi- commercial computer program developed for pavement design.

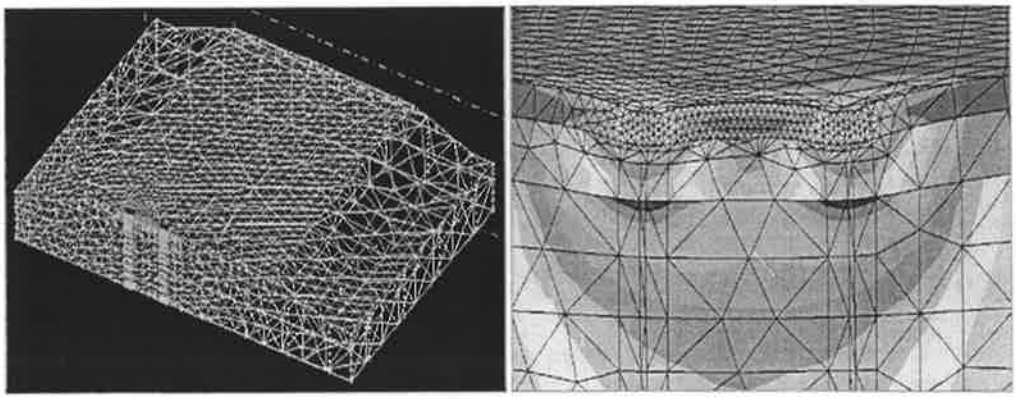

Figure 3 The FE-triangulation of the pavement model (left) and vertical strains and deformation (right).

6. Reference

[1] M.G. Lay: *Handbook of road technology. Volume1 planning and pavements (third edition)*. Transportation studies, **8**, Gordon and Breach science publishers, Melbourne, (1998).

[2] Swedish National Highway Administration, General Specification for Highway Structures 94 (Väg 94), Borlänge 1994, Sweden.

[3] H. Huang: *Analysis of accelerated pavement tests and finite element modeling of rutting phenomenon* (Dr. thesis Purdue University): UMI, Ann Arbor, Michigan 1997, USA.

[4] Y. H. Huang: *Pavement analysis and design*, Prentice-Hall, Englewood Cliffs, New York 1982. USA.

[5] O. C. Zienkiewicz and R.L. Taylor, The finite element method, vol2, Fourth Edition, McGraw-Hill book company, London, 1991.

[6] D. M. Burmister, The General Theory of Stresses and Displacements in Layered Systems I, *J. of applied physics*, Volume 16, pp. 89-94, 1945.

NUMERICAL SIMULATION OF A WORLD RECORD LONG CANTILEVER BRIDGE

P. F. TAKACS[1)] and T. KANSTAD[2)]
The Norwegian University of Science and Technology, Department of Structural Engineering
Richard Birkelands vei 1a, N-7491 Trondheim, Norway
[1)]Tlf: +47 73 59 71 51, Fax: +47 73 59 47 01, Email: Peter.Takacs@bygg.ntnu.no
[2)]Tlf: +47 73 59 45 19, Fax: +47 73 59 47 01, Email: Terje.Kanstad@bygg.ntnu.no

K. V. HØISETH
MARINTEK Structural Engineering Department
O. Nielsensvei 10, N-7450 Trondheim, Norway
Tlf: +47 73 59 29 06, Fax: +47 73 59 26 60, Email: Kalle.Hoiseth@marintek.sintef.no

T. INGEBRIGTSEN
Instanes AS – Bridge design and engineering
Storetveitvegen 96, N-5032 Bergen, Norway
Tlf: +47 55 36 36 00, Fax: +47 55 36 36 01, Email: t.ingebrigtsen@instanes.no

Summary
Stolmasundet Bridge with its 301 meter long main span is a world record long bridge among segmentally cast concrete cantilever bridges. Its long and slender superstructure and the timedependent behavior of concrete enhanced the importance of the deformation problem. Detailed finite element analysis was carried out in order to predict deformations, which would occur during construction and after long time. Effects of the segmental construction method and timedependent behavior of both concrete and prestressing steel were considered. Deformations of the main span were measured throughout the construction. The main objective of this paper is to show the numerical simulation of this pioneering bridge regarding the deformation problem and discuss comparison between calculated and measured deformations.

1 Introduction

The 301 meter long main span of Stolmasundet Bridge is the longest free concrete span ever built. Without any previous practical experience with such a long and slender concrete span, the bridge challenged both design engineers and the contractor. Deformation problem in particular was a serious concern during the design process and the construction. Expected deflections of the cantilevers were considerable due to the large slenderness of the superstructure and varied in time due to the viscoelastic behavior of the concrete. To predict deflections with reasonable precision was necessary in order to ensure the smooth joint of the two cantilevers during the construction process and also to avoid undesirable deflections throughout the entire lifetime of the bridge. An independent analysis was initiated by design engineers on the deformation problem with the objective to gain verification to their results. The analysis was carried out at the research organization SINTEF in Norway in cooperation with the Norwegian University of Science and Technology.

2 Description of Stolmasundet Bridge

Stolmasundet Bridge is a segmentally cast concrete cantilever bridge at the Norwegian west coast, not far from the city of Bergen. Construction of the bridge was completed in 1998. Total length of the bridge is 467 meter (94m+301m+72m). Box girder cross-section with variable depth was used. Cross-section depth is 15.0 meter over the columns and 3.5 meter at

the middle of the main span. The entire main span consists of 61 segments. The middle section of the main span was constructed from LC60 lightweight aggregate concrete, while the remaining part was constructed from C65 normal density concrete. Modulus of elasticity was measured in laboratory at the age of 28 days; it is 22100 MPa for the lightweight concrete and 29500 MPa for the normal density concrete.

3 Finite element analysis

General purpose finite element program system DIANA was used in the analysis. Several powerful tools are available in DIANA for numerical simulations: nonlinear timedependent analysis, phased structural analysis, viscoelastic model for aging materials, predefined concrete creep models according to some widely used design codes, embedded conventional reinforcement and prestressing tendons and preprocessing of effective prestressing force.

3.1 Geometrical model

The superstructure was modeled with curved, 3 node, two dimensional beam elements. Each element represented one segment with a length of 4-5 meter. Due to the symmetry in geometry, the box girder cross-section was simplified by an equivalent I-section. Columns were modeled with box shape cross-section. Contribution from the conventional reinforcement in the top and bottom flanges was taken into account. Prestressing tendons were approximated by a series of straight segments between beam element boundaries.

3.2 Material model

One of the key points of the analysis was to define the material model that is able to describe properly the viscoelastic material behavior of concrete. DIANA has the option to define the aging viscoelastic Kelvin chain model via a concrete creep model, which makes specification of the material model very convenient. In this analysis concrete creep model given in CEB-FIP Model Code 1990 [2] was chosen. Shrinkage was also considered according to the CEB-FIP Model Code 1990. Values of the modulus of elasticity were determined in laboratory.

3.3 Phased structural analysis

Segmental construction method with such a long span requires special care regarding to the deformation problem. To achieve the desired curvature of the superstructure, erection of the cantilevers should be carried out according to a predefined theoretical curve, which shows the necessary over-height for each individual segment and can be determined from the calculated long time deflections. When the travelling formwork is moved forward to its subsequent position, it is adjusted to that prescribed elevation.

Phased structural analysis is an ideal tool to determine the theoretical over-height. In our numerical simulation phased structural analysis was coupled with timedependent nonlinear analysis. The analysis was divided into 39 phases where each phase represented the construction of an additional segment (or a pair of segments respectively to the two cantilevers). The output from each phase was transferred automatically into the subsequent phase as input. Such way the entire construction history with a consistent time-scale was built up from individual phases. The last phase covered a 70 year long period of time modeling the behavior of the bridge from its completion. According to the CEB-FIP Model Code 1990, deformations take approximately this period of time to reach their ultimate value, however, 90 percent of those take place in the first 10 years.

4 Calculated deflections

Figure 1 shows the calculated deflections for the main span in three characteristic points of time: before the two cantilevers are coupled together, right after the entire span is completed and after 70 years. The latter curve is the one, which is particularly interesting from the point of view of the construction process. Its counterpart with opposite sign represents the theoretical over-height. The largest calculated long-time deflection is about 800 mm with an approximate contribution of 1300 mm from selfweight and 500 mm from prestressing.

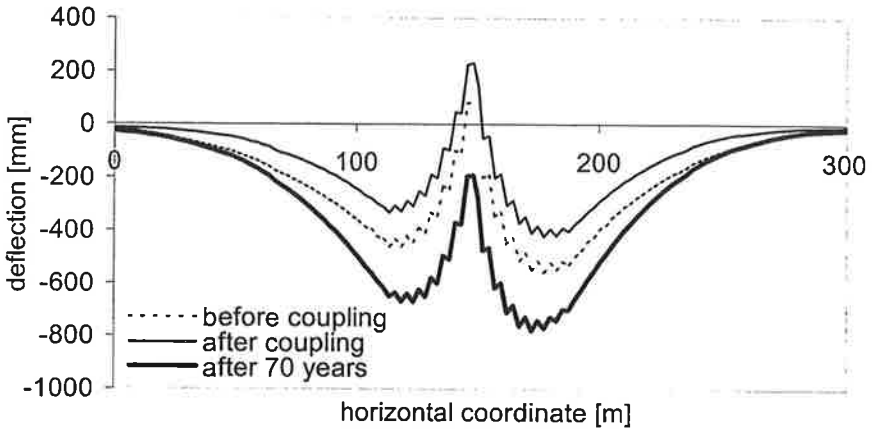

Figure 1 Calculated deflections of the main span

5 Comparison between calculated and measured deflections

The calculated theoretical over-height was not followed strictly, which caused deviations up to 130 mm from the proposed curvature. This deviation, however, did not cause any practical problem since the actual curvature is smooth and the deviation is not significant on the scale of the bridge. Figure 2 shows comparison between the calculated and measured height of the main span over the designed curvature right after the superstructure was completed.

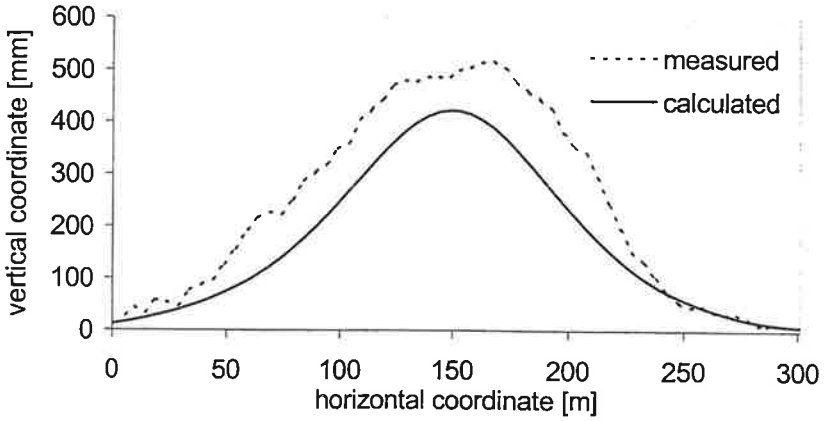

Figure 2 Calculated and measured height over the designed curvature right after the bridge was completed

On the other hand, it is difficult to evaluate the accuracy of the finite element analysis from Figure 2 since major portion of the deviation results as I mentioned above. Therefore - from this point of view -, it is more appropriate to compare the relative displacement of the bridge deck. Figure 3 shows such comparison for segment nr. 24 (124 meter from abutment) of the left cantilever. The figure shows the displacement of the segment after it was cast and the instantaneous deformation from selfweight and prestressing took place. Since this figure covers the following 28 days of the construction period, displacements shown in the figure mainly consist of the instantaneous part of the deformations due to the selfweight of the subsequent segments and prestressing.

The finite element analysis predicted somewhat larger deformations than the measured values shown in Figure 3. The difference may come partly from the higher actual effective prestressing force and the simplification that tendons were considered to be unbonded in the construction phases. The latter one resulted in slightly smaller element stiffness.

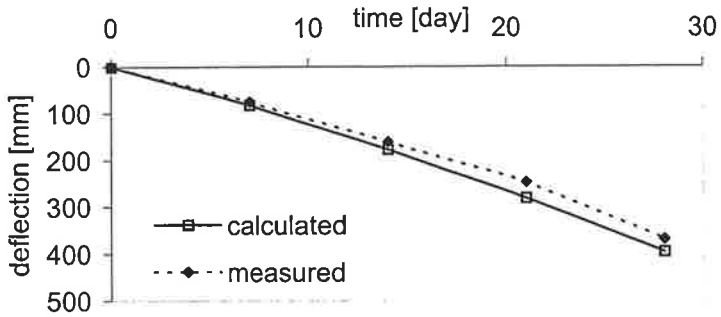

Figure 3 Development of displacement at section nr. 24 (left cantilever)

6 Plans for further work

Stolmasundet Bridge was completed at the end of 1998. At the time when this paper was prepared, the available measured data were limited to the construction period. Development of deformations during construction was mainly influenced by the instantaneous deformation due to the selfweight of the additional segments and prestressing, and creep contributed only with a minor portion. Development of long-time deformations, however, could be rather interesting for comparison with calculated results. It is our intention to follow up the development of deformations in the following years with the objective to make further evaluation of the accuracy of our numerical simulation.

References

[1] Takacs, P.F. and Kanstad, T., "Stolmasundet Bridge, Analysis in the service limit state", SINTEF Report STF22 F98734, SINTEF Civil and Environmental Engineering, Norway, 1998

[2] CEB-FIP Model Code 1990, CEB Bulletin N203, p2-29 – 2-42, Comite Euro-International du Beton, Switzerland, 1991

[3] Instanes AS, "Stolmasundet Bridge, Analysis and capacity checks", Report, Norway, 1997/1998

EXTENDED ABSTRACT
Pentti Tuominen
University of Oulu
Department of Civil Engineering

STATIC EQUATION OF AN ANALYTIC ELEMENT (second part)
(A unified theory of the stiffness, mixed and flexibility methods)

The element considered in this paper is presented in Figure 1.

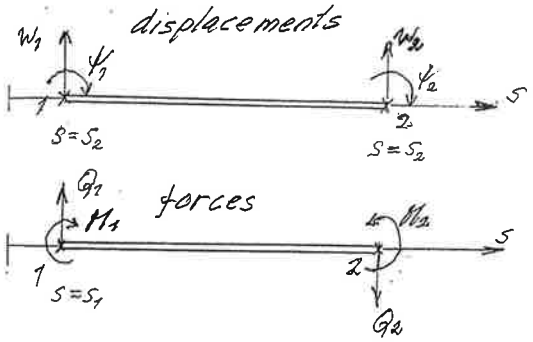

Figure 1. A structural element with displacements (w_i, Ψ_i) and forces (Q_i, M_i) at nodes 1 and 2 shown as positive.

It is expected that analytic solution of the governing differential equations is known. Expressions for quantities of Figure 1 can thus be written using four integration constants $\mathbf{c} = \{c_1\ c_2\ c_3\ c_4\}$ and particular solution terms. Two state vectors **a** and **b** have both four different quantities of Figure 1 as components. For these vectors it can be written Equations

$$\mathbf{a} = \mathbf{A}\mathbf{c} + \mathbf{a}_p \qquad (1)$$

and

$$\mathbf{b} = \mathbf{B}\mathbf{c} + \mathbf{b}_p \qquad (2)$$

where **A** and **B** are coefficient matrices of integration constants **c** and vectors $\mathbf{a}_p$ and $\mathbf{b}_p$ contain a particular solution. Vectors **a** and **b** are said to be each others complement vectors. Similarly **A** and **B** are complement matrices. Equation 1 gives the expression

$$\mathbf{c} = \mathbf{A}^{-1}\mathbf{a} - \mathbf{A}^{-1}\mathbf{a} \qquad (3)$$

Substitution of it into Equation 2 produces Equation

$$\mathbf{b} = \mathbf{B}\mathbf{A}^{-1}\mathbf{a} + \mathbf{b}_p - \mathbf{B}\mathbf{A}^{-1}\mathbf{a}_p. \qquad (4)$$

It gives the dependence of state vectors **a** and **b** on each others. Matrix $\mathbf{BA}^{-1}$ can be called an interaction matrix and vector $\mathbf{b}_p - \mathbf{BA}^{-1}\mathbf{a}_p$ a loding vector. Equation 4 is valid if matrix **A** is regular that is its inverse exists. This condition and the use of Equation 4 were handled in the first part of this study [1].

When calculating vector $\mathbf{e}(s) = \{w \ \psi \ Q \ M\}$ inside the element Equation

$$\mathbf{e}(s) = \mathbf{E}(s)\mathbf{c} + \mathbf{e}_p(s) \qquad (5)$$

is available. Here **E**(s) is the coefficient matrix of integration constants and $\mathbf{e}_p$ the particular solution vector at a point $s_1 < s < s_2$. By substituting **c** from 3 Equation

$$\begin{aligned} \mathbf{e}(s) &= \mathbf{E}(s)\,\mathbf{A}^{-1}(\mathbf{a}-\mathbf{a}_p) + \mathbf{e}_p(s) \\ &= \mathbf{E}(s)\mathbf{A}^{-1}\mathbf{a} + \mathbf{e}_p - \mathbf{E}(s)\mathbf{A}^{-1}\mathbf{a}_p \end{aligned} \qquad (6)$$

is obtained. When used with transfer matrix method it is equal with Equation 4, when the length of the element is $s\text{-}s_1$.

A numerical example:

The structure under considereration is same with the one of the first part of this study [1], an isotropic ring plate with data presented in Table 1. Its inner boundary is now fixed and the outer one is free. The loading is a uniform load $p = 1\ kN/m^2$. Calculations are made using transfer matrix and stiffness methods.

Table 1. Some notations and data of a ring plate

quantity	notation	numerical value
inner radius	s_1	1.0 m
outer radius	$a = s_2$	2.0 m
thickness	h	0.10 m
Young´s modulus	E	10000 kN/m^2
Poisson´s ratio	ν	~1./3
bending stiffness	B	0.9375 kNm
radial coordinate	$\rho = s/a$	0.5-1.0

Displacements w and ψ and forces Q and M can be presented as sum of particular and homogenous solutions. The latter one is further a sum of products of integration constants and certain functions. For a ring plate both are given in Table 2 [2, pp.253-254].

Table 2. Coefficients of integration constants and particular solution terms (uniform load p) of a ring plate. Term f is $f = 3+\nu+(1+\nu)2\ln\rho^*$. Other notations are from Figure 1 and Table 1.

quantity	integration constants and their coefficients				particular solution
	c_1	c_2	c_3	c_4	
w	1	ρ^2	$\rho^2\ln\rho$	$\ln\rho$	$pa^4\rho^4/B/64$
ψ	0	$-2\rho/a$	$-\rho(1+2\ln\rho)/a$	$1/\rho/a$	$pa^3\rho^3/B/16$
Q	0	0	$4B/\rho/a^3$	0	$3pa\rho/8$
M	0	$2(1+\nu)B/a^2$	fB/a^2 *	$-(1-\nu)B/\rho^2/a^2$	$3pa^2\rho^2/16$

When using transfer matrix method matrices **A** and **B** contain coefficients of Table 2 with argument values $\rho_1 = 0.5$ and $\rho_2 = 1$. Similarly complement vectors $\mathbf{a}_p$ and $\mathbf{b}_p$ are calculated as corredponding values of the particular solution terms, Equation 4 gets now a numerical form

$$\begin{bmatrix} w_2 \\ \psi_2 \\ Q_2=0 \\ M_2=0 \end{bmatrix} = \begin{bmatrix} 1 & -0.962098 & 0.124196 & 0.430322 \\ 0 & 1 & -0.339357 & -0.8 \\ 0 & 0 & 0.5 & 0 \\ 0 & -0.3125 & 0.587098 & 0.75 \end{bmatrix} \cdot \begin{bmatrix} w_1=0 \\ \psi_1=0 \\ Q_1 \\ M_1 \end{bmatrix} = \begin{bmatrix} +0.03411169 \\ -0.1303215 \\ +0.75 \\ +0.3627009 \end{bmatrix} .$$

According to boundary conditions (given above) two last lines can be used to solve unknown Q_1 and M_1 at the inner boundary. Vectors $\mathbf{a} = \{0\ 0\ 1.5\ -0.690595\}$ and $\mathbf{a}_p$ are both known and Equation 6 can be used by calculating matrix **E**(s) and vector $\mathbf{e}_p$(s) (Table 2) at desired points. Results are given in Table 3.

Table 3. Displacements (w, ψ) and radial forces (Q, M) of the ring plate considered above.

radius s	w	ψ	Q	M
1.0	$+ 0.5204 \cdot 10^{-16}$	0.0	1.50	0.690595
1.2	$-0.119979 \cdot 10^{-1}$	+0.107989	1.066667	0.379707
1.4	$-0.394777 \cdot 10^{-1}$	0.159695	0.728571	0.186358
1.6	$-0.736904 \cdot 10^{-1}$	0.178370	0.45	0.070912
1.8	-0.109654	0.179341	0.211111	0.012751
2.0	-0.144995	0.173762	0	0

When the stiffness method is used vector **a** contains displacements $\mathbf{a} = \{w_1\ \psi_1\ w_2\ \psi_2\}$ and **b** forces $\mathbf{b} = \{Q_1\ M_1\ Q_2\ M_2\}$. Equation 4 is now

$$\begin{bmatrix} Q_1 \\ M_1 \\ Q_2=0 \\ M_2=0 \end{bmatrix} = \begin{bmatrix} 17.1396 & -7.27054 & -17.1396 & -9.21941 \\ -7.27054 & 4.33414 & 7.27054 & 2.66084 \\ 8.56978 & -3.63527 & -8.56978 & -4.60970 \\ 4.60970 & -1.33042 & -4.60970 & -3.41707 \end{bmatrix} \cdot \begin{bmatrix} w_1=0 \\ \psi_1=0 \\ w_2 \\ \psi_2 \end{bmatrix} = \begin{bmatrix} -0.61682722 \\ +0.09875391 \\ +0.44158639 \\ +0.07462827 \end{bmatrix} .$$

To solve unknown displacement w_2 and ψ_2 two last equations are available. They give for nodal displacements

$$\mathbf{a} = \{0 \quad 0 \quad -0.144995 \quad 0.173762\}$$

After that Equation 6 can again be used Matrix **E**(s) is quite the same as used with the transfer matrix method. All the other results coincide with the ones given in Table 3. Only the deflection value

$$w_1 = 0.5551 \times 10^{-16}$$

has a minimal difference with that given in Table 3, both values due to round-off error.

It is worth to note that Equation 4 has also an alternative form

$$\mathbf{b} = [\mathbf{B}\mathbf{A}^{-1}]\,\Gamma^{-1}\mathbf{a} + \mathbf{b}_p - [\mathbf{B}\mathbf{A}^{-1}]\,\Gamma^{-1}\mathbf{a}_p, \quad (4a)$$

where I is the unit matrix. The result can be commented as follows: an interaction matrix $[\mathbf{B}\mathbf{A}^{-1}]$ has a complement. It is the unit matrix I. When this is substituted into Equation 3 we have Equation

$$\mathbf{c} = \Gamma^{-1}\mathbf{a} - \Gamma^{-1}\mathbf{a}_p = \mathbf{a}-\mathbf{a}_p \qquad (3a)$$

for integration constants **c** and we can say: Generation of a finite element can be regarded as a process, where mathematical integration constants **c** are replaced with physical ones. Equation 3a determines these constants.

Acknowledgements

The author wishes to thank professor Eero-Matti Salonen for co-operation and critic and Mrs. Mirjami Willberg for typewriting in preparing this paper.

References

1. Tuominen, P., Static Equation of an analytic element (A unified theory of the stiffness, mixed and flexibility methods). Proceedings of the NSCM-11: Nordic Seminar on Computational Mechanics, Anders Ericsson and Costin Pacoste (editors) Royal Institute of Technology, Department of Structural Engineering S-100 44 STOCKHOLM, pp. 171-174. Stockholm 1998

2. Girkmann, K., Flächentragwerke, sechste Auflage, Springer-Verlag. Wien 1963

Computational Analysis of Geometric Nonlinear Effects in Adhesively Bonded Single Lap Composite Joints

Alfred Andersen
Harald Osnes

Mechanics Division, Dept. of Mathematics,
University of Oslo, P.O. Box 1053 Blindern,
N-0316 Oslo, Norway

August 20, 1999

The use of fibre composites has shown a tremendous growth in many branches during the last decades. Now the applications of composite materials span from trivial, industrial products such as boxes and covers, that are produced in enormous numbers each day, to pipelines and large, crucial, load bearing parts of constructions. Composites are also extensively used in aerospace and marine industry. Important reasons for this popularity are the high strength (and stiffness) to weight ratio and the possibility for making products of almost any geometry.

Due to the comprehensive use the need for joining composite parts to construction details made of composites or other materials is obvious. Such joints can be constructed in numbers of ways, i.e. as bolted or other mechanically fastened joints or as bonded joints. Adhesively bonded joints have the advantages over traditional mechanically fastened joints in avoiding drilled holes (broken fibres), reducing stress concentrations, etc. Joints can be symmetric (e.g. double lap joints) or non-symmetric (e.g. single lap joints).

In the following we will analyse single lap joints where two laminated plates are bonded together by a thin layer of adhesive. Similar joints have been investigated by, e.g., Hildebrand [3] and Kairouz and Matthews [4]. They study ultimate strength of single lap joints and claim that geometric nonlinear effects are important. However, they do not investigate for what values of applied loads or prescribed end displacements nonlinear effects become significant. In the present study we will focus on that aspect by comparing finite element results from geometric nonlinear models with linear simulations. We assume that the joint is wide compared to its thickness

and the length of the overlap region. Furthermore, each laminated plate consists of eight plies with fibre directions 0 and 90 degrees. Thus, out of plane bending is avoided, and the joint can be investigated as a 2-D plane strain problem. The well-known software package *ANSYS* [1] is applied in the analysis. Additionally, the relatively complicated expressions defining relations between stresses and strains (including modifications related to the geometric nonlinear model from Zienkiewicz and Taylor [5]) for laminated composites are derived and implemented in a general elasticity module using the commercial C++ class library *Diffpack* [2]. This way of combining the use of a relatively robust method in *ANSYS* with a self-implemented module in *Diffpack*, in which all programming details are known, has been very fruitful and provided valuable insight into important modelling aspects (for example, it is observed that certain 2-D anisotropic problems are incorrectly treated by *ANSYS*). The agreement between the numerical results obtained by *ANSYS* and *Diffpack* is excellent for the problems in the present investigation.

The numerical, 2-D domain is shown in figure 1, which also defines the boundary conditions applied. The laminated plates consist of eight plies of thickness 0.125 mm, and the thickness of the adhesive layer is 0.1 mm. Two different stacking sequences are investigated: $[0/90]_{2s}$ and $[90/0]_{2s}$. The mesh consists mainly of four-noded bilinear elements. There are three elements through the thickness of each ply and six to eight through the adhesive layer. In addition to the bilinear elements there are some three-noded triangular elements in the spew fillet. The total number of elements is approximately 10000. The material properties, which are listed in the tables 1 and 2, are picked from Kairouz and Matthews [4], where the adherends are made of $XAS/914C$ carbon fibre/epoxy resin and the adhesive used is Ciba-Geigy Redux $308A$.

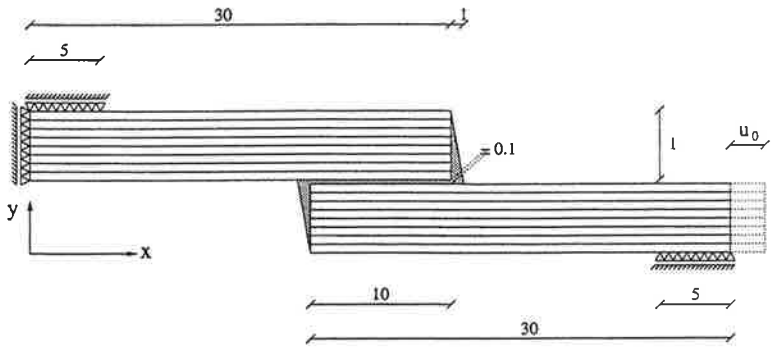

Figure 1: 2-D domain for the numerical simulations.

Firstly, we investigate the behaviour of the single lap joint with the $[0/90]_{2s}$ lay-up in the adherends. A typical distribution of the von Mises equivalent

stress, resulting from the geometric nonlinear method, is depicted in figure 2 for a crucial region of the (deformed) geometry. Here, the prescribed displacement, u_0, of the right hand side boundary is 0.1 mm, which leads to stresses and strains far below critical ply crack limits. The maximum value for the equivalent stress (as well as for σ_x and σ_y) is observed near the fillet tip, while the maximum shear stress occurs in the adhesive layer near $x = 30$. Similar behaviour and values are obtained around the spew fillet at $x = 20$.

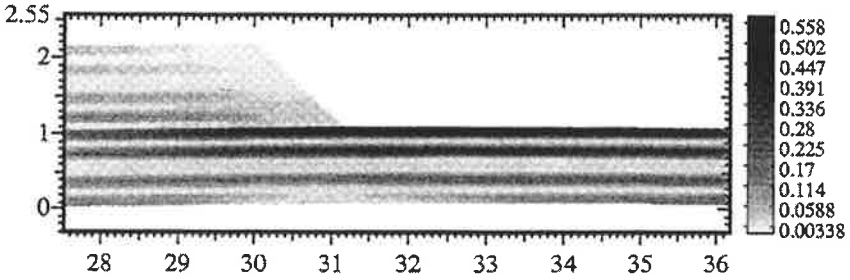

Figure 2: Distribution of von Mises equivalent stress near the fillet tip for $u_0 = 0.1$ and $[0/90]_{2s}$ stacking sequence for the adherends.

The figure 3(a) shows vertical displacement at the fillet tip as a function of u_0, while the equivalent stress is depicted as a function of the external load (per unit width) in figure 3(b). The nonlinear results are compared with solutions obtained by a linear model. Ply cracks begin to develop when $u_0 \approx 0.2$, and it is seen that nonlinear effects are significant for end displacements (or corresponding external loads) above approximately fifty percent of that value. Especially the vertical displacement shows considerable nonlinearities. However, also the equivalent stress is clearly modified

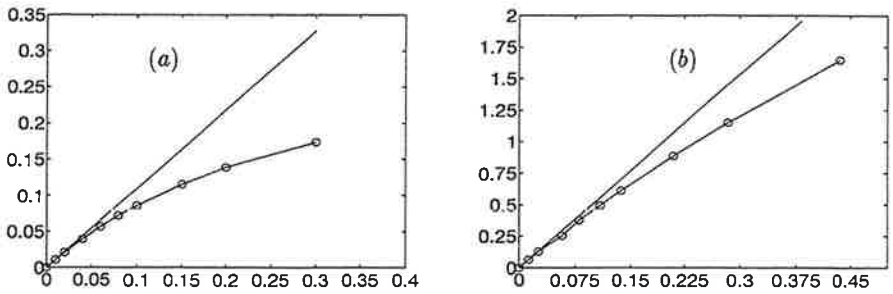

Figure 3: Comparison of geometric nonlinear (∘) and linear (solid line) results. Figure (a): Vertical displacement at the fillet tip as a function of joint end displacement. Figure (b): von Mises equivalent stress at the fillet tip as a function of external load.

by nonlinear effects. A more careful investigation of each stress component proves that the normal stresses (σ_x and σ_y) are significantly modified by nonlinear effects while the shear stress behaves nearly linear. Similar behaviour is observed for the joint with the $[90/0]_{2s}$ stacking sequence.

In the present study we have seen that considerable departure from linear behaviour is observed for a large regime of prescribed displacements or external loads. Geometric nonlinear effects begin to develop for loads far below ultimate strength limits. Thus, geometric nonlinear methods should always be applied when single lap (or non-symmetric) composite joints are analysed.

Longitudinal elastic modulus, E_1 (GPa)	138
Transverse elastic modulus, E_2 (GPa)	9.4
In-plane shear modulus, G_{12} (GPa)	6.7
Major Poisson's ratio, ν_{12}	0.32

Table 1: Mechanical properties of $XAS/914C$ composite.

Elastic modulus, E (MPa)	3000
Shear modulus, G (MPa)	1145
Poisson's ratio, ν	0.31

Table 2: Mechanical properties of Redux $308A$ adhesive.

References

[1] *ANSYS* World Wide Web home page:
http://www.ansys.com.

[2] *Diffpack* World Wide Web home page:
http://www.nobjects.com/prodserv/diffpack.

[3] Hildebrand, M., Non-linear analysis and optimization of adhesively bonded single lap joints between fibre-reinforced plastics and metals. *Int. J. Adhesion and Adhesives*, 14 (4), 1994, pp. 261-267.

[4] Kairouz, K. C., & Matthews, F. L., Strength and failure modes of bonded single lap joints between cross-ply adherends. *Composites*, 24 (6), 1993, pp. 475-484.

[5] Zienkiewicz, O. C., & Taylor, R. L., *The Finite Element Method, Fourth Edition.* McGraw-Hill Book Company, London, 1989.

Evaluation of equilibrium surfaces for parameterised non-linear structures

Anders Eriksson and Costin Pacoste,

Structural Mechanics group, Dept. Structural Engineering,
Royal Institute of Technology, S-100 44 Stockholm, Sweden

Introduction

Previous papers by the authors have described generalised path-following methods for non-linear quasi-static discretised structural instability problems, [1, 2]. These include methods for the tracing of equilibrium paths, i. e. load-displacement relations, as a special case. The methods, however, also allow the calculation of more general paths, e. g. the direct evaluation of parameter dependence in different aspects of structural response, for instance criticalities. These methods have been used to great advantage in detailed shell instability analyses, [3].

Generally speaking, instability problems can be studied in several ways. However, catastrophe theoretical concepts, [4], emphasise the need for treatment of parameterised models. From the application viewpoint, the parameterised formulation means that a specific studied load-carrying structure is just one instance of a class of similar structures.

Methods for evaluation of higher dimensional solution spaces have been mathematically described in e. g. [5]. The presentation gives some aspect on the possibilities in treating two-dimensional equilibrium manifolds, in the analysis of non-linear structural response.

Formulation and setting

The general problem setting is that of a discrete or discretised model of a quasi-static elastic structural problem. It is assumed that the internal forces in the structure can be uniquely defined from the current displacement state. When the structural model uses N degrees of freedom, the equations can be written in the generic residual form

$$\boldsymbol{G}(\boldsymbol{z}) \equiv \begin{pmatrix} \boldsymbol{F}(\boldsymbol{z}) \\ \boldsymbol{g}(\boldsymbol{z}) \end{pmatrix} = \boldsymbol{0} \qquad \boldsymbol{F}(\boldsymbol{z}) \equiv \boldsymbol{f}(\boldsymbol{d}, \boldsymbol{\Lambda}) - \boldsymbol{p}(\boldsymbol{\Lambda}) \tag{1}$$

with $\boldsymbol{F}$ N equilibrium equations, and $\boldsymbol{g}$ a set of r auxiliary equations, specifying the required subset of equilibrium states. The solution is a set of combinations $\boldsymbol{z} = [\boldsymbol{d}^T, \boldsymbol{\Lambda}^T]^T$ of N displacement variables $\boldsymbol{d}$ and p control variables $\boldsymbol{\Lambda}$ fulfilling both sets of equations.

In addition to a main load factor, extra control variables are used to specify the structural geometry, or auxiliary loads. The auxiliary equations can be used to specify the values for certain response quantities, or to demand criticality of the structure, cf. [2]. Primary interest is focussed on three cases: basic load case on parameterised structure, two independent load cases, and critical parametric combinations.

As a contrast to the treatment in [2], it is here assumed that the number of variables is two higher than the number of equations. This means that the solution manifold to Eq. (1) consists of a set of surface segments in the $(N + p)$-dimensional space. Parts of this solution space is evaluated with the present algorithm.

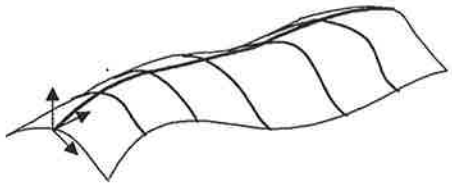

Figure 1: Solution manifold, showing the parameter dependence around a basic load case.

In the present implementation, it is possible to define problems with $p \geq 2$ control parameters, and with $r \geq 0$ auxiliary equations. Only $p = r + 2$ parameters are varied in the analysis, but further parameters can be included; these are then kept fixed at their initial values throughout the calculation.

In the present formulation, only a limited part of the total manifold is of interest, where the total problem is seen as variations, described by the additional parameters, around a basic case, i.e. a common load-displacement problem; the situation is described by Fig. 1. The basic case is defined by all additional variables vanishing.

The stated problems can be solved by path-following techniques based on the implicit function theorem. Here, the differential matrix

$$\boldsymbol{G}_{,\boldsymbol{z}} \equiv \begin{bmatrix} +\boldsymbol{F}_{,\boldsymbol{d}} & \boldsymbol{F}_{,\boldsymbol{\Lambda}} \\ \boldsymbol{g}_{,\boldsymbol{d}} & \boldsymbol{g}_{,\boldsymbol{\Lambda}} \end{bmatrix} \tag{2}$$

plays an important role in many parts. The $(N + r) \times (N + p)$ matrix, which contains the structural tangential stiffness matrix as its top left part, is used in the iterative procedure when bringing the residual function $\boldsymbol{G}(\boldsymbol{z})$ to zero, but also as an important description of structural properties.

Surface-evaluating algorithm

An algorithm has been developed for the evaluation of a specified sub-manifold of the total equilibrium solution space. With respect to the assumed context, the algorithm develops a surface around the main case, indicated by the solid line in Fig. 1. As a first step, a triangularisation is developed around this basic solution, according to Fig. 2a. The surface is described by two parameters (s, t), used to measure the placement of solution points. The parameters are incrementally defined from previous states. The mapping of the local variables is such that s always points in the direction of the basic solutions, i.e. solutions with no increment in additional parameters. This is obtained by evaluating and rotating the tangent space $\boldsymbol{T}$ of the differential $\boldsymbol{G}_{,\boldsymbol{z}}$, at each solution point, cf. Fig. 2b.

The evaluation of the two-dimensional tangent space, corresponding to the differential matrix in Eq. (2), is extensively discussed in [2]. The basic idea is a separation of this space in components in and orthogonal to the critical space of the tangent stiffness matrix $\boldsymbol{F}_{,\boldsymbol{d}}$. The method starts from the null space of only the equilibrium equations, and then studies how this null space is reduced by the auxiliary equations.

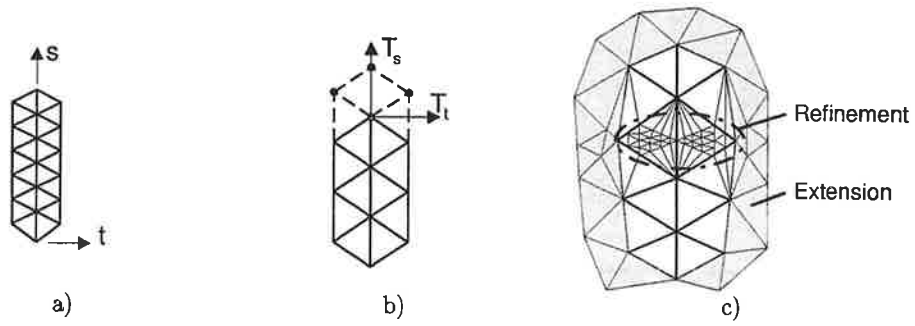

Figure 2: a) Normalised mesh coordinates. b) Tangent directions for measuring. c) Post-processing of basic solution mesh.

A step along the basic case consists of the evaluation of three new solution states, from which four triangles are added to the surface description. The iteration procedure for each state is essentially the same as in a common continuation algorithm. Thus, based on the form in Eqs. (1),(2) and adding position measuring equations, different versions of Newton-Raphson ('N-R') iterations are used.

The basic results from the algorithm is thus a small submanifold, essentially being three connected, parallel rows of solution states, cf. Fig. 2a. Based on these solutions, two types of further evaluations can be utilised. One of these is an extension of the obtained triangularisation, where one layer of new solution points, and a group of new triangles are obtained, cf. Fig. 2c. This step needs consideration of the geometry of the boundary of the starting mesh, and a choice of the outwards distance from the previous points. The step can be repeated a number of cycles.

The other additional step is similar to the 'bracketing' algorithm for isolation of special solution states on a path, cf. [2]. This refinement of the mesh is used to give a better description of surface segments where the properties of the equilibrium states change in some way. The considered properties are the degree of instability, i. e. the numbers of negative eigenvalues of the structural tangential stiffness matrix, and the signs of all control variables. Each triangle, based on three solution states, is checked for the values of these quantities. A systematic refinement of the triangle to a desired level can then be performed. In order to avoid unnecessary eigensolution extractions, the same simplified method is used as in [6].

Numerical examples

A number of examples have been analysed with the present algorithm, and will be discussed in the presentation. Some comparisons will here be made between the demonstrated numerical procedures and the generalised one-dimensional methods of [2], concerning obtained results as well as reliability and efficiency aspects.

A clamped toggle frame, previously studied analytically by Williams, [7], and numerically by several authors, can show all the discussed possibilities. The case is shown in Fig. 3, with $L = 12.943, H = 0.7$, $E = 1.03 \cdot 10^7$, and a beam section of height 0.243, width 0.753. The structure was modelled with eight elements of the type 'ST', cf. [8], not utilising the

symmetry. The model shows a snap-through behaviour under a vertical downwards point load $-P_1$, but also gives a bifurcating path. The result shows the dependence of the result on an arbitrary applied apex moment P_2. The figure clearly shows the bifurcation state, with its exchange of stability, prior to the first limit load.

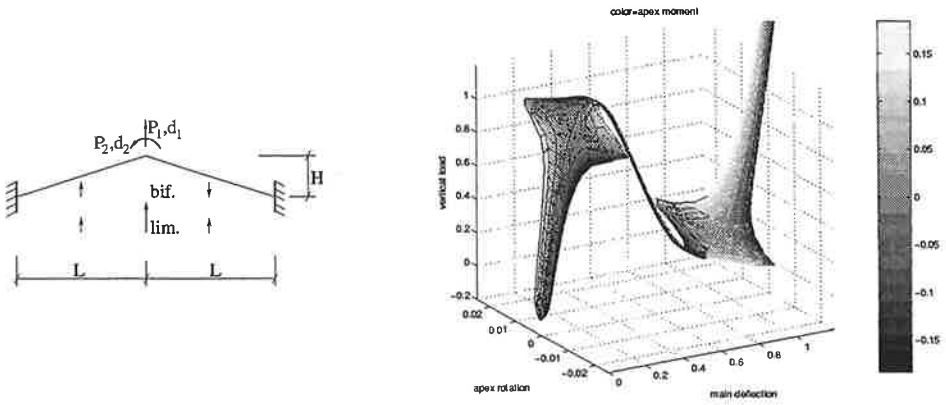

Figure 3: Clamped toggle frame, according to Williams, [7]. Load is scaled by a factor 100.

References

[1] A. Eriksson. Fold lines for sensitivity analyses in structural instability. *Comput. Methods Appl. Mech. Engrg.*, 114:77–101, 1994.

[2] A. Eriksson. Structural instability analyses based on generalised path-following. *Comput. Methods Appl. Mech. Engrg.*, 156:45–74, 1998.

[3] A. Eriksson, C. Pacoste, and A. Zdunek. Numerical analysis of omplex instability behaviour using incremental-iterative strategies. *Comput. Methods Appl. Mech. Engrg.*, 1998. In press.

[4] C. Pacoste. *On the application of catastrophe theory to stability analyses of elastic structures.* Dr. thesis, Dept. Struct. Engng., Royal Inst. Techn., Stockholm, 1993.

[5] W. C. Rheinboldt. On the computation of multi-dimensional solution manifolds of parameterized equations. *Numer. Math.*, 53:165–181, 1988.

[6] A. Eriksson. Equilibrium subsets for multi-parametric structural analysis. *Comput. Methods Appl. Mech. Engrg.*, 140:305–327, 1997.

[7] F. W. Williams. An approach to the nonlinear behavior of members of a rigid jointed plane framework with finite deflections. *Q. J. Mech. Appl. Math.*, 17:451–469, 1964.

[8] C. Pacoste and A. Eriksson. Element behaviour in post-critical plane frame analysis. *Comput. Methods Appl. Mech. Engrg.*, 125:319–343, 1995.

A CONTACT MODEL FOR THE WINDING NIP

R. VON HERTZEN[1] AND M. JORKAMA[2]

[1] Laboratory of Theoretical and Applied Mechanics, Helsinki University of Technology, P.O. Box 1100, FIN-02015 HUT, Finland.
[2] Valmet Winders, Wärtsilänkatu 100, FIN-04400 Järvenpää, Finland.

1. INTRODUCTION

The winding devices of the modern paper industry exclusively include a nip. Despite restricting air entrainment into the roll, a nip provides two additional external loads – normal and tangential – to control the wound roll structure. A winding nip typically generates a very high stress concentration in the nip area and, hence, a possibility for web and roll defects. It is also well known that in the nip area layer-to-layer slippage may occur in the wound roll. This sets demands for the winder control system to keep the nip loads in a range so that the required roll structure is achieved and, on the other hand, that roll defects due to nip induced stresses are avoided. Currently, the appropriate range of the winding parameters is sought mainly by trial and error tests.

Despite that there exists a vast amount of literature on rolling contact of two parallel cylinders, a rigorous theory applicable to the winding nip is still lacking. Bentall & Johnson [1] have studied the rolling contact of two cylinders with an elastic strip going through the nip. They restricted their treatment to isotropic materials, identical cylinders and essentially to free rolling conditions. Also, a half-space approximation for the cylinders was used and, hence, the theory is not suitable for a drum with a thin elastic cover. Tervonen [2] has extended the treatment to linear, viscoelastic cylinders and tractive rolling. His model includes covered cylinders but is also restricted to isotropic materials. In neither of these papers the winding application is considered. Soong & Li [3,4] have considered the rolling contact of two cylinders with linear, elastic and isotropic layers bonded to a hard core and driving an elastic thin sheet with extensional stiffness. All previously mentioned studies lack the proper nip exit condition for the web wound onto the roll.

In this paper a contact mechanical model for the winding nip is presented. The model consists of the wound roll, winding drum and the sheet in the nip. The wound roll and winding drum are modeled as linear, orthotropic, homogeneous cylinders with a rigid core. The elastic solutions are derived analytically in a series form. The sheet is also modeled as a linear and orthotropic material. An approximate elastic solution for the sheet is obtained by assuming an internal stress distribution compatible with the boundary conditions and by integrating the orthotropic constitutive equations (thin sheet approximation). The appropriate form of the nip exit condition of the web is considered.

2. FUNDAMENTAL ELASTIC SOLUTIONS

Let us consider a linear, orthotropic cylinder of radius R (see Fig. 1) with a rigid core of radius R_0 and loaded by the radial and tangential surface load distributions p and q, respectively. The boundary conditions in the polar coordinate system attached to the center of the core are

$$\begin{aligned} v_r(R_0,\theta) &= 0 \quad , \quad \sigma_r(R,\theta) = -p(\theta) \\ v_\theta(R_0,\theta) &= 0 \quad , \quad \tau_{r\theta}(R,\theta) = q(\theta) \ , \end{aligned} \tag{1}$$

where v_r and v_θ denote the radial and tangential displacements, and σ_r and $\tau_{r\theta}$ the radial normal and tangential shearing stresses, respectively. The linear constitutive equations of the orthotropic cylinder can be written as

$$\sigma_r = A_{rr}\frac{\partial v_r}{\partial r} + A_{r\theta}\frac{1}{r}\left(v_r + \frac{\partial v_\theta}{\partial \theta}\right), \quad \sigma_\theta = A_{r\theta}\frac{\partial v_r}{\partial r} + A_{\theta\theta}\frac{1}{r}\left(v_r + \frac{\partial v_\theta}{\partial \theta}\right),$$
$$\tau_{r\theta} = G_{r\theta}\left(\frac{1}{r}\frac{\partial v_r}{\partial \theta} + \frac{\partial v_\theta}{\partial r} - \frac{v_\theta}{r}\right), \tag{2}$$

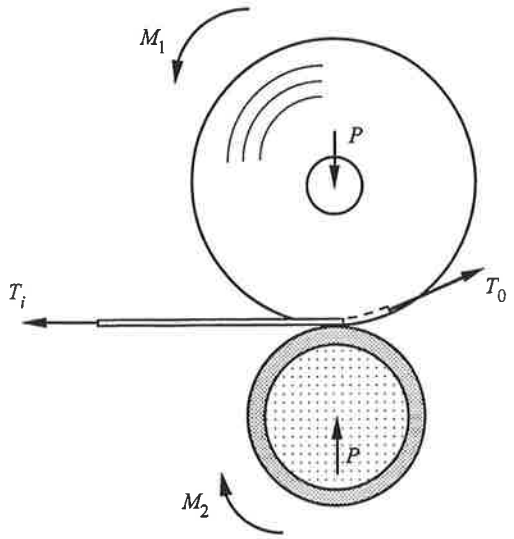

Fig. 1. Winding configuration

where the coefficients A_{rr}, $A_{r\theta}$, $A_{\theta\theta}$ and $G_{r\theta}$ are the *orthotropic elastic constants* of the material. Substituting the above equations into the equations of equilibrium

$$\frac{\partial \sigma_r}{\partial r}+\frac{1}{r}\frac{\partial \tau_{r\theta}}{\partial \theta}+\frac{\sigma_r-\sigma_\theta}{r}=0\,,\quad \frac{\partial \tau_{r\theta}}{\partial r}+\frac{1}{r}\frac{\partial \sigma_\theta}{\partial \theta}+2\frac{\tau_{r\theta}}{r}=0 \tag{3}$$

a coupled system of partial differential equations solvable by Fourier series techniques is obtained.

Let us consider next the elastic sheet in the nip. An analytical solution for the sheet can be obtained by using the method of homogeneous solutions and biorthogonality properties of the 2D elasticity problem formulated in terms of the stress function and generalized biharmonic equation [5], by using the method of separation of variables leading to a general series representation [6,7], or by using a sixth degree polynomial for the stress function accounting for linearly changing boundary loads [7]. These solutions would be valid for any sheet thickness. However, due to the thinnes of the sheet an approximate solution can be derived. Consider the sheet of Fig. 2 loaded by the normal stresses $\sigma^+(x)$ and $\sigma^-(x)$ and the shear stresses $\tau^+(x)$ and $\tau^-(x)$ at the top and bottom surfaces, respectively.

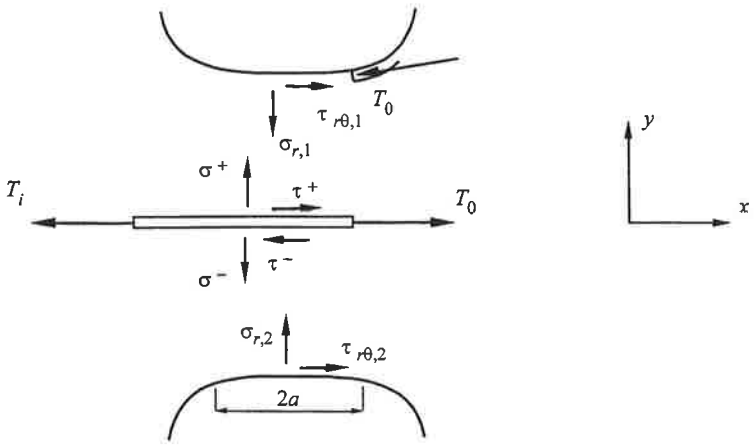

Fig. 2. Notation of the stresses within the contact area.

The web tension at the left cross-section of the sheet is T_i. Within the thin sheet approximation one can assume that $\sigma^+(x) = \sigma^-(x) \equiv \sigma^{\pm}(x)$. The stress distribution inside the sheet, compatible with the boundary conditions, takes the form

$$\sigma_x = \frac{1}{2h}\left\{T_i - \int_{-a}^{x}\left[\tau^+(\xi) - \tau^-(\xi)\right]d\xi\right\},$$

$$\sigma_y = \sigma^+(x) + \frac{1}{2}\left[\tau^{+\prime}(x) + \tau^{-\prime}(x)\right](h-y) + \frac{1}{4h}\left[\tau^{+\prime}(x) - \tau^{-\prime}(x)\right](h^2 - y^2), \qquad (4)$$

$$\tau_{xy} = \frac{1}{2}\left[\tau^+(x) + \tau^-(x)\right] + \frac{y}{2h}\left[\tau^+(x) - \tau^-(x)\right],$$

where $2h$ is the thickness of the sheet. The horizontal and vertical displacements may be integrated from the constitutive equations

$$\frac{\partial u}{\partial x} = c_{11}\sigma_x + c_{12}\sigma_y, \quad \frac{\partial v}{\partial y} = c_{12}\sigma_x + c_{22}\sigma_y,$$

$$\frac{\partial u}{\partial y} + \frac{\partial v}{\partial x} = c_{66}\tau_{xy}, \qquad (5)$$

where c_{11}, c_{12}, c_{22} and c_{66} are the compliance coefficients of the sheet.

3. FORMULATION OF THE CONTACT PROBLEM

The radial displacements of the upper and lower cylinder (roll and drum) surfaces v_1 and v_2, and the vertical displacements of the top and bottom surfaces of the sheet v^+ and v^-, respectively, must satisfy the *indentation equation*

$$v_1 + v_2 - (v^+ - v^-) = \delta_0 - \frac{1}{2R}(x^2 - 2\varepsilon_0 x) \qquad (6)$$

within the contact area. In equation (6) the coordinate x is measured along the centerline of the deformed sheet, δ_0 is the vertical approach of the cylinder centers, ε_0 the horizontal displacement of the center of the nip, and $1/R = 1/R_1 + 1/R_2$ the relative curvature of the cylinders.

In the zones of stick the velocities of the contacting surfaces must be equal. Using small displacement approximation the necessary *stick condition* between the paper roll and the sheet, and between the winding drum and the sheet can be written as

$$\varepsilon^+ - \varepsilon_1 + \xi_1 = 0, \quad \varepsilon^- - \varepsilon_2 + \xi_2 = 0, \qquad (7)$$

respectively. Here $\varepsilon^+ = \partial u(x,h)/\partial x$ and $\varepsilon^- = \partial u(x,-h)/\partial x$ are the horizontal strains of the top and bottom surfaces of the sheet, and ε_1 and ε_2 the circumferential surface strains of the roll and drum, respectively. Note that in the thin sheet approximation the condition $\varepsilon^+ = \varepsilon^-$ is valid. The constants ξ_1 and ξ_2 are the *creep ratios*, i.e., fractional differences between the speeds of the contacting bodies far away from the contact area. Within the slip areas we assume *Amonton's law* of friction, i.e.,

$$\mathrm{sgn}(V^+ - V_1)\,\tau^+ = -\mu_+\sigma^+, \quad \mathrm{sgn}(V^- - V_2)\,\tau^- = -\mu_-\sigma^-, \qquad (8)$$

where V^+ and V^- are the local speeds of the upper and lower sheet surfaces, V_1 and V_2 the local speeds of surfaces of the upper and lower cylinders, and μ_+ and μ_- the friction coefficients in the upper and lower contacts, respectively.

We can still utilize the total equilibrium conditions of the subsystems. It is easy to see from Fig. 2 that the horizontal equilibrium condition for the sheet and the torque balance conditions for the roll and drum lead to the equations

$$\int_{-a}^{a} \tau^{+}(x)\,dx - \int_{-a}^{a} \tau^{-}(x)\,dx + T_0 = T_i\,, \quad \int_{-a}^{a} \tau^{+}(x)\,dx + T_0 = \frac{M_1}{R_1}\,,$$

$$\frac{M_1}{R_1} + \frac{M_2}{R_2} = T_i\,. \tag{9}$$

In a real winding situation two of the quantities M_1, M_2 and T_i - let's say M_1 and T_i - are given. The vertical equilibrium conditions for the roll and drum give

$$\int_{-a}^{a} \sigma^{+}(x)\,dx = \int_{-a}^{a} \sigma^{-}(x)\,dx = -P\,. \tag{10}$$

If the compressive force P is given, equations (10) can be used as part of the solution procedure providing also a value for the nip contact width $2a$. If, on the other hand, the nip width is given the corresponding compressive force can be calculated by equations (10). The latter alternative is preferable since it leads to a simpler set of equations to be solved.

If the sheet goes through the nip with an externally set tension behind the nip, the tension T_0 is known. However, if the sheet is wound on the roll, the tension T_0 is not known a priori so that the number of unknowns is increased by one. The wound-on-condition, on the other hand, yields one more equation. Since the sheet behind the nip, after being stuck onto the roll surface, becomes part of the roll, one can readily conclude that the wound-on-condition takes the form

$$\xi_1 = \varepsilon_{10} - c_{11} T_0 / 2h\,, \tag{11}$$

where ε_{10} is the circumferential surface strain of the roll at the nip exit. The equations at disposal are the indentation equation (6) and the stick/slip equations (7)-(8) written at discrete points within the contact area, the equilibrium equations (9)-(10) and the wound-on-condition (11). The appropriate solution process is an extension of the *Panagiotopoulos Process* [8].

4. CONCLUSIONS

Starting from first principles we have presented the equations for the contact mechanical approach for the winding nip consisting of the wound roll, winding drum and the sheet obeying the orthotropical material law. At present we are implementing the model into a computer for nip simulations. The aim of these calculations is to find out the state of the sheet in the nip as well as the wound-on-tension needed to evaluate the stresses in the roll. The sheet model used can be progressively improved, starting from the approximate model presented in this paper and proceeding towards the more complete models of the sixth degree polynomial stress function and a general series representation.

REFERENCES

1. Betall, R.H. and Johnson, K.L., *Int J Mech Sci* **10**, 1968, 637-663.
2. Tervonen, M., Doctoral Thesis, *Acta Univ. Oul.* C 100, Finland, 1997, 123 p.
3. Soong, T.-C. and Li, C., *Int J Mech Sci* **23**, 1981, 263-273.
4. Soong, T.-C. and Li, C., *J Appl Mech* **48**, 1981, 889-894.
5. Lurie, S.A. and Vasiliev, V.V., *The Biharmonic Problem in the Theory of Elasticity*, Gordon and Breach Publishers, Luxembourg, 1995.
6. Pickett, G., *J Appl Mech* **66**, 1944, A-176 - A-182.
7. Hertzen, R. von and Jorkama, M., 'On the Solution of the Generalized Biharmonic Equation', Unpublished manuscript, 1999, 29 p.
8. Panagiotopoulos, P.D., *Ing-Arch* **44**, 1975, 421-432.

COMPLEMENTARY ENERGY, PSEUDO-STRESS ENERGY AND GEOMETRIC FLEXIBILITY

Pertti Holopainen
Institute of Applied Mechanics
Tampere University of Technology
P.O. Box 589, FIN-33101 TAMPERE, FINLAND

Extended abstract

The principle of stationary complementary work for geometrically linear structures has presented in the 1880 decade by Franceso Crotti (1839-1896) and Friedrich Engesser (1848-1931). Much later, in 1960's Charles Libove [1] and Cenap Oran [2] presented the correspondent principle for structures, where the geometric nonlinearity was also allowed. For a long time it has been accepted tat a theoretical analysis of a geometrically nonlinear elastic continuum is not possible as a function of stresses only. Not until in 1970 L.M.Zubov [3] published the principle of stationary complementary work for a nonlinear continuum. In 1973 W.T.Koiter published [4] a somewhat different derivation of the correspondent principle. Author has presented for geometrically nonlinear structures [5] and [6] the principle of stationary complementary work, where the complementary work is in two parts: 1) the stress energy caused by the elements rigid body rotations and named pseudo-stress energy and 2) the stress energy caused by the material deformations only. Both types of energies are functions of large elements rotations, expressed as a function of element forces.
In the beginning the authors presentation of complementary work is repeated using two simple examples. Later the connection with the pseudo-stress energy and the change of the geometric flexibility is presented with examples.

A single bar. Consider the bar as shown in Fig. 1a. It can be the member of truss for example.

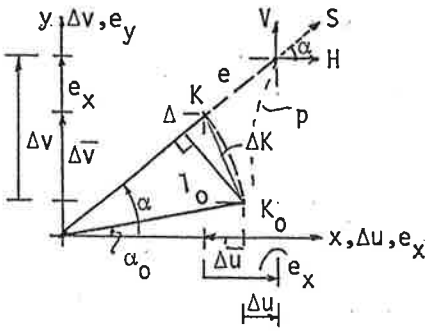

Fig. 1a

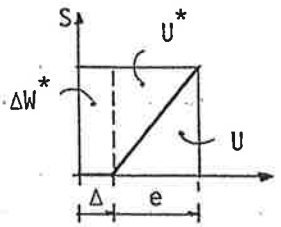

Fig. 1b.

The bar turns and stretches from the initial position into the final position on some path p (Fig 1a). When the bar is elastic, the work of force S can be calculated on the path K_0Ks. On the arc K_0K the bar turns as a rigid body and force S is equal to zero and on the line Ks the force increases to its final value S. It is assumed that the bar elongation e increases monotonically as a fuction of S. The work of S

is equal to the bar deformation energy U, as well known. It is shown in the diagram of Fig. 1b. The complementary work of S, $W^* = \Delta W^* + U^*$ (Fig. 1b), where $\Delta W^* = S\Delta$ is the pseudo-stress energy, which is caused by the bars rigid body rotation because Δ is caused by the bars rigid body rotation only. (Fig. 1a). It can be written $\Delta W^* = S\Delta = \bar{S} \cdot \Delta\bar{K} = H\overline{\Delta u} + V\overline{\Delta v}$ using the notation as in Fig. 1a. When the rigid body rotations are small as with geometrically linear structures, the $\Delta W^* \cong 0$ The stress energy $U^* = \int e(S)dS$ as with Engessers work on principle. But in the analysis of geometrically nonlinear structures it is more complicated.

A structure. Consider the geometrically nonlinear structure shown in Fig. 2a.

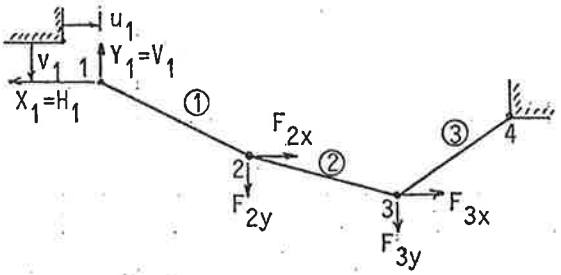

Fig. 2a

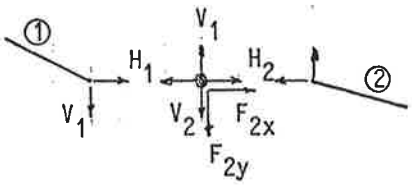

Fig. 2b

The work W and complementary work W^* of loads F_{ix}, F_{iy} and their displacements u_{ix}, v_{ix} can not be written directly without solving the structure. It is well known, that $W = U$ deformation energy for elastic linear or nonlinear structures. But what is for the elastic structures the stress energy corresponding to the complementary work W^* of loads? For a single bar as before it was obvious, that $W^* = \Delta W^* + U^*$ as derived before. But how it is in structures?

The base system (the unknown forces) must be chosen so, that the internal stress state can be expressed as a function of loads and redundants. So the deformations in material can be expressed as a function of forces. Instead of S, in a geometrically nonlinear structure, where the direction of S is changeable, its components X_1, X_2 in fixed directions must be chosen unknowns. Using the notatoin of Fig. 2a

$$W^* = -\int_0^{X_1} u_1 dX_1 - \int_0^{Y_1} v_1 dY_1 + \sum_{i=1}^{4} \int_0^{F_{ix}} u_i dF_{ix} + \sum_{i=1}^{4} \int_0^{F_{iy}} v_i dF_{iy} \qquad (1)$$

By the partial integration and taking into account, that $W = U$ it is obtainable

$$W^* = -X_1 u_1 - Y_1 v_1 + \sum_{i=1}^{4} F_{ix} u_i + \sum_{i=1}^{4} F_{iy} v_i - U \qquad (F_{ix} = F_{iy} = 0,\ i = 1,4) \qquad (2)$$

The force system X_1, Y_1, F_{ix}, F_{iy} must be in equilibrium and the compatibility of displacements must be true in the base system (Fig. 2a). Thus

$$H_1 = X_1 \qquad u_1 = -\Delta u_1 - \Delta u_2 - \Delta u_3$$
$$V_1 = Y_1 \qquad v_1 = -\Delta v_1 - \Delta v_2 - \Delta v_3$$
$$H_2 = H_1 - F_{2x} \quad (3) \qquad u_2 = -\Delta u_2 - \Delta u_3 \quad (4)$$
$$V_2 = V_1 - F_{2y} \qquad v_2 = -\Delta v_2 - \Delta v_3$$
$$H_3 = H_2 - F_{3x} \qquad u_3 = -\Delta u_3$$
$$V_3 = V_2 - F_{3y} \qquad v_3 = -\Delta v_3$$

Substituting (3) and (4) into (2) it can be obtained after manipulations

$$W^* = \sum_{i=1}^{3}(H_i \Delta u_i + V_i \Delta v_i) - U \qquad (5)$$

But

$$U = \sum_{i=1}^{3}(S_i e_i - U_i^*) = \sum_{i=1}^{3}(S_{ix} e_{ix} + S_{iy} e_{iy}) - U^* = \sum_{i=1}^{3}(H_i e_{ix} + V_i e_{iy}) - U^* \qquad (6)$$

Substituting U from (6) (the last form) into (5) it results

$$W^* = \sum_{i=1}^{3}(H_i \overline{\Delta u_i} + V_i \overline{\Delta v_i}) + U^* \qquad (7)$$

where

$$\sum_{i=1}^{3}(H_i \overline{\Delta u_i} + V_i \overline{\Delta v_i}) = \Delta W^* \qquad (8)$$

the pseudo-stress energy caused by the elements rigid body rotations only. Thus in the geometrically linear structures (elements rigid body rotations are small)

$$W^* = U^* \qquad (9)$$

A connection between the pseudo-stress energy and the geometric flexibility. Consider a structure as shown in Figs. 3a and 3b which are kept geometrically nonlinear. It is assumed here, that the displacement v(F) is single-valued, convex or concave and monotonically increasing. The flexibility c and geometric flexibility c_g

$$c = v'(F) = \frac{\partial^2 W^*}{\partial F^2}, \quad c_g = c - c_0 \qquad (10),(11)$$

Further it is assumed that for the sake of simplicity the stuctures are physically linear. So the numerica values $U = U^*$

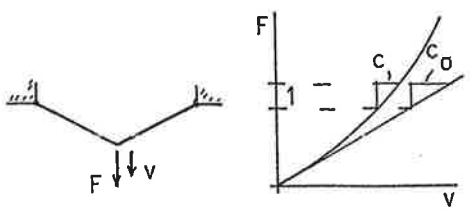

Fig. 3a

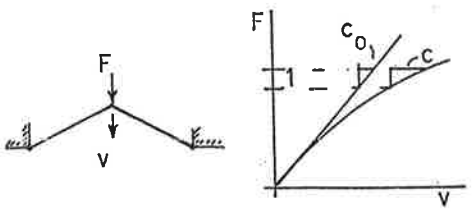

Fig. 3b

For the structure as shown in Fig. 3a the F-v diagram is shown in Fig. 3a also,

$$W^* > W = U = U^* \;\&\; W^* = \Delta W^* + U^* \Rightarrow \Delta W^* > 0 \qquad (12)$$

The geometric flexibility decreases which can be seen from diagram in Fig. 3a.

For the structure as shown in Fig. 3b, the F-v diagram is shown in Fig. 3b also,

$$W^* < W = U = U^* \; W^* = \Delta W^* + U^* \Rightarrow \Delta W^* < 0 \qquad (13)$$

The geometric flexibility increases, which can be seen from diagram in Fig. 3b.

If the structure is loaded by many forces F_1... (and includes many elements) and if the forces increase in the same way, the increase of loading can be presented by a single parameter t: $\overline{P}(t) = t\overline{F}$. Furthermore, if the structure is physically linear, only the change in geometry changes the flexibility.

$$c(t) = \frac{\partial^2 W^*}{\partial t^2} \qquad (14)$$

Conclusion. When in the physically linear structure the geometric flexibility decreases with t-increasing loading $\Leftrightarrow$ pseudo-stress energy $\Delta W^* > 0$. When geometric flexibility increases $\Leftrightarrow$ $\Delta W^* < 0$.

Examples. In Figs 4a and 4b the bar tension flexibility c=0.6487826 m/kN.

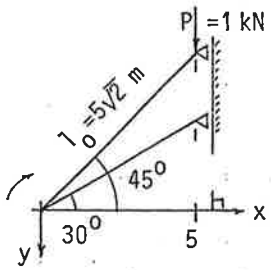

Fig. 4a

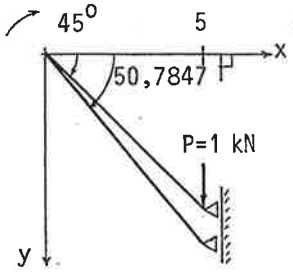

Fig. 4b

$X = -1.732186$ kN

$\Delta W^* = -0.481973$ kNm

$X = 0.816024$ kN

$\Delta W^* = 0.046474$ kNm

Bibliography

[1] Libove C., Complementary energy methods for finite deformations. JEMD, ASCE, Vol.90,No.EM6,December 1964.

[2] Oran C., Complementary energy consept for large deformations. JSD, ASCE, Vol.93,No.ST1,February 1967.

[3] Zubov L.M., The stationary principle of complementary work in nonlinear theory of elasticity. JAMM,Vol.34,No.2,1970.

[4] Koiter W.T., On the principle of stationary complementary energy in nonlinear theory of elasticity, 1973. Dep.Mech.Engin. Delft University of Technology.

[5] Holopainen P., Application of the principle of stationary complementary work to the analysis of suspension roofs. Int.Conf. of tension Roof Structures, London 1974.

[6] Holopainen P., The general theory of a suspension cable, 1975 (diss.) Helsinki University of Technology.

FULLY NONLINEAR ANALYSIS OF PLANE FRAMES USING KINEMATICALLY EXACT BEAM ELEMENTS

Sami Pajunen

Tampere University of Technology, Institute of Applied Mechanics

Introduction

In this paper we consider the so called kinematically exact finite elements in geometrically and materially non-linear structural analysis. The solution procedure used in the non-linear equilibrium path detection is based on Fried's orthogonal trajectory arc-length method [4] with the full Newton-Raphson iteration. For detailed description of the path-following computations and related items, see e.g. [5]. The considered isoparametric plane beam element based on Reissner's stress resultant theory [6] is capable of handling finite displacements, finite rotations and finite strains. Non-linearity of the material model is taken in account using a yield criterion based on the stress resultants with linearly isotropic hardening. The considered element and algorithms are numerically verified in the analysis of a cantilever beam example.

Element Description

Reissner [6] has developed a kinematically exact stress resultant theory for curved beams and arches in which the finite strains are written as

$$\begin{aligned} \varepsilon &= (x'+u')\cos\varphi + (y'+v')\sin\varphi - 1 \\ \gamma &= (y'+v')\cos\varphi - (x'+u')\sin\varphi \\ \kappa &= \varphi' - \varphi'_0 \end{aligned} \tag{1}$$

in which $(\,)' = \mathrm{d}(\,)/\mathrm{d}s$ denotes the differentiation with respect to the element axial co-ordinate s. In (1) u and v are the displacements in x- and y-directions, respectively and φ measures the angle between the beam cross section and the y-axis (in the undeformed state $\varphi=\varphi_0$). In the isoparametric case, the finite element interpolations for geometry and displacements are the same:

$$x = \mathbf{N}^{\mathrm{T}}\mathbf{x},\quad y = \mathbf{N}^{\mathrm{T}}\mathbf{y},\quad u = \mathbf{N}^{\mathrm{T}}\mathbf{u},\quad v = \mathbf{N}^{\mathrm{T}}\mathbf{v},\quad \theta \equiv \varphi - \varphi_0 = \mathbf{N}^{\mathrm{T}}\boldsymbol{\theta} \tag{2}$$

in which the vectors $\mathbf{x}$, $\mathbf{y}$, $\mathbf{u}$, $\mathbf{v}$ and $\boldsymbol{\theta}$ contain the values of x, y, u, v, and θ at the element nodes and $\mathbf{N}$ contains the associated shape functions. Inserting the finite element interpolations for u, v and θ into the virtual strain formulas results in

$$\begin{Bmatrix} \delta\varepsilon \\ \delta\gamma \\ \delta\kappa \end{Bmatrix} = \mathbf{B}\begin{Bmatrix} \delta\mathbf{u} \\ \delta\mathbf{v} \\ \delta\boldsymbol{\theta} \end{Bmatrix} \quad \text{with} \quad \mathbf{B} = \begin{bmatrix} \cos\varphi\mathbf{N}' & \sin\varphi\mathbf{N}' & \gamma\mathbf{N} \\ -\sin\varphi\mathbf{N}' & \cos\varphi\mathbf{N}' & -(\varepsilon+1)\mathbf{N} \\ 0 & 0 & \mathbf{N}' \end{bmatrix} \tag{3a,b}$$

In (3) the shape function derivatives are computed from

$$\mathbf{N}' = \frac{\mathrm{d}\mathbf{N}}{\mathrm{d}s} = \frac{\mathrm{d}\mathbf{N}}{J\mathrm{d}\xi} \quad \text{with} \quad J = \sqrt{\left(\frac{\mathrm{d}x}{\mathrm{d}\xi}\right)^2 + \left(\frac{\mathrm{d}y}{\mathrm{d}\xi}\right)^2} \tag{4a,b}$$

in which ξ is the natural co-ordinate of the element. The linear and geometrical stiffness matrices $\mathbf{K}_l$ and $\mathbf{K}_g$ can then be computed from

$$\mathbf{K}_l = \int_L \mathbf{B}^T\mathbf{D}\mathbf{B}J\mathrm{d}\xi \quad \text{and} \quad \mathbf{K}_g = b\int_L \Delta\mathbf{B}^T\mathbf{S}J\mathrm{d}\xi \tag{5a,b}$$

in which $\Delta\mathbf{B}$ can be derived from (3b) and, in Reissner's stress resultant theory, $\mathbf{D}$ transforms the strain vector $\varepsilon=[\varepsilon,\ \gamma,\ \kappa]^T$ into stress resultant vector $\mathbf{S}=[N,\ Q,\ M]^T$:

$$\mathbf{D} = Ebh\begin{bmatrix} 1 & 0 & 0 \\ 0 & 1/2(1+\nu) & 0 \\ 0 & 0 & h^2/12 \end{bmatrix} \tag{6}$$

in which E is the elastic modulus, ν is the Poisson's ratio and b and h are the width and height of the element, respectively.

Elasto-Plastic Material Model

For the stress resultant yield condition we take the well-known axial force - bending moment interaction curve [1, page 509]

$$\mathrm{F}(N,M,\kappa) = \left(\frac{N}{N_\mathrm{P}}\right)^2 + \left|\frac{M}{M_\mathrm{P}}\right| - 1 \quad \Leftrightarrow \quad \mathrm{F}(N,M,\kappa) = N^2 + \frac{4N_\mathrm{P}}{h}|M| - N_\mathrm{P}^2 \tag{7a,b}$$

in which κ is a hardening parameter, $M_\mathrm{P}=\sigma_y bh^2/4$, $N_\mathrm{P}=\sigma_y bh$ and $\sigma_y=\sigma_y(\kappa)$ is the yield stress taken from a uniaxial stress - strain curve that is now assumed to be bi-linear with tangential modulus E_t in the plastic range. Moreover, we assume that the material is isotropically hardening obeying the associative flow rule for which the elasto-plastic incremental stress resultant - strain relationship reads in

$$\mathrm{d}\mathbf{S} = \mathbf{D}_{EP}\mathrm{d}\varepsilon \tag{8}$$

in which the elasto-plastic material matrix is [9, page 463]

$$\mathbf{D}_{EP} = \mathbf{D} - \alpha\frac{\mathbf{D}[\partial\mathrm{F}/\partial\mathbf{S}]^T[\partial\mathrm{F}/\partial\mathbf{S}]\mathbf{D}}{-\partial\mathrm{F}/\partial\kappa\mathbf{S}^T[\partial\mathrm{F}/\partial\mathbf{S}]^T + [\partial\mathrm{F}/\partial\mathbf{S}]\mathbf{D}[\partial\mathrm{F}/\partial\mathbf{S}]^T} \tag{9}$$

For the particular yield condition (7b) the derivatives of the function F are

$$\partial\mathrm{F}/\partial\mathbf{S} = \left[2N,\ 0,\ \mathrm{sign}(M)\frac{4N_\mathrm{P}}{h}\right] \quad \text{and} \quad \partial\mathrm{F}/\partial\kappa = \frac{4|M|}{h}\frac{\partial N_\mathrm{P}}{\partial\kappa} - 2N_\mathrm{P}\frac{\partial N_\mathrm{P}}{\partial\kappa} \tag{10a,b}$$

Assume that the uniaxial stress resultant - strain curve is known and the hardening parameter κ is taken to be represented by the amount of plastic work as in [9], hence, $\mathrm{d}\kappa=N_\mathrm{P}\mathrm{d}\varepsilon_\mathrm{P}$ resulting in

$$\partial F / \partial \kappa = \frac{4|M|}{h}\frac{dN_P}{d\varepsilon_P}\frac{1}{N_P} - 2N_P\frac{dN_P}{d\varepsilon_P}\frac{1}{N_P} = 2E_P bh\left(\frac{|M|}{2M_P} - 1\right) \tag{11}$$

in which the plastic modulus $E_P=EE_t/(E-E_t)$ [2, page 4]. Using (10,11) it is now possible to compute the elasto-plastic material matrix (9) in which the default value of the parameter α is 1, but in the unloading phase $\alpha=0$.

In the computations the stress resultant increment due to the elasto-plastic strain increment is computed by dividing the strain increment into small steps so that the yield stress σ_y is updated after every step by forcing the stress resultant vector to remain on the boundary of the yield surface. Hence, following from (7b) the updated value of the yield stress σ_y is

$$\sigma_y = \frac{|M|b^2h^2 + \sqrt{M^2b^4h^4 + b^4h^6N^2/4}}{b^3h^4/2} \tag{12}$$

Numerical Example

As a numerical example we consider a cantilever beam discretized by 10 three-noded elements and loaded by a transverse force as depicted in Fig. 1. Using the shown material data, the computed solution is in very good agreement with the results presented in [3]. Slight difference between the computed and reference equilibrium paths follows from the fact that in the stress resultant theory partial plastification of a beam section can not be taken in account. However, this is only a minor drawback compared to the computational efficiency of the stress resultant approach. The computing times for the elastic and elasto-plastic cases with the same number of steps and same convergence tolerance were 0.55 and 0.77 seconds, respectively.

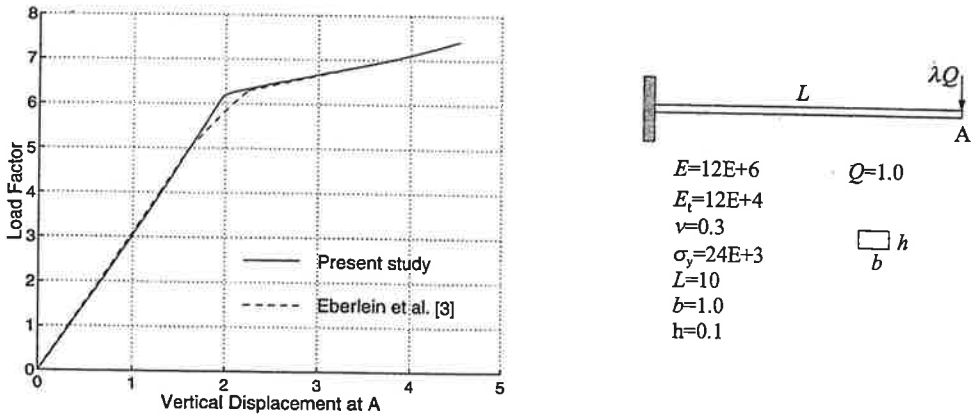

Figure 1. Cantilever beam and associated equilibrium paths.

Conclusions

The use of stress resultant based elements in fully non-linear structural analysis offers some advantages compared to the 'conventional' finite elements. In elastic range the element gives accurate results even if the tangential stiffness matrix and the internal force vector were computed using the total-Lagrangian (TL) formulation. Hence, one do not have to worry about the reference configuration updating algorithms and the handling of rigid body motions during the analysis. If the element material is considered as elasto-plastic, one has to use an

incremental formulation for the stress resultants but still the kinematic matrix **B** in (3) can be computed straight from the initial configuration. Moreover, the yield criterion is now expressed in terms of the stress resultants and this makes the analysis more efficient because the numerical integration over the height of the beam is not needed. Unfortunately, for the same reason, the element is not suitable for accurate analysis of e.g. concrete beams for which the elasto-plastic stress-strain relations in compression and tension are completely different.

In further studies the shear force will be included into the yield condition as proposed in [1] and the research will be augmented to axisymmetric elasto-plastic shells for which a similar stress resultant theory also exists [7]. Moreover, instead the used stress-updating algorithm, more sophisticated methods that quarantee the convergence rate to remain quadratic, see e.g. [8], will be tested in the computations.

References

1 Chen W.F. and Han D.J. *Plasticity for Structural Engineers*, Springer-Verlag, New York 1988.

2 Chen W.F. and Zhang H. *Structural Plasticity*, Springer-Verlag, New York 1991.

3 Eberlain R. and Wriggers P. Finite element concepts for finite elastoplastic strains and isotropic stress response in shells: theoretical and computational analysis, *Comp. Meth. Appl. Mech. Eng.* 1999; **171**: 243-279.

4 Fried I. Orthogonal trajectory accession to the nonlinear equilibrium curve, *Comp. Meth. Appl. Mech. Eng.* 1984; **47**: 283-97.

5 Kouhia R. and Mikkola M. Tracing the equilibrium path beyond simple critical points, *Int. J. Num. Meth. Eng.* 1989; **28**: 2923-41.

6 Reissner E. On one-dimensional finite-strain beam theory: the plane problem, *J. Appl. Math. Phys. (ZAMP)* 1972; **23**: 795-804.

7 Reissner E. On finite axi-symmetrical deformations of thin elastic shells of revolution, *Comp. Mech.* 1989; **4**: 387-400.

8 Simo J.C. and Hughes T.J.R *Computational Inelasticity*, Springer-Verlag, New York 1998.

9 Zienkiewicz O.C. *The Finite Element Method*, Third edition, McGraw-Hill, 1977.

POSTROCESSING TECHNIQUES IN FE-EIGENPROBLEM ANALYSIS

R. Baušys[†], N.-E. Wiberg[*]

[†] Vilnius Gediminas Technical University
LT-2040 Vilnius, Lithuania
e-mail: romas@fm.vtu.lt, web: http://www.vtu.lt/

[*] Chalmers University of Technology
SE-41296 Goteborg, Sweden
e-mail: new@vsect.chalmers.se, web: http://www.chalmers.se/

1. Introduction

Nowadays finite element (FE) simulation becomes essential tool to obtain information for practical engineering decision-making. In particular, much attention of researchers is devoted to the development of automatic adaptive FE strategies, which enables us to obtain FE solutions within a prescribed accuracy without any user intervention. The most important ingredient in those strategies is the reliable error estimation. The assessment of the discretization errors can be performed by two ways: a priori and posteriori error estimation. A priori error estimates provide only qualitative assessment of the solution and finite element mesh such as the smoothness of the solution, the regularity of the mesh, asymptotic rate of convergence, which is essential for theoretical investigation. A posteriori error estimates can be utilized to give more specific assessment of errors in different measures [1].

In this paper we focus our attention on the application of the Superconvergent Patch Recovery technique for displacements (SPRD) to the elliptic problems. The SPRD technique is based on a higher order displacement field fitted to superconvergent values in nodal points in a least squares sense over local element patches [2, 3].

For vibration problems the enhancements of the solution are provided by the local/global error control approaches. Within a framework of the local updating, the SPRD is applied to free vibration problems for improving eigenmodes and eigenfrequencies. This method shows excellent results for the lower eigenfrequencies, but for the higher eigenfrequencies the improvement of the eigenpairs is still not enough to provide reliable error estimation. Due to a too crude underlying mesh in order to improve the higher frequencies, we employ a preconditioned conjugate gradient scheme to optimize successive deflated Rayleigh quotients. The idea of global updating is to improve the FE solution of order p by the SPRD method and then use it as the starting trial eigenvector in the preconditioned conjugate gradient scheme to obtain a solution similar to the FE solution of order $p+1$ [4]. When we have obtained the global updated solution of order $p+1$, we apply again the SPRD technique to get an improved solution of order $p+2$; thus we have a global-local approach. Numerical examples show the nice properties of local/global updated solution as a basis for an error estimator and an error indicator in an adaptive finite element strategies.

In case of acoustical problems, we construct an adaptive remeshing strategy combining our error estimation technique with available commercial packages. For finite element analysis we use the commercial code SYSNOISE. The commercial package I-DEAS is

implemented to generate the initial mesh and to perform adaptive remeshing procedures [5]. The numerical methods used in the technique are outlined and example is cited to show the range of this method's applicability.

2. A Postprocessed Error Estimation

The problems discussed in this paper can be described in the form of

$$Lu + f = 0 \qquad in\,\Omega \tag{1}$$

together with appropriate boundary conditions. Here L is a differential operator acting on the unknown function u; f denotes some function, which is known inside the domain Ω.

In order to investigate the accuracy of the solution, we need to discuss the dicretization error. The point-wise discretization error is simply the difference between exact solution and the finite element solution:

$$\boldsymbol{e}_u = \boldsymbol{u} - \boldsymbol{u}^h \tag{2}$$

where $\boldsymbol{u}$ is the exact solution and $\boldsymbol{u}^h$ is the corresponding FE-approximation.

The essence of the postprocessed error estimator is to replace the exact solution with a postprocessed solution of higher quality:

$$\boldsymbol{e}_u \approx \bar{\boldsymbol{e}}_u = \boldsymbol{u}^* - \boldsymbol{u}^h \tag{3}$$

where $\bar{\boldsymbol{e}}_u$ is the point-wise estimated error. Using the improved solution we have the estimation

$$\|\bar{e}\| = \left(\int_\Omega \bar{\boldsymbol{e}}_u^T \boldsymbol{L} \bar{\boldsymbol{e}}_u \, d\Omega \right)^{\frac{1}{2}} \tag{4}$$

The quality of any error estimator is dictated by an effectivity index:

$$\theta = \frac{\|\bar{e}\|}{\|e\|} = \frac{\left\|u^* - u^h\right\|}{\left\|u - u^h\right\|} \tag{5}$$

It has been known that if the postprocessed solution exhibits superconvergence property, meaning that the rate of convergence of the postprocessed solution is at least one order higher than finite element solution, it can be shown that the postprocessed type of the error estimator is asymptotically exact. Assuming that the true error converges as $\left\|u - u^h\right\| = C_h h^p$ and the error of the postprocessed solution $\left\|u - u^*\right\| = C_* h^{p+\alpha}$ for some superconvergent solution with $\alpha \geq 1$, we can obtain

$$1 - C h^\alpha \leq \theta \leq 1 + C h^\alpha \tag{6}$$

Showing that the effectivity index approaches unity as $h \to 0$. In the above, $\alpha \geq 1$ indicates whether the recovered solution has a higher rate of convergence than the finite element solution.

3. Element Patch Recovery Technique

The idea of SPRD is to define a new displacement field of $p+1$ order over a patch of elements. This new field is required to be a least square fit to the original finite element solution at some points where the accuracy of finite element solution is higher. It has been known that the nodal points of the finite element approximation are found to be the exceptional points at which the prime variables (displacements) have higher order accuracy with respect to the global accuracy.

The new displacement field over an element $\tau \in T_h$ of the corresponding eigenmode $\boldsymbol{u}_i^*$ we construct using ordinary local basis functions of the order $p+1$

$$\boldsymbol{u}_i^*(\boldsymbol{x}) = \sum_r \boldsymbol{N}_r^*(\boldsymbol{x})(\boldsymbol{u}_r^*)_i + \sum_s \boldsymbol{N}_s^*(\boldsymbol{x})(\boldsymbol{u}_s^*)_i \tag{7}$$

where r is used to denote original finite element τ nodes and s denotes additional nodes of the element of the recovered displacement field, $\boldsymbol{N}_r^*(\boldsymbol{x})$ and $\boldsymbol{N}_s^*(\boldsymbol{x})$ are local basis functions of the order $p+1$ associated with the original element nodes and the additional ones, respectively.

The nodal values of the original finite element displacements are assumed to be the same as of the original finite element solution $(\boldsymbol{u}_r^*)_i \equiv (\boldsymbol{u}_r^h)_i$ and recovered displacement values $(\boldsymbol{u}_s{}^*)_i$ at the additional nodes are obtained by solving the following least squares problem in the element patch Ω_τ :

Find $\boldsymbol{u}_i{}^* \in \mathrm{P}_{p+1}$ such that

$$J_{\Omega_\tau}(\boldsymbol{u}_i^*) = \min_{(\boldsymbol{u}^{f*})_i \in P_{p+1}} J_{\Omega_\tau}(\boldsymbol{u}^{f*})_i \tag{8}$$

where

$$J_{\Omega_\tau}(\boldsymbol{u}^{f*})_i = \sum_{j=1}^{ns} w_j^2 \boldsymbol{R}_u^T(\boldsymbol{x}_j)\boldsymbol{R}_u(\boldsymbol{x}_j) \tag{9}$$

where the residual $\boldsymbol{R}_u(\boldsymbol{x}_j)$ is calculated at the locations where the original finite element solution is superconvergent or at least highly accurate. The residual is defined by expression as

$$\boldsymbol{R}_u = (\boldsymbol{u}^{f*})_i - (\boldsymbol{u}_r^h)_i \tag{10}$$

and $(\boldsymbol{u}^{f*})_i$ belongs to polynomial expansion of order $p+1$

$$(\boldsymbol{u}^{f*})_i = \boldsymbol{Q}(\boldsymbol{x})\boldsymbol{b} \tag{11}$$

where $\boldsymbol{Q}(\boldsymbol{x})$ is a row matrix containing monomial term of physical coordinates of $p+1$ order, and the vector $\boldsymbol{b}$ is a set of unknown parameters to be determined.

The patch equations are set up for patches of elements surrounding the master element. For each element $\tau \in T_h$ we denote be $E(\tau)$ the set of its edges. So for each element τ the patch Ω_τ which consists of the part of elements surrounded the master element is denoted by

$$\Omega_\tau = \bigcup_{\tau \in E^*(\tau')} \tau' \qquad (12)$$

For the triangular elements set $E^*(\tau')$ coincides with $E(\tau)$, for quadrilateral elements set $E^*(\tau')$ consists of the adjacent edges connected to one of the nodes of the element $E^*(\tau') \subset E(\tau)$ as shown in Fig 1.

We use a reduced element patch which has an extension of the size $2h$ (where h is a characteristic element size in the local patch) in order to maintain locality of the least squares fit. This enables us to reduce the cost of computation and at the same time to increase the accuracy of recovered displacement field. Only boundary patches, which have not enough number of elements for reduced patch, are constructed in the usual way.

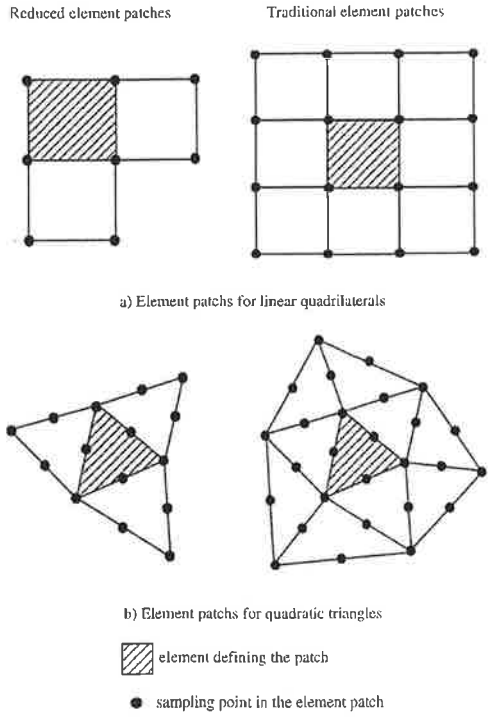

Figure 1: Possible element patches for linear quadrilateral and quadratic triangular elements

The described approach is a local updating method, so no global system of the equations has to be solved. The number of equations to be solved is small and the cost of the recovery procedure is proportional to the number degrees of freedom n of the mesh.

As a demonstration of the procedure we consider the Poisson equation over a unit domain and use the boundary condition and the 'load' function f that corresponds to an exact solution of the form

$$u(x, y) = x(1 - x)y(1 - y)(1 + 2x + 7y) \qquad (13)$$

The regular meshes are used in the computational experiments. Numerical results are presented for both quadrilateral and triangular linear elements in order to test whether the proposed SPRD procedure is adequate to estimate the error of the finite element solution.

The following labels are used in figures and text: FE for the original finite element solution, SPR for the Zienkiewicz and Zhu [6] superconvergent patch recovery technique, SPRD for the superconvergent patch recovery technique for displacements presented here [2, 3] and DI for the displacement interpolation recovery technique developed in [7].

The error in energy of recovered solutions obtained using different recovery procedures is compared with that of finite element solution in Fig 2. The improved derivatives obtained by SPRD technique exhibits $O(h^{p+1})$ superior rate of convergence as expected and shows higher accuracy than SPR and DI approaches. So the proposed SPRD technique provides asymptotically exact error estimate.

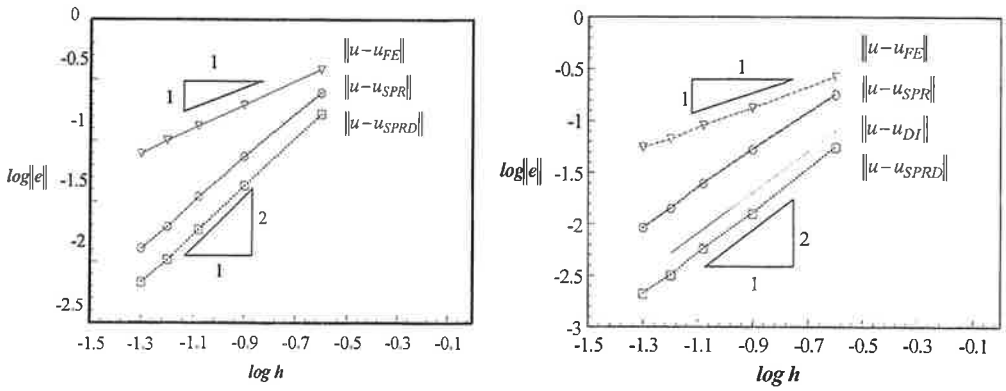

a) triangular element

b) quadrilateral element

Figure 2: Convergence of the energy norm of error

In Fig 3, the point-wise error distribution of the derivative component σ_x is shown obtained using the finite element method and recovery approaches SPR and SPRD using linear quadrilateral elements.

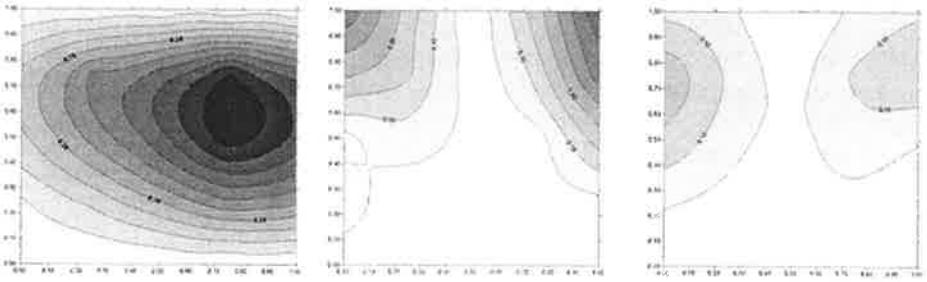

a) σ_x -FE

b) σ_x -SPR

c) σ_x -SPRD

Figure 3: Distribution of absolute error in flux component σ_x using quadrilateral elements

4. Free Vibration Problems

In FE context, we obtain the following equation

$$(\boldsymbol{K} - \lambda^h \boldsymbol{M})\boldsymbol{u}^h = \boldsymbol{0} \ , \ \ \lambda^h = (\omega^h)^2 \tag{15}$$

where $\boldsymbol{K}$ is the stiffness matrix and $\boldsymbol{M}$ is the consistent mass matrix of the structure. Equation (5) is of the form of a linear generalized eigenvalue problem for the finite dimensional discrete problem, with eigenvalues λ_i^h being equal to the squares of the eigenfrequencies ω_i^h .

In order to assess the discretization errors, we may assume the improved eigenfrequencies (of higher accuracy order) can be constructed using Rayleigh quotient

$$(\omega_i^*)^2 = \frac{\sum_K \int_{\Omega_e} (\tilde{\nabla} \boldsymbol{u}_i^*)^T \boldsymbol{D} \tilde{\nabla} \boldsymbol{u}_i^* \, dx}{\sum_K \int_{\Omega_e} (\tilde{\nabla} \boldsymbol{u}_i^*)^T \rho \tilde{\nabla} \boldsymbol{u}_i^* \, dx} \tag{16}$$

where K is the total number of elements and $\boldsymbol{u}_i^*$ is a displacement field of the eigenmode i over the elements which has a higher order of accuracy. The recovered displacement field of the eigenmode $\boldsymbol{u}_i^*$ will be determined by a postprocessed updating technique.

The quality of any error estimator is measured by effectivity index giving the ratio of the estimated errors to the actual ones as follows

$$\theta_i = \frac{\Delta \overline{\omega}_i^h}{\Delta \omega_i^h} \tag{17}$$

where the exact error in eigenfrequencies and the estimated error of the finite element solution can be written as

$$\Delta \omega_i^h = \omega_i^h - \omega_i \ , \ \ \Delta \overline{\omega}_i^h = \omega_i^h - \omega_i^* \tag{18a, b}$$

A new improved finite element solution can be constructed by the local and global updating techniques. Within a framework of the local updating the Superconvergent Patch Recovery technique for displacements (SPRD) is applied to free vibration problems for improving eigenmodes and eigenfrequencies. From the higher order accuracy displacement field an improved kinetic energy and strain energy can be calculated and thus an improved eigenfrequency can be obtained using Rayleigh quotient. This approach is a local updating method, so no global system of equations has to be constructed and solved. Details are available in [2], [3]. This method does not show sufficient improvement for the higher eigenfrequencies to provide reliable error estimation. We need improvement of the higher eigenfrequencies, for it is impossible to obtain good results based on the information obtained by performing analysis using a very coarse preliminary mesh.

In order to improve the higher frequencies, we are interested in improving the eigenfrequencies from an initial mesh using base functions of order p to obtain the solution of base functions of order $p+1$. The scheme of deflation accelerated conjugate gradients, DACG, can be employed to optimize successive deflated Rayleigh quotients based on a preconditioned conjugate gradient technique is developed as global updating.

This technique has been developed in [8]. The idea of global updating is to improve the FE solution of order p by the SPRD method and then use it as the starting trial eigenvector in the preconditioned conjugate gradient scheme to obtain a solution similar to the FE solution of order $p+1$. The SPRD improved solution used as initial trial eigenvector for the modified conjugate gradient scheme put us on the asymptotic phase of the convergence profile. We do not seek to determine a fully converged eigenpairs so we restrict the number of the iterations to in advance prescribed quantity. When we have obtained the global updated solution of order $p+1$ we apply again the SPRD technique to get an improved solution of order $p+2$, thus we have a global-local approach. The details of this global/local updating technique are available in [4].
We consider a square thin membrane, shown in Fig 4, for the case of transverse vibrations.

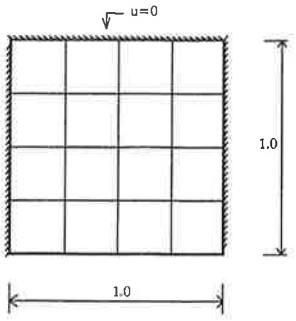

Figure 4: A finite element model of a square membrane

For simplicity, the wave propagation velocity $c = \sqrt{T/\rho}$ is assumed to be $1.0\frac{m}{s}$ where T is the uniform tension in the membrane. The study of the convergence rate of the proposed local and global updating procedures has been performed for the different eigenfrequencies as shown in Fig 5.

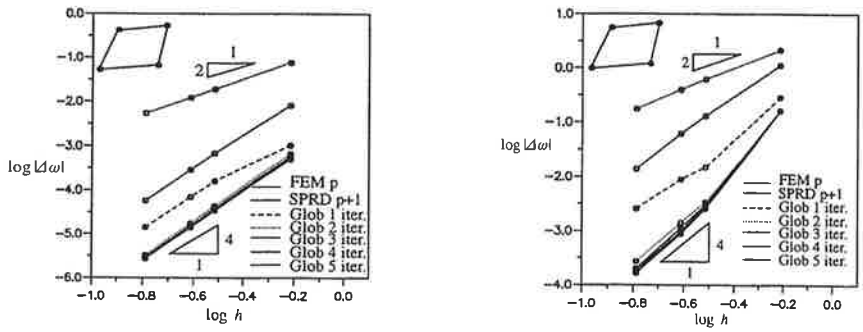

a) 1-st eigenfrequency b) 10-th eigenfrequency

Figure 5: Convergence rates in iterations of local and global updating procedure using quadrilateral elements

One can observe that the sufficient accuracy is achieved after a few global updating iterations. In order to keep computational efficiency, the number of the iterations is therefore set to be *3* for all numerical experiments.

The convergences of the effectivity indices are plotted in Fig 6.

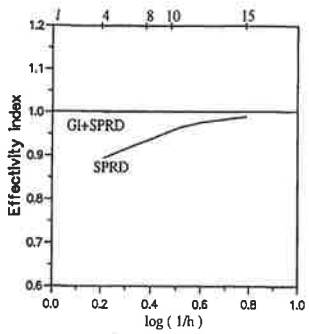

a) 1-st eigenfrequency

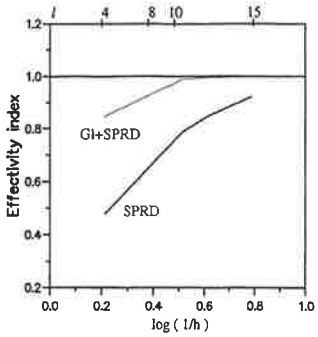

b) 10-th eigenfrequency

Figure 6: Effectivity indices by quadrilateral elements

We observe that the effectivity indices converge to one when the finite element mesh is refined. The superiority of the global updating coupled with SPRD technique (GI+SPRD) over the local updating (SPRD) is clearly demonstrated. The global updating is a more time-consuming procedure than SPRD.

5. Acoustic Problems

With finite element approximation the governing equations for the frequency domain will be of the form

$$\left(\boldsymbol{K} + j\rho\omega\boldsymbol{C} - \omega^2\boldsymbol{M}\right)\boldsymbol{q} = -j\rho\omega\boldsymbol{F} \tag{19}$$

where $\boldsymbol{K}$ is derived using kinetic energy expression, $\boldsymbol{C}$ is derived from energy dissipated on boundary walls and $\boldsymbol{M}$ is derived from fluid potential energy, ω is the angular frequency of excitation, $\boldsymbol{F}$ is the generalized excitation term and $\boldsymbol{q}$ is the vector, which contains nodal pressure values.

With the finite element solution of the problem, pressure and velocity approximations q^h and $v^h = -\frac{1}{j\rho\omega}\nabla q^h$, respectively, are obtained. To calculate steady-state pressure and velocities the commercial SYSNOISE code is employed.

In the postprocessed procedures the errors are estimated by computing the difference between an improved solution and the original finite element solution as follows

$$|\bar{e}|_1^2 = \int_\Omega (v^{*T} - v_h^T)(\bar{v}^* - \bar{v}_h)d\Omega \tag{20}$$

The improved velocity solution v^* is determined from new pressure field q^* of the higher order of accuracy, which is obtained using SPRD technique.
We construct an adaptive remeshing strategy combining our error estimation technique with available commercial packages. For finite element analysis we use the commercial code SYSNOISE. The commercial package I-DEAS is implemented to generate the initial mesh and to perform adaptive remeshing procedures.
The flowchart of a generic adaptive strategy is shown in Fig 7.

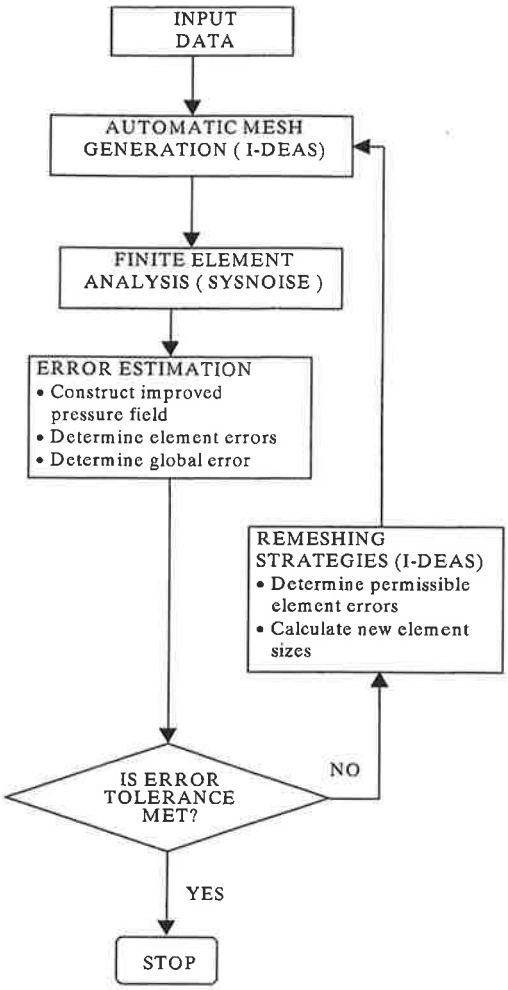

Figure 7: Flow chart of the adaptive acoustic analysis

The two dimensional model of the car enclosure is presented in Fig 8. Normal boundary velocity is set to be 0 at all sides except for the vibrating panel with velocity $v_0=3.0\text{x}10^{-4}$ m/s at the left hand side.

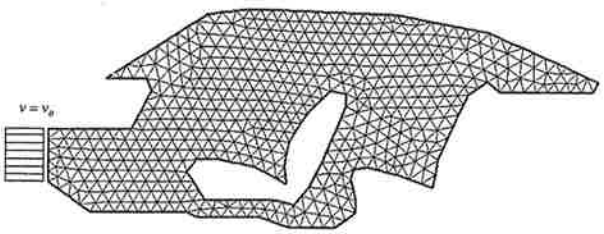

Elements=989

Figure 8: Geometry, boundary conditions and initial mesh of the car enclosure

The first five acoustic eigenfrequencies obtained by initial mesh are as follows 74.38Hz, 122.33Hz, 131.14Hz, 175.88Hz and 230.39Hz. Two different frequencies of excitation 50Hz and 350Hz are studied. The initial mesh of 989 elements used in the adaptive scheme gives the relative errors of the finite element solution as 7.41% at 50 Hz and 13.27% at 350 Hz . For both cases the final meshes are presented in Figs 9 and 10.

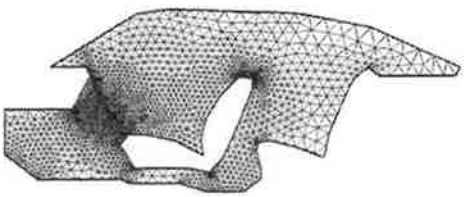

Elements=4397, error=3.65%

Figure 9: Final mesh of the car enclosure at 50 Hz

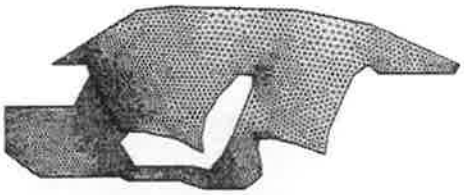

Elements=8292, error=4.45%

Figure 10: Final mesh of the car enclosure at 350 Hz

It is apparent that at the higher frequency the final mesh consists of a larger number of elements but some regions of utmost refinement coincide. The comparison of the velocity in x direction simulated by initial and optimal meshes at different frequencies is presented in Figs 11 through 14.

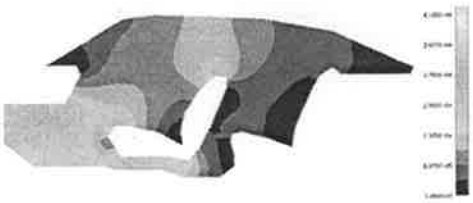

Figure 11: Velocity in car enclosure (x direction/amplitude) at 50Hz by initial mesh

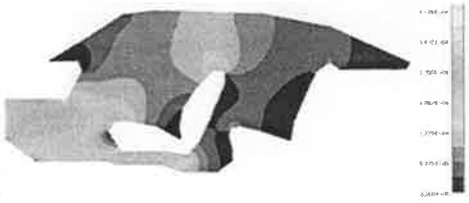

Figure 12: Velocity in car enclosure (x direction/amplitude) at 50Hz by final mesh

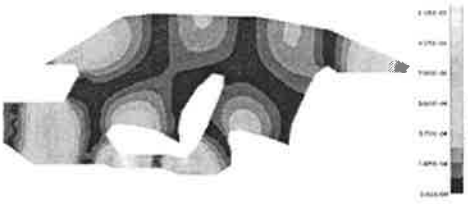

Figure 13: Velocity in car enclosure (x direction/amplitude) at 350Hz by initial mesh

Figure 14: Velocity in car enclosure (x direction/amplitude) at 350Hz by final mesh

It is evident that in the case of low frequencies of excitation, simulation by the initial mesh does not detect the singularities if the solution. In case of higher frequencies simulation by the final mesh produces the peaks of the velocity in more local regions.

6. Conclusions

A method for obtaining postprocessed solution of the higher order accuracy has been presented. The proposed SPRD technique is essentially a least square fit of the prime variables (displacements) at superconvergent points. This approach provides superconvergent displacement field u_i^* over local reduced element patches. Since the SPRD technique recovers superconvergent displacement field that is at least one order higher than finite element solution, the method can successfully be implemented in error estimation of the finite element solution.

The local and global updating techniques have been presented to improve solution of the generalized eigenvalue problem encountered in the finite element analysis of structural dynamics problems. The SPRD improved solution gives a good initial trial eigenvector for the modified conjugate gradient scheme, which immediately put us on the asymptotic phase of the convergence profile. The numerical study of the performance of the error estimator demonstrates the asymptotic exactness that shows the reliability of the proposed procedure.

The paper presents also an adaptive finite element strategy for acoustic problems. This strategy uses adaptive finite element meshing and remeshing that is performed by the commercial package I-DEAS, finite element analysis using the software SYSNOISE and error estimation is done by an additional postprocessing unit. The designed final meshes provide not only solutions of the prescribed accuracy but also detect all singularities in the solution.

References

[1] I.Babuška, T.Strouboulis, C.S.Upadhyay, S.K.Gangaraj and K.Copps. *Validation of a Posteriori Error Estimators by Numerical Approach*. Internat. J. Numer. Methods Engrg., **37**, (1994), 1073-1123.

[2] N.-E.Wiberg and R.Baušys. *Error Estimation for Eigenfrequencies and Eigenmodes in Dynamics*. In J.Pal and H.Werner (eds.), Computing in Civil and Building Engineering, A.A.Balkema, (1995), 611-616.

[3] R.Baušys. *Accuracy Estimates in Free Vibration Analysis*. Building construction. Vilnius: Technika, **4,** (1995), 5-19.

[4] N.-E.Wiberg, R.Baušys and P.Hager. *Improved Eigenfrequencies and Eigenmodes in Free Vibration Analysis*. In: Ed. B.H.V.Topping, Advances in Finite Element Technology, Civil-Comp Press, Edinburgh, (1996), 43-54.

[5] R.Baušys and N.-E.Wiberg. *Adaptive Finite Element Strategy for Acoustic Problems*. J. Sound & Vibr., (1999) (in press)

[6] O.CZienkiewicz and J.Z.Zhu. *The Superconvergent Patch Recovery and a Posteriori Error Estimates. Part 1 The Recovery Technique*. Internat. J. Numer. Methods Engrg., **33**, (1992), 1331-1364.

[7] M.Tabbara, T.Blacker and T.Belytchko. *Finite Element Derivative Recovery by Moving Least Square Interpolants* . Comput. Methods Appl. Mech. Eng., **117**, (1994), 211-223.

[8] G.Gambolati, F.Sartoretto anf P.Florian. *An Orthogonal Accelerated Deflation Technique for Large Symmetric Eigenproblems*. Comput. Methods Appl. Mech. Eng., **94**, (1992), 13-23.

Stochastic Extreme Load Predictions for Marine Structures

Jørgen Juncher Jensen

Department of Naval Architecture and Offshore Engineering
Technical University of Denmark
DK 2800 Lyngby, Denmark

Abstract. Development of rational design criteria for marine structures requires reliable estimates for the maximum wave-induced loads the structure may encounter during its operational lifetime. The paper discusses various methods for extreme value predictions taking into account the non-linearity of the waves and the response. As example the wave-induced bending moment in the ship hull girder is considered.

1. INTRODUCTION

The present paper deals with extreme value predictions for global wave loads on ships. For ships longer than about 100 m the most important load parameter is the vertical bending moment. It consists of two terms: the hydrostatic part due to the sectional difference between buoyancy and gravity forces and the hydrodynamic part due to the action of waves on the hull. The first part is easily calculated from loading conditions for the ship, whereas determination of the second part requires a solution of an extremely complicated non-linear hydrodynamic problem. A review of the current state-of-the-art can be found in Beck et *al.* (1996). The importance of the non-linearity is clearly illustrated by Figure 1, showing measured wave bending stresses in a frigate class covering approximately 20 years of operation. In a linear theory these tensile (hog) and compressive (sag) stresses in the deck plating would be equal.

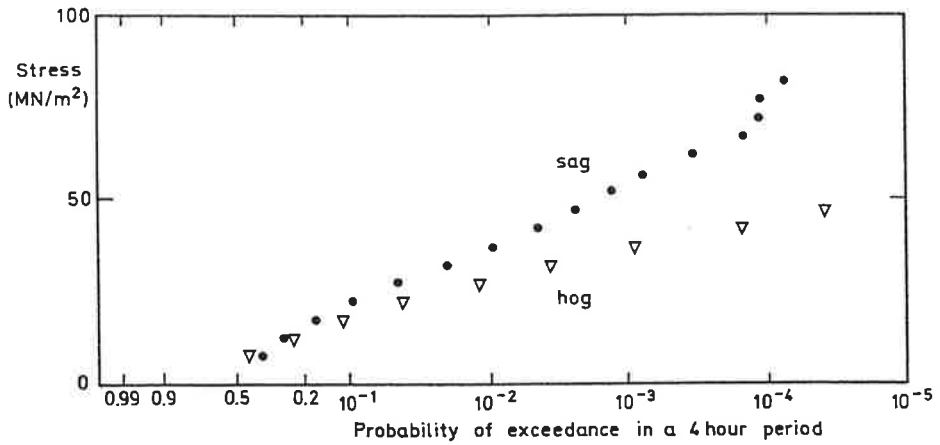

Figure 1. Gumbel plot long-term stress measurements in a frigate class. A probability of exceedance equal to $2*10^{-5}$ corresponds to a 20 years return period. Clarke (1986).

A consistent extreme value analysis requires both a correct physical (hydrodynamic) model of the behaviour of the ship in severe sea states taking due account of the various non-linear and three-dimensional effects and a proper stochastic characterisation of the ocean waves.

Depending on the complexity of the hydrodynamic load analysis applied the calculations can only be performed in selected regular waves, conditional wave episodes or short sequences of random seaway. From these results reliable predictions for the variance of the required responses can be obtained, but it is much more difficult to extrapolate the results to predict the extreme wave loads the ship may encounter during its operational lifetime.

The linear case is well understood and described in many textbooks, c.f. Price and Bishop (1974), Ochi (1990). The procedure makes use of an exact expression for the probability distribution of the individual peaks in combination with order statistics or Poisson upcrossings to arrive at a prediction for the extreme peak value within a given time period.

However, when the non-linearity in the hydrodynamic response and the non-linearity in the large ocean waves themselves are taken into account, no analytical expressions for the probability distribution of the individual peaks (the so-called initial probability distribution) can in general be determined.

To overcome this problem various semi-emperical transformations can be applied as discussed in Section 2. If applicable then the extreme values can be obtained as in the linear case from order statistics or Poisson upcrossings.

As the interest is on very rare events a correct modelling of the tail in the initial probability distribution is of utmost importance. Hence, if this distribution is not known with great accuracy it is better to work directly with the extreme value distribution of the response. In general any probability distribution can be applied if it fits to the data points available. However, as one often needs to extrapolate outside this range, the class of Generalised Extreme Value (GEV) distributions, Fisher and Tippett (1928), Gumbel (1958) is very useful as every parent distribution will tend towards one of these distributions for sufficient large exceedance level. A direct application of these distributions is to divide the available observations (data points) into equidistant time epochs, say minutes or hours, and then use only the maximum observation in each epoch to estimate the parameters in the GEV. Hereby, of course, large observations in one epoch might not be induced in the analysis. This may have serious consequences for the accuracy of the GEV, especially when used to extrapolate outside the range of observations. Methods based on exceedance provide a better use of the available data, as all values larger than a user-defined level are included. The analysis is named Peak-Over-Threshold and makes use of the Generalised Pareto (GP) distribution and a theorem relating this distribution to the GEV, Pickards (1975). The GEV and GP procedures will be discussed in Section 3.

The parameters in the GEV or GP must be determined by fitting the distributions to known data points. Various procedures available are outlined in Section 4. The data points to be applied may follow from a time-domain analysis of the response of the ship in random waves. For the most complex hydrodynamic formulations such results

cannot directly be obtained due to the excessive demand for computer power. However, with the use of rather short critical wave episodes, Torhaug, Winterstein, Braathen (1998), such time series can be constructed using only the non-linear formulation around the largest response peaks. Section 5 will address critical wave episodes.

The slamming forces in severe sea might introduce hydroelastic response components, whipping, to be superimposed on the rigid body response. Also continuously excited springing vibrations can occur. Methods to account for these effects in an extreme value analysis are discussed in Section 6.

With extreme values derived in stationary stochastic conditions, the final step is to weight these results over the operational lifetime of the ship. Here account must be taken of the operational profile including speed and course changes in heavy sea as well as the variability in the sea states encountered.

2. INITIAL PROBABILITY DISTRIBUTIONS

For Gaussian processes Cartwright and Longuet-Higgins (1956) derived the initial distribution for the individual peaks. Most linear wave load responses are sufficiently narrow-banded that this distribution can be approximated by a Rayleigh distribution.

For slightly non-linear stochastic processes a formal second-order expansion of the response around its mean value can be applied, Longuet-Higgins (1963). The response X and its time derivative is written

$$\begin{aligned} X &= \sum_{i=1}^{2n} \alpha_i Y_i + \sum_{i,j=1}^{2n} \alpha_{ij} Y_i Y_j \\ \dot{X} &= \sum_{i=1}^{2n} \beta_i Y_i + \sum_{i,j=1}^{2n} \beta_{ij} Y_i Y_j \end{aligned} \tag{1}$$

where Y_i are statistically independent standard Gaussian processes.

From this expression the joint probability density $f_{x\dot{x}}$ of the response X and its time derivative $\dot{X}$ can be derived. The result is given as an infinite series expansion, denoted Gram-Charlier, Edgeworth or Longuet-Higgins, Ochi (1990), and by integration an analytical expression for the upcrossing rate

$$\nu_x(x) = \int_0^\infty \dot{x}\, f_{x\dot{x}}(x,\dot{x})\, d\dot{x} \tag{2}$$

is obtained. Finally, upon the assumption of a narrow-banded response the cumulative distribution function of the individual peak can be approximated by

$$F_p(x) = 1 - \frac{\nu_x(x)}{\nu_x(\mu_x)} \tag{3}$$

where μ_x is the value of x maximising ν_x. For non-narrow band responses the corresponding result is derived by Longuet-Higgins (1964).

The only disadvantage in this formulation relates to the convergence of the series expansion for $f_{x\dot{x}}$, when truncated after a finite number of terms. It is well known c.f. Winterstein (1985, 1988), Ochi (1990) that negative probability densities can occur. The range of applicability of the series expansion depends both on the degree of non-linearity and the crossing level. In an example Jensen and Pedersen (1979), dealing with a container ship sailing in a sea state with H_s = 6 m, convergence was only achieved up to a level of exceedance equal to 0.01 for the individual peak bending moment responses, as shown in Figure 2. This is clearly insufficient for extreme value predictions. Furthermore, inclusion of additional number of terms in the expansion above the dominating terms does not yield better results, Jensen and Pedersen (1978), Winterstein (1988).

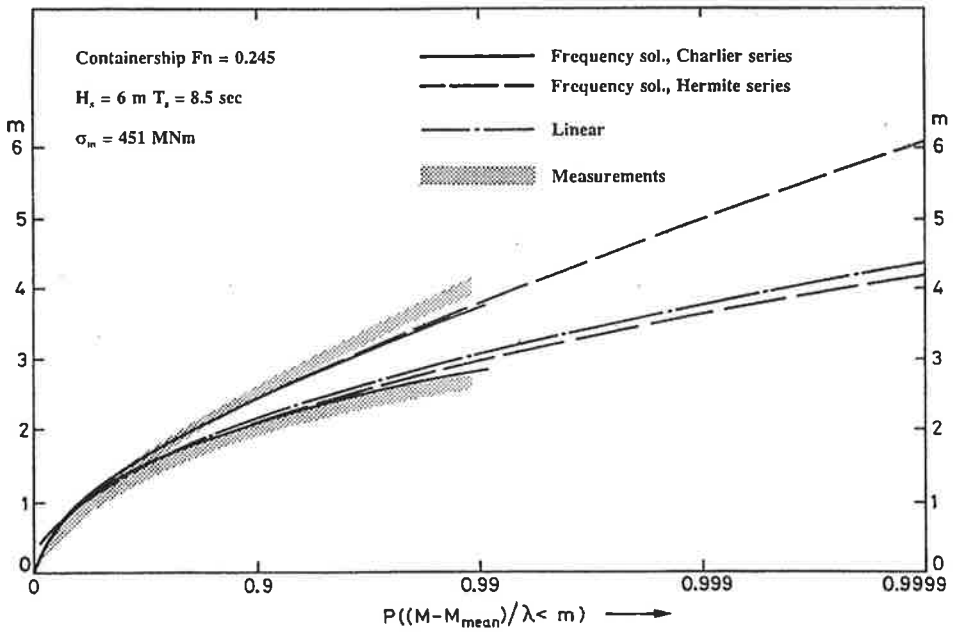

Figure 2. Probability distribution function for peak values of the non-dimensional wave bending moment amidships m = (M-E[M])/σ_m, where σ_m is the standard deviation of the linear contribution, Jensen and Pedersen (1979), measurements by Hackmann (1979).

An alternative solution procedure for the second order problem is the Kac-Siegert method, see eg. Naess (1985). It is straightforward to recast the general second-order problem into the diagonal form

$$X = \sum_{i=1}^{2n} \left(\gamma_i Y_i + \varepsilon_i Y_i^2 \right) \tag{4}$$

for the response X as function of statistically independent standard Gaussian processes Y_i,, e.g. Jensen and Dogliani (1996). Accurate numerical results are given by Naess (1995) using the steepest decent method, Figure 3.

Although a second order process is an approximation to reality for wave loads on ships, it might capture the main asymmetry in the vertical bending moment as indicated by the results in Figure 1 and 2. Therefore, as second order expansions model the skewness correctly and partly also the kurtosis, Vinje and Haver (1994), they can play an important role in transformations based on these parameters.

An approximate initial probability distribution for a non-linear variable X can often be constructed from a closed-form monotonic transformation $g(Y)$ of a variable Y with known distribution,

$$X = g(Y) \tag{5}$$

This can be done in an infinite number of ways. One of the most versatile procedures is based on a Hermite series transformation, Winterstein (1985). The response process $X(t)$ is written as a cubic polynomial in a stochastic process $Y(t)$. In the present context, where wave loads are considered, an obvious choice is to take $Y(t)$ as standard Gaussain distributed. The coefficients in the transformation are selected such that the transformed process has the same lowest order statistical moments as the probability distribution of X. Usually, the four lowest statistical moments are applied and certain bounds, Winterstein (1988), Jensen and Dogliani (1996), have to be enforced on the transformation coefficients to ensure a monotonic behaviour.

In the transformation methods the initial probability distribution for the individual peaks should in principle be determined from Eqs (2) – (3), but because of lack of knowledge of the joint probability density $f_{x\dot{x}}$, one of following approximations may be used, Winterstein (1988),

$$F_p(x) = 1 - \frac{f_x(x)}{f_x(\mu_x)}$$
$$F_p(x) = 1 - \exp\left[-\tfrac{1}{2}\left\{g^{-1}(x)\right\}^2\right] \tag{6}$$

The first approximation assumes that X and $\dot{X}$ are statistically independent, whereas the last directly apply the transformation (5) to the Rayleigh distributed peaks of $Y(t)$ Clearly, the two approximations yield different results if $X(t)$ is not linearly dependent on $Y(t)$. The last approximation is applied in Figure 2.

Generally, the Hermite transformation yields results in close agreement with those from more accurate methods, Winterstein (1988). This is also illustrated in Figure 2 and Figure 3 for the wave bending moment in a container ship with a large bow flare and, in Figure 3, sailing in a very severe sea state.

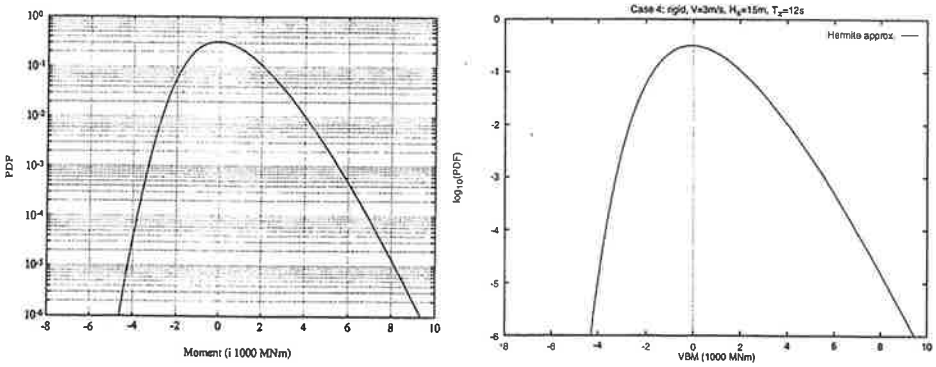

Figure 3. Logarithmic plot of the probability density function of the wave bending moment amidships, based on a second order hydrodynamic model. H_s=15m, T_z=12sec. Left: Accurate numerical results, Naess (1995). Right: Results obtained by the Hermite transformation model with four coefficients.

However, even if accurate results can be obtained for the tail of the distribution, the fundamental assumption of a second order process is an approximation for wave loads on ships. Most important, it cannot model load effects due to extreme events as water on deck and bow emergence. This might be the reason for the abrupt change in the measured probability distribution in Figure 1. The same behaviour is found in calculated time domain responses of the wave bending moments in stochastic seaways as for instance shown in Figure 4. Here the rare event of waves running over the deck introduces an increased probability of exceedance of the hogging bending moment, but only in the tail of the distribution. This is clearly so, because the event only can take place is the relative motion of the ship exceeds the freeboard.

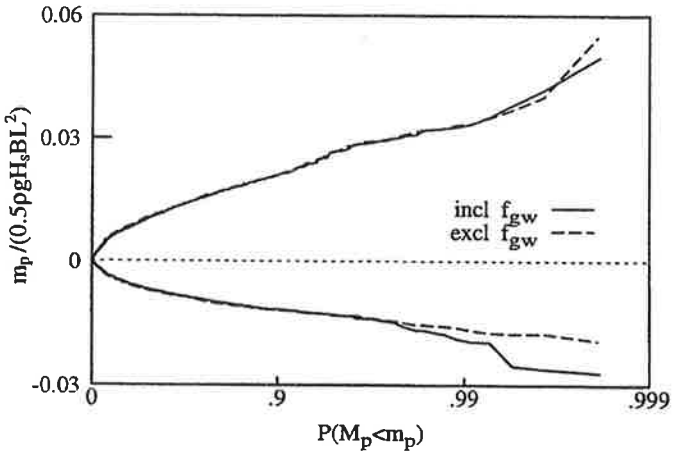

Figure 4. Cumulative probability density function for the sagging (positive) and hogging (negative) bending moment M_p amidships for a container ship sailing in head sea in a stationary sea state with H_s=8.3 m, T_z=10.2sec. Green water load f_{gw}. Wang et al. (1988).

Another general parametric expression for the initial probability distribution is, Ochi (1990)

$$F_p(x) = 1 - e^{-q(x)} \tag{7}$$

where $q(x)$ can either simply be a linear function of x, Ochi and Ahn (1994), or any smooth function satisfying, Ochi (1990),

$$\left|q''(x)/q'(x)\right| << \left|q'(x)\right| \quad ; \quad \textit{for large } x$$

If this bound holds the expected maximum value in n observations can directly be evaluated from the initial probability distribution as the value exceeded with a probability of $1/n$.

With the initial probability distribution given order statistics or Poisson upcrossings yields the most probable largest response over a given period. The two procedures are based on different assumptions, but yield asymptotically the same result for low probabilities of exceedance. Clustering effects may be accounted for by various procedures. However, for the bandwidths and levels of exceedance of interest here, these corrections are usually insignificant, Jensen and Dogliani (1996).

3. ASYMPTOTIC EXTREME VALUE DISTRIBUTIONS

If an initial probability distribution cannot be obtained as outlined above, then it might be better to work directly on the extreme values.

From the data points obtained from time simulation in random seaway any fit, either non-parametric or parametric of the extreme value distribution can be applied. However, as extrapolation outside the range of data points normally is requested for design purposes, non-parametric methods are generally useless.

Parametric expressions can be selected to obtain a good fit over all the data points available. Ochi and Whalen (1980) have suggested a rather general form,

$$\begin{aligned} F(x) &= 1 - exp[-q(x)] \\ q(x) &= ax^m \, exp(-px^k) \end{aligned} \tag{8}$$

where the four parameters a, m, p and k are determined by a non-linear optimisation procedure.

Alternatively, only the largest values of the data points are considered. In that case a family of probability distributions $H(x)$ known as the asymptotic extreme value distributions is very useful. The distributions $H(x)$ are the only non-degenerated functions satisfying

$$\lim_{n\to\infty} F^n(a_n + b_n x) = H(x) \tag{9}$$

for any initial probability distribution $F(x)$. For maxima only three different functions $H(x)$ exist, Fisher and Tippett (1928), Gumbel (1958), Castillo, (1988). In standard form they are

$$Frechet: H(x) = \begin{cases} 0 & ; \quad x \le 0 \\ \exp(-x^{-c}) & ; \quad x > 0 \end{cases} \quad ; c > 0 \tag{10a}$$

$$Weibull: H(x) = \begin{cases} \exp\left[-(-x)^{-c}\right] & ; \quad x < 0 \\ 1 & ; \quad x \ge 0 \end{cases} \quad ; c < 0 \tag{10b}$$

$$Gumbel: H(x) = \exp(-\exp(-x)) \quad ; \quad -\infty < x < \infty \tag{10c}$$

Any initial probability distribution $F(x)$ will thus belong to the domain of attraction for maxima of one of these three distributions $H(x)$. Which of them depends on the value of c obtained from the limit, Castillo (1988),

$$\lim_{\varepsilon \to 0} \frac{F^{-1}(1-\varepsilon) - F^{-1}(1-2\varepsilon)}{F^{-1}(1-2\varepsilon) - F^{-1}(1-4\varepsilon)} = 2^{c} \tag{11}$$

Equivalent formulas to Eqs. (10)–(11) exist for extremes of minima and the domain of attractions for various common initial probability distributions are shown in Table 1.

Table 1. Domains of attraction for maxima and minima for some common distributions, Castillo (1988).

DISTRIBUTION	MAXIMA	MINIMA
Normal	Gumbel	Gumbel
Exponential	Gumbel	Weibull
Lognormal	Gumbel	Gumbel
Gamma	Gumbel	Weibull
Gumbel_a	Gumbel	Gumbel
Gumbel_b	Gumbel	Gumbel
Rayleigh	Gumbel	Weibull
Uniform	Weibull	Weibull
Weibull_a	Weibull	Gumbel
Weibull_b	Gumbel	Weibull
Cauchy	Frechet	Frechet
Pareto	Frechet	Weibull
Frechet_a	Frechet	Gumbel
Frechet_b	Gumbel	Frechet
First kind beta	Weibull	Weibull
Second kind beta	Frechet	Weibull
$_a$For maxima. $_b$For minima		

Although all extreme value distributions tends towards one of the asymptotic extreme value distributions for sufficient large exceedance levels, the convergence might be slow. In such cases, a transformation $Z = h(X)$ of the original variable X can improve the convergence rate significantly if $h(x)$ is appropriately selected, Naess, Stoli and Storm (1996).

The three distributions (10) can be combined to a single distribution,

$$H(x)=exp\left[-\left(1-k\frac{x-a}{b}\right)^{1/k}\right];\ x>a+b/k\quad(k<0);\ \ x<a+b/k\quad(k>0) \tag{12}$$

for the extremes of maxima. This distribution is called the Von Mises-Jenkinson limit distribution or the Generalized Extreme Value (GEV) distribution, Castillo (1988), Lindgren (1999). In the next section, different estimation techniques for the coefficients in (12) are discussed.

The main disadvantage with the use of the Generalized Extreme Value distribution is that the data points have to be divided into either equidistant time epochs or storm events and that for each epoch or event only one data point, the largest, is used, resulting often in a large loss of information. An alternative is to assume that all data above a certain moderate threshold value u are important for the tail distributions. Thus an estimation of the cumulative distributive function $F_u(v)$ for the excess $V=X-u$ is needed. An appropriate model for $F_u(v)$ is the Generalized Pareto (GP) distribution

$$G(v)=\begin{cases}1-\left(1-k\dfrac{v}{d}\right)^{1/k} & ;v>0\ (k<0)\ ;\ 0<v<b/k\ (k<0)\\ 1-\exp\left(-\dfrac{v}{d}\right) & ;v>0\end{cases} \tag{13}$$

because, Pickands (1975), there exist a value k, independent of v, and a value of d, dependent on v, such that $F_u(v)$ is closely approximated by $G(v)$, whenever v is sufficiently close to the upper end point.

It can be shown, see e.g. Lindgren (1999), that the probability distribution of the maximum of a random number of Generalised Pareto distributed variables becomes the Generalized Extreme Value distribution of the exceedance, provided the number of peaks exceeding the threshold is Poisson distributed. The relation between the parameters in the two distributions, (5.12), (5.13) are, Lindgren (1999),

$$\begin{aligned} &b=d/\mu^k;\quad a=u-(b-d)/k &;k\neq 0\\ &b=d\qquad;\quad a=u+b\ln\mu &;k=0\end{aligned} \tag{14}$$

where μ is the expected number of exceedance per time scale (month, year). Hence, fitting the excesses to the Generalised Pareto distribution yields the corresponding Generalised Extreme Value distribution for extremes of the response. The most probable largest value over N times the time scale is finally obtained as the value with a probability of exceedance equal to $1/N$.

Basically the GP and the GEV analysis described above hold only for stationary processes. For non-stationary processes the analysis can be carried out in each stationary state and combined as described in Section.6.

4. ESTIMATION METHODS

Normally the initial probability distributions and the extreme value distributions contain free parameters to be determined such that the data available are represented as close as possible. A good overview over the most common methods can be found in Castillo (1988). The initial value distribution based on the Hermite series expansion uses the four lowest statistical moments to determine the coefficients and this estimation method is often applied due to its simplicity. However, from a statistical point-of-view the maximum likelihood method is better and straight-forward to apply to both the GEV and GP distributions, c.f. Smith (1985), although some remedies have to be applied if $k \geq 0.5$ in the GP distribution. Good alternatives are the method of probability-weighted moments, Hosking and Wallis (1987), and Bayesian inference, c.f. Smith and Naylor (1987). The least square method can also be applied but due to the dimensions of the response and non-dimensional probabilities, care has to be taken in the selection of weights. Finally, graphical methods using probability papers (Gumbel, Weibull etc.) are easy to apply, but lack a consistent evaluation of error bounds and confidence intervals.

Regarding the GP distribution, the threshold value should also be determined. Here the important property of the GP distribution is that the mean excess over a threshold u depends linearly on u, cf. Smith (1993), Lindgren (1999),

$$E[V = X - u \,|\, X > u] = \frac{d - ku}{1 + k} \tag{15}$$

becomes an easy way to check if a set of data points comes from a GP distribution. Estimators for k and d are given by de Haan (1994) and discussed for wind speed applications by Naess and Clausen (1999).

5. CRITICAL WAVE EPISODES

For the most advanced hydrodynamic formulations, the computational effort is so huge that only short time periods can be analysed. Hence, it is very important to identify the random incident wave sequences that yield extreme responses of the ship. A priori such sequences are not known and cannot be determined from the wave environment itself, as they also depend on the response type and main particulars, loading condition, heading and forward speed of the vessel.

The most straight-forward procedure is to perform a very long time domain analysis in each relevant stationary condition using linear transfer functions for the response in question (bending moment, shear force etc). The wave sequences yielding the largest linear responses are thereafter applied in the non-linear analysis and these non-linear results then replace the corresponding linear results in the extreme value analysis. The necessary number of critical wave episodes to be used in the non-linear analysis in order to obtain an accurate statistical estimate of the non-linear response has been investigated by Torhaug, Winterstein and Braathen (1998). Based on an analysis of a specific monohull vessel in head sea they find that for the vertical midship bending moment about 10-15 critical wave episodes are needed to get the hourly maximum bending moment with 5 per cent accuracy. Each wave episode should contain 2-3

wave cycles to account for memory effects and transients should be minimised using initial conditions based on the linear motions of the vessel determined from time domain simulation.

To reduce the number of the time sequences needed in the non-linear calculations, a Most Likely Response method has been proposed, Adegeest, Braathen and Vada (1998). Here the most probable extreme response is first determined by a standard linear frequency domain analysis. Then a random time domain realisation of this response using the linear response spectrum is generated and conditioned such that it has the most probable extreme response value at a prescribed time instant. This is done using the theory for Gaussian processes near a maxima, Lindgren (1970), Tromans, Anaturk and Hagemeijer (1991), Taylor, Jonathan and Harland (1995), Friis Hansen and Nielsen (1995). The mean response $\bar{x}(t)$ around the maxima x_0 *at* $t = t_0$

$$\bar{x}(t) = E\left[X(t) \middle| X(t_o) = x_o, \dot{X}(t_o) = 0\right] \qquad 16)$$

simply becomes proportional to the autocorrelation function of the response. By use of the linear transfer function for the response, the corresponding deterministic wave elevation is generated and used in the non-linear hydrodynamic calculations (SWAN). Very close agreement between the results from 1) model tests, 2) a full non-linear hydrodynamic simulation in random sea, 3) extreme values based on the Hermite transformation (see Section 2), 4) a non-linear analysis of only a few critical wave episodes and, 5) the Most Likely Response method is found for the example vessel (the container ship "Snowdrift"). The non-linearity as measured by a sag-to-hog ratio for the bending moment amidships is nearly two implying that linear theory alone is useless. The use of a regular design wave gave results that deviated significantly from the other predictions.

Although the Most Likely Response method outlined above reduces the analysis to a single wave episode, it should be recognised that this wave episode only represents the mean response around given maxima. Hence, memory effects might not be sufficiently accounted for. In a study of the deck displacement of a simplified jack-up platform, the extreme response was found to depend significantly on the random wave realisation around the maxima, Taylor, Jonathan and Harland (1995). This behaviour was mainly attributed to the low damping of the system, much lower than in the present ship motion problems. However, it will be important to verify whether the random variation of the linear response around the most probable largest maxima is important for the corresponding non-linear analysis.

The described non-linear analyses only consider as input linear waves and wave kinematics. For offshore structure, non-linear conditional waves have been applied, using either a non-linear transformation, Taylor (1992), or Stokes second order waves, Jensen (1996). This non-linear effect also deserves some consideration, as the extreme response usually is associated with rather extreme waves. Figure 5 illustrates the difference between a linear and a second order deep water conditional lond-crested wave.

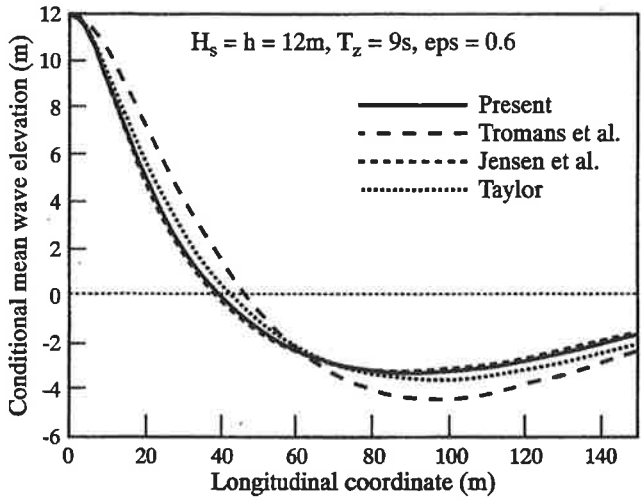

Figure 5. Conditional mean wave profile, Jensen (1996). The linear profile is the one given by Tromans et al. (1991).

Finally, the assumed correspondence between the occurrence of the maxima of the linear and the non-linear response may be questioned as the linear analysis, i.e. the transfer functions, does not account for special load effects like slamming and water on deck.

6. STOCHASTIC LOAD COMBINATIONS

In the extreme value prediction several correlated load components must often be combined. It can be load components with roughly the same frequency content, as for the vertical and horizontal wave bending moment, but it can also be loads with significant different temporal variations as the still water, the wave-induced and the vibratory response of the hull girder.

In the first case, the combination is most conveniently done directly in the time simulation, taking due account of the phase lags between the different components, and then apply the extreme value analysis to the combined response. This is not appropriate in the second case due to the large difference in time-scale and stochastic load combination procedures are therefore needed.

A large number of load combination procedures are available, e.g. Wen (1977), Madsen, Krenk and Lind (1986). Most of them are empirical or only strictly applicable to linear combinations of statistically independent processes. In a study, Wang, Jiao and Moan (1996), different procedures are used to combine the still water and wave-induced bending moment for an oil production vessel. Their findings are that the Ferry-Borges method, Ferry-Borges and Castenheta (1971), are very accurate and computationally effective and hence recommended. Turkstra's rule, Turkstra (1970), is also very useful even if it underestimates the extreme values slightly. This

is also illustrated in Mansour (1995), where a simple linear addition of two extreme values, f_1, f_2:

$$f_{1,2} = f_1 + Kf_2 \tag{17}$$

is proposed. The constant K is derived under the assumption that the two underlying processes are Gaussian and depends on the correlation between the two components as well as the ratios between the standard deviations and upcrossing rates. The analysis is later generalised to slightly non-Gaussian processes, Mansour and Jensen (1995). Related work have been done by Naess and Røyset (1999).

A somewhat similar approach is suggested in Naess (1993) for combination of a linear (Gaussian) and a second-order sum-frequency response. The main problem in both procedures is the estimation of the correlation for the extreme events. In the former procedure the correlation is given at the standard deviation level whereas the latter procedure applies the correlation determined at the 10^{-5} probability level of the combined response. The two procedures have been applied, Jensen and Dogliani (1996), in the estimation of the effect of continuous wave excitation of hull girder vibrations (springing) on the extreme vertical wave bending moment, Figure 6. This excitation is partly due to linear resonance and partly to second-order wave excitation. Due to the large separation in frequency content the correlation at the standard deviation level is zero, whereas by the second procedure it becomes 0.31 and –0.23 for the sagging and hogging bending moments, respectively. The latter results imply that for the example container vessel, the extreme sagging bending moment may increase by 10 per cent due to springing. This indicates that some concern should be paid to springing responses for certain type of ships.

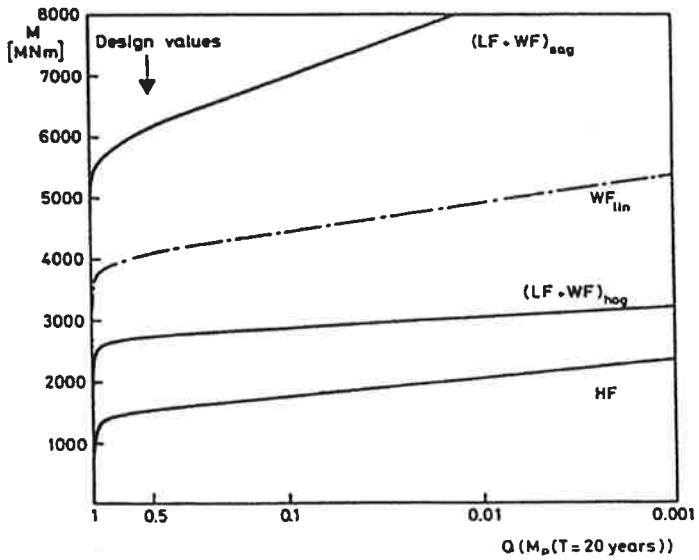

Figure 6. Long term probability of exceedance for the wave-induced bending moment amidships for a container ship, Jensen and Dogliani (1996).

However, the most severe hydroelastic hull girder response is usually due to transient vibrations following a slamming impact. For prediction of the magnitude and duration of these forces reference can be made to Zhao and Faltinsen (1993). The associated hull girder response can be determined by a Timoshenko beam modelling of the hull girder. Clearly, a strong correlation between the times of occurrence of a slamming impact and the wave-induced sagging bending moment must be expected. This correlation is taken into account in the procedure developed by Friis Hansen (1994). Furthermore, the joint probability distribution of wave amplitude and frequency at the instant of maximum slamming response within a cluster of slamming impacts are derived. One of the fundamental assumptions in the method is that the response spectrum for the relative motion is narrow-band. Thereby, memory effects might not be correctly accounted for in all cases of practical interest and deserves further studies.

7. CONCLUSIONS

Various estimation techniques for extreme wave load predictions for ships have been outlined. The usefulness of the Hermite transformation with coefficients derived from second-order hydrodynamic models have been illustrated, but also its shortcomings with regard to loads related to rare events like deck wetness.

Asymptotic extreme value distributions and the associated generalized Pareto distributions provide important prediction methods when the initial distribution is unknown. The use of proper transformations may extent their range of applicability.

Due to extensive computer resources needed to perform very detailed non-linear, three-dimensional hydrodynamic analyses, only very short time series can be covered. Hence, it becomes important to define reasonable critical wave episodes taking due consideration of both the sea state parameters and the main dimensions of the vessel.

8. REFERENCES

Adeegest, L., Braathen, A. and Vada, T. (1998). "Evaluation of Methods for Estimation of Extreme Nonlinear Ship Responses Based on Numerical Simulations and Model Tests", Proc. 22nd Symp. Naval Hydrodynamics, Washington D.C. Vol.1, pp. 70-84.

Beck, R. F., Reed, A. M. and Rodd, E. P. (1996). "Application of Modern Numerical Methods in Marine Hydrodynamics", Trans. SNAME, Vol. 104, pp. 519-537.

Cartwright, D. E. and Longuet- Higgins, M. S. (1956). "The Statistical Distribution of the Maxima of a Random Function", Proc. Royal Soc. London, Serie A, Vol. 237, pp. 212-232.

Castillo, E. (1988). "Extreme Value Theory in Engineering", Academic Press, San Diego, California.

Clarke, J. D. (1986). "Wave Loading in Warships", Proc. Advances in Marine Structures, eds. Clarke and Smith, Elsevier Applied Science, London.

Ferry-Borges, J. and Castanheta, M. (1971). "Structural Safety",Laboratoria Nacional de Engenhera Civil, Lisbon.

Fisher, R. A. and Tippett, L. H. (1928). "Limiting Forms of the Frequency Distributions of the Largest or Smallest Members of a Sample", Proc. Cambridge Phil. Soc., Cambridge, UK, Vol. 24, pp. 180-190.

Friis Hansen, P. (1994). "Reliability Analysis of a Miship Section", PhD thesis, Dept. Ocean Eng., Tech. Univ. of Denmark, Lyngby, Denmark.

Friis Hansen, P. and Nielsen, L. P. (1995). "On the New Wave Model for the Kinematics of Large Ocean Waves", Proc. OMAE'95, Vol. IA, pp. 17-24.

Gumbel, E.J. (1958). "Statistics of Extremes", Columbia University Press, New York.

Hackmann, D. (1979). Written discussion to Jensen and Pedersen (1979).

de Haan, L. (1994). "Extreme Value Statistics", in Extreme Value Theory and Applications, Vol. 1, Kluwer Academic Publishers.

Hosking, J. R. M. and Wallis, J. R. (1987). "Parameter and Quantile estimation for the Generalized Pareto Distribution", Technometrics, Vol. 29, pp. 339-349.

Jensen, J. J. and Pedersen, P. T. (1978). "On the Calculation of the Joint Probability Density of Slightly Non-linear Stochastic Processes", GAMM-Tagung, Lyngby, ZAMM Vol. 58, pp. T 481-T 484.

Jensen, J. J. and Pedersen, P. T. (1979). "Wave-induced Bending Moments in Ships - a Quadratic Theory", Trans. RINA, Vol. 121, pp. 151-165.

Jensen, J. J. (1996). "Second-order Wave Kinematics Conditional on a Given Wave Crest", Applied Ocean Research, Vol. 18, pp. 119-128.

Jensen, J. J. and Dogliani, M. (1996). "Wave-induced Ship Hull Vibrations in Stochastic Seaways", Marine Structures, Vol. 9, pp. 353-387.

Lindgren, G. (1999). "Extreme Events", Chapter 7 in "Oceans from Space", Ifremer, France.

Longuet-Higgins, M. S. (1963). "The Effect of Non-linearities on Statistical Distributions in the Theory of Sea Waves", Journal of Fluid Mechanics, Vol. 17, pp. 459-480.

Longuet-Higgins, M.S (1964). "Modified Gaussian Distribution for Slightly Non-linear Variables", Radio Science, National Bureau of Standards, Vol. 68D(9), pp. 1049-1062.

Madsen, H. O., Krenk, S. and Lind, N. C. (1986). "Methods of Structural Safety", Prentice Hall Inc., Englewood Cliffs, New Jersey.

Mansour, A. E. (1995). "Extreme Loads and Load Combinations", J. Ship Research, Vol. 39, No. 1, pp. 53-61.

Mansour, A. E. and Jensen, J. J. (1995). "Slightly Non-linear Extreme Loads and Load Combinations", Journal of Ship Research, Vol. 39, No. 2, pp. 139-149.

Naess, A. (1985). "Statistical Analysis of Second-Order Response of Marine Structures", J. Ship Research, Vol. 29, No. 4, pp. 270-284.

Naess, A. (1993). "Statistics of Combined Linear and Quadratic Springing Response of a TLP in Random Waves", Proc. OMAE´93, Glasgow.

Naess, A. (1995). "Random Vibration of Ship Hulls", Proc. IUTAM Symp. Adv. In Nonlinear Stochastic Mechanics, Kluwer Academic Publishers, pp. 311-320.

Naess, A. Røyset, J. Ø. (1999). "Estimation of Extremes of Combination of Stochastic Load Effects by Turkstra´s Rule", Proc. OMAE99, St. Johns, Canada.

Naess, A., Storli, H. and Storm, L. E. (1996). "Statistical Predictions of Long Return Period Design Values", Proc. OMAE' 96, Vol. II, pp. 17-22.

Naess, A. and Clausen, P.H. (1999). "Statistical Extrapolation and the Peak Over Treshold Method", Proc. OMAE99, St. Johns, Canada.

Ochi, M. K. (1990). "Applied Probability and Stochastic Processes". John Wiley and Sons, New York.

Ochi, M. and Ahn, K. (1994). "Probability Distribution Applicable to Non-Gaussian Random Processes", Probabilistic Eng, Mech., Vol. 9, pp. 255-264.

Ochi, M. and Whalen, J. E. (1980). "Prediction of the Severest Significant Wave Height", Proc. 17th Conf. Coastal Eng., Vol. 1, pp. 587-599.

Pickands, J. (1975). "Statistical Inference Using Extreme Order Statistics", The Annals of Statistics, Vol. 3, No. 1, pp. 119-131.

Price, W. G. and Bishop, R. E. D. (1974). "Probabilistic Theory of Ship Dynamics", Chapman and Hall, London.

Smith, R.L. (1985). "Maximum Likelihood Estimation in a Class of Nonregular Cases", Biometrika, Vol. 72, pp. 67-90.

Smith, R.L. (1993). "Multivariate Threshold Methods", Conference on Extreme Value Theory and Its Applications, NIST, US Dept. of Commerce.

Smith, R. L. and Naylor, J. C. (1987). "A Comparison of Maximum Likelihood and Bayesian Estimators for the Three Parameter Weibull Distribution", Appl. Statistics, Vol. 36, pp 358-369.

Taylor, P. H. (1992). "On the Kinematics of Large Ocean Waves", Proc. BOSS´92, Vol. 1, London, BPP Tech. Services Ltd, UK, pp. 134-145.

Taylor, P. H., Jonathan, P. and Harland, L. A. (1995). "Time-domain Simulation of Jack-up Dynamics with the Extremes of a Gaussian Process", Proc. OMAE´95, Vol. IA, Copenhagen, Denmark, pp. 313-319.

Torhaug, R., Winterstein, S.R. and Braathen, A. (1998). "Non-linear Ship Loads: Stochastic Models for Extreme Response", J. Ship Research, Vol. 43, No. 1, pp. 46-55.

Tromans, P. S., Anaturk, A. R. and Hagemeijer, P. (1991). "A New Model for the Kinematics of Large Ocean Waves - Application as a Design Wave", Proc. First ISOPE Conf., Vol. III, Edinburgh, UK, pp. 64-71.

Turkstra, C. J. (1979). "Theory of Structural Design Decision Study No. 2", Solid Mechanics Div., University of Waterloo, Ontario.

Vinje, T. and Haver, S. (1994). "On the non-Gaussian Structure of Ocean Waves". Proc. BOSS'94, Vol. II, Boston, USA, Pergamon Press, pp. 453-79.

Wang, X., Jiao, G. and Moan, T. (1996). "Analysis of Oil Production Ships Considering Load Combination, Ultimate Strength and Structural Reliability", Trans. SNAME, Vol. 104, pp. 3-30.

Wang, Z. , Jensen, J. J. and Xia, J. (1998). "On the Effect of Green Water on Deck on the Wave Bending Moments", Proc. 7th Int. Symposium on Practical Design of Ships and Mobile Units, PRADS'98, The Hague.

Wen, Y.-K. (1977). "Statistical Combination of Extreme Loads", J. Structural Division, ASCE, Vol. 103, pp. 1079-1093.

Winterstein, S. R. (1985). "Non-Normal Responses and Fatigue Damage", J. Engineering Mechanics, ASCE, Vol. 111, No. 10, pp. 1291-1295.

Winterstein, S. R. (1988).). "Nonlinear Vibration Models for Extremes and Fatigue", J. Engineering Mechanics, ASCE, Vol. 114, No. 10, pp. 1772-1790.

Advances in Computational Mechanics Software

Hans Petter Langtangen
Mechanics Division
Department of Mathematics
University of Oslo
Norway

Introduction

Many scientists and practitioners have experienced that software development and maintanence tools represent a more limiting factor for rapid progress of computational mechanics than more effective numerical methods and hardware, which traditionally have been the topics of greatest interest in research. Metal processing is an example where the models involve large systems of partial differential equations (PDEs), describing flow, deformation, heat transfer, and phase changes of a multi-component mixture, coupled through numerous constitutive relations. The whole model might also be embedded in a framework for optimal design of the process (see [9] and [10]). Building software for models of this complexity is a very complicated and time-consuming process. Traditionally, computational mechanics software has been tailored to a specific application domain. From a mathematical and numerical point of view, however, widely different physical applications may lead to the same set of program statements. Hence, code reuse is strongly motivated by the mathematics, at least conceptually. The mentioned example from metal processing illustrates the point: The models for fluid flow, solid deformation, and heat transfer appear in many other contexts, and duplicates of the numerics for the involved equations are scattered all over numerous CFD and structural analysis codes. Ideally, the implementation of the metal processing simulator should be a high-level plug-and-play operation with existing modules for flow, deformation, and heat transfer, and a new module containing the constitutive relations specific to the current physical problem. In practice, code resuse is not that easily accomplished. We lack widespread use of software constructs and programming standards that encourage the necessary modularity for code reuse. Also, many practitioners in computational mechanics are not aware of the extensive development of new programming styles and software tools during the last decade. The purpose of this article is to highlight what can be achieved by adopting new programming languages and software development techniques. In particular, we shall report experiences with the development framework Diffpack, provided by Numerical Objects (www.nobjects.com), which has been used to build, among other things, a complicated metal processing simulator in the advantageous way we outlined above [7,9,10].

Flexibility is another key factor for successful application of numerical simulations; different models and solution methods need to be compared to increase the reliability of the computations. This means that computational mechanics software should ideally offer a wide range of numerical approaches and enable the user to customize the model by adding or removing terms and equations *at run time*. Such flexible combination of software modules requires a high degree of modularity and sophisticated selection mechanisms; direct implementation of this functionality in plain Fortran 77 might end up as an impossible task for a human.

The request for flexibility, modularity, and code reuse are major issues in non-numerical computing as well. There, new programming methodolgies and supporting languages have been central in

accomplishing the mentioned demands. PC software relies today heavily on object-oriented programming and is implemented mostly in C++ and Java. The use of these languages and new programming paradigms, such as object-oriented programming and template (generic) programming, has attracted an increasing interest in scientific computing during the nineties. Migration of techniques from computer science to scientific computing must be done with great care, as the software constructs and tools from computer science might not be compatible with the strong computational efficiency requirements in scientific computing. "Efficiency" has, however, many aspects. Optimal combination of human efficiency and number crunching efficiency is probably one of the aims of computational mechanics software.

Numerous packages for numerical simulation, employing new implementation technologies, have appeared during the last decade, and programming with objects in C++, Java, and Fortran 90 has received quite some attention at conferences. The references [1,5,7,8] provide a glimpse of various activities. Without doubt, programming with objects have proved to be productivity enhancing and is now successfully established also in the scientific computing community. Along with this development, many universities apply Java as the introductory programming language, a fact that will make widespread future demand for object-oriented software in science and engineering.

Diffpack

Diffpack [4,6] was started as a research project in the beginning of the nineties, focusing on applying object-oriented programming and the C++ language to develop flexible, modular, and resuable software components for solving PDEs. Through the years, Diffpack has evolved into a flexible programming environment for PDE solvers and has been applied worldwide in diverse application areas, ranging from fluid and solid mechanics to finance and medicine.

The underlying idea of the design of Diffpack is that different applications share a common mathematical and numerical structure. This common structure can be implemented in a software kernel, with "slots" for problem-dependent information. To create an application code, the programmer implements only the problem-dependent information and relies on the kernel for the numerics that can be shared among applications. The result of such an approach is two-fold: the development time of application codes is significantly reduced, and the reliability is increased by utilizing general components that are well tested in many other applications. The disadvantage is that leaving as much numerics to general libraries as possible might reduce the flexibility of the implementation and, e.g., the ability to utilize special structures of the problem for code optimization. Our answer is to provide a *layered design*, where the bottom layer of the package contains pure C (or Fortran) array manipulations to ensure high computational efficiency, the next layers add abstractions and convenient programming interfaces, and the very top layer merely combines PDE solvers and constitutive models into new systems of PDEs. Rapid prototyping utilizes the most abstract layers, while fine-tuning of the code is enabled by operating directly at the desired lower-layer objects. More specific information about the design of Diffpack can be found in [2,3,6].

Programming with objects

Objects contain data and functions operating on the data. A matrix is a simple example. A matrix object typically contains a memory segment holding the matrix entries, integers for the number of rows and

columns, and various functions for extracting entries, multiplying matrices with vector objects and other matrix operations from linear algebra. The implementation of an object is in C++ and Java made in terms of a *class*, while in Fortran 90 the equivalent concept is *module*.

In the PDE world, many matrix formats exists and must be available to the user of a simulation package, preferably in a transparent way. Each matrix format can be represented as a class. All matrix classes should hide their internal representation of the matrix data and only show a common set of operations on matrix objects for public use. One can then collect the matrix classes in a *class hierarchy*, with an "abstract" generic matrix class as parent for all the format-specific classes. This generic parent class, often called base class or super class, contains no data; it just specifies a common interface to all matrix objects. The point of object-oriented programming is to program only in terms of the base class. This hides all the intricate details of sparse matrix storage schemes and the bunch of arrays that frequently pollute Fortran 77 codes when calling, e.g., linear system solver routines. Instead, the matrix appears as a single base class object. The magic of object-oriented programming is that the compiler generates information such that the computer keeps track, at run time, of *which* type of matrix format that is hidden under the name of a base class; the programmer never needs to know whether the base class matrix actually is a banded or a diagonal matrix. In case it is a diagonal matrix, launching a matrix-vector product will automatically lead to a transparent call to the tailored matrix-vector product implementation in the diagonal matrix class. Optimal efficiency is hence not disturbed by programming with base classes.

A similar approach can be used to make class hierarchies for different vector formats, linear system solvers, preconditioners, solvers for nonlinear algebraic systems, and so on. Throughout the code that applies solvers and preconditioners, one can only see track of the base class, not storage structures or algorithmic details of the individual numerical strategies. Adding a new preconditioner does not affect any linear solver and vica versa. With just a recompilation, the code calling linear solvers with immediately work with the new methods. Such mechanisms contribute to modularity and extensibility, as well as flexibility in combining different numerical approaches.

Grids constitute another example on the usefulness of object-oriented programming. The Diffpack finite element engine was implemented using a plain grid class. Some years later, different types of *adaptive* grid classes, enabling local mesh refinements, were added to the libraries. With a couple of new functions in the interface of the original grid class, this class could act as a base class for the adaptive grid classes. In practice, it meant that all the existing library code and applications (after a recompilation) immediately worked with any of the new adaptive grid classes.

The application code is also programmed as a class, which merely collects objects for grids, fields over grids, linear systems and solvers together with problem-dependent information about the PDEs being solved. In a finite element application, the programmer's work is limited to implementing input for physical parameters in the problem, a function for setting essential boundary conditions, and a function for sampling the integrands in the variational formulation. If the programmer wants more control, e.g., avoiding numerical integration and providing a problem-dependent preconditioner, this is straightforward. PDE solver classes can be combined to solve systems of PDEs or embedded in algorithms for optimization of design or process features. The bottom line is that objects let you build with bricks and walls instead of gluing matches.

When all parts of a package is built on object-oriented concepts, one obtains a high degree of flexibility with respect to adding new functionality and combining numerical approaches and mathematical

models. Put in another way, the functionality of the package grows exponentially as new modules are incorporated.

Support for parallel computing, domain decomposition, generic multigrid modules, and mixed finite elements have been successfully incorporated as add-on modules to the Diffpack libraries (though sometimes with small adjustments in minor parts of the libraries). It sounds reasonable that such fundamental numerical approaches would require careful consideration in the design phase of a generic package like Diffpack. Nevertheless, our experience shows that a clean design in terms of classes and class hierarchies provides the necessary modularity for allowing easy integration of new modules in an existing library. More importantly, existing applications can with the order of 10 lines of code utilize adaptivity, or multigrid, or parallel computing, or a combination of all.

We remark that the way we use object-oriented programming in Diffpack is currently supported by C++ and Java, but unfortunately not by Fortran 90/95.

What Diffpack has been used for

The basic idea of Diffpack, namely that one can provide a generic library and create small-size application codes to solve a wide range of PDE problems, is by now clearly demonstrated. Some examples on existing Diffpack simulators cover

- the equations of applied mathematics (Poisson, heat, and wave equations),
- transient thermo-elasticity,
- several types of Navier-Stokes solvers,
- large-strain elasto-plasticity for metal forming,
- optimization and design of metal forming processes,
- multi-phase porous media flow,
- stochastic groundwater flow,
- fluid-structure interactions,
- flow processes with melting and solidification,
- thermal injection molding processes with free surfaces,
- fully 3D nonlinear potential theory for water waves,
- Boussinesq models for tsunami propagation,
- option price modeling,
- the electrical activity in the heart.

Many of the mentioned simulators employ adaptivity, parallel computing, multigrid, and problem-dependent optimizations. As one can see from the list, the application of Diffpack to computational mechanics is extensive and will probably increase significantly when support for advanced numerical methods migrate from the research level to the commercial Diffpack distribution.

The real advances in computational mechanics software must also incorporate full problem solving environments, with advanced easy-to-use graphical interfaces to grid generation, problem definition, simulation, visualization, and report generation. Diffpack's focus is on being a flexible, high-quality numerical engine in such problem solving environments. Grid generation and visualization are therefore not part of Diffpack, although the package comes with simple tools for this purpose to get started smoothly. The Diffpack distribution provides an extensive set of interfaces to preprocessors and

visualization software for professional use. Diffpack has various types of user interfaces: a command-line mode, a file mode, and a GUI. The Windows version has a full-fledge graphical working environment that integrates visualization by Vtk. These environments are tailored to programmers and researchers, not end-users of industrial applications. The main source for learning Diffpack and its view on numerics and applications is the book [6], see www.nobjects.com/Book. Associated with the book is a CD-ROM containing a test version of Diffpack along with all the sample applications from the book. The examples cover heat transfer, wave phenomena, thermo-elasticity, elasto-viscoplasticity, and viscous fluid flow, whereas the numerics concentrates on finite element methods, finite difference schemes, and iterative methods for linear systems, exposed in a form that maps conveniently over to Diffpack code.

Computational efficiency is a major issue when prototype solvers from research are to be migrated to industrial codes, and the use of C++ could in this regard be of concern. C++ certainly gives lots of tools for creating very inefficient numerical code, but it also gives you some tools to beat Fortran 77 efficiency [7, ch. 2]. Our experience is that a careful use of C++, with as much number crunching as possible in lower layers, using only ''do-loops'' and plain arrays, combined with object-orientation for administering the program flow in higher layers, results in code that comes close to Fortran 77 on benchmarks. While Diffpack codes have a high degree of built-in flexibility, e.g., finite element codes works with all kinds of elements in 1D, 2D, or 3D, benchmarking often involves tailored Fortran codes with lots of hand optimizations. The structure of the general Diffpack codes enable a programmer to add optimized code in an afternoon that limits the flexibility and takes advantage of special structures in the problem and special choice of elements. Again, object-oriented programming is a key technology for going from a general to a specialized/optimized application code in a clean and fast way and for letting the two versions of the code exist side by side, sharing everything that is in common.

Bibliography

1. E. Arge, A. M. Bruaset, and H. P. Langtangen, editors. *Modern Software Tools for Scientific Computing*. Birkhauser, 1997.
2. A. M. Bruaset and H. P. Langtangen. A comprehensive set of tools for solving partial differential equations; Diffpack. In M. Dæhlen and A. Tveito, editors, *Mathematical Models and Software Tools in Industrial Mathematics*, pages 61-90. Birkhauser, 1997.
3. A. M. Bruaset and H. P. Langtangen. Object-oriented design of preconditioned iterative methods in Diffpack. *Transactions on Mathematical Software*, 23:50-80, 1997.
4. Diffpack: http://www.diffpack.com/
5. Y. Ishikawa, R. R. Oldehoeft, J. V. W. Reynders, and M. Tholburn, editors. *Scientific Computing in Object-Oriented Parallel Environments*. Springer-Verlag, 1997.
6. H. P. Langtangen. *Computational Partial Differential Equations - Numerical Methods and Diffpack Programming*. Springer-Verlag, 1999.
7. H. P. Langtangen, A. M. Bruaset, and E. Quak, editors. *Advances in Software Tools for Scientific Computing*. Springer-Verlag, 1999. In press.
8. Object-Oriented Numerics home page: http://www.oonumerics.org/
9. R. Sampath and N. Zabaras. An object-oriented implementation of adjoint techniques for the design of complex continuum systems. *Int. J. Num. Meth. Engng.*, 1999.
10. N. Zabaras and A. Srikanth. An object-oriented programming approach to the Lagrangian FEM analysis of large inelastic deformations and metal forming processes. *Int. J. Num. Meth. Engng.*, 1999.

Modelling of Microelectromechanical Systems (MEMS) - Theoretical and Computational Challenges

R.M. Nieminen, J. Järvinen and P. Råback
Laboratory of Physics–COMP
P.O. Box 1100
FIN–02015 HUT, Finland
and
Center for Scientific Computing
P.O. Box 405
FIN–02101 Espoo, Finland

Abstract

Predictive modelling of microelectromechanical (MEMS) devices and their manufacture is an important and growing area for methods developed under the domains of computational mechanics, fluid dynamics and microscopic approaches such as molecular dynamics, Monte Carlo models and quantum physics. This talk addresses some of the challenges in this area from the viewpoint of multiscale modelling, which spans several length and time scales.

1 Multiscale modelling of materials processes and structures

Modelling and computational simulation of materials and their processing is a rapidly advancing activity [1]. One can distinguish four levels of simulation: electronic structure, atomistic, mesoscale (microstructure), and continuum. These levels are individually suited to probe and investigate the properties and behavior of materials on certain length and time scales, ranging from nanometers to meters and from femtoseconds to days. Each level of simulation has a community of practitioners developing the models and computational techniques and investigating their application s.

There are two considerations which have begun to weld together the traditionally separate communities. One is based on the importance of advanced computational methods shared by all materials modellers. For example, large-scale materials simulation often focuses on the repeated manipulation of huge sparse matrices or the efficient solution of equations describing dynamical behavior.

The second consideration stems from the important couplings of the different length and time scales. As the ultimate goal is to predictively understand macroscopic materials from their microscopic constituents, these couplings have to be established as seamlessly as possible.

At the electronic-structure level, methods based on quantum-mechanical density-functional theory have reached a high level of accuracy and applicability. However, such methods are computationally very intensive and presently practical for systems containing at most a few hundred atoms.

The connection to the next, atomistic level is nowadays quite well established, and techniques such as molecular-dynamics or Monte Carlo simulations can benefit of increasingly accurate

interatomic potentials. With simplified force laws, molecular-dynamics simulations can now be performed for systems containing tens of millions of atoms.

The coupling of the atomistic description to the mesoscale models is absolutely essential to the successful realization of multiscale modelling. This area is subject to intensive current research activity [2]. One obvious possibility is to obtain such coarse-graining of molecular-dynamics trajectories that can be turned into a finite-element or finite-difference type formulations. Other suggested approaches are based on lattice-gas or cellular-automaton-type discretisations, where the local rules are obtained from coarse-grained atomistic simulations.

The general application area of micrometer-scale, three-dimensional devices based on versatile, adjustable materials properties exemplifies the emerging need for multiscale modelling and simulation. These are devices where one utilizes not only the materials' electronic and magnetic properties (derived from electronic structure) but also the mechanical properties (such as elasticity or flow).

2 The MEMS concept

The acronym MEMS (MicroElectroMechanical Systems) stands for systems which are small in size and have both electromagnetic and mechanical functions. The main application categories of MEMS are sensors which observe the chemical and physical environment and actuators which modify the environment.

The basic substrate for MEMS devices is silicon, although other semiconductor (III-V compounds, SiC, diamond) and insulator (perovskites, fluorides) materials are used as well. Magnetically controlled actuator devices such as those based on so-called magnetic shape-memory alloys are also increasing in importance.

3 Simulation of device processing

The processing of MEMS devices introduces some new computational challenges. Some of the manufacturing technologies, such as various types of litography and chemical vapor deposition (CVD), are similar to those widely used in integrated-circuit (IC) manufacturing. Specific for MEMS is the need for bulk micromachining techniques. The usual technique is some variant of chemical etching: isotropic, anisotropic and reactive ion etching.

In etching one needs to be able to simulate how the shape transforms, or at least be able to predict the final shape. A number of different computational techniques have been used to do this: cellular automata, level-set methods, front tracking etc. The difficulty is that the changes in shape cannot usually be described by continuous transformations. Also the topology of devices may change.

4 Simulation of device responses

MEMS devices are inherently coupled. In addition to mechanical and electrical response, also thermal, optical, magnetic and chemical phenomena may occur. Fluid flows within the devices may also be present. Therefore the simulation of MEMS devices usually leads to a multiphysics problem [3].

The multiphysics characteristics may be manifest in several ways. The different phenomena can have vastly different time and size scales which require special simulation strategies. For

example, the different equations need to be solved in different computational domains, with the results mapped between them.

The mapping requires often special iteration schemes. If the different phenomena are loosely coupled, a segregated scheme where the individual equations are solved alternatingly may be used. Such schemes have the advantage that it is possible to verify various physical phenomena separately. Tightly coupled systems may, however, require also concurrent approaches where all the unknown equations are solved at the same time. This increases the complexity but may pay off in faster convergence. Generally, it is not possible to prove that a coupled system has a unique solution. Therefore special care must be used to evaluate the the physical meaningfulness of the solution.

The small size introduces new physical phenomena while some features important at larger length scales may become irrelevant. As the device size shrinks, surface effects become increasingly important. For example, the capillary force due to surface tension becomes quite important in the modelling of microfluids. Likewise, electric double layers may be formed at the interfaces, with important consequences for the flow properties. The double layers are due to the electric forces between dipoles or ions at the surface. In fluid flows diffusion (friction) often dominates convection.

The devices are usually modelled by means of differential equations that assume continuity. At small sizes this assumption may become questionable. For example, at small pressures the mean free path of gas particles may be significant compared to the size of the device. Then the traditionally used Navier-Stokes equations do no longer describe the behavior accurately.

There are also some highly nonlinear phenomena. For example, in acceleration sensors it may be possible that for a split second the moving part may be at contact with the body. The capturing and modeling of this moment is a challenge.

5 Packaging and integration

MEMS devices often constitute only single components in complex, integrated circuits. The system designers cannot therefore afford to consume too much time for the modeling of the MEMS devices. Thus they need macromodels which describe the device functions in terms of "equivalent circuits". These macromodels may then be used in circuit design and analysis programs. Often the macromodels are derived from simplified representations of the components. Yet macromodels have to have the right physical dependencies. A macromodel can be made more accurate by using the simulations of the true (full) device to derive the characteristic parameters of the equivalent circuit.

6 Software for multiphysical modelling in MEMS

Numerical simulation of multiphysics problems such as encountered in MEMS is a very challenging task. Typically, commercial or in-house software packages are dedicated to specific problems, i.e., fluid dynamics, structural mechanics or electromagnetism. The trend towards multiphysical features is obvious in the future, and some steps to this direction have already been taken.

ANSYS and FIDAP are examples of commercial softwares offering multi-physical tools. ANSYS, which is a popular software suite in structural mechanics, contains ANSYS/Flotran and ANSYS/Emag modules for simulating fluid flows and electromagnetics. FIDAP covers, not only phenomena in fluid dynamics, but also interactions between fluid flows and structures.

In-house software can benefit from increased flexibility and the utilization of modern scientific computing tools. Multiphysics problems are often so complicated that self-tailoring is a necessity. Since source codes are available, phenomena in electromagnetism, fluid flow, mechanics and heat transfer can be coupled and solved efficiently. Typically, modern in-house software are based on new programming languages (F90/95, C++), state-of-the-art numerical methods (such as stabilization in finite element methods), parallelization, and advanced mathematical and visualization libraries (LAPACK, Tcl/Tk). Solving of multi-physics problems requires a large amount of computer resources, and parallelized software offers a way to speed-up the research and development cycle.

One example of in-house and multi-physical tool is ELMER software [4], which has been developed within the Finnish national computational fluid dynamics technology programme. The development has been carried out in close collaboration between research institutes (Center for Scientific Computing, Helsinki University of Technology, Technical Research Centre of Finland and University of Jyväskylä) and industry (Okmetic Ltd., Valmet Ltd.). The role of industrial companies has been considerable in order to direct the development towards multiphysical applications.

ELMER consists of a preprocessor, a solver and a postprocessor. It solves multiphysical applications such as compressible and incompressible flows, laminar and turbulent flows, heat transfer by conduction, convection and radiation, stresses and displacements in elastic bodies, problems in magnetohydrodynamics and vibration, many of which are present in MEMS applications.

Each phase of ELMER can be used independently. It supports various computer architectures, from PCs to parallel supercomputers. Universities, research institutes and industry can utilize ELMER software in their research and development. It is a national resource which can be tailored towards multiphysical application including those relevant for MEMS technology.

7 Concluding remarks

The manufacture and application of MEMS devices is replete with phenomena which challenge computational scientists. Micromachining, crack propagation in processed structures, fluid flow in micron-scale channels, coupled electromagnetic and mechanical response over large frequency intervals, and integration of MEMS devices to complex circuitry are examples of phenomena where there is growing need for accurate modelling and simulation. From the basic science point of view, a major intellectual challenge is multi-scale modelling and simulation capable of seamless description over many decades of length and time, from microscopic to macroscopic.

References

There is a rapidly increasing literature in the area of materials modelling. For example, the journal *Computational Materials Science* (Elsevier Science Publishers, Oxford, England) is completely devoted to this topic.

J. Q. Broughton, F. F. Abraham, N. Bernstein and E. Kaxiras, *Phys. Rev. B* **60**, 2391 (1999).

For a recent, extensive application of modelling to a multiphysics problem, see P. Råback: *Modeling of the sublimation growth of silicon carbide crystals*, Dr. Tech. thesis, Helsinki University of Technology, Espoo 1999.

J. Järvinen, J. Malinen and J. Ruokolainen: *ELMER: a multiphysical tool for academic and industrial research*, CSC Reports on Scientific Computing, Espoo, Finland, 1997-1998, 1999.

Artificial Finger Joints — a Mechanical and Material Design Challenge

Göran Sandberg[1], Per-Erik Austrell[1], Christer Ljung[2]

Lund University, Department of Mechanics and Materials
[1]Structural Mechanics, [2]Solid Mechanics

P.O. Box 118, SE-221 00 Lund, Sweden

e-mail: goran@byggmek.lth.se, per_erik.austrell@byggmek.lth.se, christer.ljung@solid.lth.se

Background

There are 25,000 people in Sweden who suffer from such cases of deformed and ruined joints that their chances of leading normal lives have been severely limited. Rheumatic complaints not only affect the elderly, but a substantial part of the patients suffering from rheumatoid arthritis are young people between 10 and 30 years of age; this is known as juvenile rheumatism. These people are in dire need of artificial joints to be able to perform simple, every-day chores. Rheumatoid arthritis is an inflammatory condition in bones and ligaments, which in its final stages for all practical purposes has rendered the joint immovable. The lower left-hand picture shows a hand deformed by rheumatoid arthritis, albeit not fully developed. In many cases the hand is entirely closed. In the upper right-hand part of the picture the twisted joints are shown, and in the lower part they have been corrected by substituting artificial joints for them.

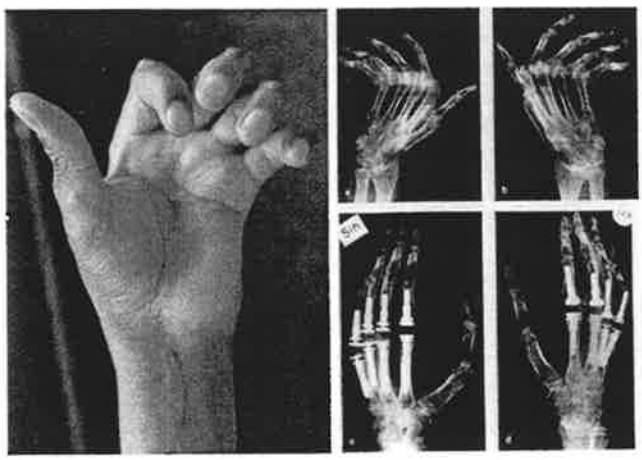

Figure 1: *Hand with a deformity caused by rheumatoid arthritis (left). "Before" and "after" surgically inserting artificial joints in the metacarpophalangeal or knuckle joint (right).*

Previous Artificial Finger Joints

In the last 40 years, several different artificial finger joints have been developed, see Ref. [1]. However, they have all shown various deficiencies. The pictures below show a number of the attempts made in this area.

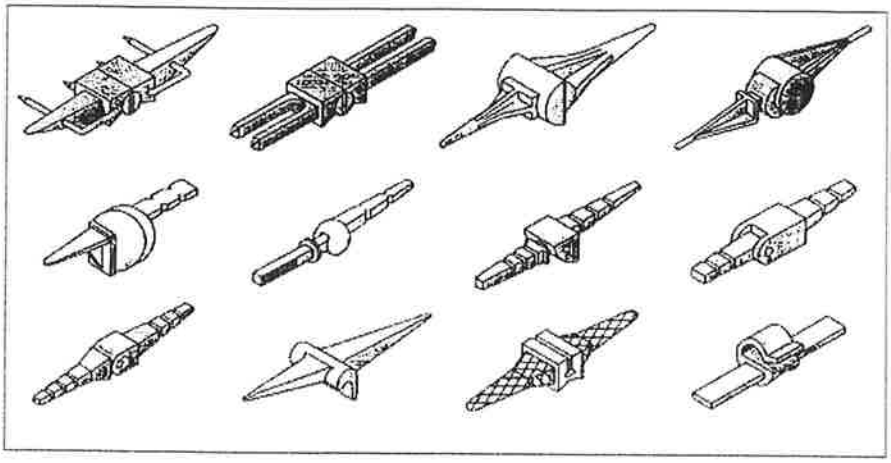

Figure 2: *This picture shows some first and second generation artificial finger joints. Design according to (top row) Brannon and Klein, Flatt, Griffith-Nicole, Schetrumpf, (middle row) Schultz, Steffee, St. Geogre-Buchholtz, KY Alumina Ceramic, (bottom row) Minami Alumina Ceramic, Swanson, Neibauer, Helal Flap.(from Ref. [1])*

These artificial finger joints have all, to a varying degree, had the ambition of producing as natural a locomotive pattern as possible. However, several of the early designs entailed substantially simplified finger movements. The early artificial finger joints were essentially simple hinge constructions, marred by a number of mechanical problems.

The artificial joints containing polymeric substances are based on silicone rubber. The Swanson joint, see Figure 2 bottom row, second from the left, for example, is made entirely of silicone rubber. In fact this is one of the most frequently used joint replacements today, particularly in the United States, despite documented insufficiencies as regards both the stability of the fixing and the mechanical functioning (Ref. [1]). This joint has no steady fixing. The artificial joint is inserted directly into the shaft of the bone. There are also artificial joints imitating real joints, including ball and socket. Such prostheses exist, but they are best suited for patients with healthy ligaments.

One of the more successful attempts was made by Professor P-I Brånemark. This artificial joint, see Figure 3, is made of silicon rubber with titanium pins fixed in titanium casings in the hand and in the finger respectively. The titanium casings are fixed in the shafts of the bone through "osseointegration", in accordance with the P-I Brånemark method.

The problem with silicone is its insufficient fatigue strength, which leads to a rather limited durability; as a result of material breakdown, approximately 10% of all patients in Sweden after as short a time as two years suffer from such substantial damages and deformities that a substitution of the joints has to be made. The insufficiencies of this artificial joint can be entirely attributed to the flexible elastomeric part of the joint, nowadays being made of a silicone rubber substance, see Ref. [3].

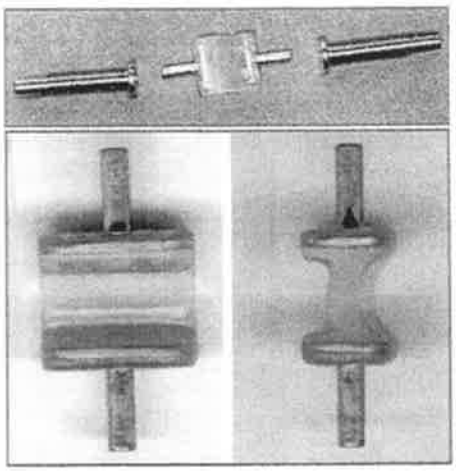

Figure 3: *The artificial finger joint according to the PI Brånemark system consists of titanium casings fixed in the shafts of the bone. The rubber construction constituting the flexible part of the joint is shown separately in two views.*

Mechanical Prerequisites

Ligaments give the healthy hand its stability and progressive stiffening at an increased bending from a state of rest, which applies to a clean bending as well as a lateral movement. In rheumatic patients, the ligaments are also damaged. This means that a functioning artificial finger joint must give the corresponding progressive stabilisation at an increased bending from a state of rest. Hence, great demands are made on materials, combination of materials and geometric design.

Figure 4 below shows the different typical handgrips that constitute the design prerequisites as regards a functioning joint. The table shows the frequency with which the different grips are used.

Table 1: *Percentage use of the eight most common handgrips in activities of daily living (from Sollerman 1995)*

Pinch (hand)	%	Grips (hand)	%
Pulp pinch	20	Diagonal volar pinch	15
Lateral pinch	20	Transverse volar grip	14
Tripod pinch	10	Spherical volar grip	4
Five-finger pinch	15	Extension grip	2

Two reference cases of loading have been used in the current study to evaluate existing designs as well as to provide a basis for a new design of the joint. The cases of loading studied are a bending of the joint without external loading, and grip loading. An important observation is the fact that almost only compressive loads are found in the natural joint. This is especially true of the grip case, when the pressure forces in the joint can become considerable. A free body diagram of a finger in connection with a grip loading, as shown in the figure, indicates that the force N in the joint must be a pressure force.

The force S from tendons on the inside of the hand produces the grip force F. The

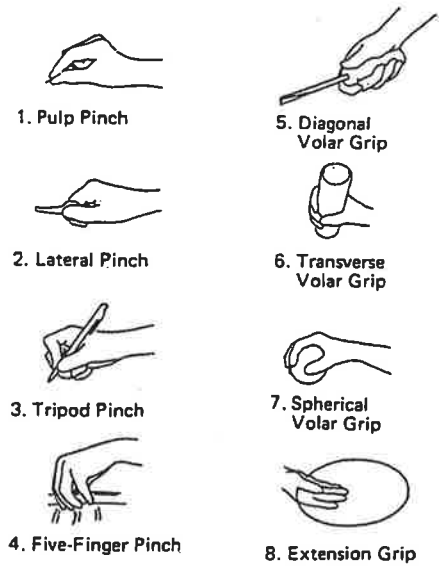

Figure 4: *Definition of different occurring finger and hand grips (from Sollerman 1995).*

moment equilibrium for the uncovered finger then demands that the force of the joint N is a pressure force, which could be several times greater than the grip force. These forces are used in the simulation of the artificial joints.

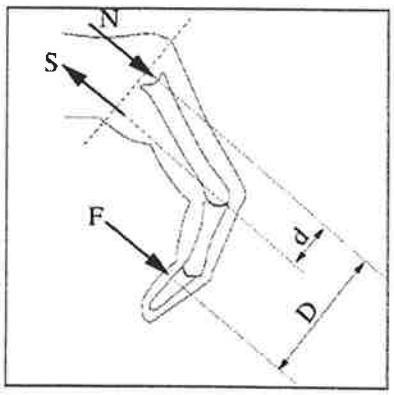

Figure 5: *To achieve a simple description of loading prerequisites, two basic load cases have been studied: Flexion without external loading and the grip case. finger joint has been studied.*

Material Prerequisites

The use of foreign materials in the human body is surrounded by rigorous regulations regarding biocompatibility. The introduction of new materials included in artificial joints must therefore be preceded by considerable investigations to find out whether the potential materials pose a risk as regards toxicity. The use of rubber materials is of a considerable

advantage because the design can be made in such a way that the progressive stiffening found in the healthy joint also can be built into the artificial joint.

Silicone rubber is a commonly used material for implantation. Several studies have indicated that this substance is biocompatible and it is used for different applications, for example as artificial joints, but also in other functions such as artificial blood vessels. Components outside the body, i.e. in connection with dialysis, also belong here.

The insufficient fatigue strength of silicone rubber is a major problem. Figure 6, below shows the fatigue limits for some rubber materials. It is obvious that silicone rubber actually is the poorest choice from a strictly mechanical viewpoint. The reasons for not changing to other substances are uncertainties concerning their biocompatibility. In several cases the elastomer has been classified as biocompatible in scientific tests. Its failure to make an impact in biomechanics and similar areas is probably caused by fear of legal complications.

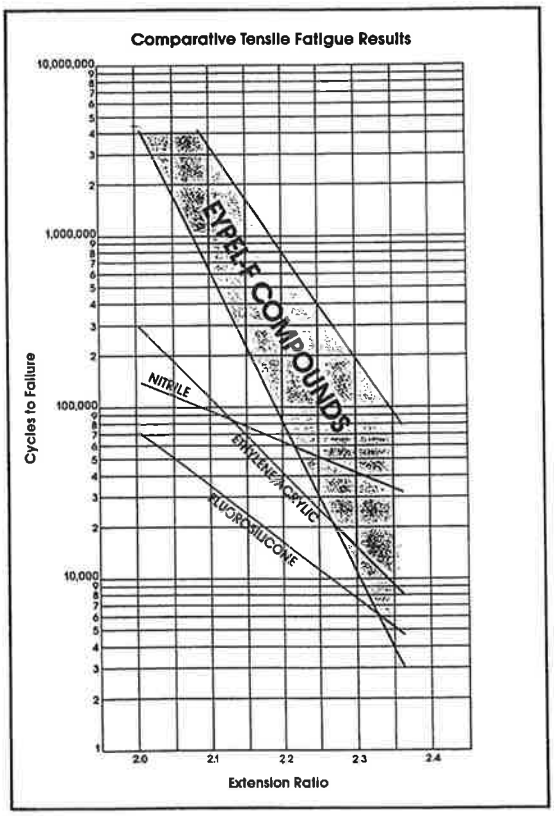

Figure 6: *Diagram of fatigue strength in some rubber substances* . Silicone has the lowest fatigue limits. From Reference [5]

Analysis of Existing Joint

An existing design, discussed earlier and shown in Figure 3, has been analysed as regards bending without external load and grip loading. Figure 7 shows the finite element mesh

of the crucial part of the artificial joint and the deformed joint in the case of grip loading. The loading case has been achieved by simulating tension loading in a tendon on the lower side of the component. The fixing of the tendon is not symmetric in relation to the component, resulting in an asymmetrical deformation as is seen in the figure.

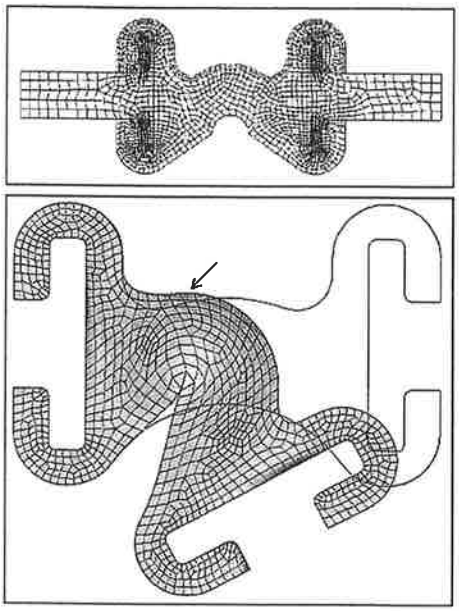

Figure 7: *Top figure show the finite element mesh for the old design. The bottom figure shows the result from one simulation of the old design. The arrow indicate the position for high tensile stress. Indeed the current design tends to break at that specific point.*

Below are some disadvantages as regards the existing design.

- The component is a "beam model", causing an increased pressure loading to increase the tension strain on the top side of the component, and hence also increasing the risk of crack formations.
- As the plates with the pin are moulded instead of vulcanised, there is a risk of wear on the rubber substance from the inside. This risk increases through the sharp-edge design of the plates.
- The symmetrical design, in combination with the design of the plates, result in a heavy loading of the component at great compressive loads as the edge of the left plate causes a concentrated loading in its contact with the right part of the component.

New Design

The ambition of the current study is to produce a design that works better as a natural joint by absorbing heavier compressive loads without becoming stiffer when bended unloaded.

The aims can be summarised as follows:

- Lessen the traction strains, which could cause fatigue cracks.
- Achieve a function resembling a natural joint in being easy to bend while at the same time having the capacity to absorb pressure forces.
- Prevent wear and crack formations at the titanium plates/pins.

References

[1] D. J. Beevers and B. B. Seedhom, *Metacarpophalangeal joint prostheses; a review of the clinical results of post and current designs*, J Hand Surg 20B:2, 1995

[2] C. Sollerman, A. Ejeskär, Sollerman *Hand function test; a standardised method and its use in tetraplegic patients*, Scand J Plast Reconstr Hand Surg 29: 167-176, 1995.

[3] J. M. T. Penrose *et. al*, *An examination of on-piece metacarpophalangeal joint implants using finite element analysis*, J Med Eng & Tech 20 (4–5): 145–150, 1996.

[4] S. D. Cook *et. al*, *Long-term follow up of pyrolytic carbon metacarpophalangeal implants*, J Bone & Joint Surg, 81–A (5): 635–648, 1999.

[5] From European Rubber Journal, 1987.

Author Index

HELSINKI UNIVERSITY OF TECHNOLOGY LABORATORY OF THEORETICAL AND APPLIED MECHANICS
PUBLICATIONS

No. 48	Salonen, E-M. and Reivinen, M. Behaviour of an Arch Element. 1998.
No. 49	Ranta, M.A, Hertzen, R. von ja Holmlund, U. Kilpajuoksun matemaattisesta teoriasta. 1998.
No. 50	Freund, J. and Salonen, E-M. Sensitizing the Timoshenko Beam and the Reissner-Mindlin Plate Finite Element Solution 1998.
No. 51	Lempinen, A. Thermomechanical Models for Expansive Clays: I. Reversible Process. 1998.
No. 52	Rahikainen, A. Kuulantyönnön pyörähdystyylin työntötekniikka 1996 ja 1997. 1998.
No. 53	Ranta, M.A., Hertzen, R. von Rahikainen, A. Laskennallinen menetelmä liikeanalyysikameran resoluution parantamiseksi. 1998.
No. 54	Taipale, J. Rakenteiden taloudellinen optimointi. 1999.
No. 55	Ranta, M.A., Hertzen, R. von and Rahikainen, A. Smoothing of Random Errors in the Analysis of Throwing Events. 1999.
No. 56	Puckett, A.D. and Hertzen, R. von State-of-the-Art Review of Rotordynamics. 1999.
No. 57	Kouhia, R. and Mikkola, M. (editors) Proceedings of the Twelfth Seminar on Computational Mechanics (NSCM-12).

ISBN 951-22-4731-3
ISSN 1456-6311